New insights into the structure of the Earth's crust on- and offshore Northern Victoria Land, Antarctica, by means of gravimetric and magnetic 3D modelling

Dissertation
zur Erlangung des akademischen Grades doctor rerum naturalium
(Dr. rer. nat.)

von
Dipl.-Geophys. Peter Schindler

vorgelegt dem Rat der
Chemisch-Geowissenschaftlichen Fakultät
der
Friedrich-Schiller-Universität Jena

Jena, im August 2016

Referees/Gutachter:

1. PD Dr. Thomas Jahr, Friedrich-Schiller-Universität Jena
2. Prof. i.R. Dr. Gerhard Jentzsch, Friedrich-Schiller-Universität Jena

Day of Defense/Tag der Verteidigung:

December 16, 2016 (16. Dezember 2016)

Abstract

Victoria Land, Antarctica, has been in the focus of German scientists for more than 30 years now. Many expeditions have been undertaken to reveal the geologic structures and clarify the geodynamic processes, which have led to the present situation. An important part in the exploration is taken by geophysical measurements, as such measurements can be carried out in places, where no outcrops exist, and with limited expenditure of personnel, time and material large areas can be covered. Thus it is possible to connect distant outcrops through glaciated areas, or extend geologic knowledge to off-shore regions. Over the past decades, especially aeromagnetic measurements have been carried out extensively. The present study for the first time combines the existing aeromagnetic data to a large data set, almost completely covering Victoria Land. These data were complemented by a gravimetric anomaly generated from a global gravity field model. With subsequent 3 D modelling, carried out separately for both data sets, it was possible to develop an idea of the crustal structures in Victoria Land.

The gravimetric model shows a distinct mountain root below the Transantarctic Mountains. As these result from rifting processes, the presence of a mountain root is not to be expected. This root most probably is a remnant of the early paleozoic, accretionary Ross orogen which forms part of the basement of the Transantarctic Mountains. Another option may be the ceasing of the rifting processes in the past, so that the Transantarctic Mountains could develop a mountain root. As the West Antarctic Rift System is still active – e.g., volcanic activity can be observed in several places – this explanation is improbable. Especially in northern Victoria Land, the model is characterized by basement highs and lows, which follow the course of known fault zones, but are anti-correlated to existing graben structures.

The magnetic model, which is limited to the northern coastal area along the Penell and Oates Coast and George V Land, shows a North-South striking basement high in the West, with gentle slopes to the West and East. The basement high coincides with a basement high from the gravimetric model and the Rennick graben, a prominent graben structure; it is, therefore, also anti-correlated. Other structural features known from geology are not obvious in the magnetic model.

In both models it is possible to trace the Rennick graben by a basement high, which thus has to be an inverted graben; glacial erosion has possibly excavated the basement at some places. The Rennick graben can also be traced through the continental shelf area

to the North, whereas other fault zones are only supported by the gravimetric model; in the magnetic model, no more structural features are obvious.

Zusammenfassung

Victoria Land in der Antarktis ist seit mehr als 30 Jahren ein Schwerpunkt deutscher Antarktis-Forschung. Viele Expeditionen wurden durchgeführt, um geologische Strukturen zu untersuchen und die geodynamischen Prozesse zu beleuchten, durch die die Entwicklung der Region geprägt wurde. Ein wichtiger Baustein in der Erforschung besteht in der Durchführung geophysikalischer Messungen. Solche Messungen können auch dort ausgeführt werden, wo keine Aufschlüsse existieren. Außerdem ist es möglich, mit begrenztem Einsatz von Personal und Material und in einem begrenzten Zeitraum große Gebiete abzudecken. Dadurch können entfernte Aufschlüsse auch über vergletscherte Bereiche hinweg miteinander in Beziehung gebracht oder bestehende geologische Kenntnisse auch über die Küstenlinie hinaus in den Schelfbereich hinein erweitert werden.

In den letzten Jahrzehnten wurden insbesondere großräumige aeromagnetische Messkampagnen durchgeführt. Die vorliegende Arbeit kombiniert erstmals die verfügbaren aeromagnetischen Datensätze zu einem großen Datensatz, der Victoria Land fast vollständig abdeckt. Dazu wurden die Daten der einzelnen Messkampagnen auf die einheitliche Epoche 1980.00 transformiert und auf eine gemeinsame Messhöhe von 2700 m fortgesetzt. Anschließend erfolgte eine Angleichung der Daten aneinander. Diesen Daten steht ein Datensatz zur Schwereanomalie gegenüber, der aus einem globalen Schwerefeldmodell abgeleitet wurde. Derartige Schwerefeldmodelle werden auf Grundlage verschiedenster Daten berechnet. Neben terrestrischen Messungen gehören dazu auch Ergebnisse von Schiffs-, Flug- und Satellitengravimetrie. Auf Basis dieser Daten kann eine Kugelfunktionsentwicklung des Schwerefeldes durchgeführt werden, die es erlaubt, für jeden Punkt der Welt einen Schwerewert zu bestimmen. Mit Hilfe der nachfolgenden 3 D-Modellierung, die getrennt für beide Datensätze ausgeführt wurde, war es möglich, eine Vorstellung der Krustenstuktur in Victoria Land zu entwickeln.

Im gravimetrischen Modell ist eine ausgeprägte Gebirgswurzel unter dem Transantarktischen Gebirge zu erkennen. Da dieses jedoch durch Rifting entstanden ist, kann man eine Gebirgswurzel nicht erwarten. Die Gebirgswurzel ist wahrscheinlich als Relikt des frühpaläozoischen akkretionären Ross-Orogens anzusehen, das im Grundgebirge des modernen Transantarktischen Gebirges erhalten ist. Eine andere Möglichkeit wäre, dass die Extensionsbewegung bereits vor längerer Zeit endete, sodass sich nachträglich eine Gebirgswurzel entwickeln konnte. Da das Westantarktische Riftsystem jedoch nach wie vor aktiv ist – unter anderem gibt es in verschiedenen Bereichen vulkanische Aktivität –

ist diese Möglichkeit unwahrscheinlich. Insbesondere im nördlichen Victoria Land ist das Modell von regionalen Hochs und Tiefs des Basements gekennzeichnet, die dem Verlauf bekannter Störungszonen folgen, aber mit vorhandenen Grabenstrukturen antikorreliert sind.

Das magnetische Modell, das den nördlichen Küstenbereich entlang der Penell- und Oates-Küste und George-V-Land umfasst, ist durch ein nord-süd streichendes Basement-Hoch im Westen gekennzeichnet, das nach Westen und Osten sanft abfällt. Dieses Basement-Hoch stimmt mit einem Basement-Hoch aus dem gravimetrischen Modell überein und erstreckt sich entlang des Rennick-Grabens, einer großen Grabenzone. Auch das magnetische Modell zeigt demnach eine antikorrelierte Struktur. Weitere aus geologischen Untersuchungen bekannte Strukturen sind im magnetischen Modell nicht zu erkennen.

In beiden Modellen tritt entlang des Rennick-Grabens ein Basement-Hoch auf; daher muss der Graben invertiert worden sein. Möglicherweise wurde das Basement an einigen Stellen durch glaziale Erosion aufgeschlossen. Der Rennick-Graben kann außerdem entlang des Basement-Hochs nach Norden hin durch den Kontinentalschelf verfolgt werden, während andere Störungszonen nur durch das gravimetrische Modell gestützt werden und im magnetischen Modell nicht erkennbar sind.

Auf Basis der so gewonnenen Erkenntnisse können durch neue bzw. weitere Messmethoden und weitere Daten die erstellten Modelle überprüft und in Details ausgearbeitet werden.

Contents

List of Figures

List of Figures

List of Tables

List of Abbreviations

ADMAP	Antarctic Digital Magnetic Anomaly Project
a.s.l.	above sea level
BFZ	Balleny Fracture Zone
BGR	Bundesanstalt für Geowissenschaften und Rohstoffe, Hannover (Federal Institute for Geosciences and Natural Resources, Hanover)
DGRF	Definitive Geomagnetic Reference Field
EIGEN	European Improved Gravity model of the Earth by New techniques
Ganovex	German Antarctic North Victoria Land Expedition
GFZ	Helmholtz-Zentrum Potsdam – Deutsches GeoForschungsZentrum (Helmholtz-Centre Potsdam – German Research Centre for Geosciences)
GITARA	German Italian Aeromagnetic Research in Antarctica
GMT	Generic Mapping Tools
ICGEM	International Centre for Global Earth Models
IGRF	International Geomagnetic Reference Field
IGY	International Geophysical Year
IPY	International Polar Year
NGDC	National Geophysical Data Center
NOAA	National Oceanic and Atmospheric Administration
NVL	northern Victoria Land
PNRA	Programma Nazionale di Ricerche in Antartide (Italian Antarctic Research Program)
RAMP	Radarsat Antarctic Mapping Project
SCAR	Scientific Committee on Antarctic Research
SV	secular variation
SVL	southern Victoria Land
TAM	Transantarctic Mountains
TAMARA	Transantarctic Mountains Aerogeophysical Research Activities
TFZ	Tasman Fracture Zone
USGS	United States Geological Survey
WARS	West Antarctic Rift System

Chapter 1

Introduction

1.1 Antarctica

Antarctica is located almost completely south of 62.5° south (Faure & Mensing, 2010). It can be divided into the Antarctic Peninsula, West Antarctica, and East Antarctica. The border between West and East Antarctica is commonly drawn along the Transantarctic Mountains, the Pensacola Mountains, and the eastern border of the Filchner Ice Shelf. East Antarctica, which is located mostly at eastern longitudes, is the larger part (Fig. 1.1; Tingey, 1991). Another common method is to divide the continent into several sectors. Chiappini et al. (2002) name an East Antarctic, a Weddell Sea, and a Ross Sea sector, whereas others define different sectors like an Atlantic and an Indian Ocean sector as well as, consequently, a Pacific Ocean sector (e.g. Fischer et al., 2007). The Ross Sea sector, as given by Chiappini et al. (2002), ranges from 135° east to 255° east (105° west) and covers not only the Ross Sea itself but also neighbouring land areas, including the Transantarctic Mountains and Victoria Land.

The Transantarctic Mountains (TAM) rise up to more than 4.500 m above sea level (a.s.l.), while the Antarctic ice sheet mean surface elevation reaches more than 2.000 m a.s.l. In some parts, mainly in West Antarctica, but also at a few places in East Antarctica, the ice sheet thickness exceeds the surface elevation; the bedrock surface elevation is below sea level there (Faure & Mensing, 2010). The freely available ETOPO 1 data set of elevations of ice surface as well as bedrock surface (Amante & Eakins, 2009) shows this clearly. Fig. 1.2 and 1.3 illustrate the elevation situation in Victoria Land. Especially the bedrock surface elevation map (Fig. 1.3) reveals the line of the Transantarctic Mountains. All maps in this study not cited as taken from external sources were created with the "Generic Mapping Tools" (GMT) software package (Wessel & Smith, 1991; Wessel et al., 2013); several maps incorporate data from the coastline database contained in the software.

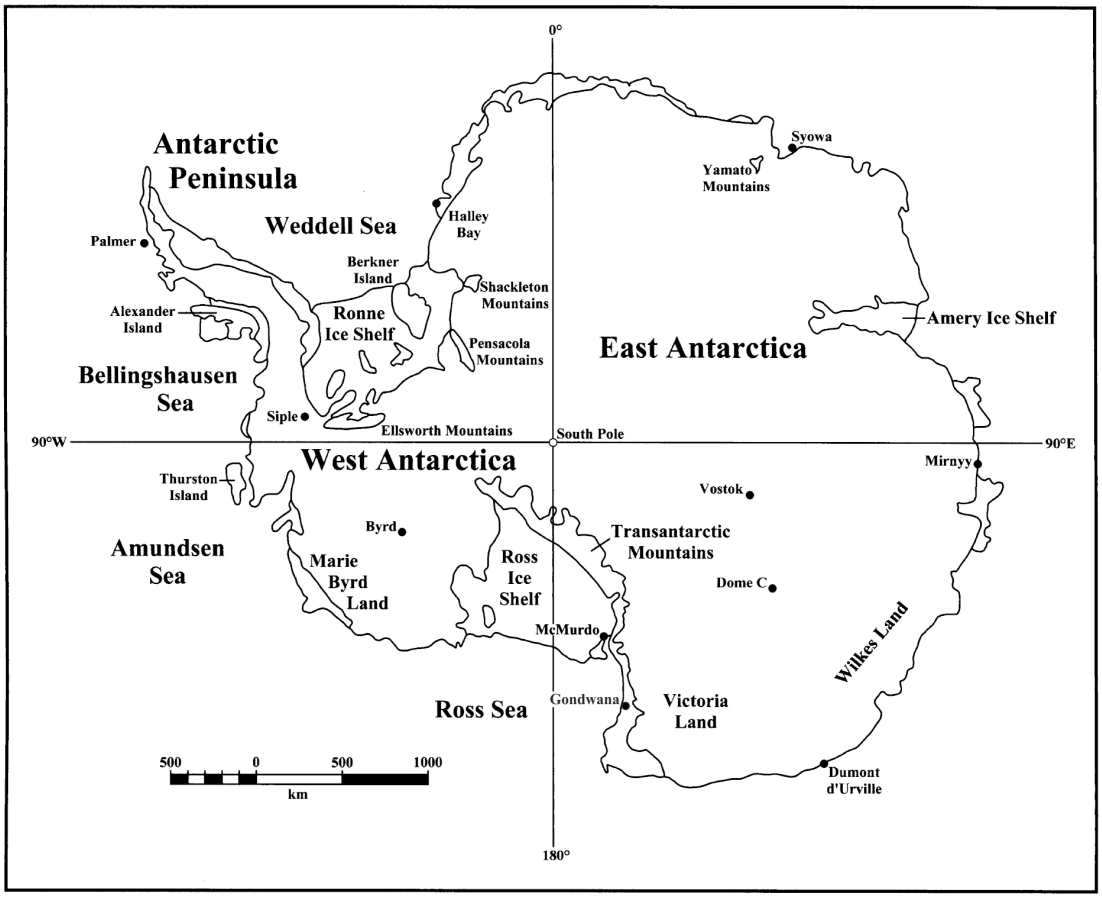

Figure 1.1: Map of Antarctica, showing West and East Antarctica and the Antarctic Peninsula, as well as some other geographic features. Several scientific stations are indicated by dots (after Faure & Mensing, 2010).

1.2 International Antarctic research

A good overview on the exploration of Antarctica can be found in the first chapter of Faure & Mensing (2010). The history of Antarctic research starting in the 18th century is described there, with details on several very famous expeditions like those led by Roald Amundsen or Robert Scott. Faure & Mensing (2010) name eight expeditions undertaken during the 19th century, and 19 more until 1950.

The exploration of Antarctica was supported very much through the first International Geophysical Year (IGY) 1957/58 which succeeded the two International Polar Years (IPY) in 1882/83 and 1932/33. During this time, 55 research stations in Antarctica were built by twelve nations. As a result of the IGY, in 1959 the Antarctic Treaty was signed by those twelve countries to enable further research in Antarctica in peace, without raising territorial conflicts, and preserving the environment; the territorial claims already named before are suspended. To coordinate the international research in Antarctica, the Scientific Committee on Antarctic Research (SCAR) was established. Actually,

around 30 countries are full members of the Antarctic Treaty, more than 20 additional countries are observing members. All full member countries appoint members to SCAR.

1.3 German research in Victoria Land

Victoria Land, and especially the northern part of it, has been a major target of German Antarctic research for almost 40 years now. From the late 1970s to the present, ten expeditions of the Ganovex program (German Antarctic North Victoria Land Expedition), organized by the German Federal Institute for Geosciences and Natural Resources (BGR), have been carried out (Bundesregierung, 2011; BGR, 1981; Roland, 1984; Tessensohn & Roland, 1987; Damaske & Dürbaum, 1988; Damaske & Fritsch, 1993; Roland, 1996; Estrada, 2003; Bozzo & Damaske, 2001; Damaske & Bozzo, 2003, 2004). Additionally, cooperations with institutions from different countries have led to the participation of German scientists in international expeditions; one very fruitful cooperation exists between BGR and the Italian Antarctic Research Program (PNRA).

As Victoria Land is characterized by the Transantarctic Mountains, a large number of geological outcrops exists and has been investigated. In addition to geologic, stratigraphic and geochronologic studies, over the past decades several kinds of geophysical measurements have been carried out, ranging from land-based gravimetric and ground-penetrating radar surveys to airborne magnetic campaigns, covering also the adjacent marine areas. The terrestrial gravity data can be augmented by marine measurements and nowadays also by high-resolution satellite gravity field data.

Mainly off-shore, in southern Victoria Land (SVL) also on-shore, seismic experiments have been carried out to reveal the crustal structure and help interpreting the geological findings with respect to the history and development of this part of Antarctica.

1.4 Impact of Antarctic research

Antarctic research is important for several reasons: One important fact is, that the Antarctic continent is a landmass larger than Australia, but due to the ice cover the relationship between Antarctica and the other continents is still not obvious. For the full understanding of recent and prediction of future plate tectonic processes it is necessary to know about the past development.

Also the climatic history of Antarctica can give clues for the recent climatic change, as can give the observation of the Antarctic ice sheet. The total volume of the Antarctic ice sheet has been estimated to be about $30 \cdot 10^6\,\mathrm{km}^3$ or 90 % of the Earth's ice masses (Faure & Mensing, 2010; Stonehouse, 2002). A complete deglaciation would result in a sea level rise of several tens of meters and therefore have a severe impact on life.

Connected to deglaciation, an isostatic adjustment of the Antarctic continent is expected. This adjustment is observable by geodetic and geophysical measurements, and

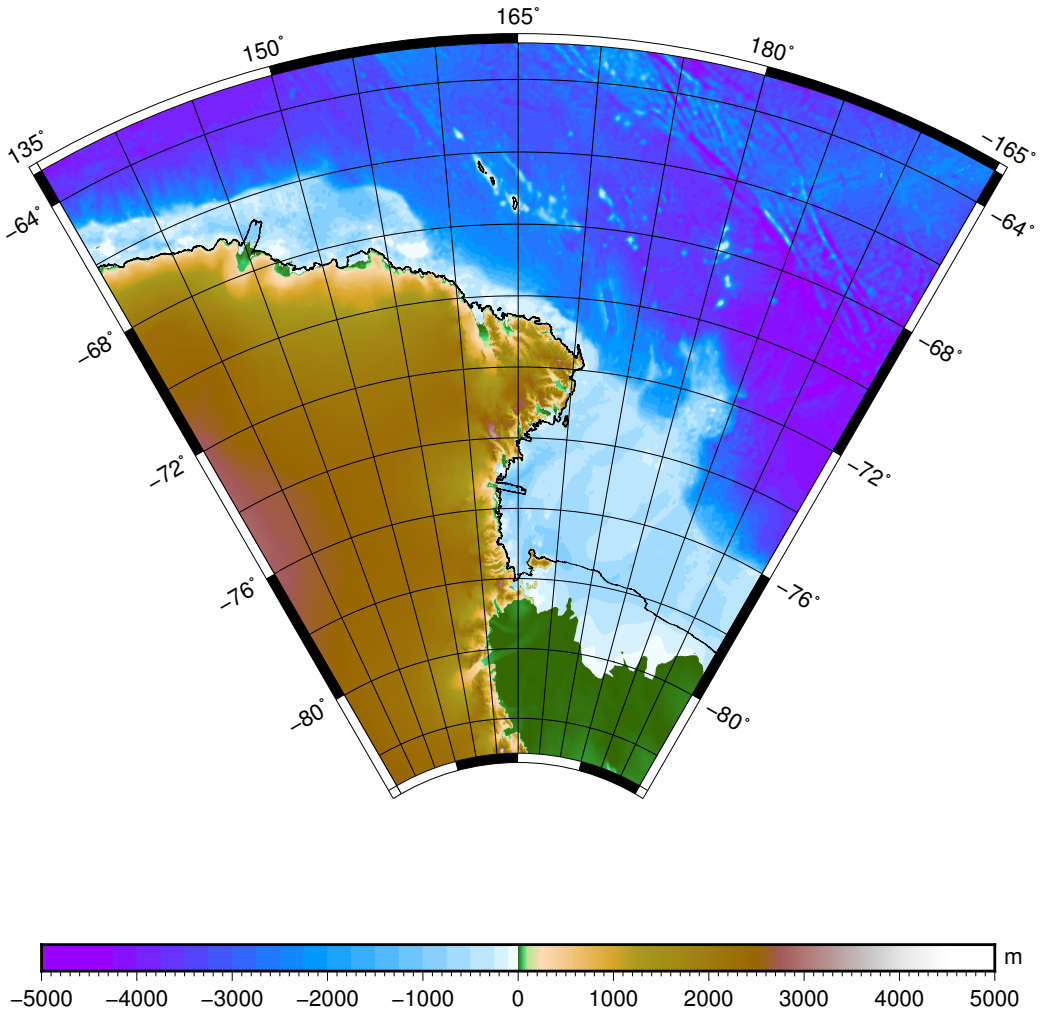

Figure 1.2: ETOPO 1 ice elevation data.

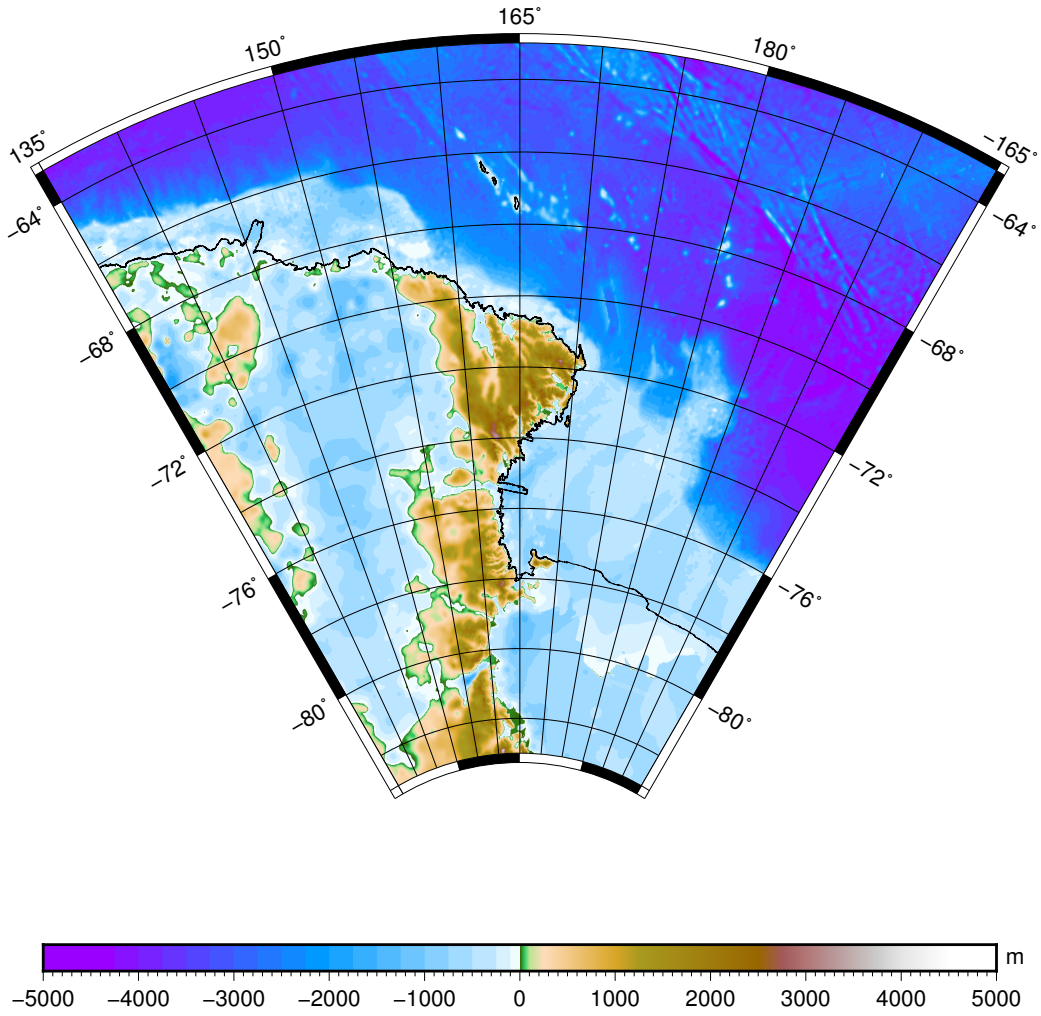

Figure 1.3: ETOPO 1 bedrock elevation data.

the results of such measurements can as well give hints on the rate of melting (or, on the other hand, accumulation) of ice, and thus support predictions of future climate on Earth.

1.5 Objective of this work

This work aims at utilizing geophysical data, especially potential field data (gravity and magnetic total intensity), to model the deep structures of the Earth's crust and lithosphere. These models shall help to identify and understand the processes which have led to the present situation. To reach this, some work on the data had to be done before modelling the crustal structures. For modelling itself, the software IGMAS+ (Götze & Lahmeyer, 1988; Schmidt et al., 2011) has been used. It enables the creation of three-dimensional models of arbitrary extent in all three dimensions by combining several parallel 2 D sections to one 3 D model.

The following chapters aim to summarize the current level of scientific knowledge regarding the structural and historical geology of Antarctica. For this purpose, gravity and magnetic field data shall be presented and analysed. Finally, the models created on the basis of this analysis shall be interpreted in the current research context.

Chapter 2

Geology

2.1 Introduction

As the Antarctic continent is almost completely covered by an ice sheet – only 2.4 % of the entire land mass are at least seasonally ice-free (Faure & Mensing, 2010) – the knowledge about the geology of Antarctica is, in general, sparsely distributed and limited to the coast and mountainous areas as the TAM. Geophysical investigations can provide additional information, especially in areas where no or only few outcrops exist. However, due to the conditions – low temperatures, strong wind, remote location – all scientific studies in and around Antarctica are difficult and expensive to conduct. Therefore, many questions regarding the geology and the development of Antarctica are still open.

2.2 Main features of Antarctic geology

Fig. 2.1 shows Antarctica with the mountains and ice-free coastal areas. The continent can be divided into West Antarctica and East Antarctica. The Transantarctic Mountains follow the boundary between both parts of Antarctica. Robinson & Splettstoesser (1986) note that the sedimentary layers in the TAM are not folded or thrust-faulted, hence the TAM are not the result of a continent-continent collision. As the geology of West Antarctica is totally different from that of the TAM, the authors draw the conclusion that West and East Antarctica must have been independent lithospheric plates in the past. The crust in West Antarctica is younger and less thick than in East Antarctica.

Fig. 2.1 shows also the approximate boundary of the West Antarctic Rift System (WARS) which was defined by Behrendt & Cooper (1991); Behrendt et al. (1991a,b). This rift can be compared to the East African Rift (Behrendt, 1999). Inside the rift the crust is thinned to approx. 21 km (Winberry & Anandakrishnan, 2004), whereas the crustal thickness in East Antarctica is between 35 km and 45 km (Melles et al., 2015). The sedimentary basins inside the WARS reach up to 14 km depth. The TAM are today seen as the elevated rift shoulder of the WARS. However, the huge uplift may be not

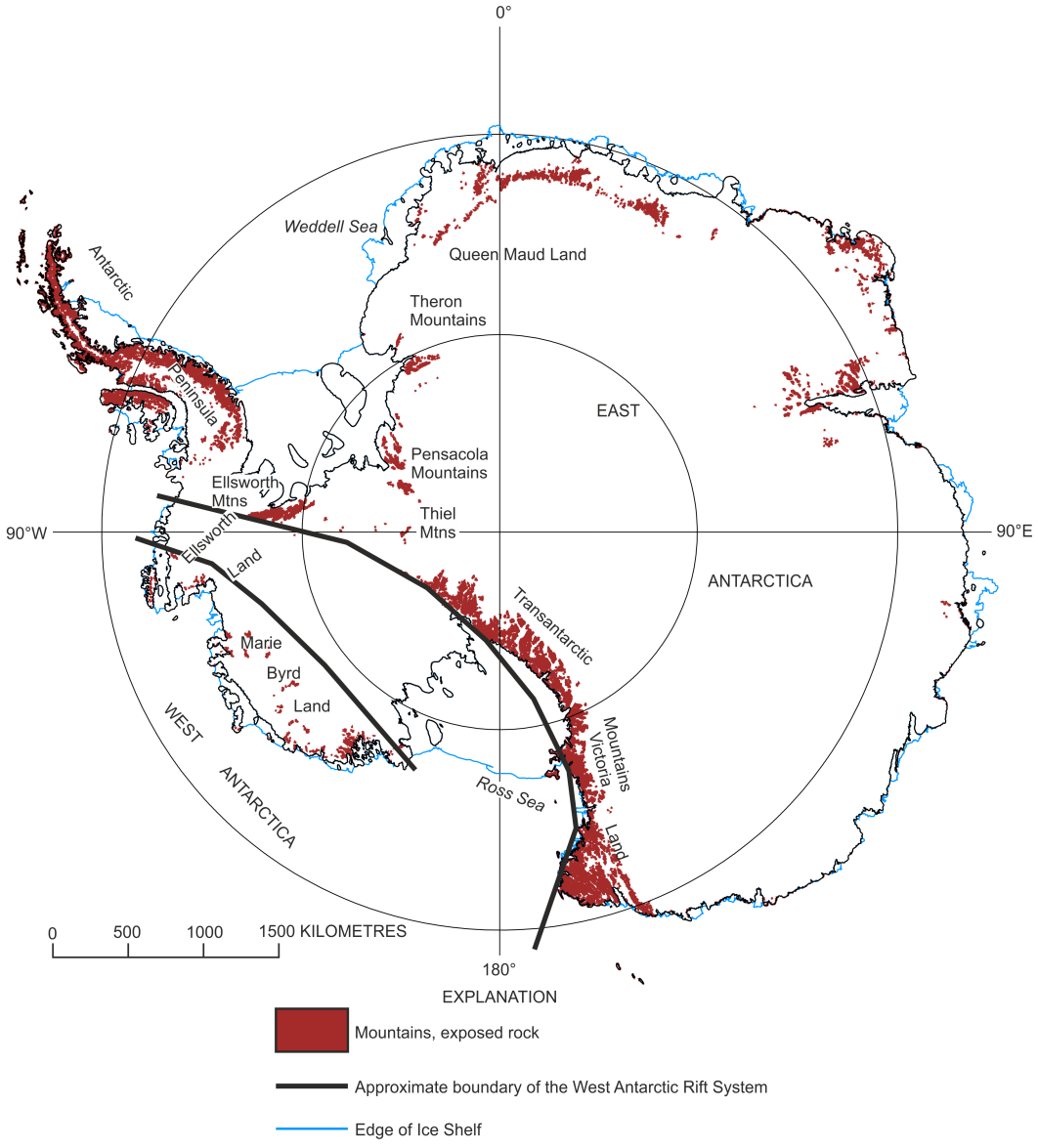

Figure 2.1: Map of Antarctica showing ice-free areas with the bedrock accessible as well as the approximate boundary of the West Antarctic Rift System (WARS) (after Behrendt & Cooper, 1991;coastlines and rock outcrops from SCAR, 2015).

only due to rifting; also a combination of different causes is also under discussion (cf. Faure & Mensing, 2010).

2.3 Regional geologic setting of Victoria Land

2.3.1 Paleozoic Formation of Victoria Land

According to Roland et al. (2004), since the 1980s northern Victoria Land (NVL) has been interpreted as amalgamation of three terranes, which are from west to east the Wilson terrane, the Bowers terrane, and the Robertson Bay terrane. The boundary between Wilson and Bowers terrane is formed by the Lanterman Fault whereas the Robertson Bay terrane is separated from the Bowers terrane by the Leap Year Fault. All these features can be seen in Fig. 2.2. The idea of different terranes building up NVL was introduced by Weaver et al. (1984) and further developed by Bradshaw et al. (1985). Weaver et al. interpreted the fault zones as strike-slip faults, whereas Kleinschmidt & Tessensohn (1987) interpreted the fault zones as remnants of the accretion of the three terranes to form one larger land mass. This model includes two subduction zones with similar orientation of the plate boundary, as well as the same direction of movement; the collisions between the terranes were interpreted as the main suture zones of the Ross Orogen, which formed around 500 Myr ago during the Cambrian period. A sketch showing the different stages of collision and subduction, taken from Kleinschmidt & Tessensohn (1987), is displayed in Fig. 2.3. According to this sketch the intrusive rocks found in the Wilson terrane are the result of subduction-related magmatism.

Roland et al. (2004) propose a new model which differs from the common one by estimating only the central Bowers unit as a terrane. In this new model, the western unit is seen as Wilson Mobile Belt, and interpreted as former platform area of the East Antarctic Craton lying further to the west, with intrusions built during orogeny. The platform area was reorganised due to the subduction at the active continental margin of Gondwana. The Bowers unit is interpreted as an island arc related to an intra-oceanic subduction zone originally located outside the active continental margin. After the collision of the Bowers Arc Terrane at the East Gondwana margin, the main subduction zone migrated outward and an accretionary wedge was formed. The easternmost Robertson Bay unit is, according to Roland et al. (2004), composed of the sediments of this wedge; hence, this unit is called in this model Robertson Bay Wedge. In other models (Federico et al., 2009, e.g.) the Bowers unit is interpreted as back-arc basin due to the mixture of magmatic and sedimentary rocks as well as chemical and isotope data.

The different possibilities of origin of the terranes have also been discussed by Tessensohn & Henjes-Kunst (2005) who compare the field observations, which support different models. The exact formation of NVL is still not known, but can only be assumed, based on geologic field observations. Thus, the investigation of deep lithospheric structures – e.g., to proof whether there are still remnants of subducted tectonic plates – can give

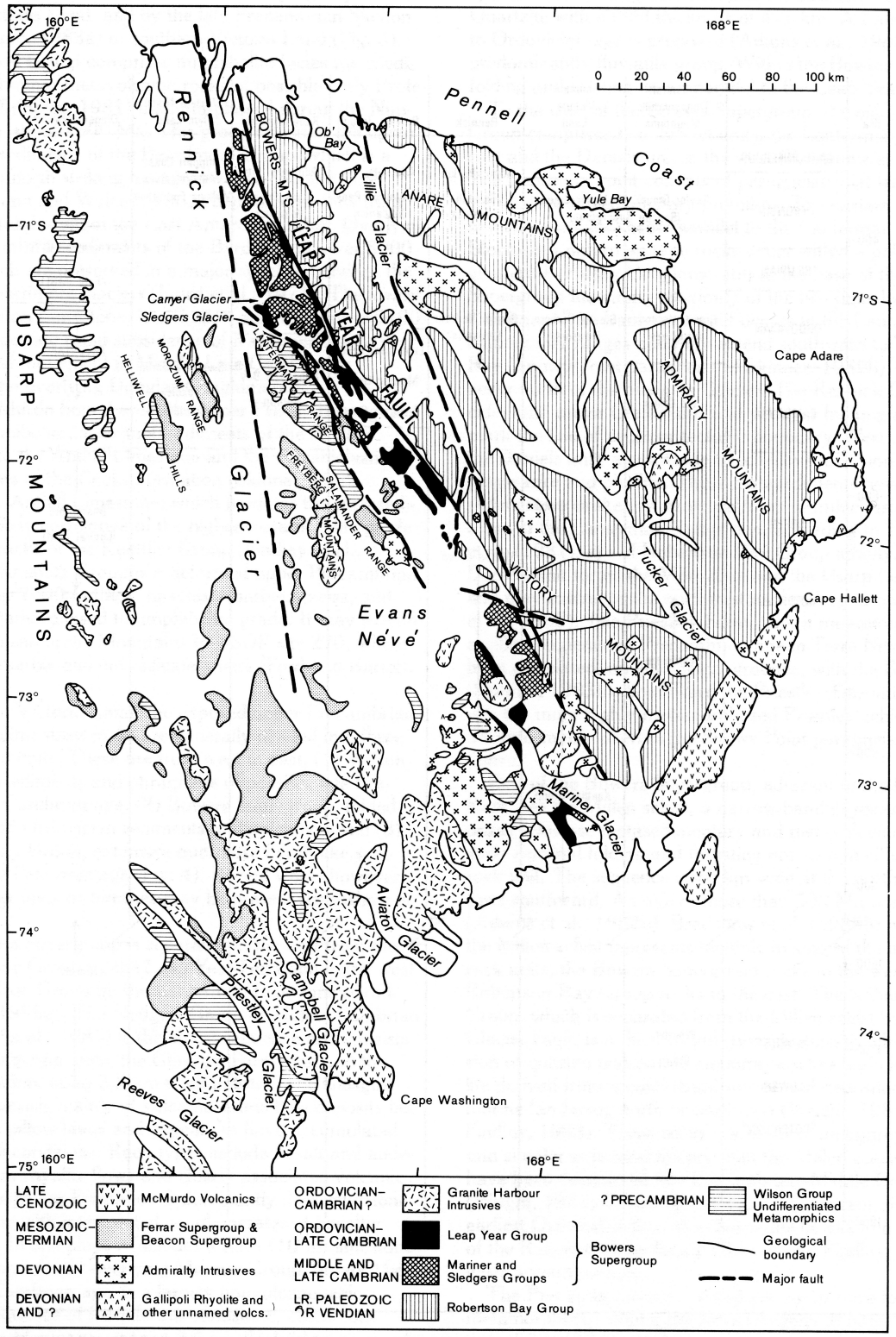

Figure 2.2: Geologic map of northern Victoria Land (Davey, 1987). Several major faults are shown.

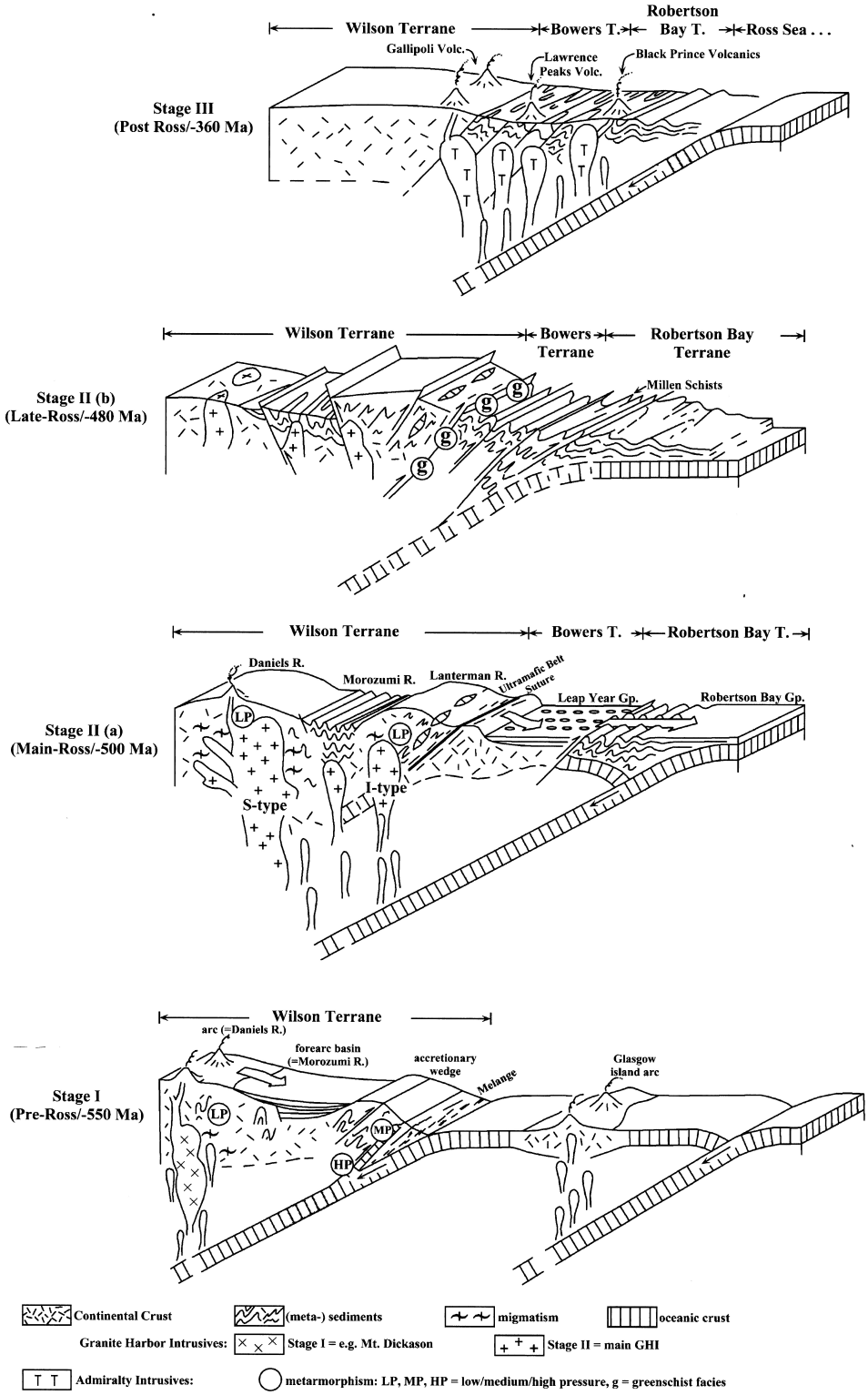

Figure 2.3: Sketch illustrating the possible evolution of northern Victoria Land with two subduction zones (Kleinschmidt & Tessensohn, 1987).

additional information to support one of the two models explained above, or to develop a new model.

2.3.2 Uplift of the Transantarctic Mountains

The TAM are not a collisional orogen, but result from rifting processes between West and East Antarctica (Behrendt, 1999). They represent the elevated rift shoulder at the East Antarctica side of the WARS. Therefore, only low or even no deformation at all occurred during the formation of the TAM; the undeformed layers have only been displaced. As a consequence, faults laid out previously, e.g. during the Ross orogeny, have been preserved and were not overprinted. Flöttman et al. (1993) and especially Finn et al. (1999) show that the TAM mainly follow the line of the Ross orogen. This suggests a reactivation of the Ross orogeny fault zones.

According to Behrendt et al. (1991a,b), the uplift of the TAM started around 60 Myr ago. However, the uplift rate was not constant but rather episodic; also different parts of the TAM were not uplifted together. New results (e.g. Lisker & Läufer, 2013) show that the uplift started only 35 Myr ago; before, the region was characterized by a wide sedimentary basin. The sediments have been completely eroded during uplift.

2.3.3 Cenozoic tectonic development

Around 35 Myr ago the Tasman (or Tasmanian) Gateway between Australia-Tasmania and Antarctica opened (Stickley et al., 2004). Starting at 30 Myr, a transtensional tectonic regime has reactivated paleozoic NW-SE faults in NVL. Inherited extensional structures have been overprinted by the Cenozoic transtensional tectonics; the motion along the transtensional faults is right-lateral. The concurrence of extension and strike-slip motion reactivated existing and generated new basins oriented N-S to NNW-SSE (Salvini et al., 1997). The present-day structural features in NVL are shown in Fig. 2.4, including the three-part structure and, to some extent, the faults shown in Fig. 2.2.

Salvini et al. (1997) track the NW-SE trending fault zones from the northern coast of NVL to the SE through the continent and far into the Ross Sea (cf. Fig. 2.4). At the northern coast of NVL these fault zones can be tracked into the offshore area as well; a connection to major transform faults of the Australia-Antarctica mid-ocean ridge, e.g. the Balleny Fracture Zone (BFZ) and the Tasman Fracture Zone (TFZ), is possible (Fig. 2.5).

According to Läufer & Rossetti (2001) and Rossetti et al. (2003b), the dextral strike-slip fault systems overprint an older extensional tectonic regime oriented E-W. During this extensional phase several tectonic depressions like the Rennick Graben and the Lillie Graben have formed. A relation of this extension to the opening of the Ross Sea has been discussed as well (e.g. Rossetti et al., 2003b). After Rossetti et al. (2003a) the opening of the Adare Trough, an oceanic spreading ridge east of NVL, which formed

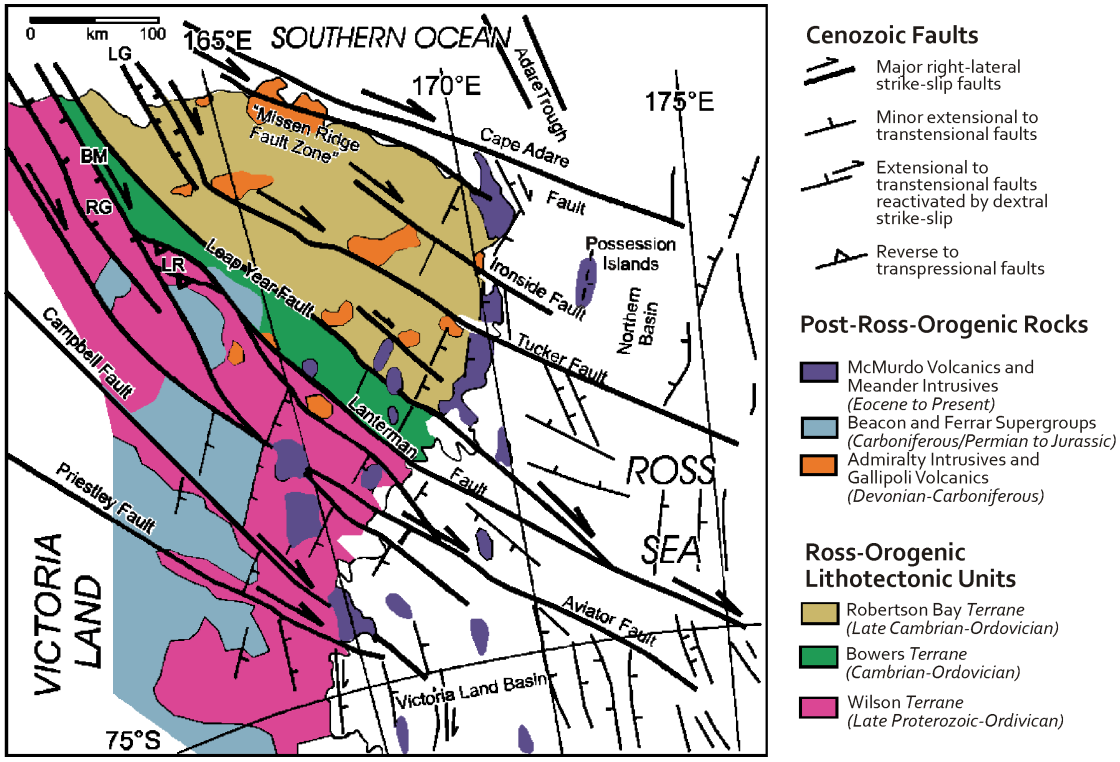

Figure 2.4: Tectonic sketch map of northern Victoria Land with the major Cenozoic fault systems (after Läufer et al., 2011). LG = Lillie Graben; BM = Bowers Mountains; RG = Rennick Graben; LR = Lanterman Range.

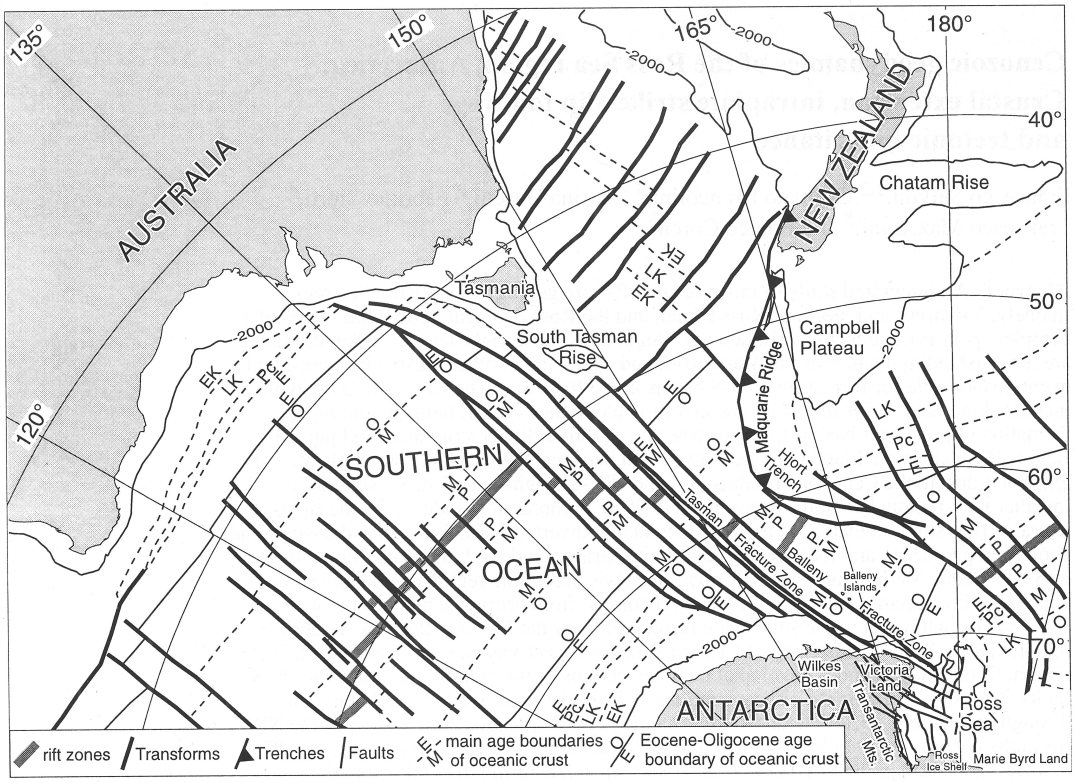

Figure 2.5: Large-scale map of the geodynamic framework along the Australia-Antarctica plate boundary. Magnetic anomaly ages are shown, as well as main transform fault zones correlated with the main NW-SE fault zones in NVL. P = Plio-Pleistocene; M = Miocene; O = Oligocene; E = Eocene; Pc = Paleocene; LK = Late Cretaceous; EK = Early Cretaceous. (Salvini et al., 1997).

between 43 Myr and 27 Myr (Cande et al., 2000), is possibly also related to the same extensional phase.

2.4 Open questions regarding the lithospheric structures in NVL

The most important question regarding the tectonic framework of northern Victoria Land is the possible relation between the oceanic fracture zones (BFZ, TFZ) and the major intra-continental structures in NVL (cf. Salvini et al., 1997). Several other minor questions arise from the occurrence of volcanic rocks, especially along the northern coast of NVL; the extent of those rocks off-shore as well as the possible connection to the existing fault zones is not yet known.

The TAM represent the elevated rift shoulder of the WARS (Behrendt & Cooper, 1991); due to the ice cover the inland boundary of the uplifted block is not visible. Thus, geophysical modelling can give constraints to define this boundary. The shape of a possible mountain root of the TAM and the present isostatic state of the mountains are still under discussion, too.

Chapter 3

Data

The modelling approach is based on potential field data, especially on gravity and magnetic total intensity data. The following sections give an overview of the available data, the different steps of data preparation for the data to be suitable for use with IGMAS+ as well as some error estimation.

As the inversion of potential field data cannot be unique, an infinite number of structural models exists, which might explain the measured values quite well; due to measuring errors even more models can be found. Therefore, additional information is necessary to reduce the number of possible models. These constraints can be other geophysical data like seismic and borehole measurements, but geologic results from field studies are of great importance as well.

Unfortunately, due to the remote area and the rugged terrain, other geophysical data are limited to few very local campaigns. Seismic profiles exist mainly for the Ross Sea; one single profile between 75° and 76° south crosses the Transantarctic Mountains from the coast inland with a length of 150 km (Della Vedova et al., 1997).

3.1 Gravimetry

3.1.1 Data sources

Gravimetric data in Victoria Land, including the surrounding marine areas, have been collected during several decades in the frame of many different programmes including the German GANOVEX programme, the Italian Antarctic Research Program as well as American and British. Reitmayr (1997) gives an overview of the available data covering Victoria Land to several hundreds of kilometres inland with land-based measurements, the entire western part of Ross Sea with marine gravity data and the area offshore the northern coastline of Victoria Land with satellite data. A complete list of available datasets can be found in appendix A (p. 85). Unfortunately, for large areas the data distribution is very coarse and uneven; therefore large uncertainties might arise when using these data for 3D modelling. Also the data processing has been done in different

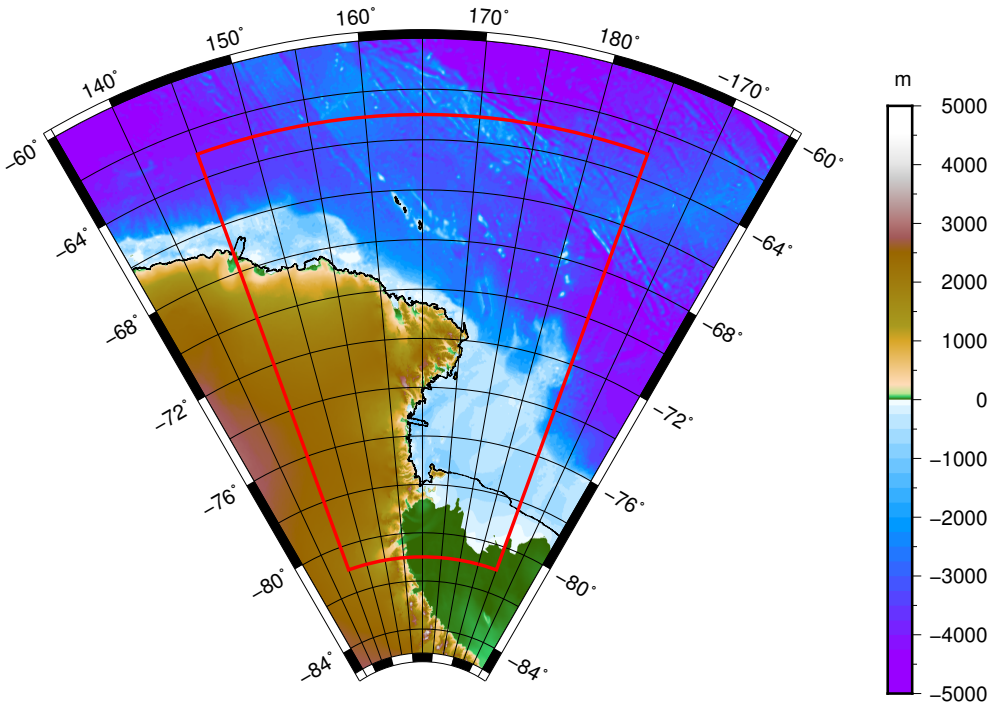

Figure 3.1: ETOPO1 surface map of Victoria Land and neighbouring regions, showing the area for which EIGEN-6C3stat data have been obtained.

ways: for some points the errors resulting from Bouguer and terrain corrections using the standard density[1] of 2.670 kg m^{-3}, which is by far too high for ice masses, were accounted for with the introduction of new correction terms using a density of 870 kg m^{-3} for the ice masses (e.g., Reitmayr & Thierbach, 1996), for other points such corrections were not applied.

Nowadays global gravity field models are available, which incorporate data from satellite mission like CHAMP, GRACE and GOCE. Such data can be obtained online from the International Centre for Global Earth Models (ICGEM) at GFZ Potsdam[2]. With those data errors resulting from the inhomogeneities of the available terrestrial gravity measurements can be avoided; therefore a data set was generated through the ICGEM online calculation service. This data set was generated from the harmonic coefficients of the EIGEN-6C3stat global gravity field model (Förste et al., 2013), which includes, among others, data from the DTU10 (Andersen et al., 2010; Andersen, 2010) and EGM2008 (Pavlis et al., 2012) data sets . Figure 3.1 shows the area for which EIGEN-6C3stat data have been obtained and the Bouguer anomaly computed.

[1] 1.000 kg m^{-3} = 1 g cm^{-3}
[2] http://icgem.gfz-potsdam.de/ICGEM/ICGEM.html

3.1.2 Data preparation

The ICGEM calculation service offers several functionals of the Earth's geopotential. For this work two of these were to be considered: the so-called *classical gravity anomaly* which is the *free-air anomaly*, and the *Bouguer anomaly* which in fact is the *simple* Bouguer anomaly – only the planar Bouguer correction has been applied compared to the classical gravity anomaly. The Bouguer correction provided by ICGEM uses a density of $1.025\,\mathrm{kg\,m^{-3}}$ for heights below zero and $2.670\,\mathrm{kg\,m^{-3}}$ else; the ice masses on Greenland and in Antarctica are not taken into account[3]. As a consequence, the classical gravity anomaly (free-air anomaly) might be favoured for 3D modelling, which therefore would have to comprise the topography and bathymetry of the model area as well as the ice cover as one or a couple of anomaly generating bodies. Due to the large extent of the model area this is quite impractical as both topography and ice cover would have to be defined by a large amount of points in IGMAS+. The distances between the sections of the IGMAS+ model also need to be very small (and thus the total number of sections very high) to correctly calculate short-wavelength effects of the topography and the ice cover. These problems can be avoided through the usage of a refined Bouguer anomaly. The refinement consists of two different tasks: the application of a corrected Bouguer slab model, accounting for the density difference between the ice and rock masses, and a correction of the effects of topography of both the top and bottom of the ice masses or, as it is denoted e.g. in Reitmayr & Thierbach (1996), a correction of the topography in general and an additional term dealing with lateral changes in ice thickness. The final result of this refinement yields the *complete Bouguer anomaly*.

Calculation of the refined Bouguer slab

The gravity attraction of the Bouguer slab is analytically defined as

$$g_{bp} = 2\pi G \varrho h \tag{3.1}$$

with G gravitational constant ($6.672 \cdot 10^{-11}\,\mathrm{m^3\,kg^{-1}\,s^{-2}}$),
ϱ constant density,
h thickness of the slab.

It does not depend on the distance from the slab as the slab itself is laterally infinite. Therefore, the effect of the Bouguer slab on gravimetric measurements is identical for a station directly on top of the slab and a station several kilometres above[4].

In northern Victoria Land, for the calculation of the Bouguer slab three different cases have to be considered, which are also illustrated in Fig. 3.2:

A. station on top of a glacier; a density of $870\,\mathrm{kg\,m^{-3}}$ is used to subtract the gravity

[3] ibid.

[4] This is also true for a spherical Bouguer correction where the gravity attraction is analytically defined to be twice that of the planar correction.

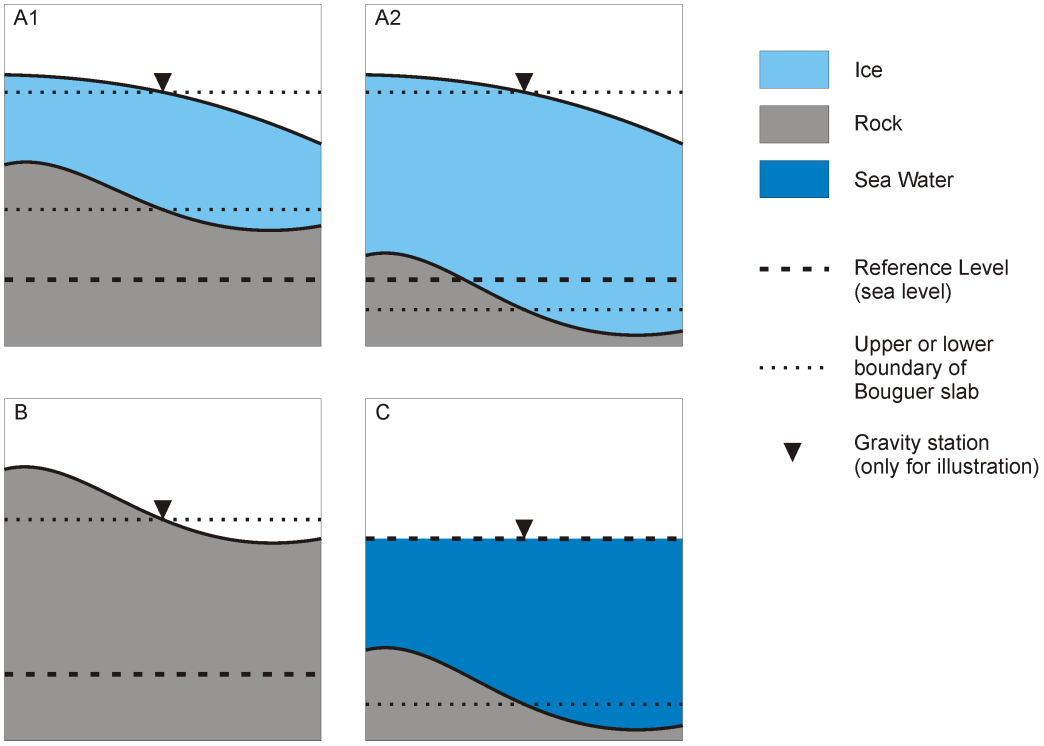

Figure 3.2: Different cases for Bouguer slab calculation. A1 and A2: gravity station on a glacier; B: gravity station on rock; C: off-shore gravity station.

effect of the ice, and a density of $(2,670-870)\,\mathrm{kg\,m^{-3}}$ to either remove the residual gravity effect of the rock masses below the ice but above the reference level or add that effect to virtually replace ice masses below the reference level by rock masses;

B. station on ice-free land; a density of $2.670\,\mathrm{kg\,m^{-3}}$ is used;

C. marine station; a density of $(2,670-1,030)\,\mathrm{kg\,m^{-3}}$ is used to add, to the measured gravity effect of the sea water, the residual effect of matter with the density difference to obtain the gravity effect of rock masses.

For the computation of the Bouguer anomaly data sets of topography, bathymetry and ice thickness are necessary. Amante & Eakins (2009) have compiled global datasets of both the topography/bathymetry including the heights on top of Antarctica and Greenland ice sheets and the bedrock elevation below these ice sheets (ETOPO1). For Antarctica, two different sources were used: for the topography including the ice sheet the Radarsat Antarctic Mapping Project Digital Elevation Model (RAMP DEM; Liu et al., 1999), itself being compiled from many local to regional surveys, was utilized; the bedrock elevations and the bathymetry around Antarctica to 60° south are based on the BEDMAP project (Lythe et al., 2000). Both versions are shown in Fig. 1.2 and 1.3.

The obtained simple Bouguer anomaly is shown in Fig. 3.3. It ranges from −361 mGal

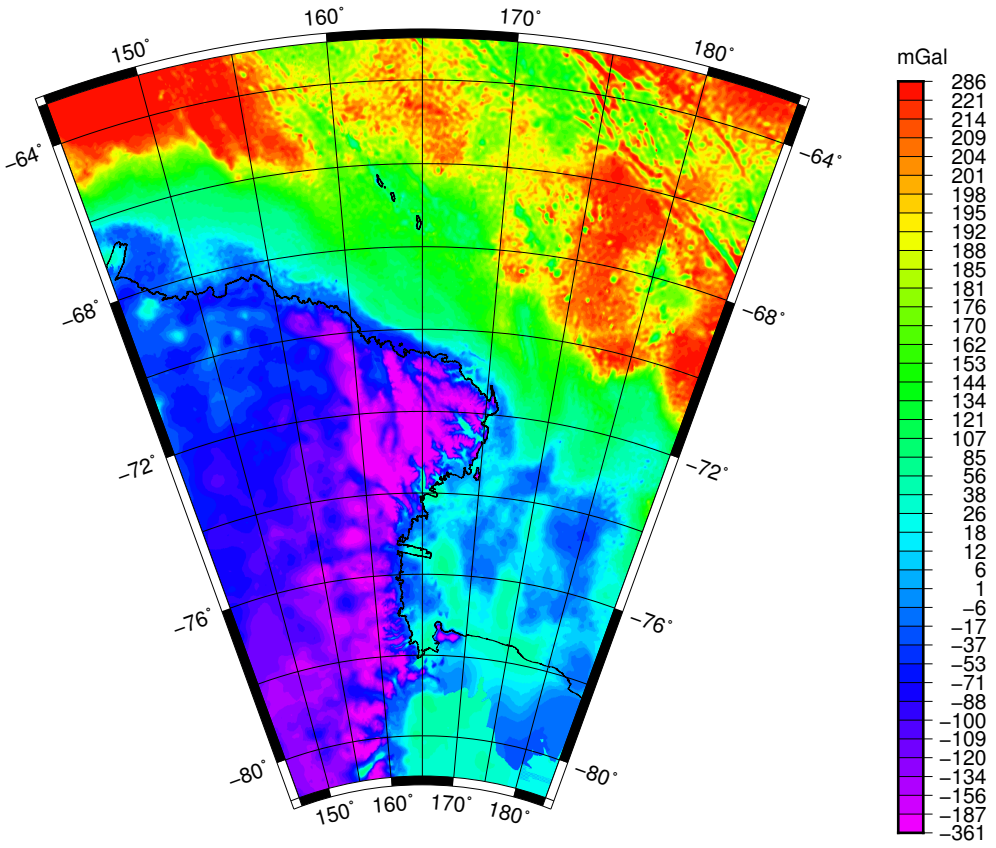

Figure 3.3: Simple Bouguer anomaly, calculated from EIGEN-6C3stat free-air anomaly and ETOPO1 topography data. The color scale is non-linear, roughly giving equal areas for the different colors. 1 mGal = 10 µm s^{-2}.

to 286 mGal[5] and clearly still shows many important features of the topography. Obviously the mass distribution is not exactly that of a Bouguer slab, so errors introduced by the assumption of a slab have to be investigated. This includes the effects of varying topography, which are discussed later, but also the deviation of the true figure of the Earth from the slab approach. This second effect has first been taken into account by Bullard (1936); later the effect has been named "Bullard B", with "Bullard A" referring to the Bouguer slab, and "Bullard C" to the corrections of the topographic effects (e.g., LaFehr, 1991). Bullard developed a table of values for the effect of Earth's curvature which gives values between 1.7 mGal and −1.0 mGal, depending on the station elevation, for elevations from 0 m to 5.000 m; apparently, these values are calculated for a spherical cap with a surface radius of 166.7 km around the gravity station (equivalent to 1°29′28″), which is based on a procedure developed by Hayford & Bowie (1912) for computation

[5] 1 mGal = 10 µm s^{-2}. In general, it is favourable to use SI units; as the data which were used for this study were provided in mGal and the modelling software works with the same unit, anyhow mGal are used throughout the whole text.

of the gravity effect of the topography.

LaFehr (1991) provides a new table, using the same surface radius for computation, with Bullard B correction values between 1.518 mGal and −1.497 mGal for the same elevation range. Taking into account the much larger range of the simple Bouguer anomaly as well as the possible errors of the elevation data used for the calculation of the Bouguer slab values (given by Liu et al. 1999 for the RAMP DEM data to be of the order of 100 m; with the density of 870 kg m^{-3} used for ice, the error in the slab value is of the order of 3.65 mGal), it is not necessary to calculate Bullard B correction values as they clearly would lie within the error range.

Correction of topographic effects

As the TAM rise to more than 4.000 m a.s.l. whereas the sea floor depth reaches the same magnitude, with strong gradients at least in some parts of the region, the topography in general as well as the varying thickness of the ice cover have effects on gravity which have to be taken into account. For the terrestrial measurements put together by Reitmayr (1997) these effects were estimated to be in the order of 20 mGal to 30 mGal for many points but at some places reach values above 100 mGal (Reitmayr & Thierbach, 1996; Dürbaum et al., 1989).

Approaches for the computation of topographic effects on gravity measurements have already been made by Hayford & Bowie (1912) and later by Hammer (1939) and Nagy (1966a,b). A common method is to discretise the area around a single station to a certain distance limit, based on horizontal distance and angular direction. The single compartments can be approximated as rectangular or pie-shaped prisms with a mean vertical extent. Together with a mean density, which can be constant for all compartments or vary between them, the gravitational effect of their masses can be estimated.

The EIGEN-6C3stat data are calculated from spherical harmonic coefficients, which themselves were computed from original data of varying origin. Large amounts of data were collected with several satellite missions like GRACE or GOCE, but also terrestrial data, marine and aerogeophysical campaigns were included (Förste et al., 2013). Due to those diverse data sources it is not possible to define a station location for which the effects of topography should be estimated. As these effects mainly depend on the spatial distance of the topographic feature from the station the resultant correction values would be totally different if calculated for a station on ground or at satellite level.

Additionally, if ground stations were assumed, each station could be located on ice, on rock, or on water; also each compartment to be considered for calculation (i.e., within the distance limit) can consist of water, rock, ice, or the combination of the latter. Together with the fact that in some parts of the continental area in and around Victoria Land the sub-ice elevations are below sea level, many different cases can be found, which have to be distinguished between; for each case another combination of elevation data and densities has to be applied to the algorithm used for the computation of the gravitational

effect.

Altogether, this leads to the conclusion that the topographic effect has to be disregarded. Instead, the topography and other near-surface sources of the gravity anomaly can be excluded from the data by using a low-pass wavelength filter. This approach clearly introduces uncertainties into the data in the order of 10 mGal to 20 mGal. However, as the topography data also would introduce uncertainties of the same order, it is preferable to set aside any correction for topographic effects. Otherwise anomalies might be interpreted which originate only in such uncertainties. It is therefore very important not to interpret the anomaly field for local structures.

3.1.3 Filtering of the data

Based on Jung (1961), and further specified by Giebeler-Degro (1986) and Gabriel (1998), the spectrum of the anomalies can help to define depth levels or depth intervals for the anomaly-generating bodies. Due to the potential field character of gravity there is a permanent ambiguity regarding the depth and shape of the anomaly source, but an estimation of the maximum depth of a source can be made from the width of the anomaly and, therefore, its wavelength. The approximate relation between the maximum source depth z_s and the effective cut-off wavelength $\lambda_{c,eff}$, as given by Gabriel (1998), is

$$\lambda_{c,eff} \approx 3 \cdot z_s \tag{3.2}$$

with $\lambda_{c,eff}$ effective cut-off wavelength,
z_s maximum source depth.

As the investigation area is located at high latitudes and the characteristics of common filters are defined by metric instead of angular parameters, the simple Bouguer anomaly was projected onto a Cartesian coordinate system, utilizing a Lambert Conic Conformal projection with the same parameters as applied by Reitmayr (1997) for the terrestrial gravity measurements. These are listed in Tab. 3.1. The origin of the projected coordinates is located in the vicinity of the German Gondwana Station at Terra Nova Bay.

Three different filters have been used to investigate the spectrum of the simple Bouguer anomaly. All filtering processes were carried out with GMT (Wessel & Smith, 1991; Wessel et al., 2013), applying a cosine-taper to the filter flanks to avoid instabilities due to steps in the filter characteristics. For the near-surface sources a high-pass filter with the effective cut-off wavelength of 90 km was used, giving a maximum source depth of about 30 km; the depth interval from 30 km to 70 km was investigated using a band-pass filter with effective cut-off wavelengths of 90 km and 210 km, respectively. Finally, a low-pass filter with an effective cut-off wavelength of 210 km, corresponding to a maximum source depth of more than 70 km, was applied to the data. The results of the different filters are shown in Fig. 3.4 and 3.5. By adding up the low-pass, band-

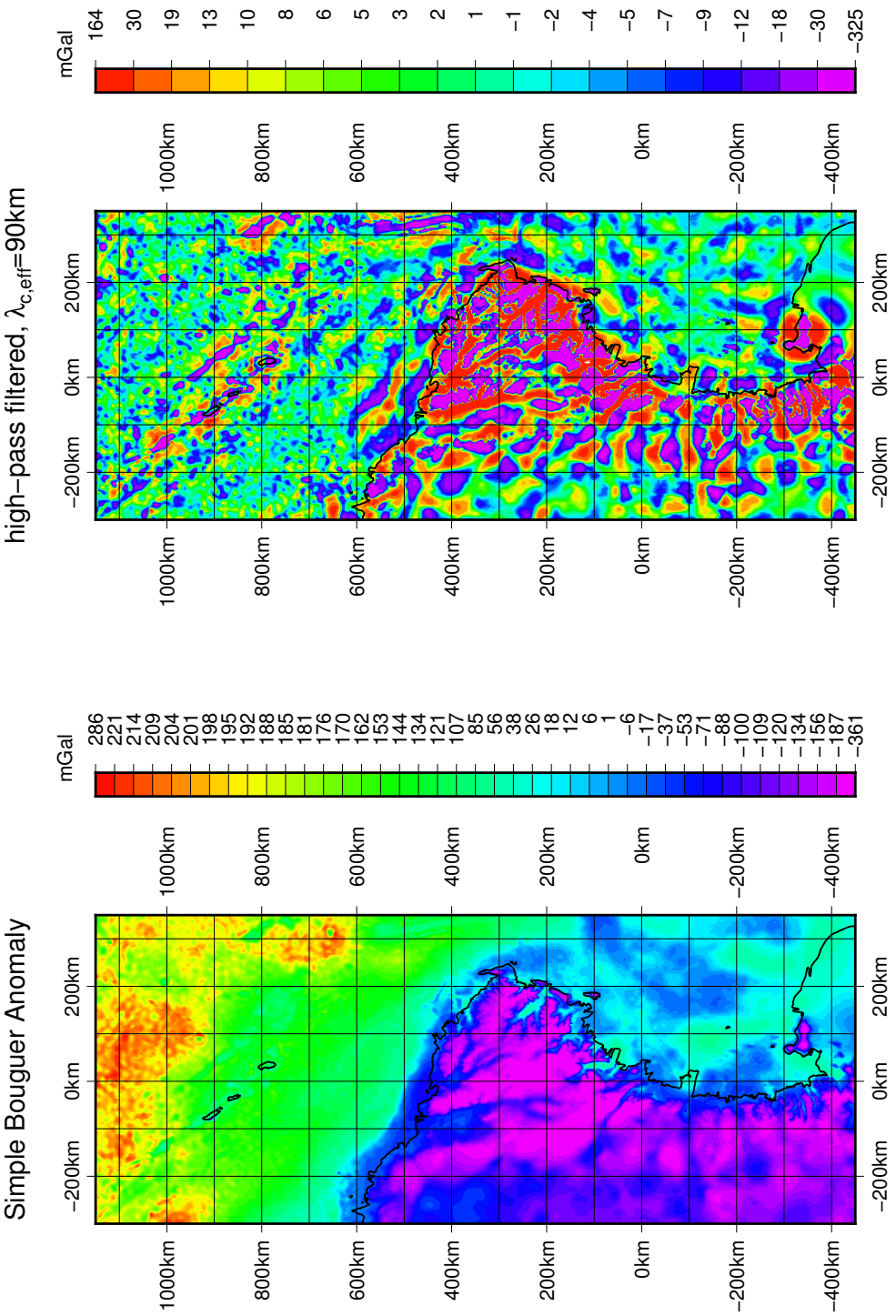

Figure 3.4: Simple Bouguer anmomaly of northern Victoria Land and adjacent areas (bottom) and high-pass filtered data (top). The coastline is given in black for orientation. $1\,\mathrm{mGal} = 10\,\mu\mathrm{m\,s^{-2}}$.

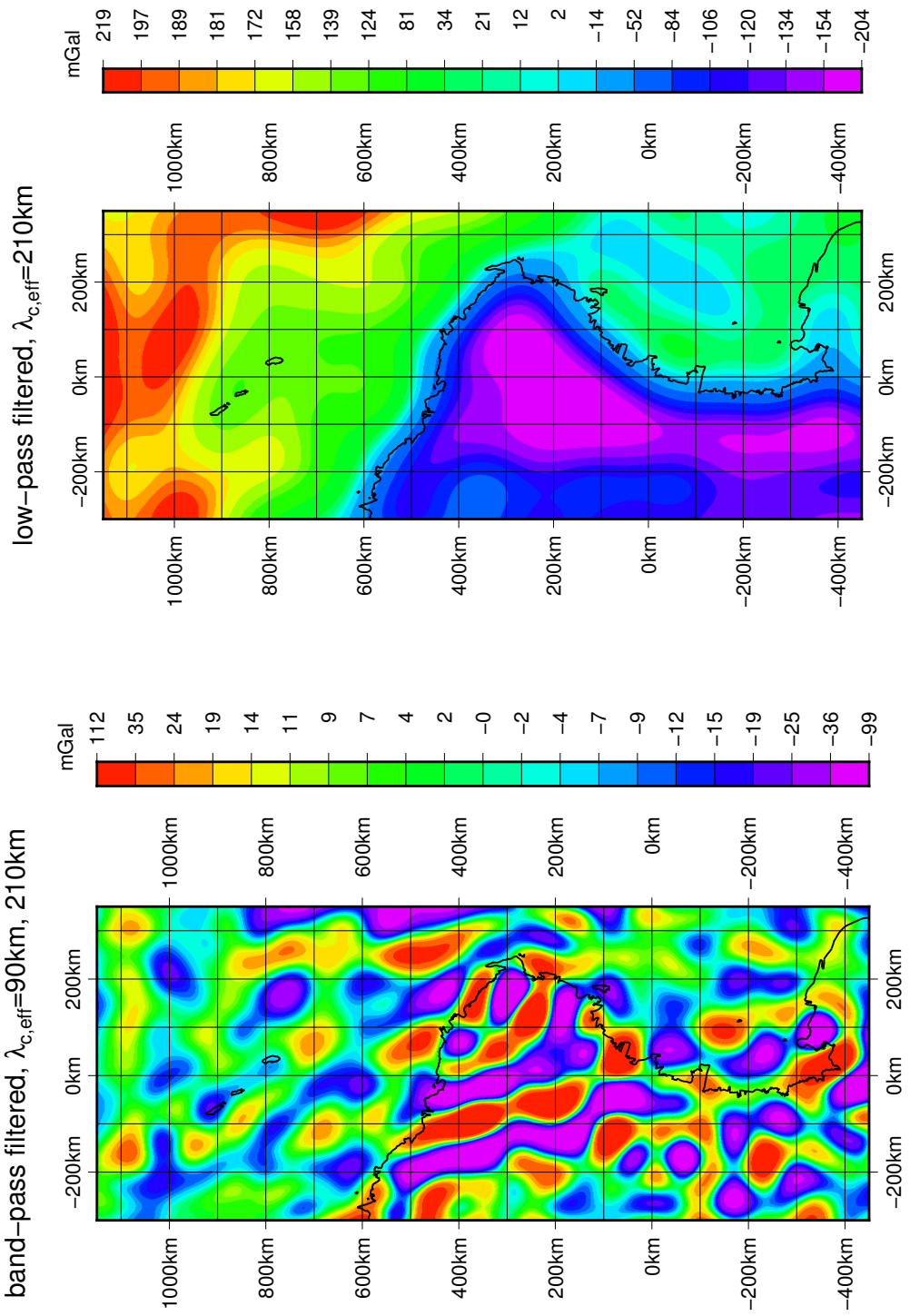

Figure 3.5: Results of band-pass (bottom) and low-pass (top) filtering. The coastline is given in black for orientation. $1\,\mathrm{mGal} = 10\,\mu\mathrm{m\,s^{-2}}$.

Table 3.1: Parameters of the Cartesian coordinate projection used.

Projection	Lambert Conic Conformal
Central meridian	164° east
Central latitude	74.5° south
Parallels	75.333° south
	72.6667° south
False Northing	0.0
False Easting	0.0
Scale factor	1.0

pass, and high-pass filtered data, the original data can be restored with only very small discrepancies.

As stated before, the simple Bouguer anomaly shows many features connected to the topography. This is also true for the results of the high-pass filtering, where the large valleys of the TAM can be seen. The noisy pattern off-shore is mainly an artefact based on the satellite tracks of the EIGEN data sources.

The band-pass filtering shows large linear structures which in the off-shore part north of 600 km northing fit the strike of the transform faults of the Indian-Antarctic ridge further to the north. On-shore the strike seems to be connected to the known large fault zones. In the southernmost part the pattern is not as clear as in northern Victoria Land, but in the Ross Sea area the anomaly pattern can be linked to structural features of the sea-floor.

The low-pass filtered data show large negative anomalies along the TAM, with changing width from north to south. As crustal rocks are less dense than the Earth's mantle these anomalies obviously show the mountain root of the Transantarctic Mountains. This result is also consistent with Block et al. (2009), who estimated the crustal thickness of whole Antarctica from GRACE data. The high positive anomalies off-shore can therefore be explained as thinning of the oceanic crust when approaching the Indian-Antarctic ridge.

3.2 Magnetics

Measurements of the magnetic field have been carried out extensively in northern Victoria Land. The region is formed for large parts by volcanic and intrusive rocks of different origin and age. Thus the magnetic anomaly can show structures of such units of rock, even where they may be covered by ice or other rocks, or off-shore where no direct evidence is possible.

The magnetic field data originate from different aeromagnetic surveys carried out during several German and joint German-Italian Antarctica expeditions. Tab. 3.2 gives

an overview of the surveys and the appropriate references, Fig. 3.6 shows the areas covered by the individual surveys.

The surveys were carried out over a period of 21 years and differ also partly in their characteristics: some surveys were flown by plane at constant altitude, while others were done by helicopter with varying altitude, which is commonly called a "draped" survey. Generally, two different types of profile lines were measured: the survey lines, which cover the entire survey area at the desired spatial resolution, and the tie lines, which are oriented perpendicular to the survey lines at a much larger spacing; the tie lines are necessary for error checking (e.g. Militzer & Weber, 1984). The line spacing of the survey lines was the same for almost all surveys, as was the tie line spacing; it was found to be a good compromise between resolution and area coverage to conduct the measurements with a line spacing of 4.4 km and a tie line spacing of 22 km (Damaske, 1989). Only few surveys which aimed at higher resolution over a smaller area instead of regional reconnaissance were flown with narrow line spacing of 0.5 km and correspondingly smaller tie line spacing.

3.2.1 Processing of the aeromagnetic data

To use the magnetic field data for studying the Earth's crust, the 24 data sets had to be homogenized. For that purpose, the scheme used by Gabriel et al. (2011) was applied. It consists of five steps:

1. Calculation of the original geomagnetic reference field and addition to the anomaly data
2. Correction for regional variations of the secular variation
3. Calculation and subtraction of a common geomagnetic reference field
4. Field continuation to a common altitude
5. Calculation of offsets between adjacent surveys and merging of the surveys.

These five steps are explained in detail in the following sections.

Addition of the original geomagnetic reference field

The first homogenization step is to calculate the values of the geomagnetic reference field which were previously subtracted during data processing. The necessary information on the reference field models, epochs and heights used is listed in Tab. 3.3.

The International Geomagnetic Reference Field (IGRF) values are based on the IGRF coefficients which are computed from magnetic field permanent station recordings and satellite data under the auspices of the International Association for Geomagnetism and Aeronomy (IAGA). These coefficients represent a model of that part of the Earth's magnetic field which is produced by internal sources. As the magnetic field can be

Table 3.2: Overview over the individual aeromagnetic surveys carried out in northern Victoria Land (sorted by date). Where available, abbreviations for the surveys are given in parentheses.
Gitara is the abbreviation of *German-Italian Aeromagnetic Research in Antarctica.*

Expedition	Year	Survey Area	Reference
Ganovex 4	1984/1985	Polar Plateau (pla)	Bachem et al., 1989
		Ross Sea (ros)	Bachem et al., 1989
		Mountains ("Gebirge" – geb)	Bachem et al., 1989
Ganovex 5	1988/1989	Rennick Glacier (rgl)	Damaske, 1993
		Rennick Plateau (rpl)	Damaske, 1993
		Rennick Central (rce)	Damaske, 1993
		Rennick to Wilson Hills (rwi)	Damaske, 1993
Ganovex 6	1990/1991	Pennell Coast (pen)	Damaske, 1996
		Bowers Mountains (bow)	Damaske, 1996
		Ross Ice Shelf (ris)	Damaske, 1996; Damaske et al., 1994
ItaliAntartide 7	1991/1992	Gitara 1 (git)	Bozzo et al., 1994a,b
Ganovex 7/ItaliAntartide 8	1992/1993	Gitara 2 – Mt. Bellingshausen (bel)	Bozzo et al., 1997c,a
ItaliAntartide 9	1993/1994	Gitara 3 (gid)	Bozzo et al., 1997c,a
ItaliAntartide 10	1994/1995	Gitara 4 – Cape Roberts (cpr)	Bozzo et al., 1997b
ItaliAntartide 12	1996/1997	Gitara 5 (gic)	Bozzo et al., 1999
Tamara[a]	1997/1998	Tamara (tam)	Damaske et al., 2002
Ganovex 8/ItaliAntartide 15[b]	1999/2000	Oates Coast (oat)	Damaske et al., 2003
		Mertz & Ninnis Glaciers (men)	Damaske et al., 2003
		Cook Ice Shelf (cis)	Damaske et al., 2003
		Lillie Glacier region (lil)	Damaske et al., 2003
ItaliAntartide 17	2001/2002	Maganter	Armadillo et al., 2006, 2007; Ferraccioli et al., 2009a,b
		Asap (asp)	Wilson et al., 2007
Ganovex 9	2005/2006	Cape Hallet, Cape Adare (had)	Damaske et al., 2007
Ganovex 10/ItaliAntartide 25	2009/2010	Mesa Range (msr)	Damaske et al., 2014

[a] Abbreviation of "Transantarctic Mountains Aerogeophysical Research Activities".
[b] Surveys were carried out in the frame of the Gitara programme (Gitara 6).

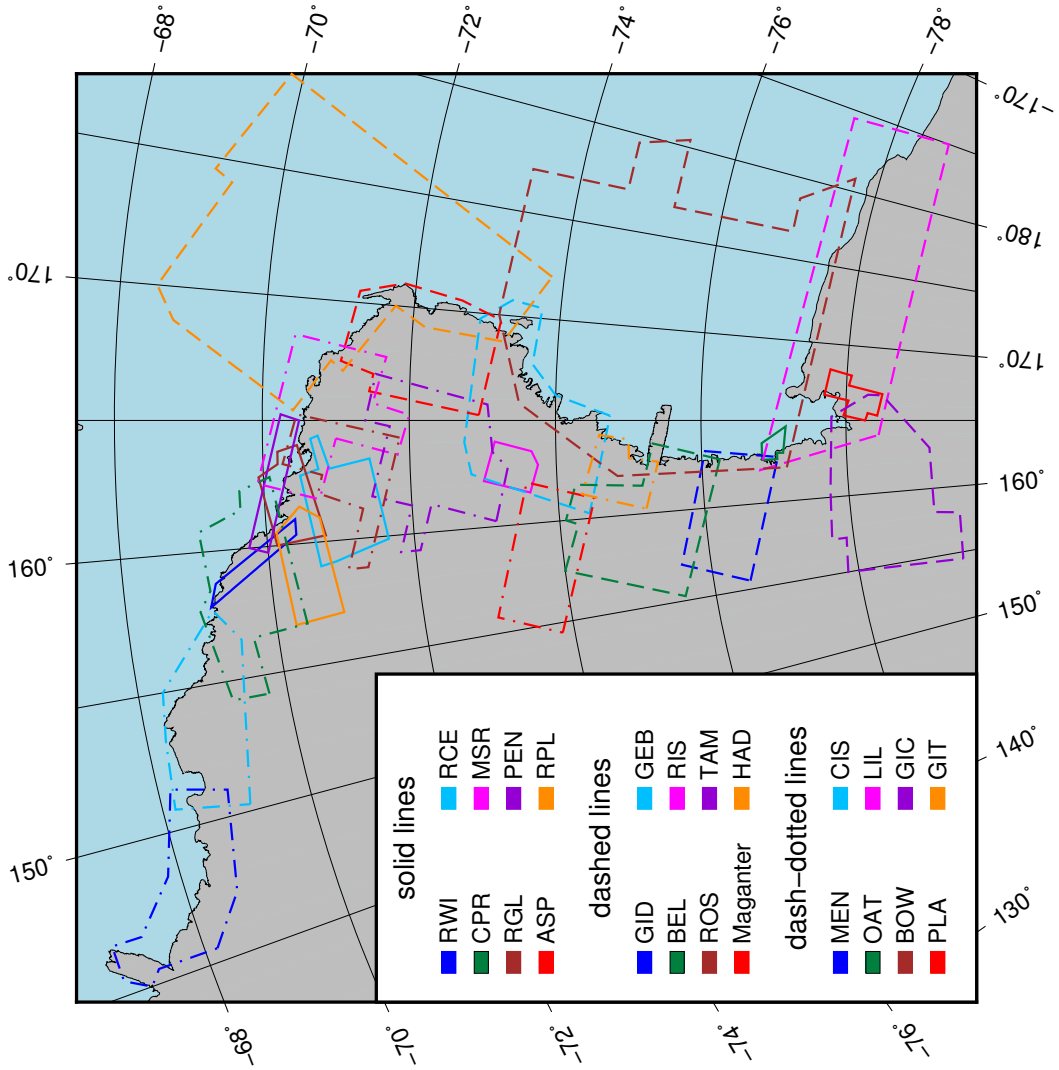

Figure 3.6: Area covered by the 24 aeromagnetic surveys (comp. Tab. 3.2).

Table 3.3: Geomagnetic Reference Fields and heights of measurements used during original processing. The GRF values were subtracted from the original data.

Survey (abbr.)	height	IGRF epoch	Reference
asp	draped (GPS)	IGRF2000 2002JAN21	Wilson et al., 2007
bel	2.700 m	IGRF1990 1993.10	Bozzo et al., 1996
bow	2.745 m	IGRF1990 1991.00	Damaske, 1996
cis	draped	IGRF2000 2000JAN15	Damaske et al., 2003
cpr	125 m barom.	IGRF1990 1994.90	Bozzo et al., 1997b
geb[a]	3.660 m	IGRF1980 1985.00	Bachem et al., 1989
gic[b]	0 m	IGRF1995 1996.87	Damaske, pers. comm.
gid[c]	2.750 m	IGRF1990 1994.10	Bozzo et al., 1996; Damaske, pers. comm.
git	2.700 m	IGRF1990 1992.10	Bozzo et al., 1996
had	600 m/ draped (GPS)	IGRF2005 2005DEZ12	Damaske et al., 2007
lil	draped	IGRF2000 2000JAN15	Damaske et al., 2003
Maganter[d]	GPS	IGRF2000 2002FEB02	Damaske, pers. comm.
men	draped	IGRF2000 2000JAN15	Damaske et al., 2003
msr	draped (GPS)	IGRF2005 2010JAN11	Damaske et al., 2014
oat	draped	IGRF2000 2000JAN15	Damaske et al., 2003
pen	610 m	IGRF1990 1991.00	Damaske, 1996
pla[a]	2.745 m	IGRF1980 1985.00	Bachem et al., 1989
rce[e]	2.590 m	IGRF1985 1989.13	Damaske, 1993
rgl[e]	1.220 m	IGRF1985 1989.13	Damaske, 1993
ris	610 m	IGRF1990 1991.00	Damaske, 1996
ros[a]	610 m	IGRF1980 1985.00	Bachem et al., 1989
rpl[e]	2.590 m	IGRF1985 1989.13	Damaske, 1993
rwi[e]	2.590 m	IGRF1985 1989.13	Damaske, 1993
tam	draped	IGRF1995 1998JAN12	Damaske et al., 2002

[a] The IGRF correction was calculated by transforming the IGRF coefficients to a local Lambert coordinate system. A height of 2.000 ft a.s.l. (equivalent to 610 m) was used and constant offsets independently for each survey area computed from the vertical IGRF gradient were applied.

[b] Bozzo et al. (1999) refer to the IGRF 1995 at epoch 1996.11 and a height of 9.000 ft a.s.l. (equivalent to 2.700 m). According to Damaske (pers. comm.) this is incorrect; epoch 1996.87 and a height of 0 m have been used instead (details see text).

[c] In Bozzo et al. (1996) the supposedly erroneous epoch 1994.10 of IGRF1990 is given. Instead, the correction was presumably applied independently for each survey date. However, the epoch 1994.10 has been used for further data treatment (details see text).

[d] A base station value of −64.267 nT was subtracted.

[e] The IGRF correction was calculated by transforming the IGRF coefficients to a local Lambert coordinate system, using the respective heights.

expressed as the gradient of a scalar potential, this potential is then expanded into a series of spherical harmonics (e.g. Finlay et al., 2011).

The actual 11th generation (Finlay et al., 2011) comprises coefficients for epochs every five years beginning with the epoch 1900.00 and ranging to epoch 2010.00. For extrapolation purposes for the period until 2015.00 coefficients for the secular variation are given whereas for epochs between the given ones the secular variations can be calculated from the neighbouring epochs. For the epochs 1900.00 to 1995.00, the coefficients are given to degree 10, for the epochs 2000.00 to 2010.00 they are given to degree 13. The coefficients for the extrapolation of the secular variation until epoch 2015.00 are given to degree 8. The coefficients for the epochs 1945.00 to 2005.00 are set to a 'definitive' state; they will not be changed in the future as no new data are expected to become available.

Six IGRF generations have been used for the 24 surveys. However, for seven surveys the IGRF values were not calculated directly from the spherical harmonics (cf. Tab. 3.3, notes a and e); only four IGRF generations have been directly used (Langel, 1992; Barton, 1997; Mandea & Macmillan, 2000; Maus et al., 2005). The computation of the IGRF values for the 17 remaining surveys has been carried out with the program *Geomag 7.0* which is available online from the IAGA as well as the coefficients of all IGRF generations (cf. Finlay et al., 2011). With this software the IGRF values were calculated in each case using the set of coefficients which was available during original processing; in doing so, discrepancies due to later updates of the coefficients could be avoided.

In case of the surveys which were carried out in the frame of expeditions Ganovex 4 and 5 (i.e. geb, pla, ros; rce, rgl, rpl, rwi) the original IGRF values have been computed after a transformation into a local Lambert coordinate system. The projection details as well as the projected IGRF coefficients can be found in Damaske (1988) for the first three surveys from Ganovex 4, and in Damaske (1990) for the other surveys. For several of the surveys offsets have been found and corrected together with the IGRF removal which is also documented in the references cited above. All computations could be reproduced and so the IGRF removal be undone.

In two cases the IGRF information given in literature seems to be incorrect. This regards the surveys **gic** and **gid**; both are explained in detail:

gic In Bozzo et al. (1999) the IGRF1995 epoch 1996.11 is given. As the survey was flown from October 29 to November 29, 1996 (Müller et al., 1997), the epoch 1996.87 (equivalent to November 14, 1996, the central date of the survey) was chosen for further data treatment. According to Damaske (pers. comm.) also the height of 9.000 ft a.s.l. (equivalent to 2.700 m) given in Bozzo et al. (1999) was replaced by 0 m for IGRF calculation.
In summary, IGRF1995 epoch 1996.87 and a height of 0 m have been chosen for the first processing step.

gid Bozzo et al. (1996) give the IGRF1990 epoch 1994.10 which is incorrect according to Damaske (pers. comm.). The IGRF removal instead was computed independently for each survey date. Tests with *Geomag 7.0* showed only small changes of the IGRF total intensity values over the period of the survey (December 26, 1993 – January 9, 1994; Damaske, pers. comm.) in the order of few nT whereas the anomalies cover a range of about 2.500 nT. Also the IGRF total intensity values vary little between epochs 1994.00 (centre of surveying period) and 1994.10 (given in the reference cited above) in the order of about 5 nT. Therefore, the differences between the IGRF values which were removed during original processing and the values computed for epoch 1994.10 are negligible, especially compared to the dynamics of the anomalies.

Regional variations of the secular variation

Due to the large area covered by most of the surveys each of the data sets has to be corrected for regional variations in the secular variation (SV) of the geomagnetic field. This can be done by fitting a polynomial of 2nd degree to the values of the magnetic total intensity measured at observatories (Wonik, 1992). Obviously the quality of the fit depends on the number of stations, but also on the distances between the stations as well as the distances from the survey area to the stations. Therefore, it is much easier to compute a polynomial for Europe than for Antarctica as the number of observatories (and likewise the number of repeat stations which can also be used) is much higher and the distances much smaller. Another problem might arise from the fact that, compared with other regions of the world, the SV of the total intensity is relatively small for Europe (Wonik, 1992; Finlay et al., 2011). SV computation from the IGRF generation 11 shows, however, that the absolute value of the SV of the total intensity is not much higher for Victoria Land than for Europe.

The fitting of a polynomial of 2nd degree produces ten coefficients: one constant term, three linear terms for three coordinates, three 2nd degree terms, and finally three 2nd degree terms with mixed coordinates. As a consequence, a minimum of ten observatories is required for the fitting. As the observatories in and around Antarctica are limited in number and the distances are much higher than in Europe, distances of the observatories from the survey area of more than 7.000 km have to be accepted. Due to the location of the survey areas near the geographic pole there has to be applied a transformation of the station coordinates as well as all survey point coordinates into a geocentric Cartesian coordinate system, as the differences between the geographic and Cartesian coordinates are too large to be neglected.

Magnetic field data for more than 300 observatories are provided by the World Data Center (WDC) for Geomagnetism at the British Geological Survey (BGS) in Edinburgh[6]. The data can be downloaded as hourly means, for many observatories also 1-minute data

[6] `www.wdc.bgs.ac.uk`

are available. In total, 27 observatories in and around Antarctica, including Australia, New Zealand, southern Indian Ocean islands and South Pacific islands, were found, for which at least for some days equivalent to the survey epochs of Tab. 3.3 hourly means are available through the BGS/WDC website. 26 of these 27 observatories were used for the SV computation. The data from the German Antarctic station Neumayer III were not taken into account, as the station is placed on a floating ice shelf; as a consequence, the exact location and, more important, orientation of the sensors changes over time, but, according to the WDC meta information, readjustments are not executed to avoid disturbances and gaps in the data. The names and locations of the 26 observatories are listed in Tab. 3.4; Fig 3.7 shows the distribution of the observatories in and around Antarctica.

The files with the hourly means also contain a daily mean value for each magnetic field component given as long as none of the hourly means for the whole day for the respective component is missing due to data gaps in the original data. The BGS/WDC website, though, provides only data base structures and a web interface; the data are put into the data base by the observatories themselves. This causes differences in the magnetic field components available through the website. Some observatories provide X, Y, and Z components, some also add total intensity F, others provide a horizontal intensity H and the two angular functionals, declination D and inclination I. As the aeromagnetic survey data only cover the magnetic total intensity also only total intensity daily means of the observatory data are of interest for the SV computation. From the daily means of the components given, a total intensity value can be calculated, the formula depending on the given components (Eq. 3.3 to 3.5):

$$\overline{F} = \sqrt{\overline{X}^2 + \overline{Y}^2 + \overline{Z}^2} \tag{3.3}$$

$$= \sqrt{\overline{H}^2 + \overline{Z}^2} \tag{3.4}$$

$$= \overline{H} / \cos I \tag{3.5}$$

with	$\overline{F}$	daily mean of magnetic total intensity,
	$\overline{X}$, $\overline{Y}$, $\overline{Z}$	daily means of the Cartesian components of the magnetic field,
	$\overline{H}$	daily mean of the horizontal component of the magnetic field,
	$\overline{I}$	daily mean of inclination.

Where a daily mean value for the total intensity is available, it has been computed from the original 1-minute data or from hourly means, the second case being expressed as a formula in Eq. 3.6.

Table 3.4: Geomagnetic observatories in and around Antarctica which were used for SV corrections.

Code	Name	Country	Latitude [deg.]	Longitude [deg.]	Altitude [m]
AIA	Faraday Isl. (Argentine Isl.)	Antarctica	−65.245	295.742	10
AMS	Martin-de-Viviés/Île Amsterdam	French Southern and Antarctic Lands	−37.8	77.57	50
API	Apia	Samoa	−13.815	188.219	4
ARC	Arctowski	Antarctica	−62.16	301.522	16
ASP	Alice Springs	Australia	−23.762	133.883	557
CNB	Canberra	Australia	−35.315	149.363	859
CSY	Casey	Antarctica	−66.283	110.533	41
CTA	Charters Towers	Australia	−20.09	146.264	370
CZT	Port Alfred/Îles Crozet	French Southern and Antarctic Lands	−46.431	51.867	155
DRV	Dumont d'Urville	Antarctica	−66.667	140.007	30
DVS	Davis	Antarctica	−68.583	77.967	0
EYR	Eyrewell	New Zealand	−43.422	172.355	120
GNA	Gnangara	Australia	−31.78	115.947	60
KDU	Kakadu	Australia	−12.686	132.472	14.6
LIV	Livingston Island	Antarctica	−62.662	299.605	19.4
LRM	Learmonth	Australia	−22.222	114.101	4
MAW	Mawson	Antarctica	−67.604	62.879	12
MCQ	Macquarie Islands	Australia	−54.5	158.95	8
MIR	Mirny	Antarctica	−66.55	93.017	20
PAF	Port-aux-Francais/Îles Kerguelen	French Southern and Antarctic Lands	−49.353	70.262	35
PPT	Pamatai (Papeete)/Tahiti	French Polynesia	−17.567	210.426	357
PST	Port Stanley/Falkland	British Overseas Territory	−51.704	302.107	135
SBA	Scott Base	Antarctica	−77.58	166.763	16
SNA	Sanae III	Antarctica	−70.312	357.59	52
TRW	Trelew	Argentina	−43.267	294.617	15
VOS	Vostok	Antarctica	−78.45	106.867	3500

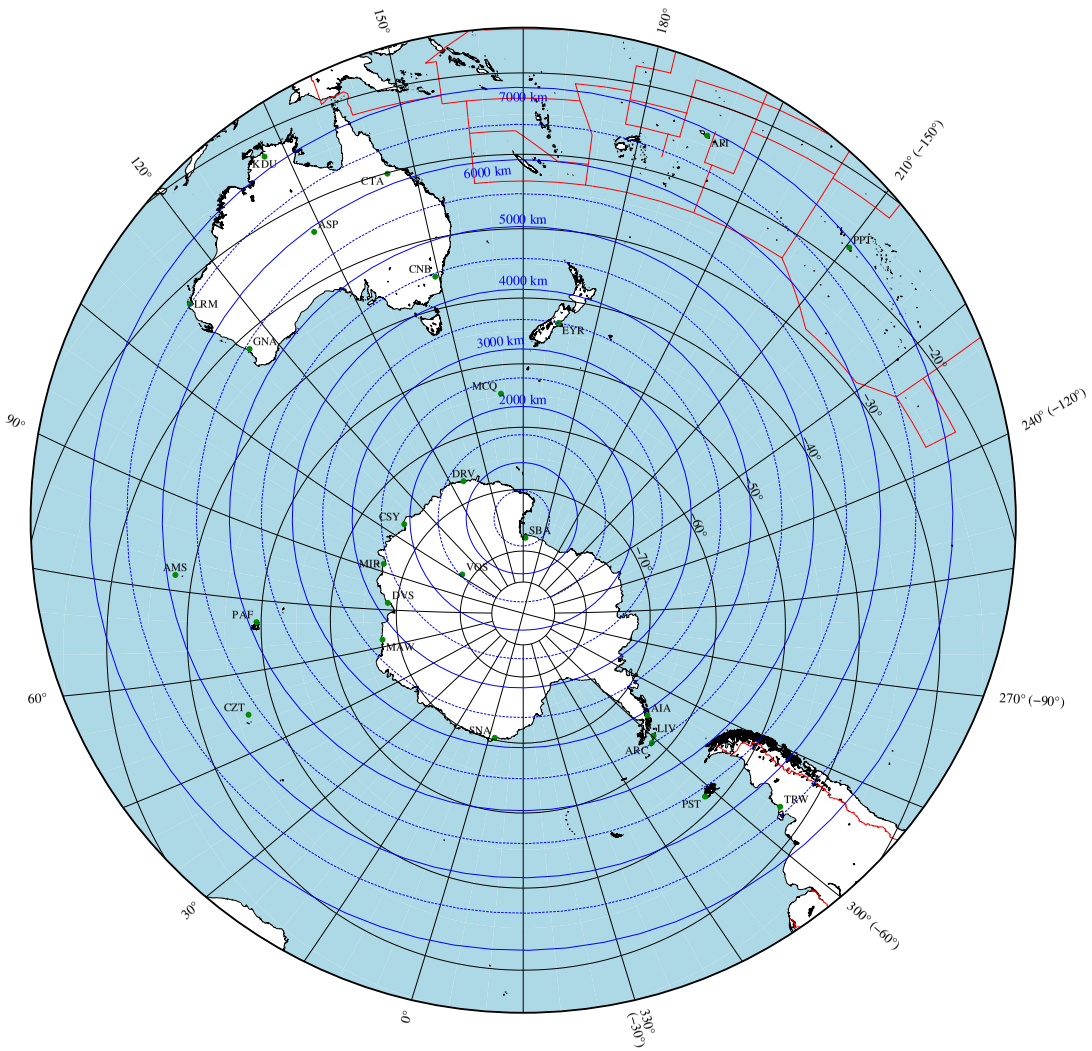

Figure 3.7: Distribution of geomagnetic observatories in and around Antarctica, which were used for the SV correction (comp. Tab. 3.4). Distances to the German Gondwana station (located centrally in the area covered by the aeromagnetic data) are shown as blue circles. For details on the data availability for the different epochs, see Tab. 3.5.

$$\overline{F} = \frac{1}{24} \sum_{i=1}^{24} F_i \tag{3.6}$$

with $\overline{F}$ daily mean of magnetic total intensity,
F_i hourly means of magnetic total intensity.

Obviously there is a difference between both methods of calculating a daily mean of the total intensity. Tests for stations where hourly and daily means for X, Y, Z and F are available showed, however, that the differences between daily means of the total intensity computed by the two approaches are in the order of 0.1 nT and can therefore be neglected.

After transformation of the geomagnetic observatory coordinates as well as of the coordinates of the data points from all surveys into an Earth-centered, Earth-fixed coordinate system, which was carried out using GMT software, a Python script was used to fit second-degree polynomials to the observatory daily means for each epoch needed. In total, 15 epochs were selected: 14 epochs cover the aeromagnetic surveys, and the epoch 1980.00 was chosen as new reference epoch, thus being consistent with the approaches of Wonik (1992) and Gabriel et al. (2011).

A second-degree polynomial function in 3D Cartesian coordinates needs ten parameters: three pure squared terms, three mixed squared terms, three linear terms, and one constant value (Eq. 3.7). Therefore, to fit such functions to measured data, at least ten data points (in this case observatories) are necessary to define all parameters.

$$\begin{aligned} F = a \cdot x^2 + b \cdot y^2 + c \cdot z^2 + d \cdot x \cdot y + e \cdot x \cdot z + f \cdot y \cdot z + \\ g \cdot x + h \cdot y + i \cdot z + k \end{aligned} \tag{3.7}$$

with F magnetic total intensity,
x, y, z Cartesian coordinates,
$a \ldots k$ parameters of the polynomial fit.

For the fits calculated for the Victoria Land data, between 13 and 22 observatories provided data for the different epochs (details can be found in Tab. 3.5); thus also standard deviations for the parameters as well as a RMS error could be computed. The relative RMS errors vary between 1.16 % and 3.26 %. All fit results, including the parameters with their standard deviations as well as the RMS values, are listed in Tab. B.1 in appendix B.

Table 3.5: Overview over the data availability from the geomagnetic observatories for the survey epochs.

Observatory code	1980/01/01 (1980.00)	1985/01/01 (1985.00)	1989/02/17 (1989.13)	1991/01/01 (1991.00)	1992/02/06 (1992.10)	1993/02/06 (1993.10)	1994/02/06 (1994.10)	1994/11/25 (1994.90)	1996/11/14	1998/01/12	2000/01/15	2002/01/21	2002/02/02	2005/12/12	2010/01/11	count
AIA	x		x	x					x	x	x	x	x	x	x	10
AMS		x	x	x	x	x	x	x	x	x	x	x	x	x		13
API		x	x		x	x	x	x	x	x	x	x	x	x		12
ARC	x	x	x	x	x	x	x	x								8
ASP						x	x	x	x	x	x	x	x	x	x	10
CNB	x	x	x	x	x	x	x	x	x	x	x	x	x	x	x	15
CSY			x		x	x	x	x	x	x	x	x	x	x	x	12
CTA				x	x	x	x	x	x	x	x	x	x	x	x	12
CZT	x	x	x	x	x	x	x	x	x	x	x	x	x	x	x	15
DRV	x	x	x	x	x	x	x	x	x	x	x	x	x	x	x	15
DVS			x			x	x	x	x	x	x					7
EYR	x	x	x	x	x	x	x	x	x	x	x	x	x	x	x	15
GNA	x	x	x		x	x	x	x	x	x	x	x	x	x	x	14
KDU									x		x			x	x	4
LIV										x	x	x	x	x	x	6
LRM				x	x	x	x	x	x	x	x	x	x	x	x	12
MAW	x			x	x	x	x	x	x	x	x	x	x	x	x	13
MCQ						x	x	x		x	x	x	x	x	x	9
MIR	x	x							x							3
PAF	x	x	x	x	x	x	x	x	x	x	x	x	x	x	x	15
PPT	x	x	x	x	x	x	x	x	x		x	x	x	x	x	14
PST							x	x	x	x	x			x		6
SBA	x	x	x	x	x	x		x	x	x	x		x	x	x	13
SNA	x	x	x													3
TRW							x	x			x	x	x	x	x	7
VOS	x	x				x				x						4
	14	14	15	13	15	19	19	20	20	20	22	18	19	21	18	

With the fitted parameters, for any point and for the distinct epochs, geomagnetic total field values can be calculated. The SV correction for a particular survey point itself is the difference between those values for the survey epoch and the reference epoch (Eq. 3.8).

$$F_{SV} = F_{\text{epoch}} - F_{1980.00} \tag{3.8}$$

with F_{SV} magnetic total intensity secular variation correction value,
F_{epoch} magnetic total intensity at survey epoch,
$F_{1980.00}$ magnetic total intensity at epoch 1980.00.

This SV value is finally subtracted from the measured (or pre-processed) value to virtually shift the measurement to the reference epoch (Eq. 3.9).

$$F_{corr} = F_{measured} - F_{SV} \tag{3.9}$$

with F_{corr} corrected magnetic total intensity,
$F_{measured}$ measured magnetic total intensity.

Applying a common Geomagnetic Reference Field

After subtraction of SV effects, the correction of the data for a common Geomagnetic Reference Field can be applied. As stated above, the epoch 1980.00 has been chosen. The reference field values have been calculated from DGRF1980 coefficients, using the software "Geomag" again, as done in the first step. The height information used now is the same as for the first step; only the survey **gic** is an exception. In the first step a height of 0 m has been used, as suggested by Damaske (pers. comm.); for the application of a common Geomagnetic Reference Field, the original survey altitude of 2.700 m, as given by Bozzo et al. (1999), has been chosen.

The result of this step yields data with a common reference date, thus enabling true comparison between the different surveys in the overlapping areas. Surveys measured at the same altitude could now already be put together; as only few surveys share the same altitudes of measurement, the next processing step has to be a field continuation to a common level.

Gridding and field continuation

For the purpose of gridding, the data have been projected into a Lambert Conic Conformal coordinate system in the same way as the gravity data (see Sec. 3.1.3; comp. also Reitmayr, 1997). This enables later comparison between gravimetric and magnetic data and models and is, in general, consistent with the approach of Wonik (1992) and Gabriel et al. (2011) as well as the various published single-survey results (see Tab. 3.2 for references).

Gridding itself has been done using the 'nearneighbor' gridding algorithm of GMT (Wessel & Smith, 1991; Wessel et al., 2013). This algorithm calculates the grid node values as a weighted mean of neighbouring data. It is possible to define a search radius as well as divide the search area into sectors. A common search radius of 6 km was chosen for the 24 data sets, and sectoral search was set to eight sectors, of which five had to be filled with data to generate a grid value.

The cell size of the resulting grids was chosen according to the distances between the survey lines of the different surveys. Most of the surveys were carried out as reconnaissance surveys, sharing the same survey line and tie line spacing of 4.4 km and 22 km, respectively (Damaske, 1989; cf. also references in Tab. 3.2). For several surveys, a grid cell size of 440 m has been used before (e.g., Damaske, 1996; Damaske & Bozzo, 2003). For better comparison with gravimetric data, a more regular value of 500 m was selected.

The three surveys **asp**, **cpr**, and **msr**, however, were laid out not as reconnaissance surveys but as local measurements. These surveys were carried out with much lower survey line spacing of only 500 m, and a cell size of 100 m was used (Wilson et al., 2007; Bozzo et al., 1997b; Damaske et al., 2014). It is sensible to choose the same cell size, but then low-pass filtering would be necessary to fit those data into the combination of the other 21 surveys. This would be the case also if those data were gridded with a cell size of 500 m, though.

The field continuation is, in general, a process of filtering, with the filter depending on the direction of continuation. As the magnetic field inversely depends on the distance to its source, at higher measurement altitudes near-surface, high-frequency anomalies cannot be resolved significantly. On the other hand those anomalies dominate when the field is measured on the surface, and deeper structures corresponding to low-frequency anomalies are only visible after applying a low-pass filter to the data. Field continuation algorithms use these relations and amplify the shorter wavelengths when continuing downward, and the longer wavelengths when continuing upward. In case of downward continuation additional filtering may be necessary to avoid over-amplification of very local anomalies to extreme amplitudes (cf. Grauch, 1984).

Special treatment of data is needed if the survey was carried out with varying altitude, e.g. if measurements on the surface have to be continued to a certain level above, or if the reverse is requested. Standard algorithms for field continuation which often use Fast Fourier Transforms cannot achieve such calculations. Grauch (1984) developed a Fortran programme named *TAYLOR* which relies on Taylor series expansion. By this approach the programme is not only able to continue from one level to another, but also from surface to level and vice versa. This programme has successfully been used by Wonik (1992) as well as Gabriel et al. (2011); it has also been used in this study.

Some data sets had to be prepared for the use with *TAYLOR* for different reasons. The survey **had** was mostly flown at an almost constant level of 600 m a.s.l. off-shore, but approaching the coast the level changes rapidly, thus giving artefacts during continuation. Therefore, small amounts of data were cut away. The survey **maganter** showed the same

problem vice versa: this survey covers a mountainous area with the highest altitudes of NVL, but along the coast the survey altitude was often much lower than in the landward part of the survey area.

In case of the survey **ros** *TAYLOR* was very unstable and crashed several times and with different parts of the whole data grid. The problem seemed to be the orientation of the survey area with respect to the chosen Lambert system. Gridding the original data with the same parameters as before, but using as central meridian of the Lambert system 174° east instead of 164° east, produced a grid which *TAYLOR* was able to continue. The different Lambert systems can be transformed into each other mainly by one rotation computation. Therefore, the grid node coordinates of the 'standard' system were transformed to coordinates in the special system and there filled with data by bi-cubic interpolation. Thus, the grid values could be assigned to the 'standard' coordinates with only one interpolation step.

The common level for continuation was chosen to be 2.700 m. Criteria for the selection of the common level were the altitudes of the surveys and of the terrain, as continuation below the surface is, in general, dangerous, and anomalies in those parts must not be interpreted. Three surveys were measured at the selected level, and only small areas in the mountains have higher altitudes; on the other hand the off-shore surveys don't loose to much information by upward continuation. However, in case of the surveys **maganter** and **geb**, the filtering option of *TAYLOR* had to be used as both data sets were continued downward.

Combination of the data

The final step to produce a single magnetic anomaly data set is the combination of the different surveys. As each survey overlaps with one or more other surveys, offsets between the surveys can be calculated and one survey shifted by such an offset to fit the data level of the neighbouring surveys. In some cases a constant offset is not sufficient as the differences between the surveys vary too much. Linear regressions were applied to the differences in those cases. This approach is consistent with Wonik (1992).

3.2.2 Final anomaly map

The final anomaly map (Fig. 3.8) covers a range of −923 nT to 3.245 nT. The general data level varies between 800 nT and 1.400 nT; the lowest values can be found in the central part of northern Victoria Land in those areas where the topography reaches altitudes of more than 3.000 m, and therefore the common altitude of the data is superseded. Those anomalies must not be interpreted, as one prerequisite of downward continuation is not fulfilled there: The volume between original and continuation level is not source-free. The highest anomaly values are situated along the Ross Sea coast of Victoria Land, and mainly represented by circular structures with very high gradients. A comparison with the tectonic sketch map from Läufer et al. (2011), presented in Fig. 2.4,

shows that at least some of these anomalies can possibly be connected to the occurrence of young magmatic rocks, which are summarised by these authors as 'McMurdo Volcanics and Meander Intrusives'. For example, Mount Melbourne, a volcano belonging to this group of rocks, and presumably still active, which is located only about 30 km NE of Gondwana Station (the origin of the coordinate system), is visible as small-area, high-intensity anomaly.

The area between 50 km and 250 km Easting and 100 km and 400 km Northing, which is mainly covered by data from the survey **maganter**, is heavily disturbed by artefacts. The survey **maganter** was carried out as draped survey with a survey line spacing of 4.4 km; intermediate lines were added at 2.2 km spacing especially in the southern part. In many cases the altitudes at which neighbouring lines were flown differ by 100 m or more. As a consequence, the SV correction values differ also clearly by 1.000 nT or more. Those differences are too large to be filtered properly. Unfortunately, only the survey lines of **maganter** were available, but not the tie lines. Additional levelling, which could have helped to reduce the effect of these large altitude differences, was therefore not possible.

Also the area of the **tam** survey, between −200 km and 0 km Easting and south of −350 km Northing, are not to be interpreted. The survey tam can only be connected at its eastern boundary to other surveys. Additionally, the largest part of tam was flown over the Antarctic plateau, whereas the easternmost part, which is overlapping with other surveys, was flown at much lower altitudes. Thus, a secondary discrepancy between the main part of tam and the neighbouring surveys to the east arises from the large impact of those altitude changes on field continuation. If the gap to the north of tam could be filled with data, the combination of tam into the whole anomaly map would be clearly supported.

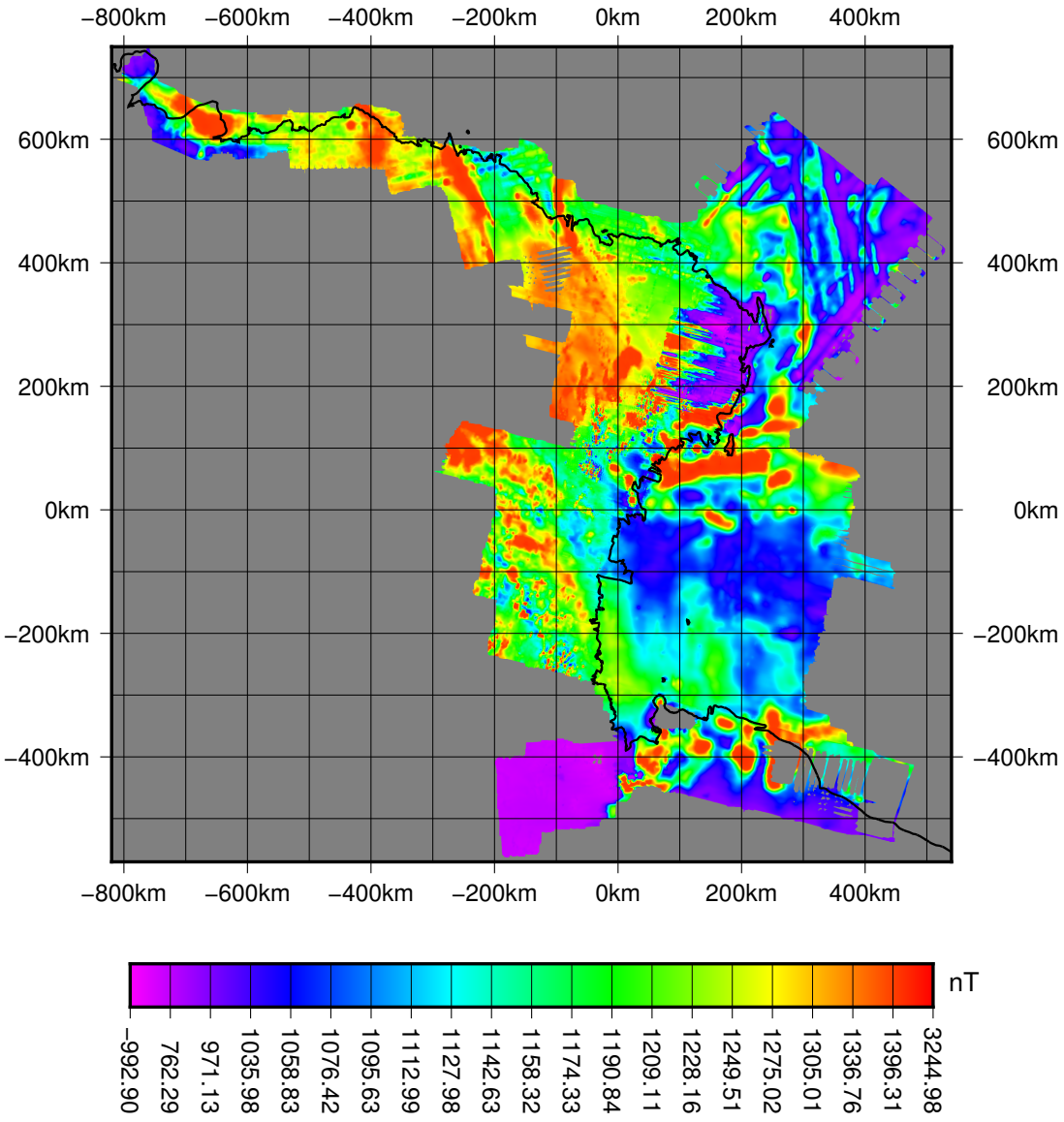

Figure 3.8: Final aeromagnetic anomaly map. The aeromagnetic total intensity anomalies are shown for a common altitude of 2.700 m; the DGRF1980 (e.g. Finlay et al., 2011) at epoch 1980.00 has been used for all data.

Chapter 4

Potential field modelling

4.1 Modelling software *IGMAS+*

A common method of potential field modelling is the 2 D method, e.g. based on the algorithm of Talwani et al. (1959), where one single section through the ground is created. Along that section, polygons are defined as cross-sections of the anomaly-creating bodies. These bodies are infinite perpendicular to the section. A more sophisticated way is to model bodies which can have finite lengths perpendicular to the section. This method is called 2.5 D method if all the bodies end at the same distance from the section, or 2.75 D if the extents of the different bodies vary.

The software *IGMAS+* (Götze & Lahmeyer, 1988; Schmidt et al., 2011) used in this study enables 3 D modelling by use of several sections. Each section contains polygons as cross-sections through the different bodies which the subsurface consists of. The formation of 3 D bodies is done by triangulation between the sections (Fig. 4.1). Physical properties can be assigned to different bodies, i.e. a density for gravimetric modelling, or a susceptibility for magnetic modelling. *IGMAS+* enables calculation of all three components of the gravity vector – the vertical component is commonly referenced to as gravity – as well as the six components of the gravity gradient tensor. All three components of the magnetic field can be calculated, as can be the magnetic total field anomaly and the vertical gradient of the total field.

The distances between the model sections can be constant throughout the whole model, but also arbitrary spacing is possible to increase the resolution of the model in a certain area. The orientation of the sections with respect to the model coordinate system can be chosen as needed, as can be the horizontal and vertical extent of the model. Finally, *IGMAS+* can do inversions of the measured anomaly fields together with the modelled structures to refine the previously chosen values of the physical properties.

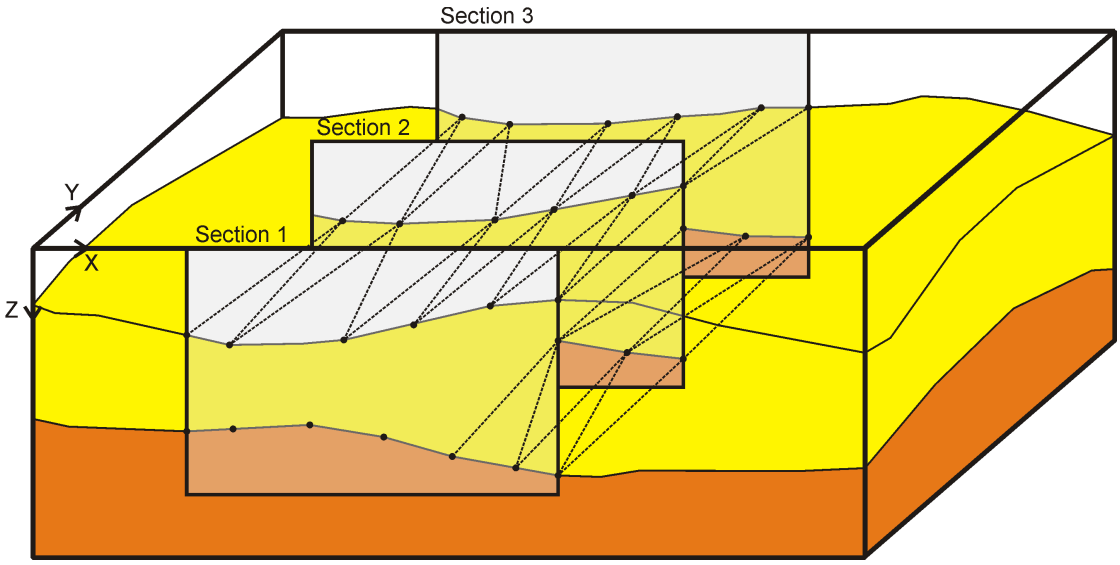

Figure 4.1: Working scheme of *IGMAS+*, showing cross-sections and triangulation of bodies between the sections (after Götze & Lahmeyer, 1988).

4.2 Gravimetric modelling

4.2.1 Models based on wavelength-filtered data

As described in section 3.1.3, the EIGEN-6C3stat data set has been split into three data sets, each limited to a certain part of the spectrum. This approach enables estimations of the maximum depth of the sources of the gravity anomalies. Thus, the different stockworks of the lithosphere can be separated. However, it is important to keep in mind the fact that the estimated source depth is the maximum depth possible – an apparently deep source, i.e. a source corresponding to long wavelengths and low frequencies in the anomaly field, can be a deeply located point source as well as a shallow source with a broad shape.

The models developed on basis of the filtered data cover an area ranging from approx. 64° south to 78° south, 650 km wide in west-east direction. The north-south extent is 1.600 km. The models consist of 33 sections, oriented perpendicular to the central meridian of the Cartesian map projection used (see section 3.1.3 for details), i.e. perpendicular to 165° east (Fig. 4.2); the sections are spaced every 50 km. The model area has been shrunk on all four sides by 100 km against the filtered data; thus the incorporation of edge effects from the filtering process into the models could be avoided.

Low-pass filtered data

The low-pass filtered anomaly shows very low gravity values on-shore, following the course of the TAM, whereas off-shore and with growing distance to the shore especially to the north (i.e. to the Indian-Antarctic Ridge as the next divergent plate boundary)

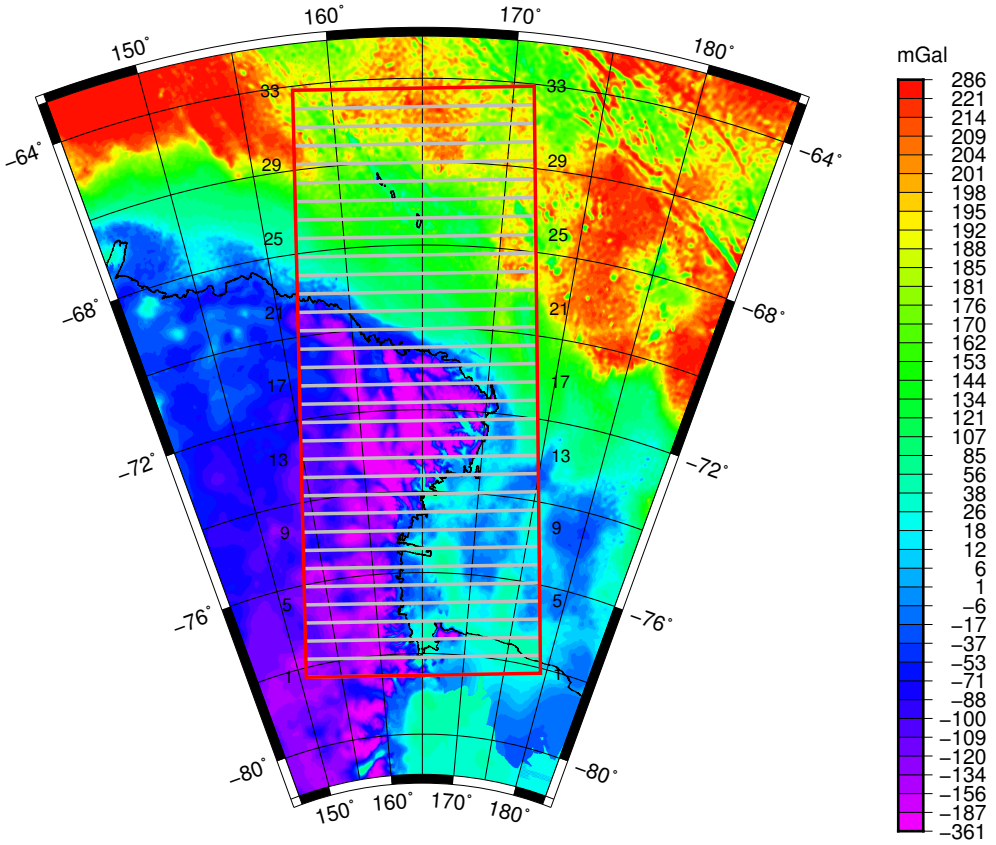

Figure 4.2: Simple Bouguer anomaly (as shown before), with the location of the model area and the 33 model sections. The sections are numbered from 1 to 33 from south to north. The colour scale is the same as before.

the gravity values are increasing. In total a range of more than 400 mGal is covered. Together with the approximate maximum source depth of more than 70 km one can conclude that the anomaly is mainly originating from the varying depth of the Moho.

A model was developed to test this hypothesis. This model, containing only two bodies (crust and mantle), could support the hypothesis. The Moho as boundary between crust and mantle, representing a density contrast of $650\,\mathrm{kg\,m^{-3}}$ (the mantle having the higher density), explains the low-wavelength part of the anomaly completely, leaving only a few mGal of residual anomaly. This residual anomaly, ranging from -7 mGal to 3 mGal, is partly based on the locally insufficient resolution of the model, and may partly be resulting from errors in the data which were used to calculate the Bouguer anomaly.

The resultant Moho depth (Fig. 4.3) varies between 18 km and 41 km. The most shallow parts of the Moho are located off-shore to the north, near to the Indian-Antarctic Ridge. The deepest parts of the Moho are connected to the TAM and represent the root of the Transantarctic Mountains. A comparison of the modelled Moho depths to the results of Block et al. (2009), who computed Moho depths for the whole continent of Antarctica from GRACE satellite data, shows good agreement between both. The GRACE results show similar values for the Moho depth in Victoria Land, as does the EIGEN-6Cstat model presented here.

The horizontal extent of the model is enlarged with respect to the data by 300 km to the west as well as to the east to avoid edge effects. The northern and southern edges of the model have been extended internally in *IGMAS+* by 500 km for the same reason. The extensional parts of the model should not be interpreted, as they are not fully supported by the anomaly data. Therefore the Moho depth map in Fig. 4.3 is limited to the area covered by the anomaly data.

Band-pass filtered data

The band-pass filtered data represent sources from intermediate depths between 70 km and 30 km. The anomaly ranges from -99 mGal to 112 mGal. Especially on-shore in NVL, but partly also off-shore to the north, the anomaly shows linear patterns which are very strong on-shore, covering the complete range of the anomaly at distances of less than 100 km. The horizontal gradients are therefore of the order of more than $2\,\mathrm{mGal\,km^{-1}}$. In SVL the anomaly pattern is dominated by approximately circular anomalies which often are isolated from each other by areas of mean anomaly; this is partly also true off-shore in the Southern Ocean. Comparison with geologic maps supports the assumption of the linear pattern in NVL being connected to known fault zones; these fault zones then would reach at least several kilometres into the crust and thus had to be very large.

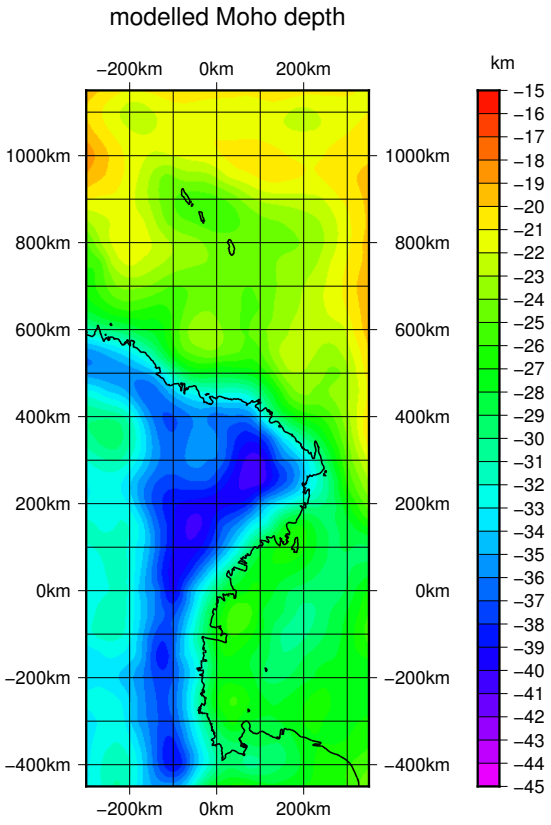

Figure 4.3: Modelled Moho depth.

High-pass filtered data

The high-pass filtered part of the gravity anomaly contains only sources shallower than 30 km. Thus, the effects of topography, which can be clearly seen in the data, can also be found in the high-pass filtered anomaly (comp. Fig. 3.4). Additionally, especially in the Southern Ocean part of the data, the high-pass filtered anomaly is dominated by speckles resulting from satellite tracks, as data from several satellite missions have been incorporated into the EIGEN-6C3stat gravity field model. Therefore, the high-pass filtered data have not been modelled, as only weak boundary conditions from geology or other geophysical methods exist which could help to find a plausible model.

Combination of low- and band-pass models

The two models covering the low-pass and band-pass data were combined to one single model. This model consists of upper and lower crust and lithospheric mantle. The sections of this model together with the summarized low- and band-pass anomalies are shown in Appendix C (p. 95 ff.). Based on this model, a structural interpretation can be carried out.

The results of the modelling are shown exemplarily for three west-east running cross-sections (Fig. 4.4, Fig. 4.5, and Fig. 4.6). The model depth is 50 km, the horizontal extension ranges from −600 km to 650 km. As for the low-pass model, the sections are extended against the anomaly data to avoid edge effects. The band-pass model implements a boundary between lower and upper crust, representing a density contrast of $450\,\mathrm{kg\,m^{-3}}$ (the lower crust has a higher density). The model shows a boundary between upper and lower crust which is undulating with large amplitudes on-shore, whereas off-shore this undulation is much less distinct. This result is shown in a 3 D plot of the boundary in Fig. 4.7.

4.2.2 Subduction zone models

Based on the geologic idea of Kleinschmidt & Tessensohn (1987), who describe the development of NVL as two-step subduction process (cf. Sec. 2.3.1), and the geologic sketches (Fig. 2.3), two simple models were designed: One shows two subduction zones, with the crustal segment in between being very narrow; the other consists of only one subduction zone. Thus the first model at the surface follows the present situation with the three tectonic units Wilson Terrane, Bowers Terrane, and Robertson Bay Terrane, whereas the second model implies that remains of two distinct subduction zones can not be resolved from the gravity data as the distance between the two subducted slabs is too small.

The anomalies resulting from those models are shown in Fig. 4.8. Both models produce a strong negative anomaly along the subduction zones. The anomaly field differs in the width and amplitude of this anomaly; due to the small distance between the two

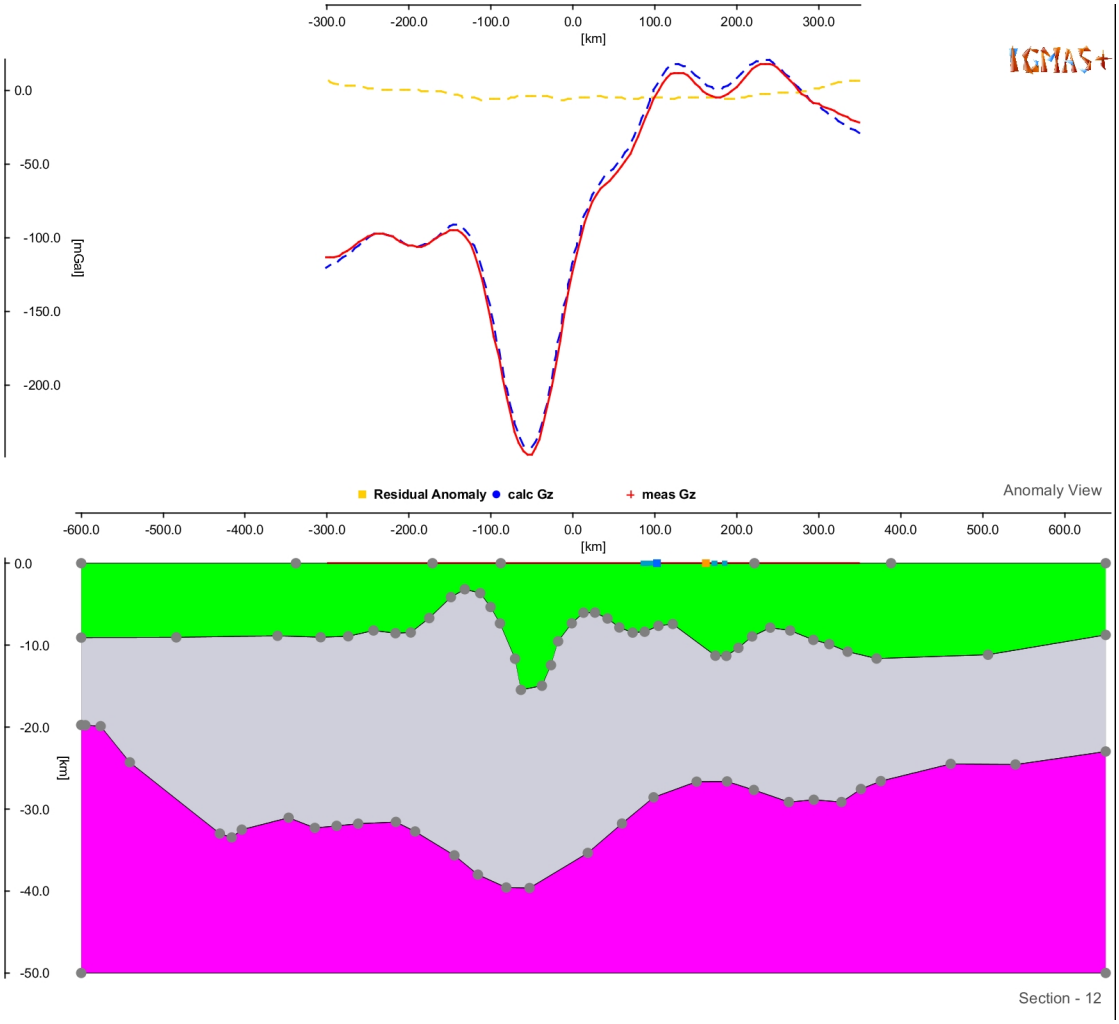

Figure 4.4: Section 12 of the *IGMAS+* gravity model (comp. Fig. 4.2 for exact location of the sections). It shows the lithospheric mantle (magenta) which is separated from the lower crust (grey) by the Moho. The upper crust is shown in green. The upper part of the figure shows the measured anomaly as solid red line, the anomaly calculated from the model as dashed blue line, and the residual anomaly as dashed yellow line. The subsurface is vertically exaggerated by a factor of 10.

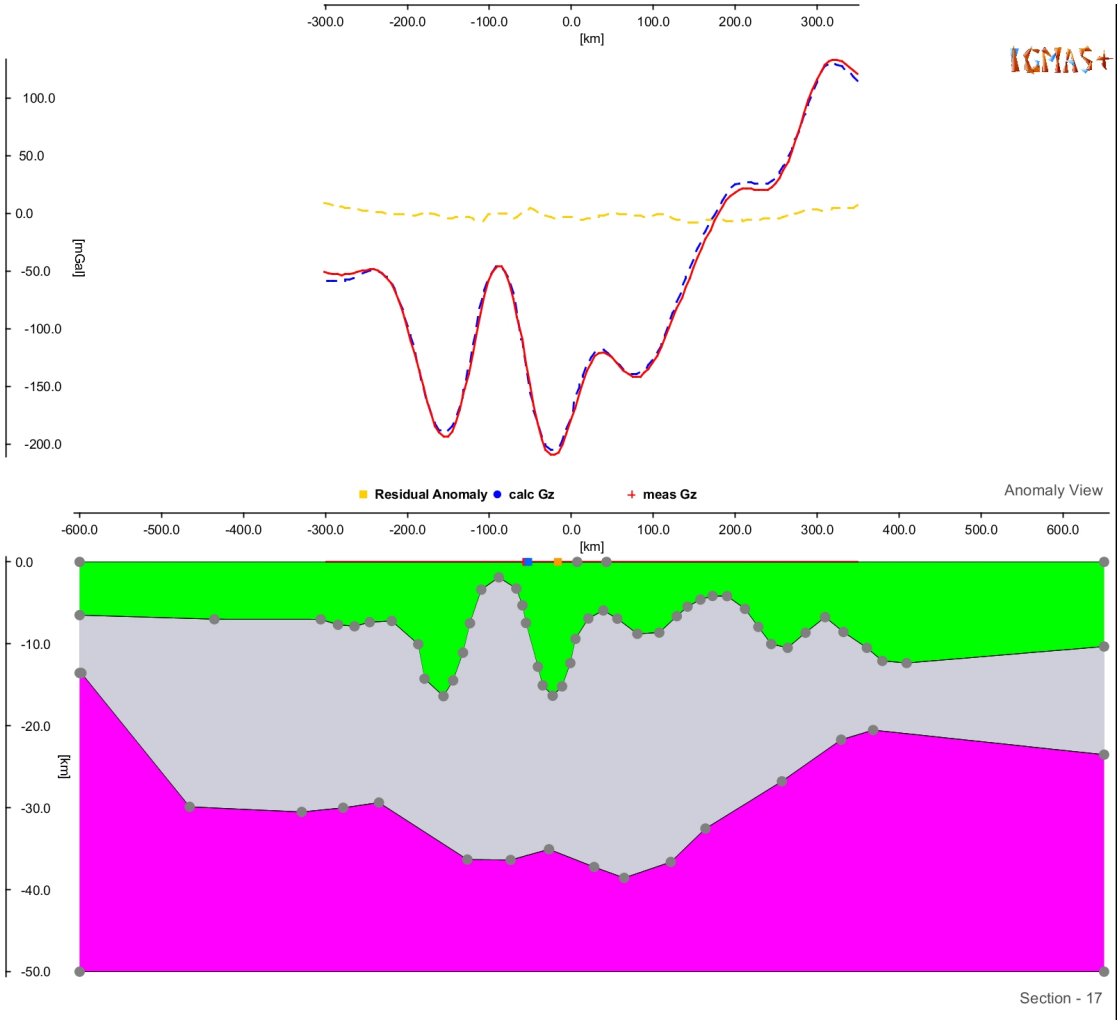

Figure 4.5: Section 17 of the *IGMAS+* gravity model (comp. Fig. 4.2 for exact location of the sections). It shows the lithospheric mantle (magenta) which is separated from the lower crust (grey) by the Moho. The upper crust is shown in green. The upper part of the figure shows the measured anomaly as solid red line, the anomaly calculated from the model as dashed blue line, and the residual anomaly as dashed yellow line. The subsurface is vertically exaggerated by a factor of 10.

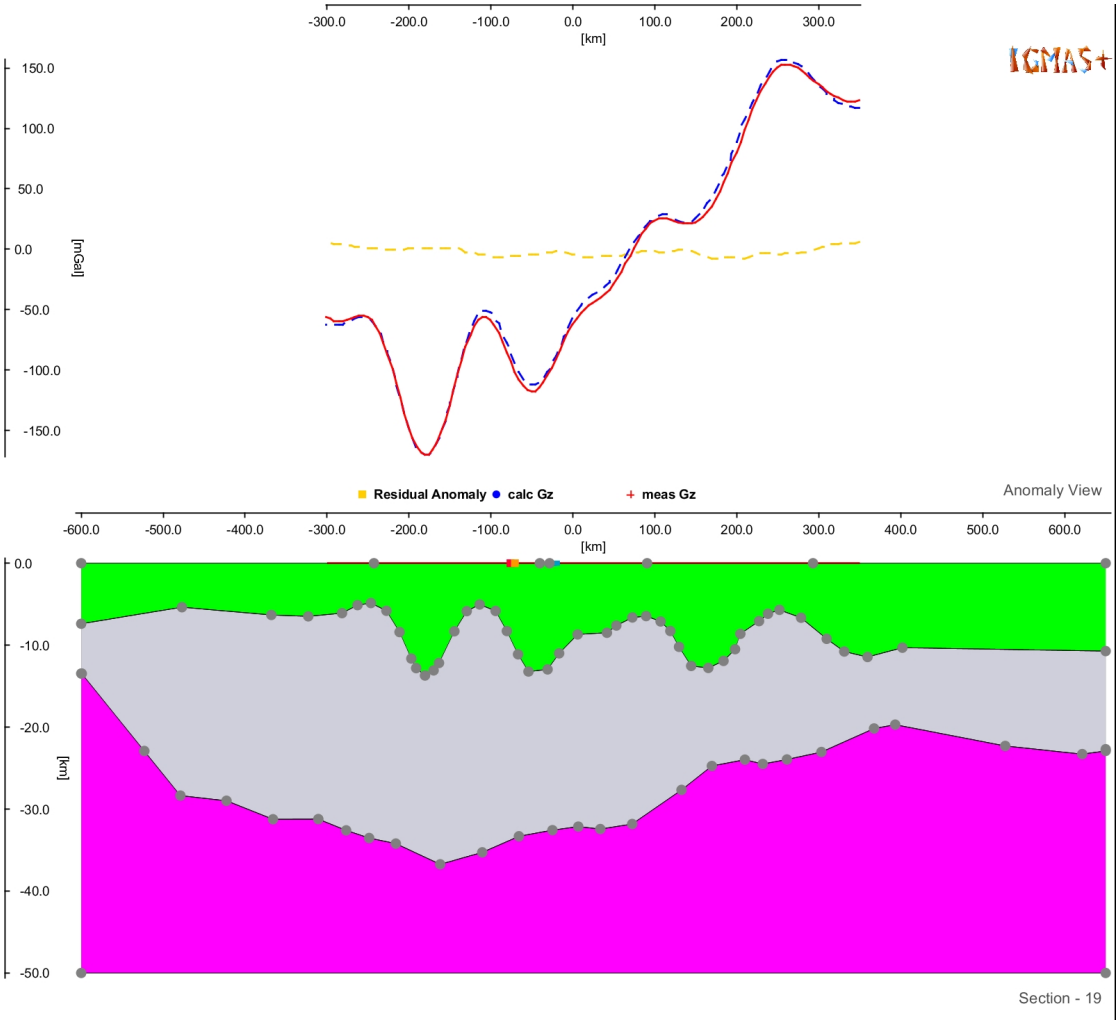

Figure 4.6: Section 19 of the *IGMAS+* gravity model (comp. Fig. 4.2 for exact location of the sections). It shows the lithospheric mantle (magenta) which is separated from the lower crust (grey) by the Moho. The upper crust is shown in green. The upper part of the figure shows the measured anomaly as solid red line, the anomaly calculated from the model as dashed blue line, and the residual anomaly as dashed yellow line. The subsurface is vertically exaggerated by a factor of 10.

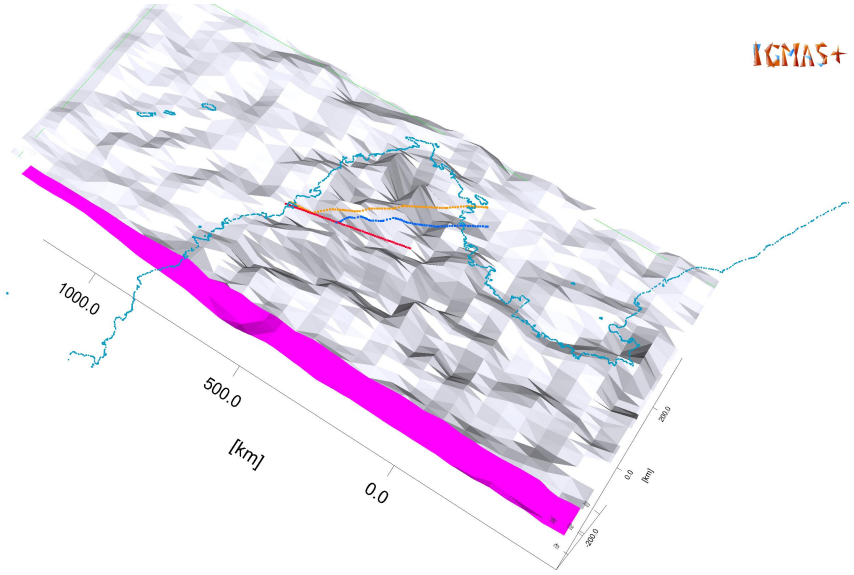

Figure 4.7: 3 D view of the gravimetric band-pass model. The grey boundary divides the crust into an upper and a lower part, the magenta boundary is the Moho. The coastline is given in light blue, three major fault zones are shown as red, blue, and yellow lines. North is to the upper left.

subduction zones in the first model the two negative anomalies can not be separated. Instead they combine to build a bigger anomaly with strong horizontal gradients compared with the anomaly of the single subduction zone model.

4.2.3 Summary of gravimetric modelling

In general, the investigation of crustal features with gravimetric modelling is possible for remote areas like Antarctica as well. As, due to the remote and glaciated nature of Antarctica, the data basis made up from terrestrial gravity measurements is very much non-uniform, it is a good alternative to use data generated from a global gravity model like EIGEN-6C3stat (Förste et al., 2013). As those models incorporate data from different kind and origin, deviations of gravity field data derived from those models from the true gravity field may be, in general, too large to be neglected. However, the available topography and ice thickness data also have strong standard deviations. Therefore, the gravity models can show only medium to long wavelength features; interpretation of gravity data, whether reduced for topographic effects or not, for near-surface structures or small features can not be made with confidence, as the anomalies generated by such structures or features are in the same order as the presumed standard deviations of the gravity data used.

Since the NVL region has probably evolved from subduction processes (Kleinschmidt & Tessensohn, 1987), two simple subduction models have been tested. Both show similar anomalies, as one model contains only one subduction zone whereas the other consists

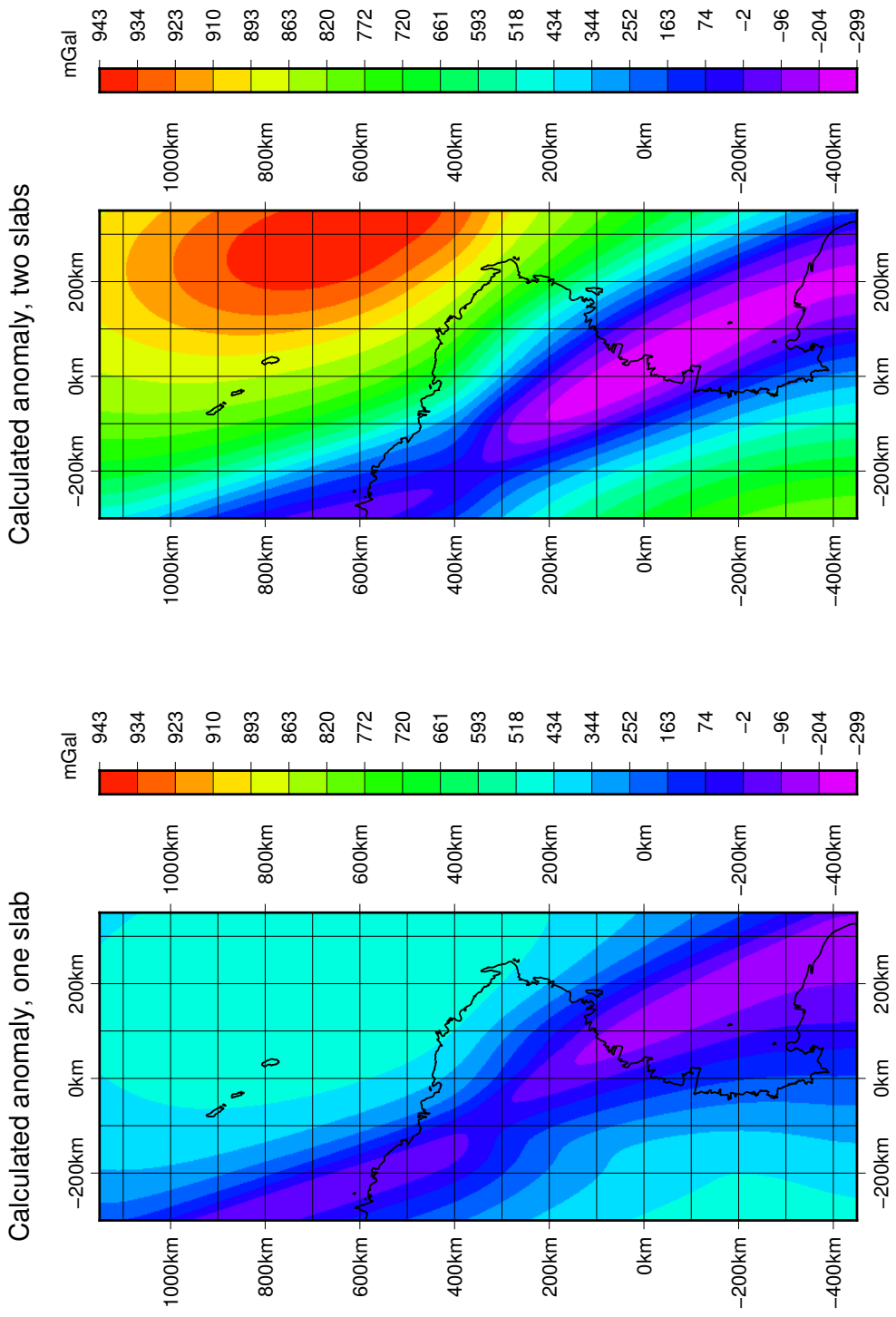

Figure 4.8: Gravity anomalies calculated from two simple subduction models: Model with two subducted slabs (top), model with one single slab (bottom). For better comparison, the colour scale is the same for both figures.

of two subduction zones separated by a small distance. In both cases the anomalies calculated from those models do not fit the gravity anomalies derived from the EIGEN-6C3stat gravity model.

After filtering of the EIGEN-6C3stat anomaly data, two new models were generated. One model explains the low-frequency part of the anomaly field with variations in Moho depth; the result (Fig. 4.3) shows especially that the TAM have a distinct mountain root. The second model, which is based on the Moho model, divides the crust into an upper and a lower part. The mean-frequency part of the anomaly field can be explained by this interface with good results, too; the dip angles of the interface reach 34°. As no good boundary conditions exist, also other models can explain the data, e.g. using more geologic units; large-scale seismic measurements could possibly help to prove the model developed here true or wrong.

4.3 Magnetic modelling

4.3.1 Overview

Magnetic modelling was limited to a region along the northern coast of NVL, where the assumed ocean-continent transition of the faults and fault systems may be found. This area is covered by a large amount of magnetic measurements but the doubtful parts of the final magnetic anomaly map are mostly located outside; only a small part of the **maganter** survey is included in the SE (Fig. 4.9).

As the magnetic field decreases faster with distance from source than gravity, the model has to be developed with higher resolution, i.e. the section distance has to be reduced. For the model of northern Victoria Land coast a section distance of 10 km has been chosen. The edges of the model are extended by 100 km to the West and East, whereas the southernmost and northernmost sections are mirrored away from the centre by the same amount. In total, the model covers an area from −300 km to 400 km Easting and 200 km to 650 km Northing. The depth was limited to 20 km; with a geothermal gradient of 25 °C km^{-1} a temperature of 500 °C can be assumed for that depth. However, the Curie temperature of many minerals is below this value; the Curie temperature of Magnetite as the most important magnetization-bearing mineral is 578 °C (Merrill et al., 1996) for pure Magnetite, but decreases fast with increasing impurity. Therefore the space below the chosen depth can be assumed to be almost free of sources of magnetic anomalies.

The magnetic field model relies on the physical parameter of susceptibility; this parameter is dimensionless. In the past, the cgs system of physical units was used; today the SI units are common standard. Regarding electromagnetic units, the two systems differ by a factor of 4π; this factor has also to be applied to susceptibilities. Susceptibilities in the cgs system have to be multiplied by that factor to retrieve susceptibilities in the SI system. It is, therefore, necessary to name the system the susceptibilities are

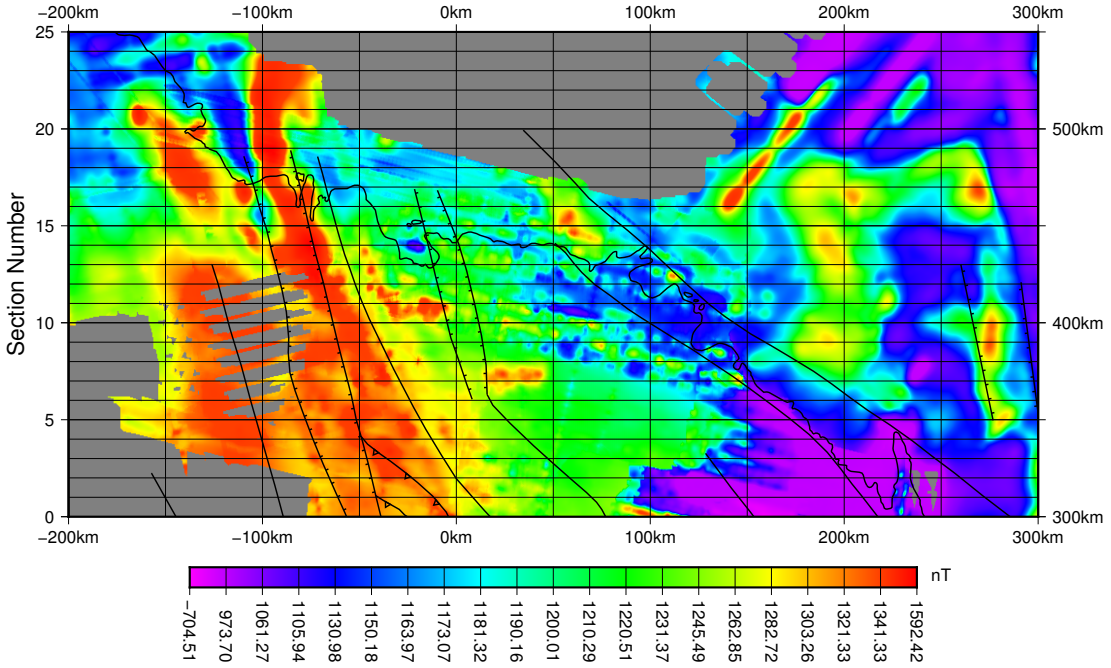

Figure 4.9: Magnetic anomaly map of the model area at the northern coast of NVL. The left axis gives the section number in the model, the right axis gives the northing coordinate. The coastline is shown in black for orientation. Anomalies are given at 2.700 m altitude level at epoch 1980.00. Faults after Läufer et al. (2011).

given in.

As for gravity, *IGMAS+* needs also for magnetic field modelling a reference value for the respective physical parameter. Most rock types can have a susceptibility of 0.01 (SI). In case of sedimentary rocks this value is relatively high, but for magmatic and metamorphic rocks this value is common for a large number of rock types (Militzer & Weber, 1984). Therefore this value has been chosen as reference value.

No correction regarding the topography and bathymetry has been applied to the data; thus, the model has to include these features. With the chosen section spacing, this can naturally only be an approximation to reality. The modelled land surface and seafloor follow the ETOPO1 data, which have been re-sampled to a lower resolution to better fit the resolution of the model. As water is diamagnetic with a suszeptibility value of $-9.03 \cdot 10^{-6}$ (SI) (Kuchling, 2004), which is more than three orders of magnitude below the reference value, it can be assumed to have no magnetic effect at all; this is also true for the glaciers on land. Thus, the ocean and glaciers are ignored and not introduced as bodies into the model.

Furthermore, as no boundary conditions exist (e.g., seismic profiles), the subsurface structures are not to be modelled too detailed. Instead, the model has to remain as simple as possible. Therefore a model has been developed, which consists of only two bodies. As before in case of gravity, the crust is divided into an upper and a lower part.

The upper part has a susceptibility of 0.02 (SI) and represents mainly the younger parts of the crust like sedimentary rocks as well as volcanics. The lower body with a very high susceptibility of 0.14 (SI) comprises the magnetic basement, consisting of mainly basic intrusive rocks (e.g. Militzer & Weber, 1984).

4.3.2 Structure of the magnetic basement

The magnetic basement shows some interesting features. In some parts basement highs can be seen, in one place along the Rennick glacier reaching the surface, whereas other regions are characterized by strong basement lows. Comparison with the known fault zones shows anti-correlation with the Rennick graben where the most prominent basement highs can be found. On the other hand, especially in the eastern part basement lows dominate, mostly with very steep slopes. Three sections of the model are shown exemplarily in Fig. 4.10, Fig. 4.11, and Fig. 4.12.

Section 19 (Fig. 4.10) runs about 15 km north of the Rennick glacier tongue. In prolongation of the Rennick graben (about −100 km easting) the magnetic basement is very shallow. 60 km to the South, at section 13 (Fig. 4.11), an even more prominent basement high can be seen. This basement high can be followed through the whole Rennick graben area. In the south it has a broad shape and is deeper than in the central and northern part of the model area. In the central part and further to the north, and restricted to the Rennick graben, the basement high nearly reaches the surface (i.e. the rock surface, which may be covered by ice); in the central area the basement is exposed below the Rennick glacier as well as along its eastern flank.

The Lillie graben, which is located about 80 km east of the Rennick graben, is not visible either as basement low or basement high in the model. In this part of the model, the basement is characterized mainly by a soft dipping from West to East. The Cape Adare Fault and the Missen Ridge Fault Zone, two right-lateral strike-slip fault zones along the coast between 50 km to 300 km easting, also do not show up in the crustal structure as modelled here. In case of the Cape Adare Fault, this fits with the results of Läufer et al. (2011).

In section 19, east of 250 km easting, a feature is visible, which can possibly be interpreted as northern prolongation of the Adare Trough. The basement shows a local deep with steep slopes and a central high. As the data set used for modelling is limited to 300 km easting, misinterpretation is possible, though. In section 13, only a small local high can be found in the corresponding part of the model, whereas a graben-like structure is not obvious. In section 8 (Fig. 4.12) two small basement highs can be seen corresponding to the proposed boundaries of the trough. It is therefore not possible to proof the extent of the Adare Trough by this model.

A 3 D view of the top of the magnetic basement is presented in Fig. 4.13. This view shows, especially in the eastern part, a very rough topography with strong gradients. The western part is much smoother.

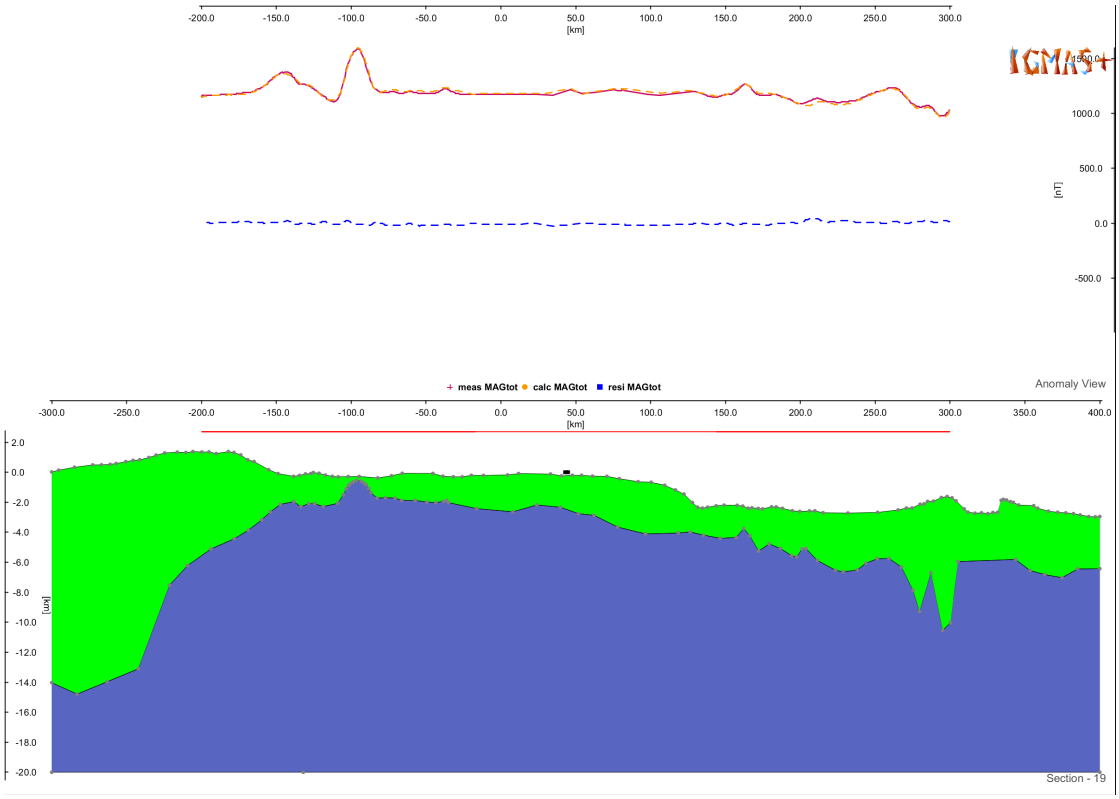

Figure 4.10: Section 19 of the *IGMAS+* magnetic field model (comp. Fig. 4.9 for exact location of the sections). It shows the magnetic basement (blue) and the upper crust (green). Black dots mark the approximate intersection with a strike-slip fault after Läufer et al. (2011). The upper part of the figure shows the measured anomaly as solid red line, the anomaly calculated from the model as dashed blue line, and the residual anomaly as dashed yellow line. The subsurface is vertically exaggerated by a factor of 10.

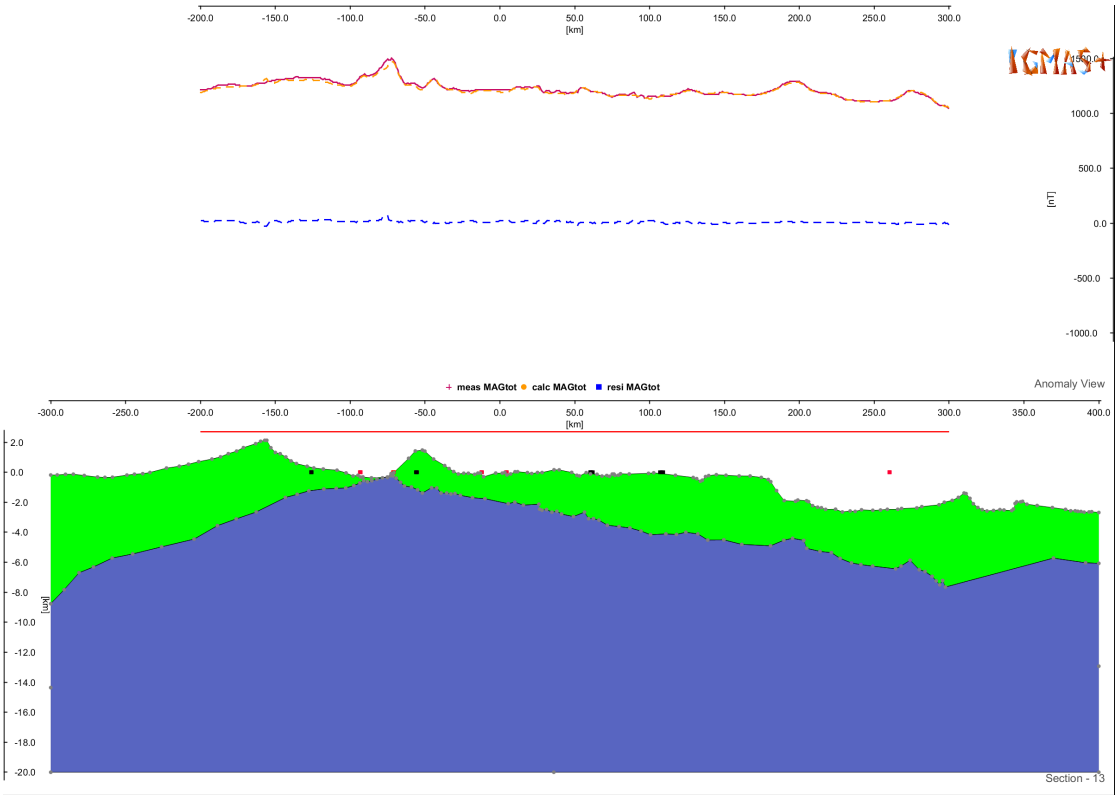

Figure 4.11: Section 13 of the *IGMAS+* magnetic field model (comp. Fig. 4.9 for exact location of the sections). It shows the magnetic basement (blue) and the upper crust (green). Black and red dots mark the approximate intersection with a strike-slip fault and a normal fault, respectively; fault locations after Läufer et al. (2011). The upper part of the figure shows the measured anomaly as solid red line, the anomaly calculated from the model as dashed blue line, and the residual anomaly as dashed yellow line. The subsurface is vertically exaggerated by a factor of 10.

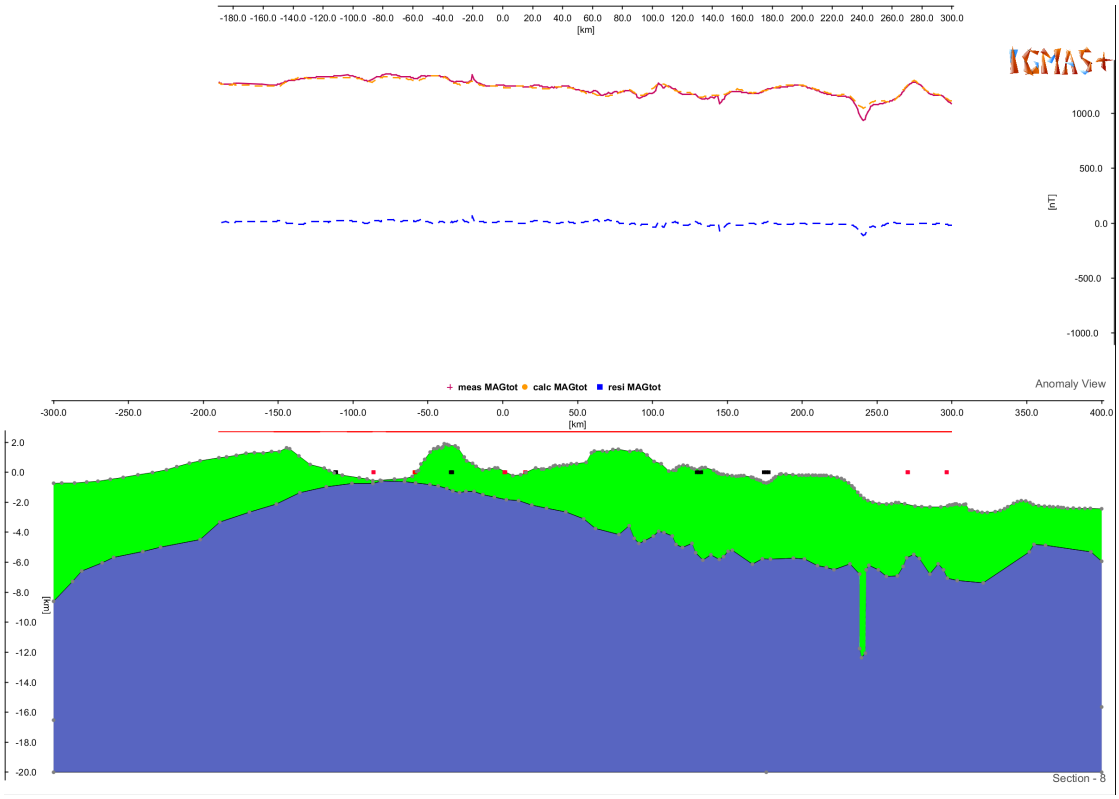

Figure 4.12: Section 8 of the *IGMAS+* magnetic field model (comp. Fig. 4.9 for exact location of the sections). It shows the magnetic basement (blue) and the upper crust (green). Black and red dots mark the approximate intersection with a strike-slip fault and a normal fault, respectively; fault locations after Läufer et al. (2011). The upper part of the figure shows the measured anomaly as solid red line, the anomaly calculated from the model as dashed blue line, and the residual anomaly as dashed yellow line. The subsurface is vertically exaggerated by a factor of 10.

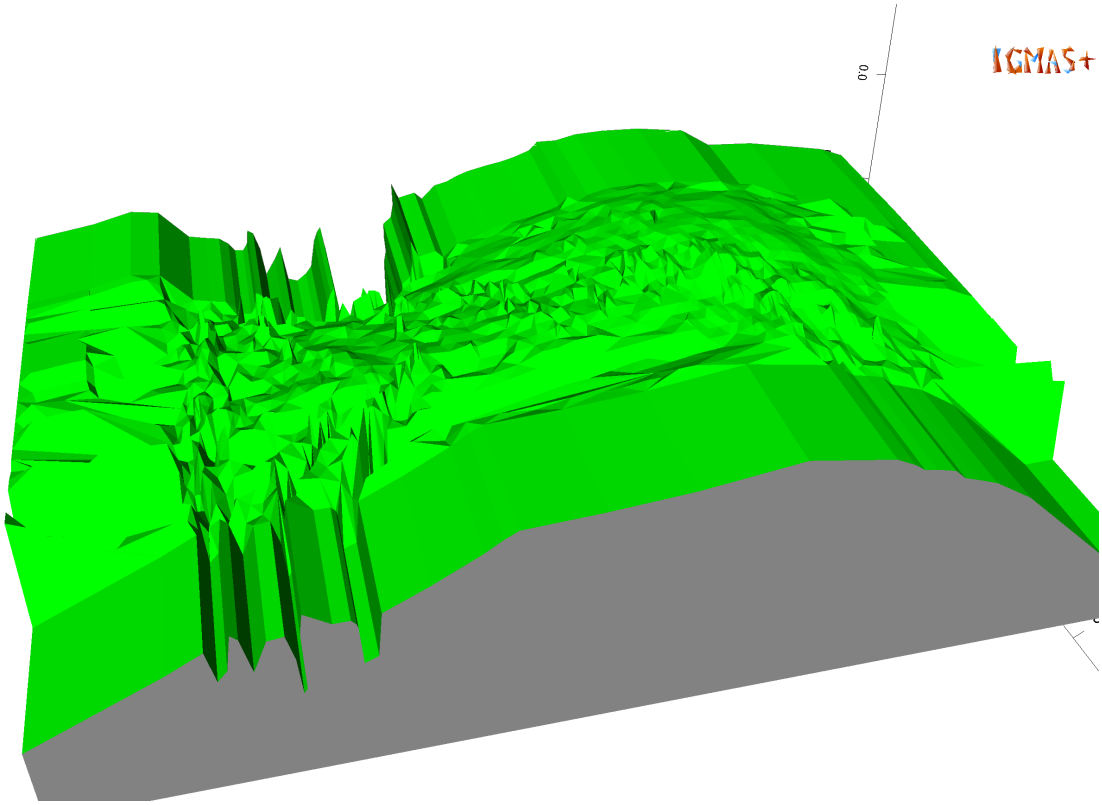

Figure 4.13: 3 D view of the magnetic field model. The view from NNE shows the interface between magnetic basement and upper crust. The model is vertically exaggerated by a factor of 10.

4.3.3 Uncertainties

As stated before, due to doubtful data the modelling result must not be interpreted too detailed. In general, the residual magnetic anomaly varies between −50 nT to 50 nT, but at some places values of −1.200 nT or 300 nT can be observed. Such extreme values occur mostly between the model sections and can hardly be avoided. In the south-eastern part of the model area, where the **maganter** survey was carried out, the strongest residuals can be found; the errors introduced by data from that survey have been discussed earlier.

The overall correlation between measured and modelled anomaly field is 0.96, and the standard deviation of the residual anomaly is 37.21 nT. If the highest and lowest two percent of the residual data are ignored, i.e. the anomalies located between the sections or resulting from erroneous data, the standard deviation is reduced to 17.1 nT. Taking into account the occasionally large errors of the measured data or the processing steps, which are described in this study, this value is very good and shows, that a trustful model could be developed.

Chapter 5

Interpretation regarding the geotectonic and geodynamic evolution of northern Victoria Land

5.1 The terrane model

As introduced by Weaver et al. (1984) and Bradshaw et al. (1985), NVL can be structurally divided into three main units; these are often called terranes, but there exists other nomenclature as well (Roland et al., 2004; Federico et al., 2009). Based on Schmidt & Rowley (1986), lateral movement during Mesozoic may have caused the juxtaposition of the three units. On the other hand, Kleinschmidt & Tessensohn (1987) have developed the idea of successive subduction during the Paleozoic. As subduction is connected to magmatic processes, the presence of intrusive bodies as well as some effusive rocks can be explained by the subduction approach.

The subduction processes involved in the Ross orogeny are not yet fully known regarding the direction of subduction and the number of subduction zones. To clarify this tests have been carreid out with two simple models. One model consists of only one subduction zone whereas the other model is characterized by two subduction zones with only small distance, thus representing the recent situation with large outer geologic units and a small geologic unit in between. The anomalies calculated from both models differ only in the width and amplitude of the negative gravity anomaly, but have, in general, the same shape. Such shape can not be found in the measured gravity data. This fact does not support any possible subduction process, but can neither prove it wrong, as due to the supposed age of subduction no distinct remnants of the subducted crustal slabs may have outlasted to present time.

5.2 The Transantarctic Mountains

The TAM have evolved due to rifting between West and East Antarctica and represent the East Antarctica rift shoulder of the WARS. The rifting is still active, as the TAM are uplifted in NVL by several $\mathrm{mm\,yr^{-1}}$ (Capra et al., 2007); also, volcanic and seismic activity can be observed. The uplift may also originate in isostatic compensation processes due to changes in ice mass onshore, or be caused by a combination of different sources. This question has recently been investigated by means of micro-gravimetric measurements (Jentzsch et al., 2014; Jentzsch, 2014), but results can at the earliest be expected after at least a second campaign.

The modelled Moho depth (Fig. 4.3) shows a distinct mountain root under the TAM. As NVL was strongly influenced by the Ross orogeny about 500 Myr ago, it is possible that the observed mountain root represents the root of the Ross orogen. On the other hand, the uplift of the TAM due to rifting should also have uplifted the ancient mountain root. A comparison with the Cenozoic rift along the Upper Rhine Graben in central Europe shows that the rift shoulders (Black Forest and Vosges mountains) there have no mountain root. Instead, the Moho depth is very uniform over the whole area affected by the rifting process (e.g. Zeis et al., 1990). It is therefore imaginable that along the TAM the rifting-driven uplift has ceased in the past and gravitational sinking prevailed over the uplift. When the force driving uplift ceased, isostatic adjustment would have led to the formation of a new mountain root adapted to the shape and extent of the rift shoulder (or, precisely, the still elevated part of the rift shoulder). As a consequence, recent uplift as observed by GPS measurements would have to result from either a new tectonic process or the isostatic adjustment due to loss of onshore ice masses. However, seismic and volcanic activity shows that rifting is still in progress alog the WARS

Especially along the TAM, the Moho depth shows slight variations. These variations should not be interpreted considering the uncertainties of the underlying gravity anomaly data. The uncertainties of the original EIGEN-6C3stat data are unknown; however, the Bouguer slab reduction is corrupted by the large uncertainties of the ETOPO topography data, which lead to uncertainties in the order of at least 3.65 mGal in the Bouguer anomaly.

5.3 The interior structure of the crust

The mean-wavelength gravimetric anomaly led to a model of the interior structure of the crust in Victoria Land. As no additional boundary conditions like seismic data were available, it is reasonable not to over-interpret the gravity data. Thus, the modelled structure with upper and lower crust may be interpreted as basement rocks overlain by younger sedimentary as well as magmatic rocks, which may also be overprinted by metamorphic processes.

A comparison with known fault structures at the surface shows the possibility of

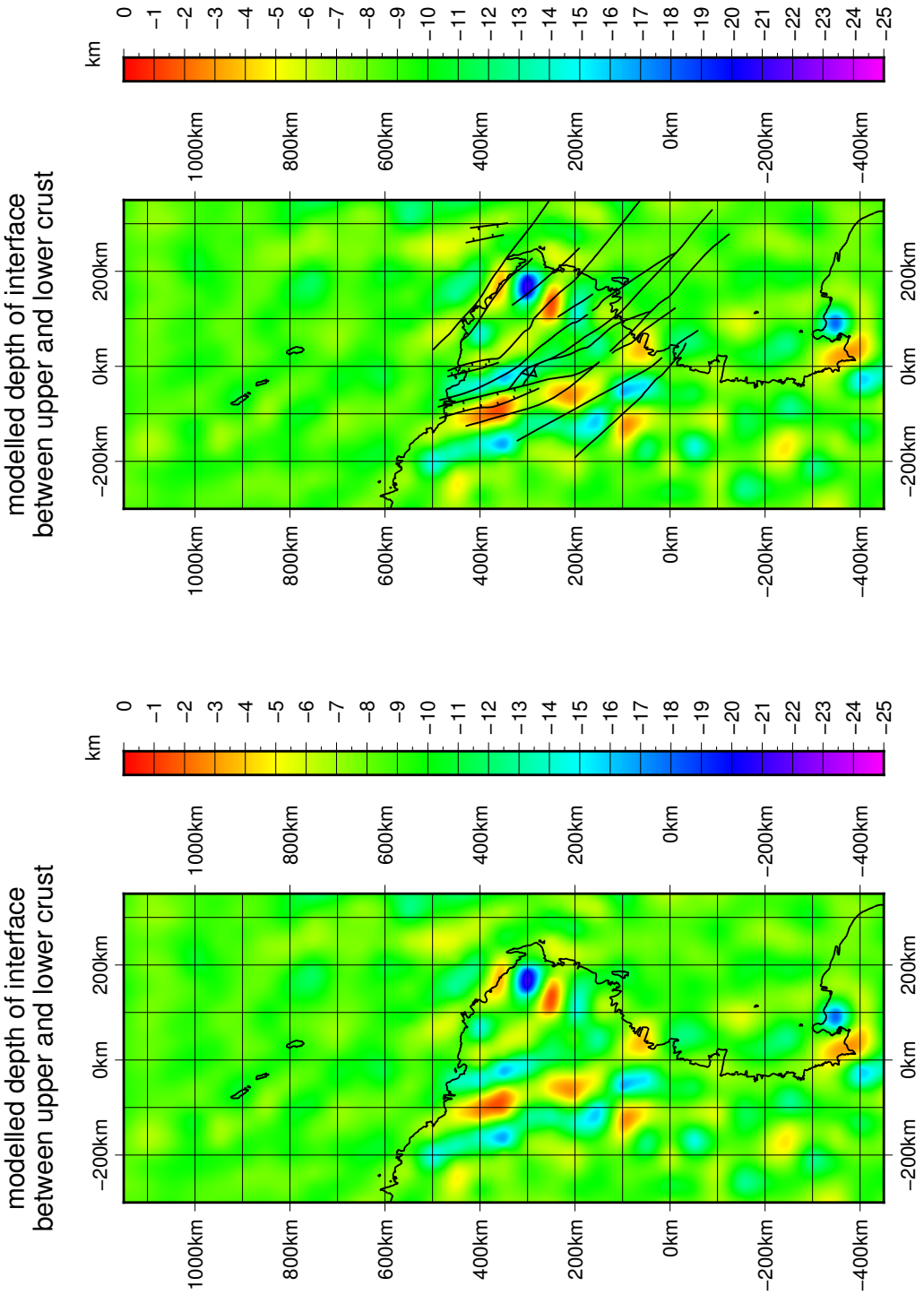

Figure 5.1: Map showing the depth of the boundary between upper and lower crust (bottom) as inferred from gravity modelling. The top figure shows the same map, overlain with the Cenozoic faults after Läufer et al. (2011). The coastline is given in black for orientation.

inverted graben structures, e.g. in the Rennick Glacier area (Fig. 5.1) where inversion has been observed, amongst others, by Rossetti et al. (2003a,b) . In general, the comparison shows linear features oriented North-South to Northwest-Southeast. This directional trend coincides with the Cenozoic fault pattern mapped by Läufer et al. (2011). However, those features seem to be limited to the on-shore area; off-shore only slight changes in the depth of the interface between upper and lower crust are visible. Thus, a connection between on-shore faults and the large transform faults of the Indian-Antarctic ridge, like the BFZ or the TFZ, is not traceable.

The northern coastal area has been modelled also with respect to the magnetic total field anomaly. This model also shows a two-part crustal structure: a basement, mainly composed of basic intrusives and metamorphic rocks, and a cover of sedimentary and volcanic rocks. Along the Rennick graben, the basement is very shallow; in the central part of the model it is exposed at the surface. This is consistent with the gravity model and supports the idea of an inverted graben. It is possible to follow the Rennick graben to the north about 50 km off-shore; further prolongation is not possible as the data coverage is limited to the coastal area. On the other hand, the Lillie graben, which can be seen in the gravity model as similar structure like the Rennick graben, is not visible in the magnetic field model. This can be explained by smaller differences between the magnetic properties of the rocks inside and outside the Lillie graben, compared to the Rennick graben.

A comparison between the basement depths from gravity and magnetic field models shows the consistency in the western part of the magnetic field model area, whereas in the eastern part the two models show completely different behaviour (Fig. 5.2). The magnetic basement is characterized by a very long wavelength, and shows several very local extrema, which mainly result from bad data coverage. In contrast, the gravimetric basement shows a sequence of elongated highs and lows, which are all oriented in similar direction.

Both models show the deepest basement at the southern boundary, between 100 km to 200 km easting. This should, however, not be interpreted as consistent results of both models, as the magnetic anomaly in this part is heavily disturbed by doubtful data.

Reitmayr et al. (2003) have done a joint model of gravity and magnetic field data along a single profile crossing Matusevich glacier. This approach of joint modelling has not been chosen for this study due to several reasons. The model of Reitmayr et al. (2003) is a 2 D model over a single profile of about 100 km length, where both gravity and magnetic field data have been measured during one campaign, sharing the same measurement points. The models developed in this study are both much larger as they are true 3 D models, and, more important, the data have very diverse origin. This includes not only differences in lateral positions and spacing, but also the altitude at which the measurements have been taken, and therefore the distance from source.

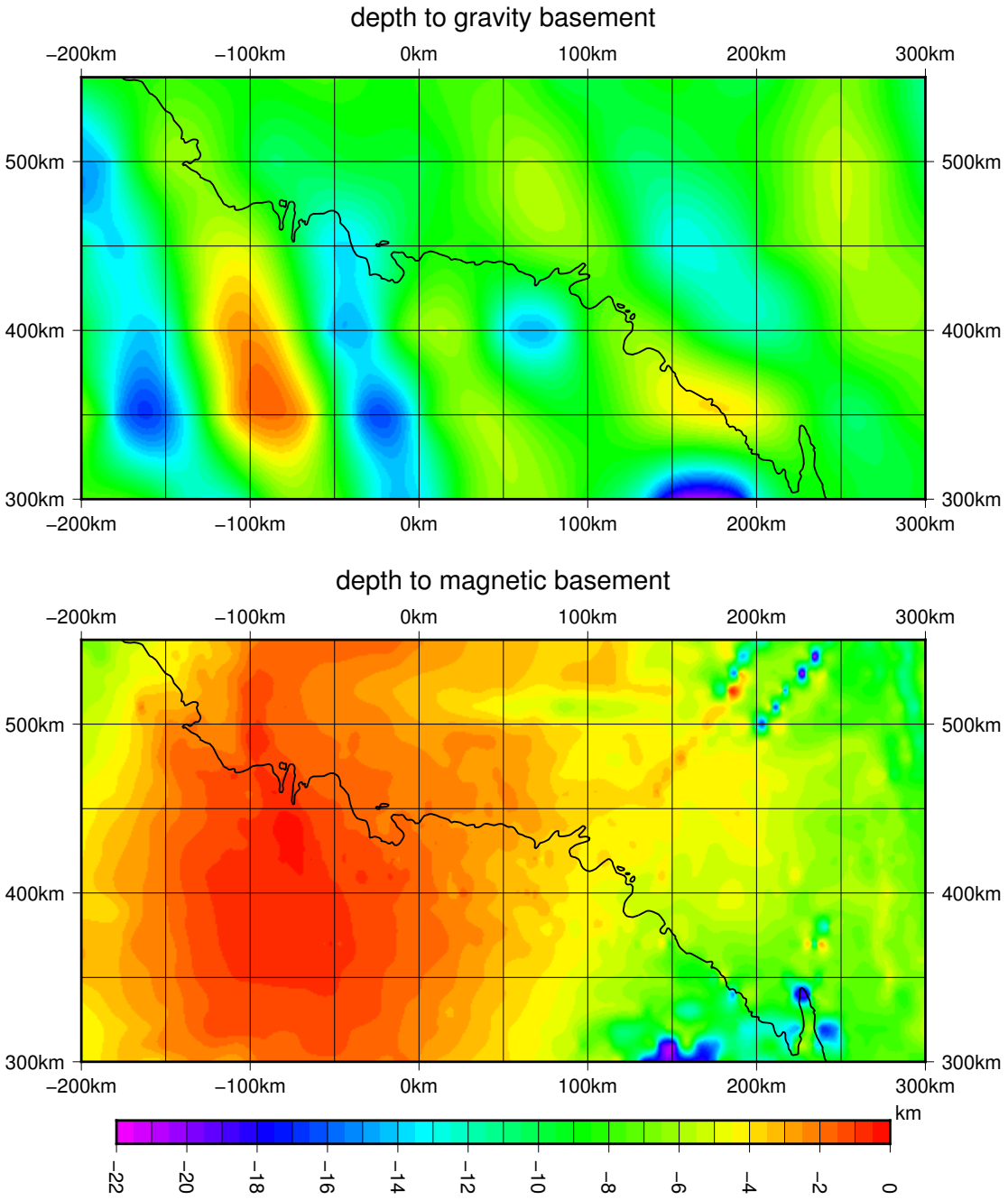

Figure 5.2: Basement depth maps from gravity (top) and magnetic field modelling (bottom).

5.4 Final Remarks

The models, which were created on basis of the available data, have of course to be taken as preliminary, as the data themselves and the data treatment are afflicted with problems and error sources, as stated before. With additional data, obtained from other measurement methods like seismic campaigns, it is possible to refine these models in detail in the context of actual geologic and geophysical research. Thus, for example the open questions regarding the Rennick graben could be further investigated. With the available data and the models based thereon it is not possible to answer the question, whether the transform faults of the Indian-Antarctic Ridge are connected to the on-shore fault system in NVL as discussed by Salvini et al. (1997) or Läufer & Rossetti (2001). The models show that a prolongation of on-shore faults into the shelf area is possible, but they cannot finally proof such a connection to off-shore faults.

Acknowledgements

My first thanks go to Prof. i.R. Dr. Gerhard Jentzsch, who gave me the opportunity for this study. He developed the idea for this study together with Dr. Detlef Damaske from the Federal Institute for Geosciences and Natural Resources (BGR) in Hanover. I thank Dr. Damaske and his colleague Dr. Andreas Läufer, also from the Federal Institute for Geosciences and Natural Resources (BGR), for co-supervising my research. Detlef Damaske also provided me with the aeromagnetic data as well as local gravity data. I also have to thank PD Dr. Thomas Jahr and Dr. Adelheid Weise for their support. I am indebted to Dr. Anne Hegewald, who introduced me to the Generic Mapping Tools software package.

Of course all members of the geophysics group at the Institute of Geosciences of the Friedrich Schiller University Jena as well as all colleagues who attended my presentations at conferences helped me by discussing my results and problems and giving me valuable hints on datasets to be used or publications related to the subject of my work.

This project was partially funded by the Deutsche Forschungsgemeinschaft (German National Science Foundation) in the frame of Priority Programme 1158 'Antarctic research with comparative investigations in Arctic ice areas'.

I also wish to thank Sarah Böhlau for proofreading the manuscript.

Finally, I want to thank my parents as well as my sisters, who encouraged me over the last years to keep things going.

Bibliography

Amante, C. & B. W. Eakins (2009). ETOPO 1 Arc-Minute Global Relief Model: Procedures, Data Sources and Analysis. Tech. Rep. NESDID NGDC-24, National Geophysical Data Center, National Oceanic and Atmospheric Administration. doi: 10.7289/V5C8276M. Data download: March 22, 2012.
`www.ngdc.noaa.gov/mgg/global/global.html`

Andersen, O. B. (2010). The DTU10 Gravity field and Mean sea surface. 2nd International Symposium of the Gravity Field of the Earth (IGFS2), Fairbanks, Alaska, September 20-22, 2010.

Andersen, O. B., P. Knudsen & P. A. M. Berry (2010). The DNSC08GRA global marine gravity field from double retracked satellite altimetry. *J. Geodes.* 84(3), 191–199. doi:10.1007/s00190-009-0355-9.

Armadillo, E., E. Bozzo, G. Caneva, F. Ferraccioli & G. Tabellario (2006). Recent Aeromagnetic and Deep Electromagnetic Exploration Projects in East Antarctica. *Terra Antartica Rep.* 12, 167–176.

Armadillo, E., F. Ferraccioli, A. Zunino, E. Bozzo, S. Rocchi & P. Armienti (2007). Aeromagnetic Search for Cenozoic Magmatism over the Admiralty Mountains Block (East Antarctica). *USGS Open-File Rep.* 2007-1047 Short Research Paper 075. doi: 10.3133/of2007-1047.srp075.

Bachem, H.-C., D. C. Boie & D. Damaske (1989). Data Processing and Production of the Anomaly Maps of the Total Magnetic Field in the North Victoria Land/Ross Sea Area of the Antarctic. *Geol. Jb.* E38, 81–89.

Barton, C. E. (1997). International geomagnetic reference field: The seventh generation. *J. Geomagn. Geoelectr.* 49(2-3), 123–148.

Behrendt, J. C. (1999). Crustal and lithospheric structure of the West Antarctic Rift System from geophysical investigations – a review. *Global Planet. Change* 23(1), 25 – 44. doi:10.1016/S0921-8181(99)00049-1.

Behrendt, J. C. & A. Cooper (1991). Evidence of rapid Cenozoic uplift of the shoulder escarpment of the Cenozoic West Antarctic rift system and a speculation on possible climate forcing. *Geology* 19(4), 315–319. doi:10.1130/0091-7613(1991)019<0315:EORCUO>2.3.CO;2.

Behrendt, J. C., W. E. LeMasurier, A. K. Cooper, F. Tessensohn, A. Trehu & D. Damaske (1991a). Geophysical Studies of the West Antarctic Rift System. *Tectonics* 10(6), 1257–1273. doi:10.1029/91TC00868.

Behrendt, J. C., W. E. LeMasurier, A. K. Cooper, F. Tessensohn, A. Trehu & D. Damaske (1991b). The West Antarctic Rift System: A Review of Geophysical Investigations. In: Elliot, D. H. (ed.), *Contributions to Antarctic Research II*, *Antarctic Research Series*, 53. Am. Geophys. Union, 67–112. doi:10.1029/AR053p0067.

Bennett, D. J. & B. A. Sissons (1984). Gravity models across the Transantarctic Mountain Front near New Harbour, McMurdo Sound, Antarctica. *New Zealand J. Geol. Geophys.* 27(4), 413–424. doi:10.1080/00288306.1984.10422263.

BGR (ed.) (1981). *GANOVEX – German Antarctic North Victoria Land Expedition 1979/80. Geol. Jb.*, B41.

Block, A. E., R. E. Bell & M. Studinger (2009). Antarctic crustal Thickness from satellite gravity: Implications for the Transantarctic and Gamburtsev Subglacial Mountains. *Earth Planet. Science Lett.* 288(1-2), 194–203. doi:10.1016/j.epsl.2009.09.022.

Bozzo, E. & D. Damaske (eds.) (2001). *GANOVEX VIII – ItaliAntartide XV Antarctic Expedition 1999-2000. Terra Antartica Rep.*, 5.

Bozzo, E., A. Colla, G. Caneva, A. Meloni, A. Caramelli, G. Romeo, D. Damaske & D. Moeller (1994a). Technical procedures for aeromagnetic surveys in Antarctica during the Italian expeditions (1988-1992). *Ann. Geofis.* 37(5 Suppl.), 1283–1294. doi:10.4401/ag-4173.

Bozzo, E., A. Colla, G. Caneva, A. Meloni, A. Caramelli, G. Romeo, D. Damaske & D. Moeller (1994b). Technical procedures for aeromagnetic surveys in Antarctica during the Italian expeditions (1988-1992). *Terra Antartica* 1(1), 178–180.

Bozzo, E., G. Caneva, M. Chiappini, A. Colla, D. Damaske, F. Ferraccioli, M. Gambetta, A. Meloni & H. D. Moeller (1996). Total Magnetic Anomaly Map of Victoria Land (Central – Southern Part), GITARA 1–3 1991–94, Sheets A–B. *Antarctic Geomagnetic 1:250 000 Map Series*, Bozzo, E. & D. Damaske (eds.). Ministero dell'Università e della Ricerca Scientifica e Tecnologica, Programma Nazionale delle Ricerche in Antartide, Museo Nazionale dell'Antartide, Sezione di Scienze della Terra, Siena.

Bozzo, E., F. Ferraccioli, M. Gambetta, G. Caneva, D. Damaske, M. Chiappini & A. Meloni (1997a). Aeromagnetic Regional Setting and Some Crustal Features of Central-Southern Victoria Land from the GITARA Surveys. In: Ricci, C. A. (ed.), *The Antarctic Region: Geological Evolution and Processes*. 7th International Symposium on Antarctic Earth Sciences, Siena, Terra Antartica Publication. ISBN 88-900221-0-8, 591–596.

Bozzo, E., D. Damaske, G. Caneva, M. Chiappini, F. Ferraccioli, M. Gambetta & A. Meloni (1997b). A High Resolution Aeromagnetic Survey over Proposed Drill Sites Off Shore of Cape Roberts in the southwestern Ross Sea (Antarctica). In: Ricci, C. A. (ed.), *The Antarctic Region: Geological Evolution and Processes*. 7th International Symposium on Antarctic Earth Sciences, Siena, Terra Antartica Publication. ISBN 88-900221-0-8, 1129–1133.

Bozzo, E., G. Caneva, M. Chiappini, A. Colla, D. Damaske, F. Ferraccioli, M. Gambetta, D. Moeller & A. Meloni (1997c). Total Magnetic Anomaly Map of Victoria Land (Central-Southern Part), Antarctica. In: Ricci, C. A. (ed.), *The Antarctic Region: Geological Evolution and Processes*. 7th International Symposium on Antarctic Earth Sciences, Siena, Terra Antartica Publication. ISBN 88-900221-0-8, 1165–1166.

Bozzo, E., F. Ferraccioli, M. Gambetta, G. Caneva, M. Spano, M. Chiappini & D. Damaske (1999). Recent progress in magnetic anomaly mapping over Victoria Land (Antarctica) and the GITARA 5 survey. *Antarct. Sci.* 11(2), 209–216. doi: 10.1017/S0954102099000279.

Bradshaw, J. D., S. D. Weaver & M. G. Laird (1985). Suspect Terranes and Cambrian Tectonics in Northern Victoria Land, Antarctica. In: Howell, D. G. (ed.), *Tectonostratigraphic Terranes of the Circum-Pacific Region*, *Earth Science series*, 1. Circum-Pacific Council for Energy and Mineral Resources, 467–479.

Brancolini, G., M. Busetti, A. Marchetti, L. De Santis, C. Zanolla, A. K. Cooper, G. R. Cochrane, I. Zayatz, V. Belyaev, M. Knyazev, O. Vinnikovskaya, F. J. Davey & K. Hinz (1995). Descriptive Text for the Seismic Stratigraphic Atlas of the Ross Sea, Antarctica. In: Cooper, A. K., P. F. Barker & G. Brancolini (eds.), *Geology and Seismic Stratigraphy of the Antarctic Margin*, *Antarctic Research Series*, 68. American Geophysical Union, A271–A286. doi:10.1002/9781118669013.app1.

Bullard, E. C. (1936). Gravity Measurements in East Africa. *Philos. Transact. R. Soc. London, Ser. A, Math. Phys. Sci.* 235(757), 445–531. doi:10.1098/rsta.1936.0008.

Bundesregierung (2011). Deutsches Engagement für den weißen Kontinent: Antarktisvertrag – 30 Jahre Konsultativstatus.

Cande, S. C., J. M. Stock, R. D. Müller & T. Ishihara (2000). Cenozoic motion between East and West Antarctica. *Nature* 404, 145–150. doi:10.1038/35004501.

Capra, A., F. Mancini & M. Negusini (2007). GPS as a geodetic tool for geodynamics in northern Victoria Land, Antarctica. *Antarct. Sci.* 19(1), 107–114. doi:10.1017/S0954102007000156.

Casazza, G., R. Cervellati & M. C. Ramorino (1990). Rapporto preliminare sulla Campagna Antartica 1989-90. Tech. rep., Programma Nazionale di Ricerche in Antartide. `www.pnra.it/biblioteca/docs/rapporti_campagna/CA89-90.pdf`

Cerutti, G., F. Alasia, A. Germak, E. Bozzo, G. Caneva, R. Lanza & I. Marson (1992). The Absolute Gravity Station and the Mt. Melbourne Gravity Network in Terra Nova Bay, North Victoria Land, East Antarctica. In: Yoshida, Y., M. Kaminuma & K. Shiraishi (eds.), *Recent Progress in Antarctic Earth Science*. 6th International Symposium on Antarctic Earth Sciences, Ranzan, Terra Scientific Publishing Company, Tokyo, 589–593.

Chiappini, M., F. Ferraccioli, E. Bozzo & D. Damaske (2002). Regional compilation and analysis of aeromagnetic anomalies for the Transantarctic Mountains –Ross Sea sector of the Antarctic. *Tectonophys.* 347(1-3), 121–137. doi:10.1016/S0040-1951(01)00241-4.

Crary, A. P. (1963). *Results of United States Traverses in East Antarctica, 1958-1961*, *IGY Glaciological Report*, 7. World Data Center A: Glaciology, American Geographical Society.

Damaske, D. (1988). *Aeromagnetic Survey During the Expedition GANOVEX IV 1984/85 – Victoria Land/Ross Sea, Antarctica.* Technical Descriptions of the 1:250 000 Maps of the Anomalies of the Total Magnetic Field, Bundesanstalt für Geowissenschaften und Rohstoffe.

Damaske, D. (1989). Spatial Resolution of the Aeromagnetic Flight Grid – North Victoria Land, Antarctica. *Geol. Jb.* E38, 91–110.

Damaske, D. (1990). *Aeromagnetic Survey During the Expedition GANOVEX V 1988/89 – Lower Rennick Glacier, North Victoria Land, Antarctica.* Technical Descriptions of the 1:250 000 Maps of the Anomalies of the Total Magnetic Field, Bundesanstalt für Geowissenschaften und Rohstoffe.

Damaske, D. (1993). Layout, Execution, and Data Processing of the Aeromagnetic Survey in the Lower Rennick Glacier Area, North Victoria Land, Antarctica. *Geol. Jb.* E47, 115–137.

Damaske, D. (1996). The Aeromagnetic Programme of GANOVEX VI - Lay-Out, Execution, and Data Processing. *Geol. Jb.* B89, 295–319.

Damaske, D. & E. Bozzo (eds.) (2003). *Scientific Results from the Joint German-Italian 1999-2000 Antarctic Expedition. Terra Antartica*, 10(3).

Damaske, D. & E. Bozzo (eds.) (2004). *Scientific Results from the Joint German-Italian 1999-2000 Antarctic Expedition – Second Part. Terra Antartica*, 11(1).

Damaske, D. & H.-J. Dürbaum (eds.) (1988). *German Antarctic North Victoria Land Expedition 1984/85 – GANOVEX IV. Geol. Jb.*, E38.

Damaske, D. & J. Fritsch (eds.) (1993). *German Antarctic North Victoria Land Expedition 1988/89 – GANOVEX V. Geol. Jb.*, E47.

Damaske, D., J. C. Behrendt, A. McCafferty, R. Saltus & U. Meyer (1994). Transfer faults in the western Ross Sea: new evidence from the McMurdo Sound/Ross Ice Shelf aeromagnetic survey (GANOVEX VI). *Antarct. Sci.* 6(3), 359–364. doi:10.1017/S0954102094000556.

Damaske, D., C. A. Finn, H.-D. Moeller, C. Demosthenous & E. D. Anderson (2002). Aeromagnetic data centered over Skelton Neve, Antarctica: A website for distribution of data and maps (on-line edition). *USGS Open-File Rep.* 02-452.
`pubs.usgs.gov/of/2002/ofr-02-452/`

Damaske, D., F. Ferraccioli & E. Bozzo (2003). Aeromagnetic Anomaly Investigations along the Antarctic Coast between Yule Bay and Mertz Glacier. *Terra Antartica* 10(3), 85–96.

Damaske, D., A. L. Läufer, F. Goldmann, H.-D. Möller & F. Lisker (2007). Magnetic anomalies northeast of Cape Adare, northern Victoria Land (Antarctica), and their relation to onshore structures. In: Cooper, A. K., P. J. Barrett, H. Stagg, B. Storey, E. Stump, W. Wise & 10th ISAES editorial team (eds.), *Antarctica: A Keystone in a Changing World*. 10th International Symposium on Antarctic Earth Sciences, Santa Barbara, National Academies Press. doi:10.3133/of2007-1047.srp016. USGS Open-File Report 2007-1047 Short Research Paper 016.
`pubs.usgs.gov/of/2007/1047/srp/srp016/`

Damaske, D., B. Schreckenberger & F. Goldmann (2014). A High Resolution Aeromagnetic Survey over the Mesa Range, Northern Victoria Land, Antarctica. *Polarforsch.* 84(1), 1–13. doi:10.2312/polarforschung.84.1.1.

Davey, F. J. (1987). Geology and Structure of the Ross Sea Region. In: Davey, F. J. & K. Cooper, Alan (eds.), *The Antarctic Continental Margin: Geology and Geophysics of the Western Ross Sea*, *Earth Science Series*, 5B. Circum-Pacific Council for Energy and Mineral Resources, 1–16.

Della Vedova, B., G. Pellis, H. Trey, J. Zhang, A. K. Cooper, J. Makris & The ACRUP Working Group (1997). Crustal Structure of the Transantarctic Mountains, Western Ross Sea. In: Ricci, C. A. (ed.), *The Antarctic Region: Geological Evolution and*

Processes. 7th International Symposium on Antarctic Earth Sciences, Siena, Terra Antartica Publication. ISBN 88-900221-0-8, 609–618.

Dürbaum, H.-J., G. Druivenga, H. Geipel & G. Merkel (1989). Gravity Measurements along a Traverse from Mt. Melbourne to the Polar Plateau in North Victoria Land, Antarctica. *Geol. Jahrb.* E38, 231–243.

Estrada, S. (ed.) (2003). *Geology and Geophysics of Marie Byrd Land, Northern Victoria Land, and Oates Coast – GANOVEX VII. Geol. Jb.*, B95.

Faure, G. & T. M. Mensing (2010). *The Transantarctic Mountains: Rocks, Ice, Meteorites and Water*. Springer, Dordrecht. ISBN 978-1-4020-8406-5. doi:10.1007/978-90-481-9390-5.

Federico, L., L. Crispini, G. Capponi & J. Bradshaw (2009). The Cambrian Ross Orogeny in northern Victoria Land (Antarctica) and New Zealand: A synthesis. *Gondwana Res.* 15(2), 188 – 196. doi:10.1016/j.gr.2008.10.004.

Ferraccioli, F., E. Armadillo, T. Jordan, E. Bozzo & H. Corr (2009a). Aeromagnetic exploration over the East Antarctic Ice Sheet: A new view of the Wilkes Subglacial Basin. *Tectonophys.* 478(1-2), 62–77. doi:10.1016/j.tecto.2009.03.013.

Ferraccioli, F., E. Armadillo, A. Zunino, E. Bozzo, S. Rocchi & P. Armienti (2009b). Magmatic and tectonic patterns over the Northern Victoria Land sector of the Transantarctic Mountains from new aeromagnetic imaging. *Tectonophys.* 478(1-2), 43–61. doi:10.1016/j.tecto.2008.11.028.

Finlay, C. C., S. Maus, C. D. Beggan, T. N. Bondar, A. Chambodut, T. A. Chernova, A. Chulliat, V. P. Golovkov, B. Hamilton, M. Hamoudi, R. Holme, G. Hulot, W. Kuang, B. Langlais, V. Lesur, F. J. Lowes, H. Lühr, S. Macmillan, M. Mandea, S. McLean, C. Manoj, M. Menvielle, I. Michaelis, N. Olsen, J. Rauberg, M. Rother, T. J. Sabaka, A. Tangborn, T. Tøffner-Clausen, E. Thébault, A. W. P. Thomson, I. Wardinski, Z. Wei, T. I. Zvereva & IAGA WG V-MOD (2011). International Geomagnetic Reference Field: the eleventh generation. *Geophys. J. Int.* 183(3), 1216–1230. doi:10.1111/j.1365-246X.2010.04804.x.

Finn, C., D. Moore, D. Damaske & T. Mackey (1999). Aeromagnetic legacy of early Paleozoic subduction along the Pacific margin of Gondwana. *Geol.* 27(12), 1087–1090. doi:10.1130/0091-7613(1999)027<1087:ALOEPS>2.3.CO;2.

Fischer, H., F. Fundel, U. Ruth, B. Twarloh, A. Wegner, R. Udisti, S. Becagli, E. Castellano, A. Morganti, M. Severi, E. Wolff, G. Littot, R. Röthlisberger, R. Mulvaney, M. A. Hutterli, P. Kaufmann, U. Federer, F. Lambert, M. Bigler, M. Hansson, U. Jonsell, M. de Angelis, C. Boutron, M.-L. Siggaard-Andersen, J. P. Steffensen, C. Barbante, V. Gaspari, P. Gabrielli & D. Wagenbach (2007). Reconstruction of millennial changes

in dust emission, transport and regional sea ice coverage using the deep EPICA ice cores from the Atlantic and Indian Ocean sector of Antarctica. *Earth Planet. Science Lett.* 260(1-2), 340–354. doi:10.1016/j.epsl.2007.06.014.

Flöttman, T., G. M. Gibson & G. Kleinschmidt (1993). Structural continuity of the Ross and Delamerian orogens of Antarctica and Australia along the margin of the paleo-pacific. *Geol.* 21(4), 319–322. doi:10.1130/0091-7613(1993)021<0319:SCOTRA>2.3.CO;2.

Fritsch, J. & P. Kewitsch (1993). Gravity Measurements in the Western Ross Sea. *Geol. Jahrb.* E47, 211–228.

Förste, C., S. Bruinsma, J.-C. Marty, F. Flechtner, O. Abrikosov, C. Dahle, J.-M. Lemoine, K. H. Neumayer, R. Biancale, F. Barthelmes & R. König (2013). EIGEN-6C3stat – the newest High Resolution Combined Gravity Field Model based on the 4th Release of the GOCE Direct Approach. GFZ/GRGS, Potsdam/Toulouse, September, 2013.
`icgem.gfz-potsdam.de/ICGEM/documents/Foerste-et-al-EIGEN-6C3stat.pdf`

Gabriel, G. (1998). *Der Harz und sein südliches Vorland: Interpretation der Bouguer-Anomalie und spezielle Studien zur Geodynamik mit der Methode der finiten Elemente*. Papierflieger, Clausthal-Zellerfeld. ISBN 3-89720-098-8. Dissertation, Technische Universität Clausthal.

Gabriel, G., D. Vogel, R. Scheibe, H. Lindner, R. Pucher, T. Wonik & C. M. Krawczyk (2011). Anomalies of the Earth's total magnetic field in Germany – the first complete homogenous data set reveals new opportunities for multiscale geoscientific studies. *Geophys. J. Int.* 184(3), 1113–1118. doi:10.1111/j.1365-246X.2010.04924.x.

Giebeler-Degro, M. (1986). *Zur Tiefenerkundung des Niedersächsischen Tektogens durch dreidimensionale Simulationsrechnnungen*. Ph.D. thesis, Technische Universität Clausthal.

Grauch, V. J. S. (1984). TAYLOR: A FORTRAN program using Taylor series expansion for level-surface or surface-level continuation of potential field data. *USGS Open-File Rep.* 84-501.
`pubs.usgs.gov/of/1984/0501/report.pdf`

Götze, H.-J. & B. Lahmeyer (1988). Application of 3-dimensional interactive modeling in gravity and magnetics. *Geophys.* 53(8), 1096–1108. doi:10.1190/1.1442546.

Hammer, S. (1939). Terrain corrections for gravimeter stations. *Geophys.* 4(3), 184–194. doi:10.1190/1.1440495.

Hayes, D. E. & F. J. Davey (1975). A Geophysical Study of the Ross Sea, Antarctica. In: Hayes, D. E., L. A. Frakes, P. J. Barrett, D. A. Burns, P.-H. Chen, A. B. Ford, A. G. Kaneps, E. M. Kemp, D. W. McMollum, J. W. Piper, R. E. Wall & P. N. Webb (eds.), *Initial Reports of the Deep Sea Drilling Project*, 28. US Government Printing Office Washington, DC, 887–907. doi:10.2973/dsdp.proc.28.134.1975.

Hayford, J. F. & W. Bowie (1912). The Effect of Topography and Isostatic Compensation Upon the Intensity of Gravity. *U.S. Coast Geodet. Survey Spec. Pub.* 10. `www.lib.noaa.gov/collections/imgdocmaps/cgs_specpub.html`

Hinz, K. & M. Block (1984). Results of geophysical investigations in the Weddell Sea and in the Ross Sea, Antarctica. In: *Proceedings 11th World Petroleum Congress, London*, 2. 79–91.

Jentzsch, G. (2014). Micro-Gravity Measurements in Northern Victoria Land, Antarctica, as Contribution to Geodynamic Investigations – a Feasibility Study. *Polarforsch.* 84(1), 15–21. doi:10.2312/polarforschung.84.1.15.

Jentzsch, G., R. Ricker, A. Weise, A. Capra, M. Dubbini & A. Zanutta (2014). Micro-Gravity Measurements in Northern Victoria Land, Antarctica: A Feasibility Study. In: Rizos, C. & P. Willis (eds.), *Earth on the Edge: Science for a Sustainable Planet*, *International Association of Geodesy Symposia*, 139. Springer, Berlin, Heidelberg, 429–434. doi:10.1007/978-3-642-37222-3_57.

Jung, K. (1961). *Schwerkraftverfahren in der angewandten Geophysik*. Akademische Verlagsgesellschaft Geest & Portig, Leipzig.

Kienle, J., T. F. Redfield & A. M. Goodliffe (1992). Gravity Study of the Mt. Melbourne Quadrangle and the lower Rennick Glacier Area in North Victoria Land, Antarctica, and the Relation of the Rennick Graben Structure to Rifting Processes in the Ross Sea. In: Yoshida, Y., M. Kaminuma & K. Shiraishi (eds.), *Recent Progress in Antarctic Earth Science*. 6th International Symposium on Antarctic Earth Sciences, Ranzan, Terra Scientific Publishing Company, Tokyo, 523–534.

Kleinschmidt, G. & F. Tessensohn (1987). Early Paleozoic Westward Directed Subduction at the Pacific Margin of Antarctica. In: McKenzie, G. D. (ed.), *Gondwana Six: Structure, Tectonics, and Geophysics*. 6th International Gondwana Symposium, Columbus, American Geophysical Union. ISBN 0-87590-064-X, 89–105.

Kuchling, H. (2004). *Taschenbuch der Physik*. Fachbuchverlag Leipzig im Carl Hanser Verlag, München, Wien. ISBN 3-446-22883-7.

LaFehr, T. R. (1991). An exact solution for the gravity curvature (Bullard B) correction. *Geophys.* 56, 1179–1184. doi:10.1190/1.1443138.

Langel, R. A. (1992). International Geomagnetic Reference Field: The 6th Generation. *J. Geomagn. Geoelectr.* 44(9), 679–707.

Lisker, F. & A. L. Läufer (2013). The Mesozoic Victoria Basin: Vanished link between Antarctica and Australia. *Geology* 41(10), 1043–1046. doi:10.1130/G33409.1.

Liu, H., K. C. Jezek & B. Li (1999). Development of an Antarctic digital elevation model by integrating cartographic and remotely sensed data: A geographic information system based approach. *J. Geophys. Res.* 104(B10), 23 199–23 213. doi: 10.1029/1999JB900224.

Läufer, A. L., D. Damaske & F. Lisker (2011). Neogene Tectonics in the Edisto and Tucker Inlet Region and Its Correlation with Offshore Magnetic Anomalies North of Cape Adare, Northern Victoria Land, Antarctica. *Polarforsch.* 80(2), 111–126. doi: 10.2312/polarforschung.80.2.111.

Läufer, A. L. & F. Rossetti (2001). Brittle Deformation Features in the Rennick Glacier-Yule Bay Area, Northern Victoria Land, Antarctica. *Terra Antart. Rep.* 5, 77–80.

Lythe, M. B., D. G. Vaughan & the BEDMAP Consortium (2000). BEDMAP – bed topography of the Antarctic. *BAS Miscellaneous Series* Sheet No. 9. British Antarctic Survey, Cambridge.

Mandea, M. & S. Macmillan (2000). International Geomagnetic Reference Field – The Eighth Generation. *Earth, Planets, Space* 52(12), 1119–1124.

Maus, S., S. Macmillan, T. Chernova, S. Choi, D. Dater, V. Golovkov, V. Lesur, F. Lowes, H. Lühr, W. Mai, S. McLean, N. Olsen, M. Rother, T. Sabaka, A. Thomson & T. Zvereva (2005). The 10th-Generation International Geomagnetic Reference Field. *Geophys. J. Int.* 161(3), 561–565. doi:10.1111/j.1365-246X.2005.02641.x.

Melles, M., B. Diekmann, S. Estrada, C. Gaedicke, K. Gohl, W. Jokat, L. Lembke-Jene, A. Läufer, F. Lisker, K. Piepjohn et al. (2015). Geowissenschaftliche Polarforschung in Deutschland–globale Bedeutung und Perspektiven–. *Polarforsch.* 85(1), 1–64. `hdl.handle.net/10013/epic.47368.d001`

Merrill, R. T., M. W. McElhinny & P. L. McFadden (1996). *The Magnetic Field of the Earth*, *International Geophysics Series*, 63. Academic Press, San Diego, London. ISBN 0-12-491245-1.

Militzer, H. & F. Weber (eds.) (1984). *Angewandte Geophysik – Gravimetrie und Magnetik*. Springer-Verlag Wien, Akademie-Verlag Berlin. ISBN 978-3-211-81740-7, 978-0-387-81740-8.

Müller, J., T. Pugliatti, M. C. Ramorino & C. A. Ricci (1997). Rapporto sulla Campagna Antartica Estate Australe 1996-97: ItaliAntartide 12. Tech. rep., Programma

Nazionale di Ricerche in Antartide.
www.pnra.it/biblioteca/docs/rapporti_campagna/CA96-97.pdf

Nagy, D. (1966a). The Gravitational Attraction of a Right Rectangular Prism. *Geophys.* 31(2), 362–371. doi:10.1190/1.1439779.

Nagy, D. (1966b). The Prism Method for Terrain Corrections Using Digital Computers. *Pure Appl. Geophys.* 63(1), 31–39. doi:10.1007/BF00875156.

Pavlis, N. K., S. A. Holmes, S. C. Kenyon & J. K. Factor (2012). The development and evaluation of the Earth Gravitational Model 2008 (EGM2008). *J. Geophys. Res.* 117(B4). doi:10.1029/2011JB008916.

Redfield, T., J. Kienle & F. Heimberg (1993a). Complete Bouguer Gravity Map of North Victoria Land between the Rennick and the Matusevich Glaciers. *Geol. Jahrb.* E47, 185–196.

Redfield, T., J. Kienle & F. Heimberg (1993b). Complete Bouguer Gravity Map of the Mount Melbourne Quadrangle, North Victoria Land. *Geol. Jahrb.* E47, 169–184.

Redfield, T. F. & J. C. Behrendt (1992). Gravity Modeling Across the Transantarctic Mountains, Nporthern Victoria Land. In: Yoshida, Y., M. Kaminuma & K. Shiraishi (eds.), *Recent Progress in Antarctic Earth Science.* 6th International Symposium on Antarctic Earth Sciences, Ranzan, Terra Scientific Publishing Company, Tokyo, 535–544.

Reitmayr, G. (1994). Fieldreport on Gravity, GPS-Positioning and EMR-Ice Thickness Measurements Accompanying the ACRUP1 Experiment 1993/94, Antarctica. Tech. Rep. 111951, Bundesanstalt für Geowissenschaften und Rohstoffe, Hannover.

Reitmayr, G. (1997). Gravity Studies of Victoria Land and the Adjacent Oceans, Antarctica. In: Ricci, C. A. (ed.), *The Antarctic Region: Geological Evolution and Processes.* 7th International Symposium on Antarctic Earth Sciences, Siena, Terra Antartica Publication. ISBN 88-900221-0-8, 597–602.

Reitmayr, G. (2003). Continuation of Gravity Measurements in Victoria Land and at the Oates Coast, Antarctica, during GANOVEX VII. *Geol. Jahrb.* B95, 209–235.

Reitmayr, G., W. Korth, G. Caneva & F. Ferraccioli (2003). Gravity Survey at the Oates Coast Area, Antarctica, during the Joint German-Italian Expedition 1999/2000. *Terra Antart.* 10, 97–104.

Reitmayr, G. & R. Thierbach (1996). Gravity Surveys in Northern Victoria Land, Antarctica, during GANOVEX VI. *Geol. Jahrb.* B89, 343–370.

Ricker, R. (2011). *Mikrogravimetrische Messungen in Nord-Viktorialand, Antarktis.* Diploma thesis, Friedrich-Schiller-Universität Jena. (unpubl.).

Robinson, E. S. & J. E. Splettstoesser (1986). Structure of the Transantarctic Mountains Determined From Geophysical Surveys. In: Turner, M. D. & J. E. Splettstoesser (eds.), *Geology of the Central Transantarctic Mountains*, *Antarctic Research Series*, 36. Am. Geophys. Union, 119–162. doi:10.1029/AR036p0119.

Roland, N. W. (ed.) (1984). *German Antarctic North Victoria Land Expedition 1982/83 – GANOVEX III – Volume 1. Geol. Jb.*, B60.

Roland, N. W. (ed.) (1996). *German Antarctic North Victoria Land Expedition 1984/85 – GANOVEX – From Oates Coast to Marie Byrd Land. Geol. Jb.*, B89.

Roland, N. W., A. L. Läufer & F. Rossetti (2004). Revision of the Terrane Model of Northern Victoria Land (Antarctica). *Terra Antart.* 11(1), 55–65.

Rossetti, F., F. Lisker, F. Storti & A. L. Läufer (2003a). Tectonic and denudational history of the Rennick Graben (North Victoria Land): Implications for the evolution of rifting between East and West Antarctica. *Tectonics* 22(2). doi: 10.10229/2002TC001416.

Rossetti, F., A. L. Läufer & F. Storti (2003b). Structural Architecture and Tectonic Evolution of the Rennick Glacier Area (Northern Victoria Land, Antarctica) – Insights for the Cenozoic Tectonic Evolution of the Ross Sea Region. *Terra Antart.* 10(3), 141–156.

Salvini, F., G. Brancolini, M. Busetti, F. Storti, F. Mazzarini & F. Coren (1997). Cenozoic geodynamics of the Ross Sea region, Antarctica: Crustal extension, intraplate strike-slip faulting, and tectonic inheritance. *J. Geophys. Res.* 102(B11), 24 669–24 696. doi:10.1029/97JB01643.

Sandwell, D. T. & D. C. McAdoo (1990). High-Accuracy, High-Resolution Gravity Profiles From 2 Years of the Geosat Exact Repeat Mission. *J. Geophys. Res.* 95(C3), 3049–3060. doi:10.1029/JC095iC03p03049.

SCAR (2015). SCAR Antarctic Digital Database. Data downloaded April 27, 2015. `add.scar.org`

Schmidt, D. L. & P. D. Rowley (1986). Continental rifting and transform faulting along the Jurassic Transantarctic Rift, Antarctica. *Tectonics* 5(2), 279–291. doi: 10.1029/TC005i002p00279.

Schmidt, S., C. Plonka, H.-J. Götze & B. Lahmeyer (2011). Hybrid modelling of gravity, gravity gradients and magnetic fields. *Geophys. Prospect.* 59, 1046–1051. doi:10.1111/j.1365-2478.2011.00999.x.

Stickley, C. E., H. Brinkhuis, S. A. Schellenberg, A. Sluijs, U. Röhl, M. Fuller, M. Grauert, M. Huber, J. Warnaar & G. L. Williams (2004). Timing and nature of the deepening of the Tasmanian Gateway. *Paleoceanogr.* 19(4). doi: 10.1029/2004PA001022.

Stonehouse, B. (ed.) (2002). *Encyclopedia of Antarctica and the Southern Oceans*. Wiley, Chichester. ISBN 978-0-471-98665-2.

Talwani, M., J. L. Worzel & M. Landisman (1959). Rapid gravity computations for two-dimensional bodies with application to the Mendocino submarine fracture zone. *J. Geophys. Res.* 64(1), 49–59. doi:10.1029/JZ064i001p00049.

Tessensohn, F. & F. Henjes-Kunst (2005). Northern Victoria Land terranes, Antarctica: far-travelled or local products? In: Vaughan, A. P. M., P. T. Leat & R. J. Pankhurst (eds.), *Terrane Processes at the Margins of Gondwana*. No. 246 in Geol. Soc. Spec. Pub., Geological Society, London, 275–291.

Tessensohn, F. & N. W. Roland (eds.) (1987). *German Antarctic North Victoria Land Expedition 1982/83 – GANOVEX III – Volume 2. Geol. Jb.*, B66.

Tingey, R. J. (1991). The Regional Geology of Archaean and Proterozoic Rocks in Antarctica. In: Tingey, R. J. (ed.), *The Geology of Antarctica*, *Oxford monographs on geology and geophysics*, 17. Oxford University Press, 1–73.

Weaver, S. D., J. D. Bradshaw & M. G. Laird (1984). Geochemistry of Cambrian volcanics of the Bowers Supergroup and implications for the Early Palaeozoic tectonic evolution of northern Victoria Land, Antarctica. *Earth Planet. Science Lett.* 68(1), 128 – 140. doi:10.1016/0012-821X(84)90145-6.

Wessel, P. & W. H. Smith (1991). Free software helps map and display data. *Eos, Transact. Am. Geophys. Union* 72(41), 441–446. doi:10.1029/99EO00319.

Wessel, P., W. H. F. Smith, R. Scharroo, J. Luis & F. Wobbe (2013). Generic Mapping Tools: Improved Version Released. *Eos, Transact. Am. Geophys. Union* 94(45), 409–410. doi:10.1002/2013EO450001.

Wilson, G., D. Damaske, H.-D. Möller, K. Tinto & T. Jordan (2007). The geological evolution of southern McMurdo Sound – new evidence from a high-resolution aeromagnetic survey. *Geophys. J. Int.* 170(1), 93–100. doi:10.1111/j.1365-246X.2007.03395.x.

Winberry, J. P. & S. Anandakrishnan (2004). Crustal structure of the West Antarctic rift system and Marie Byrd Land hotspot. *Geology* 32(11), 977–980. doi:10.1130/G20768.1.

Wonik, T. (1992). *Kompilation und Interpretation der magnetischen Anomalien der Totalintensität in Zentral- und Nordeuropa*. Ph.D. thesis, Georg-August-Universität Göttingen.

Zeis, S., D. Gajewski & C. Prodehl (1990). Crustal structure of southern Germany from seismic refraction data. *Tectonophys.* 176(1-2), 59–86. doi:10.1016/0040-1951(90)90259-B.

Appendix A

Available terrestrial, marine, and satellite gravity data

A.1 Data used by Reitmayr (1997)

Tab. A.1 contains all terrestrial, marine, and satellite gravity data used by Reitmayr (1997) for the compilation of a Bouguer anomaly map of Victoria Land (Fig. A.1) and the respective references. Unfortunately, this information was not included in the data themselves, but was reconstructed from Reitmayr (1997) as well as the references listed below. Part of the information needed was retrieved from the webgis viewer of the National Geophysical Data Center (NGDC) of the National Oceanic and Atmospheric Administration (NOAA) (`maps.ngdc.noaa.gov/viewers/geophysics/`). For one data set no reference could be found. Not all of the other references contain tabled data; some only show maps of data distribution, which were compared to the distribution of the available data. Also, in some cases, typing errors were identified either in the digital data tables or the references.

Table A.1: Terrestrial, marine, and satellite gravity data of Victoria Land.

Dataset	Area or Expedition	Year	Reference
acc	ACRUP1 experiment	1993/1994	Reitmayr (1994)
aci	ACRUP1 experiment	1993/1994	Reitmayr (1994)
acr	ACRUP1 experiment	1993/1994	Reitmayr (1994)
ben	McMurdo Sound		Bennett & Sissons (1984)
brm	Brimstone Peak	1990/1991	Redfield & Behrendt (1992)
cap	Cape Williams	1990/1991	Reitmayr & Thierbach (1996)
dry	Drygalski area	1990/1991	Redfield & Behrendt (1992)
due	GANOVEX 4	1984/1985	Dürbaum et al. (1989)

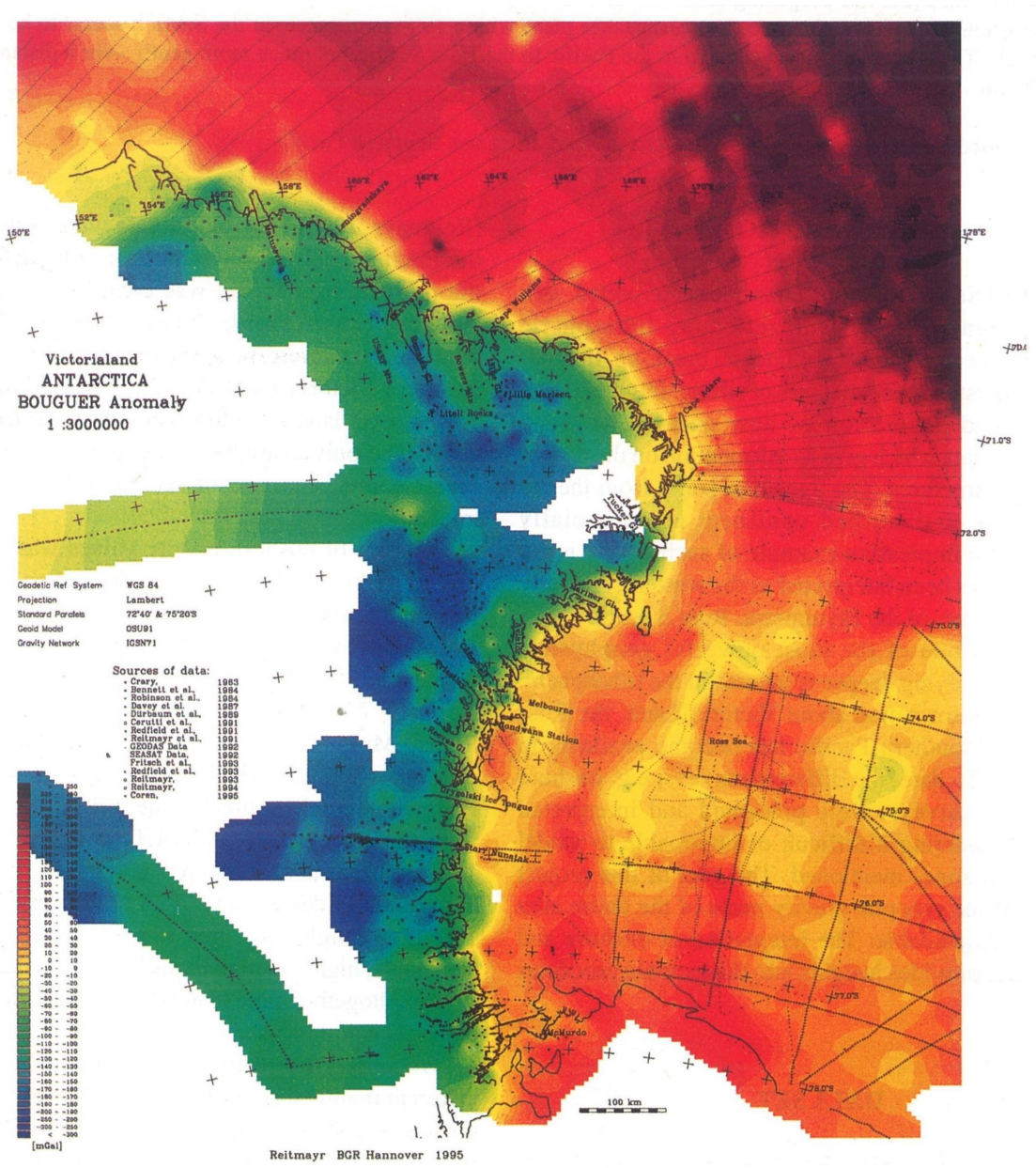

Figure A.1: Bouguer anomaly map of Victoria Land, based on terrestrial data and augmented by marine and satellite data (Reitmayr, 1997).

Table A.2 (*continued*): Terrestrial, marine, and satellite gravity data of Victoria Land.

Dataset	Area or Expedition	Year	Reference
fra	marine gravity data	1990	(reference unknown)[a]
fri	marine gravity data	1988/1989	Fritsch & Kewitsch (1993)
ga8	GANOVEX 8	1999/2000	Reitmayr et al. (2003)
geo	marine gravity data	1967/1968, 1972	Hayes & Davey (1975)
gi1	GANOVEX 8	1999/2000	Reitmayr et al. (2003)
gi2	GANOVEX 8	1999/2000	Reitmayr et al. (2003)
go7	GANOVEX 7	1992/1993	Reitmayr (2003)
gon	Gondwana station	1990/1991	Reitmayr & Thierbach (1996)
gov	GANOVEX 7	1992/1993	Reitmayr (2003)
hin	marine gravity data	1980	Hinz & Block (1984)
ki1	Mt. Melbourne	1988/1989	Kienle et al. (1992) Redfield et al. (1993b)
ki2	Rennick glacier	1988/1989	Kienle et al. (1992) Redfield et al. (1993a)
lil	Lillie glacier	1992/1993	Reitmayr (2003)
liv	Lillie glacier	1992/1993	Reitmayr (2003)
mat	Matusevich glacier	1999/2000	Reitmayr et al. (2003)
oat	Oates Coast	1992/1993	Reitmayr (2003)
rob			Robinson & Splettstoesser (1986)
soe	satellite data		Sandwell & McAdoo (1990)
ter	Mt. Melbourne		Cerutti et al. (1992)
usg	large traverses	1958 – 1960	Crary (1963)

[a] The data set, consisting of two profiles from West to East at 76° South, originates from an Italian survey (cf. Brancolini et al., 1995, Plate 2). Casazza et al. (1990) give technical details on instrumentation and execution of measurements, but no results are included.

A.2 Other gravity data

Terrestrial measurements

Additional terrestrial gravity data are available from Jentzsch et al. (2014); Jentzsch (2014). As the campaign aimed at high precision for comparison with GPS vertical movement data, only few points have been measured. Also no corrections regarding topography or ice masses were applied to the data (Ricker, 2011).

Data from global gravity models

As the terrestrial measurements, due to the conditions in Victoria Land, are distributed very uneven, i.e. the distances between measurement locations vary very much, and ship-

based measurements are also only available at certain profiles, it is important to take into account global gravity models as data source. One global model is the DTU10 gravity field model (Andersen, 2010; Andersen et al., 2010); another model is the EIGEN-6C3 model (Förste et al., 2013). Many global gravity field models are available online at the International Centre for Global Earth Models (ICGEM; `http://icgem.gfz-potsdam.de/ICGEM/`).

Appendix B

Geomagnetic reference stations

The corrections for the Secular Variation applied to the aeromagnetic data are based on observatory time-series from stations in and around Antarctica (cf. Sec. 3.2.1). The names and locations of these stations are given in Tab. 3.4; Fig. 3.7 shows the station distribution. Daily means of geomagnetic total intensity were not available from all observatories for all epochs of the aeromagnetic surveys. Tab. 3.5 gives an overview, which observatories could be used for the different epochs. The parameters of the polynomial fit are shown in Tab. B.1; the fit equation (Eq. 3.7) is given here again.

$$F = a \cdot x^2 + b \cdot y^2 + c \cdot z^2 + d \cdot x \cdot y + e \cdot x \cdot z + f \cdot y \cdot z + g \cdot x + h \cdot y + i \cdot z + k \tag{B.1}$$

with F magnetic total intensity,
x, y, z Cartesian coordinates,
$a \ldots k$ parameters of the polynomial fit.

Table B.1: Parameters of the polynomial fit to the daily means of geomagnetic total intensity for the different epochs of the aeromagnetic surveys.

epoch	a $[\mathrm{nT\,m^{-2}}]$	b $[\mathrm{nT\,m^{-2}}]$	c $[\mathrm{nT\,m^{-2}}]$
1980/01/01	$-67.389 \cdot 10^{-9}$	$-67.238 \cdot 10^{-9}$	$-65.018 \cdot 10^{-9}$
	$\pm 28.3 \cdot 10^{-9}$	$\pm 28.3 \cdot 10^{-9}$	$\pm 28.3 \cdot 10^{-9}$
1985/01/01	$-71.008 \cdot 10^{-9}$	$-70.751 \cdot 10^{-9}$	$-68.849 \cdot 10^{-9}$
	$\pm 31.0 \cdot 10^{-9}$	$\pm 31.0 \cdot 10^{-9}$	$\pm 31.2 \cdot 10^{-9}$
1989/02/17	$114.89 \cdot 10^{-9}$	$115.17 \cdot 10^{-9}$	$118.42 \cdot 10^{-9}$
	$\pm 183.0 \cdot 10^{-9}$	$\pm 183.0 \cdot 10^{-9}$	$\pm 184.0 \cdot 10^{-9}$
1991/01/01	$334.32 \cdot 10^{-9}$	$334.73 \cdot 10^{-9}$	$338.61 \cdot 10^{-9}$
	$\pm 404.0 \cdot 10^{-9}$	$\pm 404.0 \cdot 10^{-9}$	$\pm 407.0 \cdot 10^{-9}$
1992/02/06	$5.6721 \cdot 10^{-9}$	$5.9458 \cdot 10^{-9}$	$7.684 \cdot 10^{-9}$
	$\pm 337.0 \cdot 10^{-9}$	$\pm 337.0 \cdot 10^{-9}$	$\pm 340.0 \cdot 10^{-9}$
1993/02/06	$-42.788 \cdot 10^{-9}$	$-42.493 \cdot 10^{-9}$	$-41.239 \cdot 10^{-9}$
	$\pm 50.2 \cdot 10^{-9}$	$\pm 50.2 \cdot 10^{-9}$	$\pm 50.5 \cdot 10^{-9}$
1994/02/06	$5.7946 \cdot 10^{-9}$	$6.1064 \cdot 10^{-9}$	$7.4471 \cdot 10^{-9}$
	$\pm 242.0 \cdot 10^{-9}$	$\pm 242.0 \cdot 10^{-9}$	$\pm 244.0 \cdot 10^{-9}$
1994/11/25	$96.844 \cdot 10^{-9}$	$97.132 \cdot 10^{-9}$	$99.498 \cdot 10^{-9}$
	$\pm 223.0 \cdot 10^{-9}$	$\pm 223.0 \cdot 10^{-9}$	$\pm 224.0 \cdot 10^{-9}$
1996/11/14	$-25.2 \cdot 10^{-9}$	$-24.907 \cdot 10^{-9}$	$-23.814 \cdot 10^{-9}$
	$\pm 253.0 \cdot 10^{-9}$	$\pm 253.0 \cdot 10^{-9}$	$\pm 255.0 \cdot 10^{-9}$
1998/01/12	$-26.392 \cdot 10^{-9}$	$-25.911 \cdot 10^{-9}$	$-24.669 \cdot 10^{-9}$
	$\pm 44.1 \cdot 10^{-9}$	$\pm 44.1 \cdot 10^{-9}$	$\pm 44.3 \cdot 10^{-9}$
2000/01/15	$74.648 \cdot 10^{-9}$	$75.006 \cdot 10^{-9}$	$76.665 \cdot 10^{-9}$
	$\pm 231.0 \cdot 10^{-9}$	$\pm 231.0 \cdot 10^{-9}$	$\pm 233.0 \cdot 10^{-9}$
2002/01/21	$-9.8196 \cdot 10^{-9}$	$-9.4898 \cdot 10^{-9}$	$-8.2601 \cdot 10^{-9}$
	$\pm 242.0 \cdot 10^{-9}$	$\pm 242.0 \cdot 10^{-9}$	$\pm 244.0 \cdot 10^{-9}$
2002/02/02	$71.614 \cdot 10^{-9}$	$71.911 \cdot 10^{-9}$	$74.135 \cdot 10^{-9}$
	$\pm 225.0 \cdot 10^{-9}$	$\pm 225.0 \cdot 10^{-9}$	$\pm 227.0 \cdot 10^{-9}$
2005/12/12	$70.179 \cdot 10^{-9}$	$70.543 \cdot 10^{-9}$	$72.212 \cdot 10^{-9}$
	$\pm 237.0 \cdot 10^{-9}$	$\pm 237.0 \cdot 10^{-9}$	$\pm 239.0 \cdot 10^{-9}$
2010/01/11	$321.84 \cdot 10^{-9}$	$322.31 \cdot 10^{-9}$	$325.77 \cdot 10^{-9}$
	$\pm 207.0 \cdot 10^{-9}$	$\pm 207.0 \cdot 10^{-9}$	$\pm 209.0 \cdot 10^{-9}$

Table B.1 (*continued*): Parameters of the polynomial fit to the daily means of geomagnetic total intensity for the different epochs of the aeromagnetic surveys.

epoch	d $[\mathrm{nT\,m^{-2}}]$	e $[\mathrm{nT\,m^{-2}}]$	f $[\mathrm{nT\,m^{-2}}]$
1980/01/01	$-277.83 \cdot 10^{-12}$	$1.9008 \cdot 10^{-9}$	$-2.7172 \cdot 10^{-10}$
	$\pm 209 \cdot 10^{-12}$	$\pm 0.459 \cdot 10^{-9}$	$\pm 3.85 \cdot 10^{-10}$
1985/01/01	$-93.755 \cdot 10^{-12}$	$1.6427 \cdot 10^{-9}$	$0.113\,78 \cdot 10^{-10}$
	$\pm 236.0 \cdot 10^{-12}$	$\pm 0.594 \cdot 10^{-9}$	$\pm 4.07 \cdot 10^{-10}$
1989/02/17	$6.7538 \cdot 10^{-12}$	$1.6281 \cdot 10^{-9}$	$1.8147 \cdot 10^{-10}$
	$\pm 249.0 \cdot 10^{-12}$	$\pm 0.58 \cdot 10^{-9}$	$\pm 4.21 \cdot 10^{-10}$
1991/01/01	$37.91 \cdot 10^{-12}$	$1.5389 \cdot 10^{-9}$	$-0.913\,29 \cdot 10^{-10}$
	$\pm 501.0 \cdot 10^{-12}$	$\pm 1.0 \cdot 10^{-9}$	$\pm 8.85 \cdot 10^{-10}$
1992/02/06	$-34.278 \cdot 10^{-12}$	$1.4612 \cdot 10^{-9}$	$-2.2723 \cdot 10^{-10}$
	$\pm 477.0 \cdot 10^{-12}$	$\pm 1.1 \cdot 10^{-9}$	$\pm 8.34 \cdot 10^{-10}$
1993/02/06	$-4.0221 \cdot 10^{-12}$	$1.3428 \cdot 10^{-9}$	$-1.5024 \cdot 10^{-10}$
	$\pm 347.0 \cdot 10^{-12}$	$\pm 0.817 \cdot 10^{-9}$	$\pm 6.17 \cdot 10^{-10}$
1994/02/06	$-46.622 \cdot 10^{-12}$	$1.2281 \cdot 10^{-9}$	$-2.527 \cdot 10^{-10}$
	$\pm 140.0 \cdot 10^{-12}$	$\pm 0.504 \cdot 10^{-9}$	$\pm 3.06 \cdot 10^{-10}$
1994/11/25	$2.7869 \cdot 10^{-12}$	$1.4314 \cdot 10^{-9}$	$-1.2591 \cdot 10^{-10}$
	$\pm 131.0 \cdot 10^{-12}$	$\pm 0.452 \cdot 10^{-9}$	$\pm 2.79 \cdot 10^{-10}$
1996/11/14	$-42.268 \cdot 10^{-12}$	$1.4577 \cdot 10^{-9}$	$-2.9864 \cdot 10^{-10}$
	$\pm 181.0 \cdot 10^{-12}$	$\pm 0.524 \cdot 10^{-9}$	$\pm 3.59 \cdot 10^{-10}$
1998/01/12	$-6.7229 \cdot 10^{-12}$	$1.4309 \cdot 10^{-9}$	$-4.47 \cdot 10^{-10}$
	$\pm 151.0 \cdot 10^{-12}$	$\pm 0.434 \cdot 10^{-9}$	$\pm 2.95 \cdot 10^{-10}$
2000/01/15	$22.839 \cdot 10^{-12}$	$1.2182 \cdot 10^{-9}$	$-2.1717 \cdot 10^{-10}$
	$\pm 119.0 \cdot 10^{-12}$	$\pm 0.395 \cdot 10^{-9}$	$\pm 2.39 \cdot 10^{-10}$
2002/01/21	$-32.624 \cdot 10^{-12}$	$1.1827 \cdot 10^{-9}$	$-2.9391 \cdot 10^{-10}$
	$\pm 124.0 \cdot 10^{-12}$	$\pm 0.503 \cdot 10^{-9}$	$\pm 2.54 \cdot 10^{-10}$
2002/02/02	$-8.5622 \cdot 10^{-12}$	$1.4187 \cdot 10^{-9}$	$-2.3378 \cdot 10^{-10}$
	$\pm 121.0 \cdot 10^{-12}$	$\pm 0.433 \cdot 10^{-9}$	$\pm 2.43 \cdot 10^{-10}$
2005/12/12	$5.7777 \cdot 10^{-12}$	$1.1848 \cdot 10^{-9}$	$-3.0255 \cdot 10^{-10}$
	$\pm 124.0 \cdot 10^{-12}$	$\pm 0.413 \cdot 10^{-9}$	$\pm 2.54 \cdot 10^{-10}$
2010/01/11	$3.8308 \cdot 10^{-12}$	$1.3066 \cdot 10^{-9}$	$-2.5893 \cdot 10^{-10}$
	$\pm 105.0 \cdot 10^{-12}$	$\pm 0.32 \cdot 10^{-9}$	$\pm 2.0 \cdot 10^{-10}$

Table B.1 (*continued*): Parameters of the polynomial fit to the daily means of geomagnetic total intensity for the different epochs of the aeromagnetic surveys.

epoch	g $[\mathrm{nT\,m^{-1}}]$	h $[\mathrm{nT\,m^{-1}}]$	i $[\mathrm{nT\,m^{-1}}]$
1980/01/01	$4.848\,71 \cdot 10^{-3}$ $\pm 2.713 \cdot 10^{-3}$	$0.670\,37 \cdot 10^{-3}$ $\pm 1.962 \cdot 10^{-3}$	$21.119 \cdot 10^{-3}$ $\pm 6.525 \cdot 10^{-3}$
1985/01/01	$3.161\,16 \cdot 10^{-3}$ $\pm 3.478 \cdot 10^{-3}$	$2.139\,24 \cdot 10^{-3}$ $\pm 2.006 \cdot 10^{-3}$	$17.815\,77 \cdot 10^{-3}$ $\pm 7.686 \cdot 10^{-3}$
1989/02/17	$2.932\,49 \cdot 10^{-3}$ $\pm 3.421 \cdot 10^{-3}$	$3.015\,52 \cdot 10^{-3}$ $\pm 2.125 \cdot 10^{-3}$	$18.400\,42 \cdot 10^{-3}$ $\pm 7.434 \cdot 10^{-3}$
1991/01/01	$2.262\,24 \cdot 10^{-3}$ $\pm 5.934 \cdot 10^{-3}$	$1.509\,66 \cdot 10^{-3}$ $\pm 4.383 \cdot 10^{-3}$	$10.869\,03 \cdot 10^{-3}$ $\pm 12.265 \cdot 10^{-3}$
1992/02/06	$2.138\,15 \cdot 10^{-3}$ $\pm 6.48 \cdot 10^{-3}$	$1.072\,87 \cdot 10^{-3}$ $\pm 4.112 \cdot 10^{-3}$	$11.3871 \cdot 10^{-3}$ $\pm 13.22 \cdot 10^{-3}$
1993/02/06	$1.566\,34 \cdot 10^{-3}$ $\pm 4.874 \cdot 10^{-3}$	$1.3964 \cdot 10^{-3}$ $\pm 3.028 \cdot 10^{-3}$	$9.9717 \cdot 10^{-3}$ $\pm 10.634 \cdot 10^{-3}$
1994/02/06	$1.164\,83 \cdot 10^{-3}$ $\pm 2.67 \cdot 10^{-3}$	$0.956\,95 \cdot 10^{-3}$ $\pm 1.233 \cdot 10^{-3}$	$8.063\,15 \cdot 10^{-3}$ $\pm 7.73 \cdot 10^{-3}$
1994/11/25	$2.083\,59 \cdot 10^{-3}$ $\pm 2.467 \cdot 10^{-3}$	$1.443\,08 \cdot 10^{-3}$ $\pm 1.138 \cdot 10^{-3}$	$11.589\,44 \cdot 10^{-3}$ $\pm 6.742 \cdot 10^{-3}$
1996/11/14	$2.046\,34 \cdot 10^{-3}$ $\pm 2.857 \cdot 10^{-3}$	$0.603\,58 \cdot 10^{-3}$ $\pm 1.626 \cdot 10^{-3}$	$8.019\,04 \cdot 10^{-3}$ $\pm 6.685 \cdot 10^{-3}$
1998/01/12	$1.737\,26 \cdot 10^{-3}$ $\pm 2.478 \cdot 10^{-3}$	$-0.318\,59 \cdot 10^{-3}$ $\pm 1.426 \cdot 10^{-3}$	$10.819\,66 \cdot 10^{-3}$ $\pm 6.061 \cdot 10^{-3}$
2000/01/15	$0.878\,01 \cdot 10^{-3}$ $\pm 2.117 \cdot 10^{-3}$	$1.090\,02 \cdot 10^{-3}$ $\pm 1.003 \cdot 10^{-3}$	$6.602\,05 \cdot 10^{-3}$ $\pm 5.476 \cdot 10^{-3}$
2002/01/21	$0.927\,61 \cdot 10^{-3}$ $\pm 2.63 \cdot 10^{-3}$	$0.932\,49 \cdot 10^{-3}$ $\pm 1.056 \cdot 10^{-3}$	$7.933\,64 \cdot 10^{-3}$ $\pm 7.699 \cdot 10^{-3}$
2002/02/02	$2.045\,13 \cdot 10^{-3}$ $\pm 2.332 \cdot 10^{-3}$	$1.169\,49 \cdot 10^{-3}$ $\pm 1.017 \cdot 10^{-3}$	$11.881\,84 \cdot 10^{-3}$ $\pm 6.43 \cdot 10^{-3}$
2005/12/12	$0.802\,78 \cdot 10^{-3}$ $\pm 2.196 \cdot 10^{-3}$	$0.833\,51 \cdot 10^{-3}$ $\pm 1.054 \cdot 10^{-3}$	$6.900\,01 \cdot 10^{-3}$ $\pm 5.607 \cdot 10^{-3}$
2010/01/11	$1.163\,12 \cdot 10^{-3}$ $\pm 1.654 \cdot 10^{-3}$	$0.969\,15 \cdot 10^{-3}$ $\pm 0.829 \cdot 10^{-3}$	$7.834\,59 \cdot 10^{-3}$ $\pm 4.109 \cdot 10^{-3}$

Table B.1 (*continued*): Parameters of the polynomial fit to the daily means of geomagnetic total intensity for the different epochs of the aeromagnetic surveys.

epoch	k [nT]	RMS [nT] RMS [%]	number of stations used
1980/01/01	2 821 000.0 ±1 150 000.0	577.188 339 96 1.161 017 934 18	14
1985/01/01	2 955 000.0 ±1 260 000.0	648.861 096 449 1.261 666 216 26	14
1989/02/17	−4 607 200.0 ±7 440 000.0	748.829 738 545 1.557 970 646 76	15
1991/01/01	−13 552 000.0 ±16 400 000.0	1097.259 875 97 2.201 503 567 51	13
1992/02/06	−179 530.0 ±13 700 000.0	1387.681 959 82 2.878 262 681 26	15
1993/02/06	1 787 400.0 ±2 040 000.0	1424.369 242 38 2.734 865 078 82	19
1994/02/06	−192 750.0 ±9 830 000.0	1368.461 953 37 2.845 338 321 04	19
1994/11/25	−3 887 900.0 ±9 050 000.0	1397.295 857 52 2.881 508 850 67	20
1996/11/14	1 070 100.0 ±10 300 000.0	1488.028 045 77 3.109 182 233 06	20
1998/01/12	1 122 200.0 ±1 800 000.0	1256.404 052 31 2.209 836 119 74	20
2000/01/15	−2 998 400.0 ±9 400 000.0	1516.473 136 35 3.209 271 510 09	22
2002/01/21	440 890.0 ±9 820 000.0	1331.413 652 12 2.728 045 096 13	18
2002/02/02	−2 861 700.0 ±9 140 000.0	1367.156 109 31 2.810 396 361 37	19
2005/12/12	−2 816 500.0 ±9 630 000.0	1518.591 053 95 3.259 191 951 26	21
2010/01/11	−13 055 000.0 ±8 420 000.0	1015.378 699 54 1.871 385 985 8	18

Appendix C

IGMAS+ gravity model

This chapter summarizes the 33 sections of the *IGMAS+* model which was developed based on the low-pass and band-pass filtered gravity data. The sections are sorted from south to north and represented in Fig. C.1 to Fig. C.33. For better comparison between the figures, the anomaly axis is the same for all sections. The subsurface is vertically exaggerated by a factor of 10 in all sections.

As before, the upper part of each figure shows the anomalies: measured anomaly (red), calculated anomaly (blue), and residual anomaly (yellow). The subsurface structure consists of the lithospheric mantle (pink), the lower crust or basement (grey), and the upper crust (green).

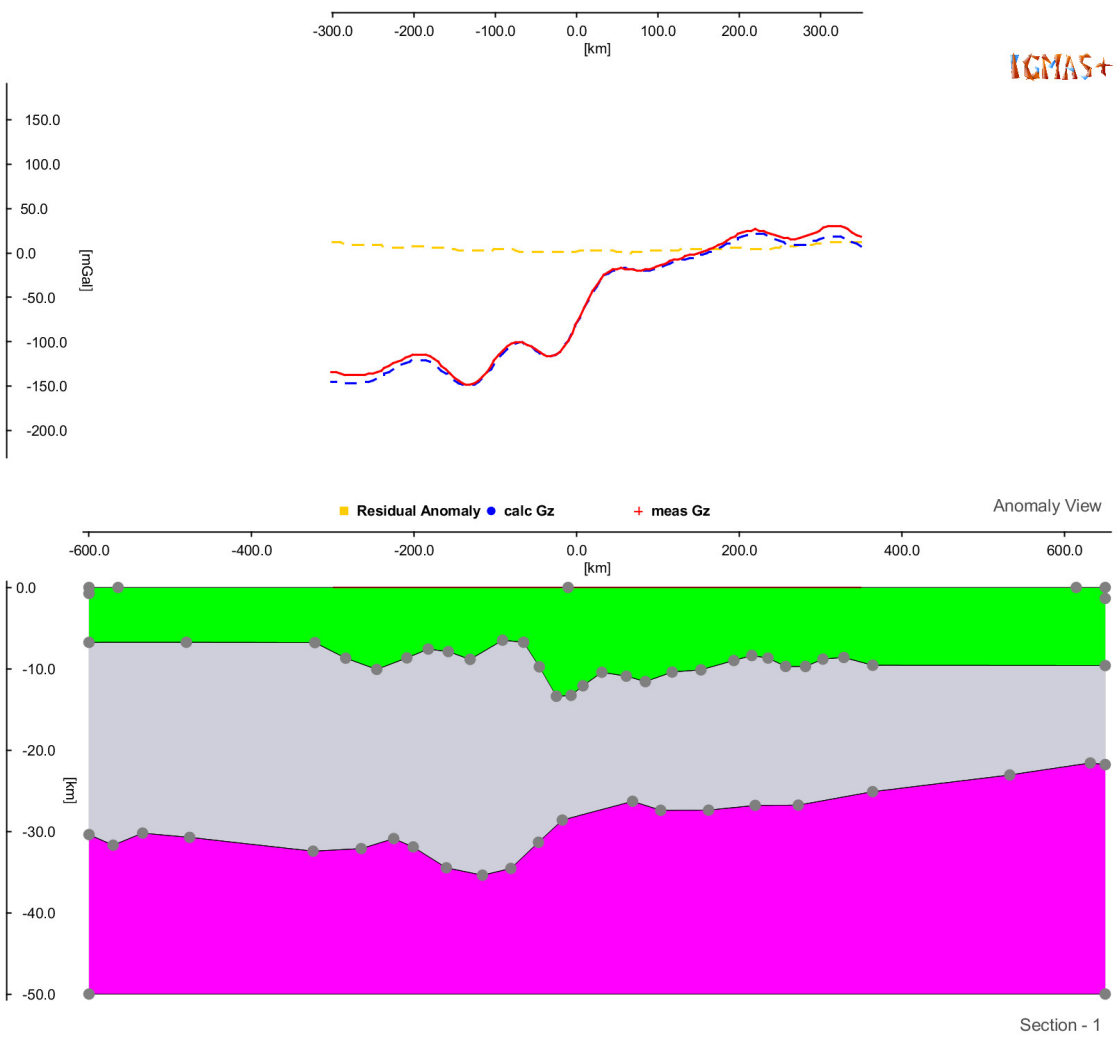

Figure C.1: Section 1 at −450 km northing.

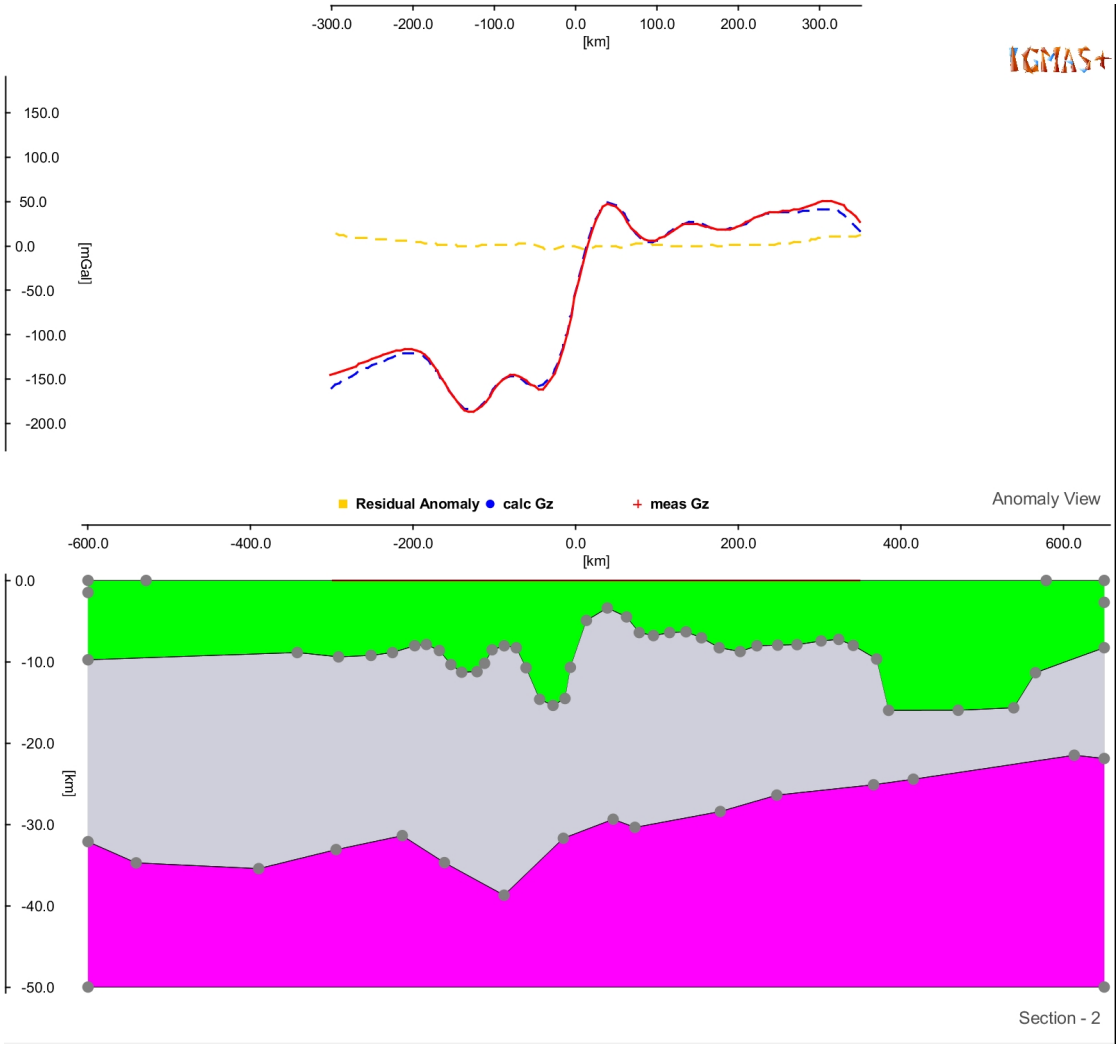

Figure C.2: Section 2 at −400 km northing.

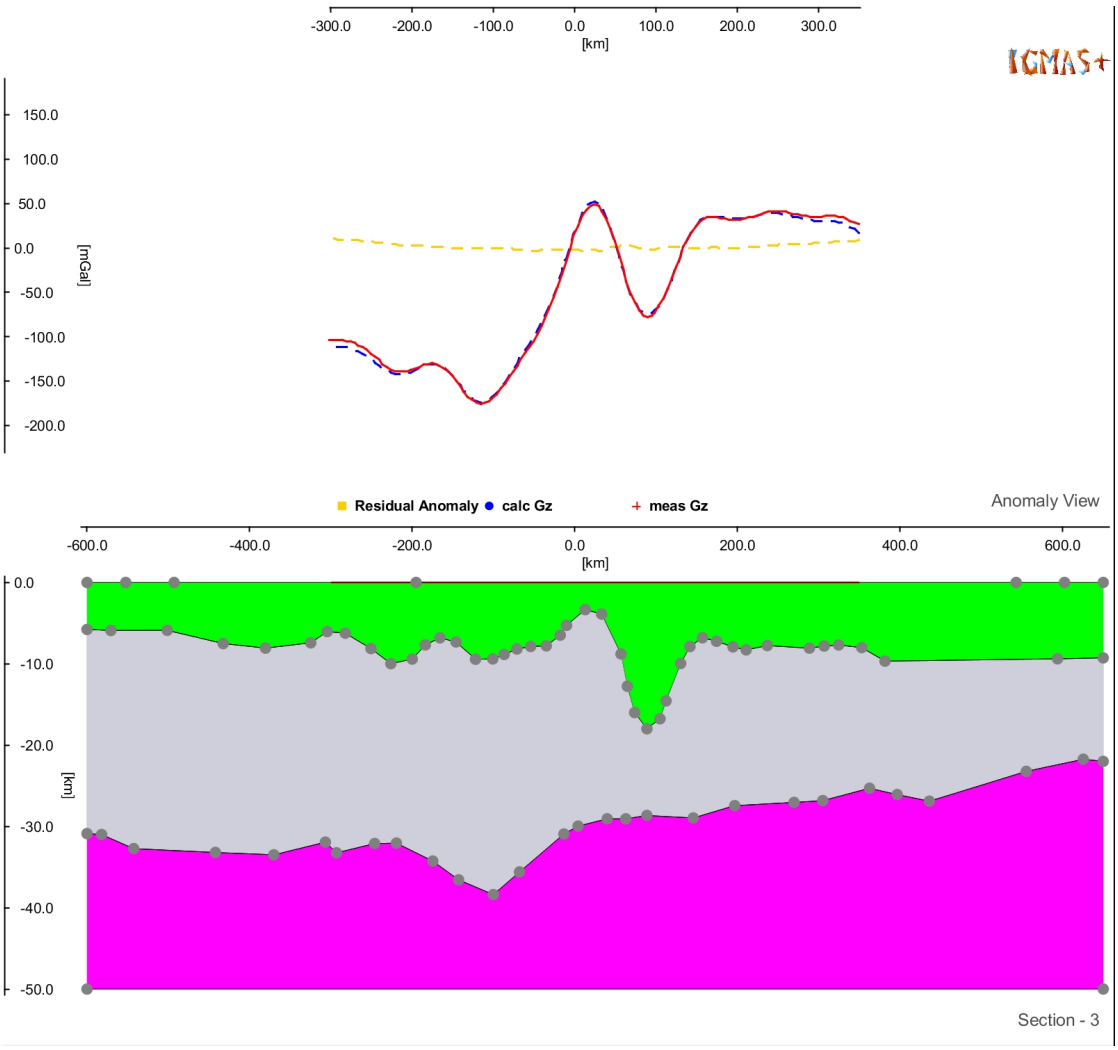

Figure C.3: Section 3 at −350 km northing.

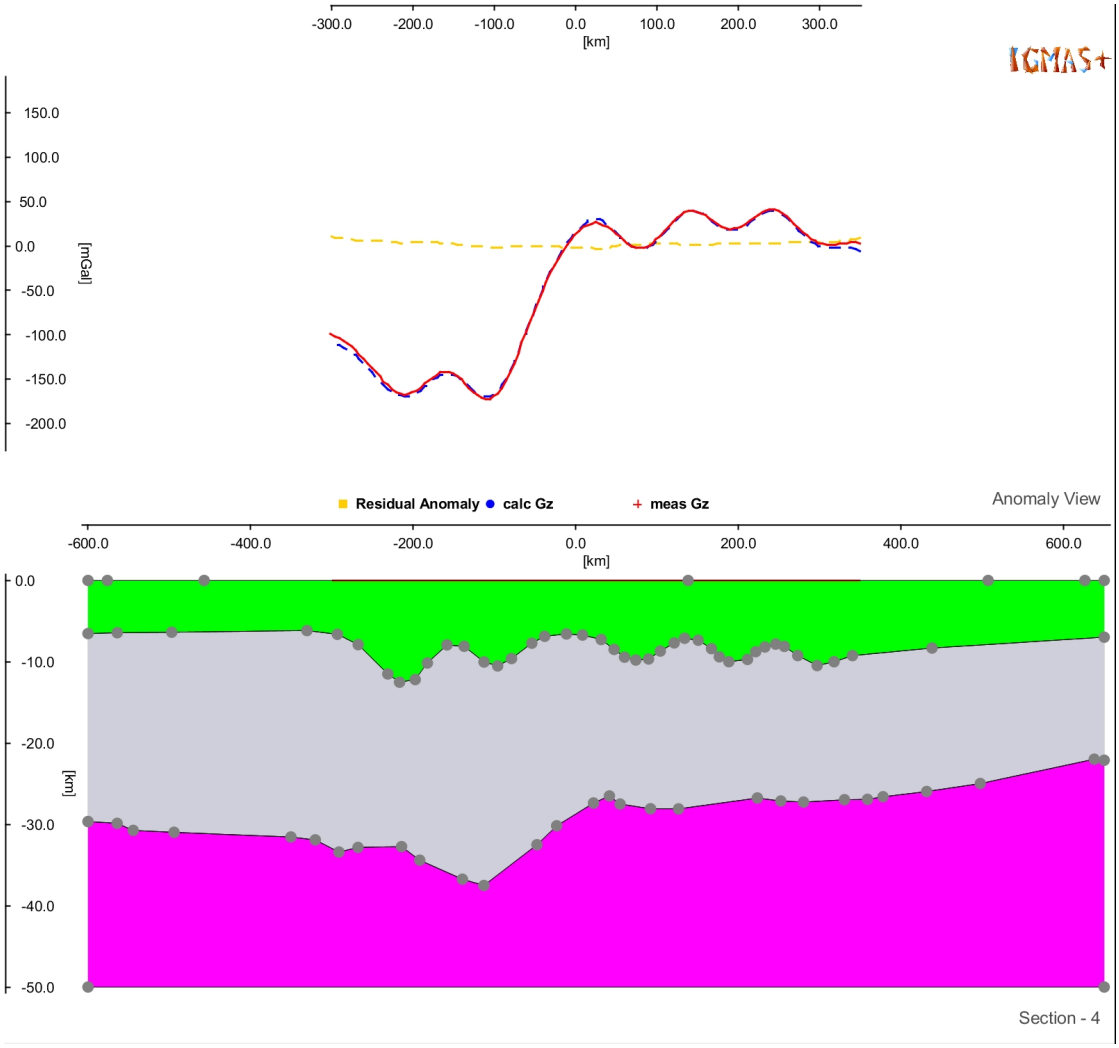

Figure C.4: Section 4 at −300 km northing.

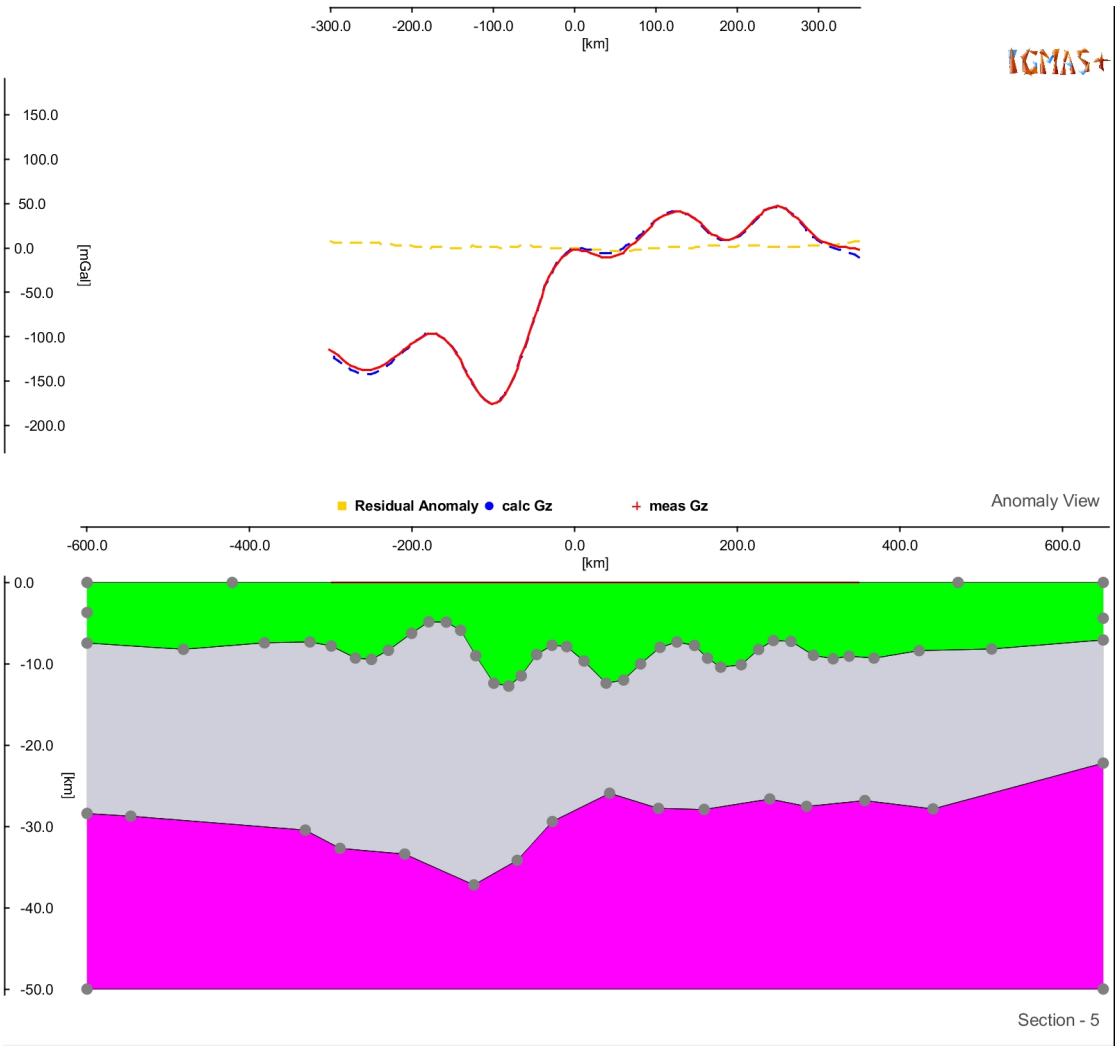

Figure C.5: Section 5 at −250 km northing.

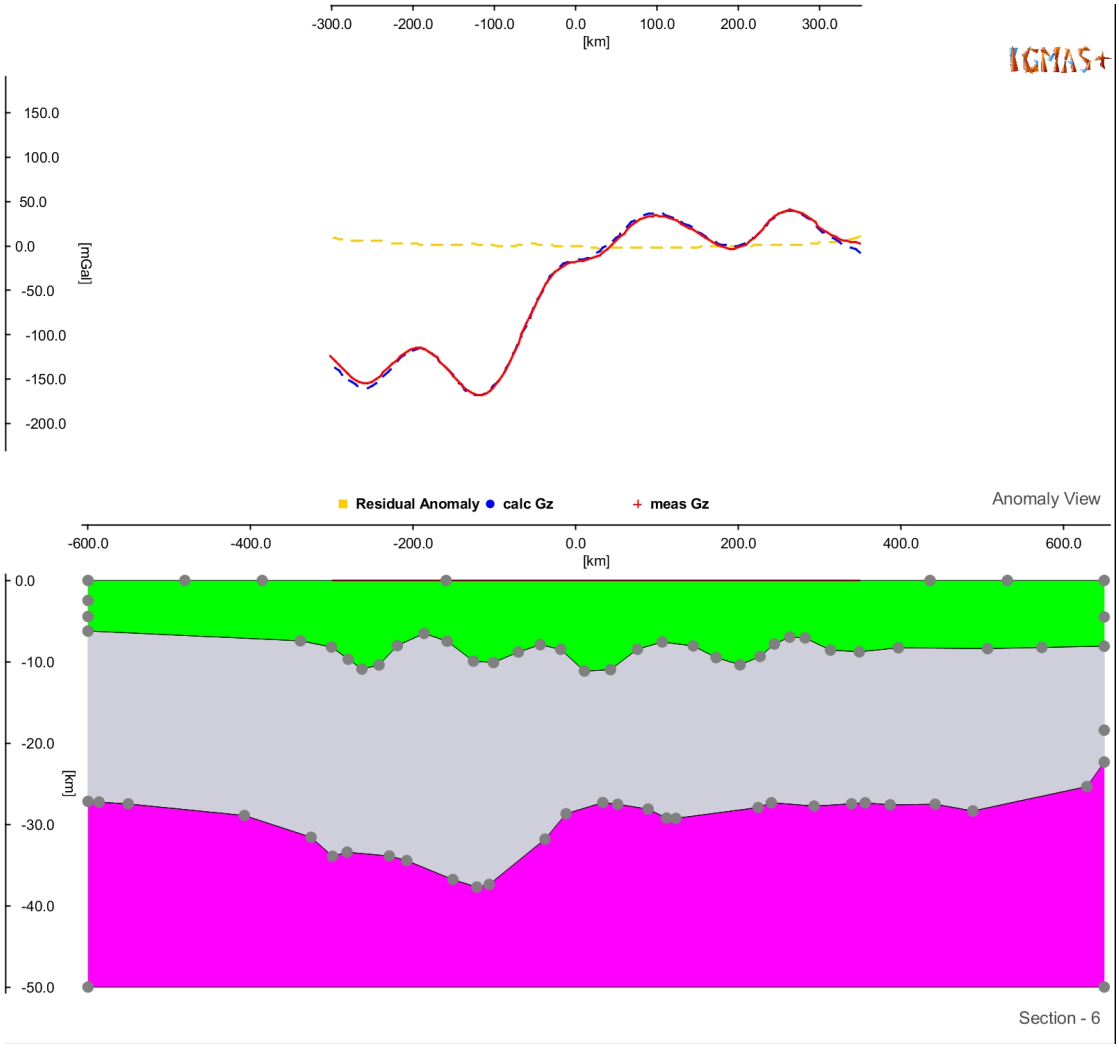

Figure C.6: Section 6 at −200 km northing.

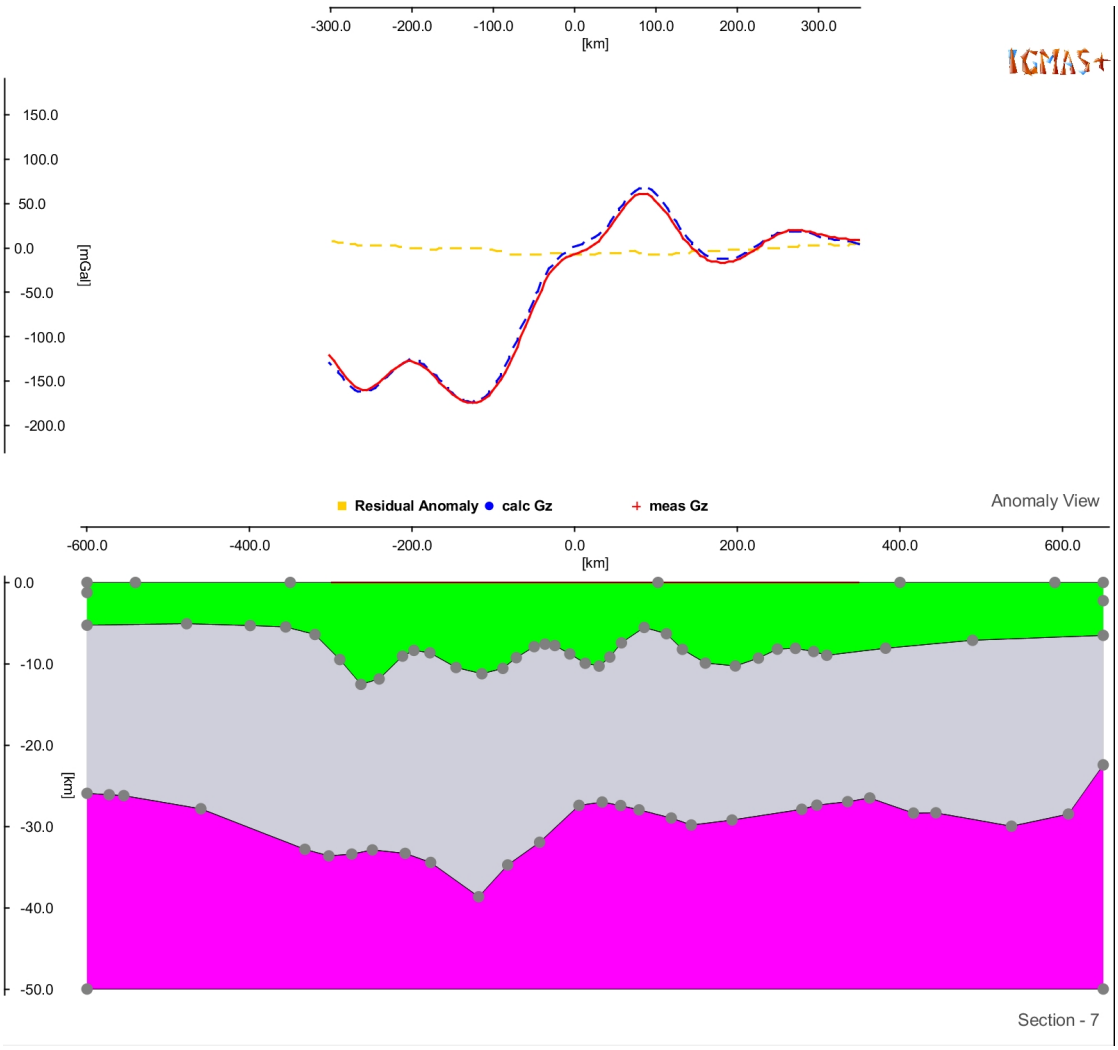

Figure C.7: Section 7 at −150 km northing.

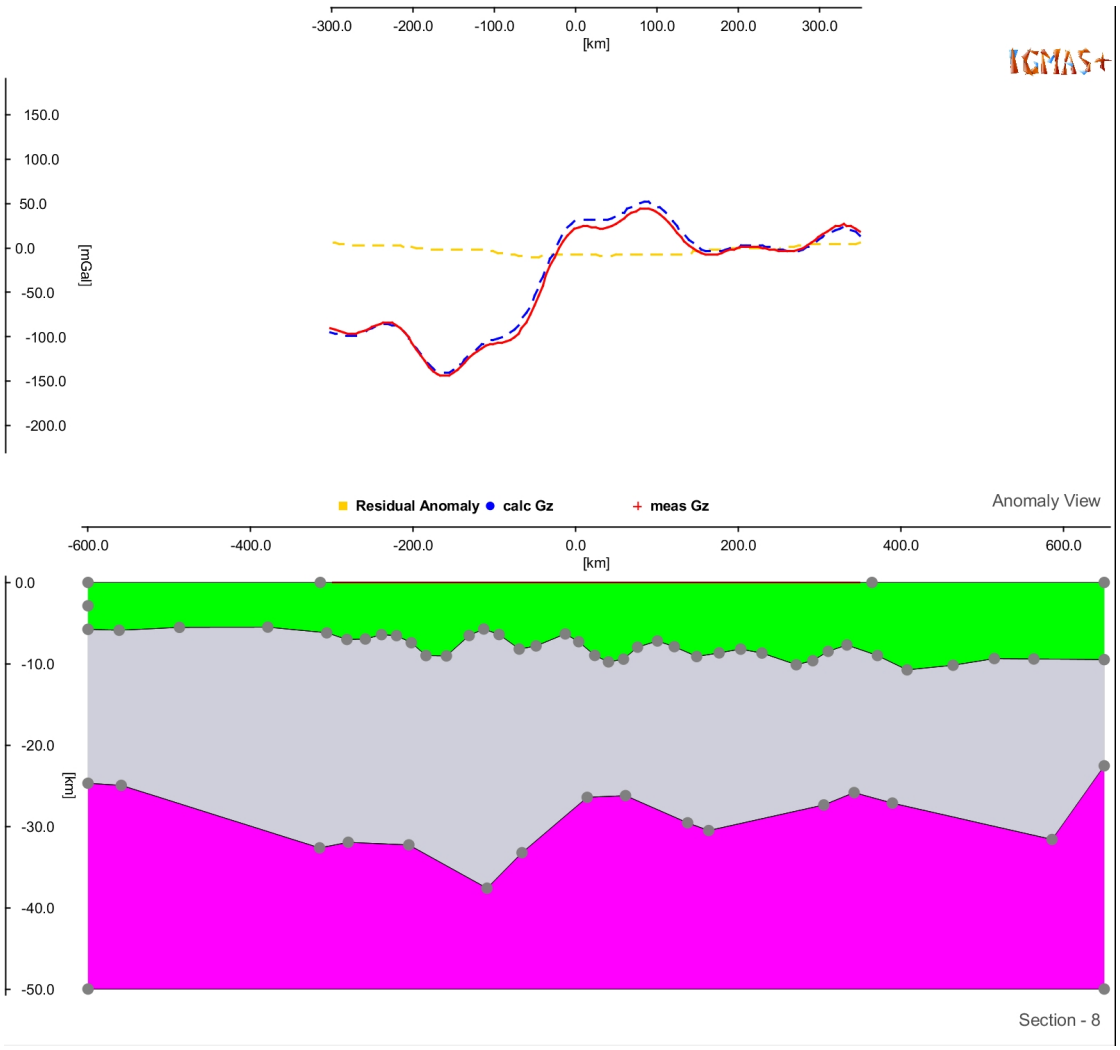

Figure C.8: Section 8 at −100 km northing.

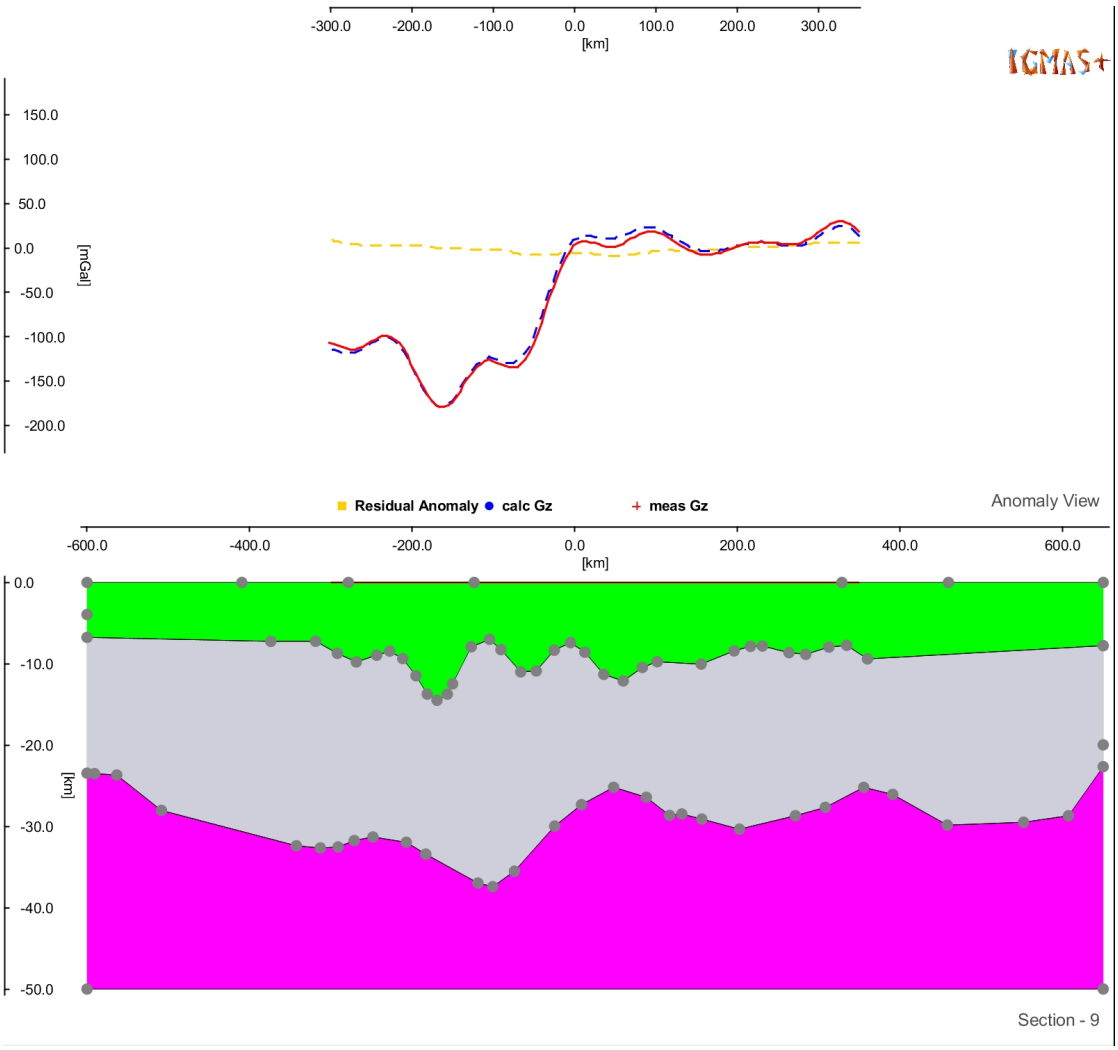

Figure C.9: Section 9 at −50 km northing.

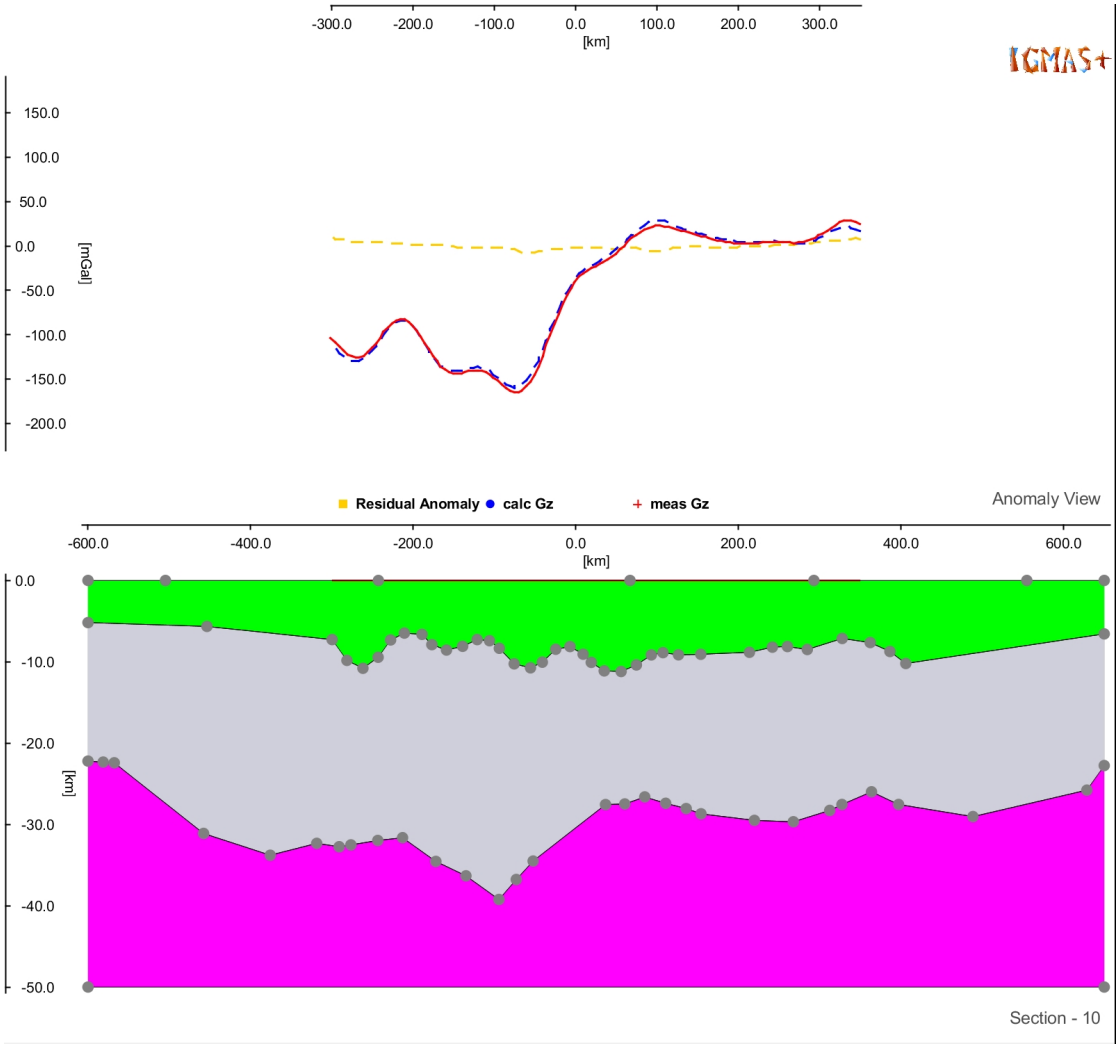

Figure C.10: Section 10 at 0 km northing.

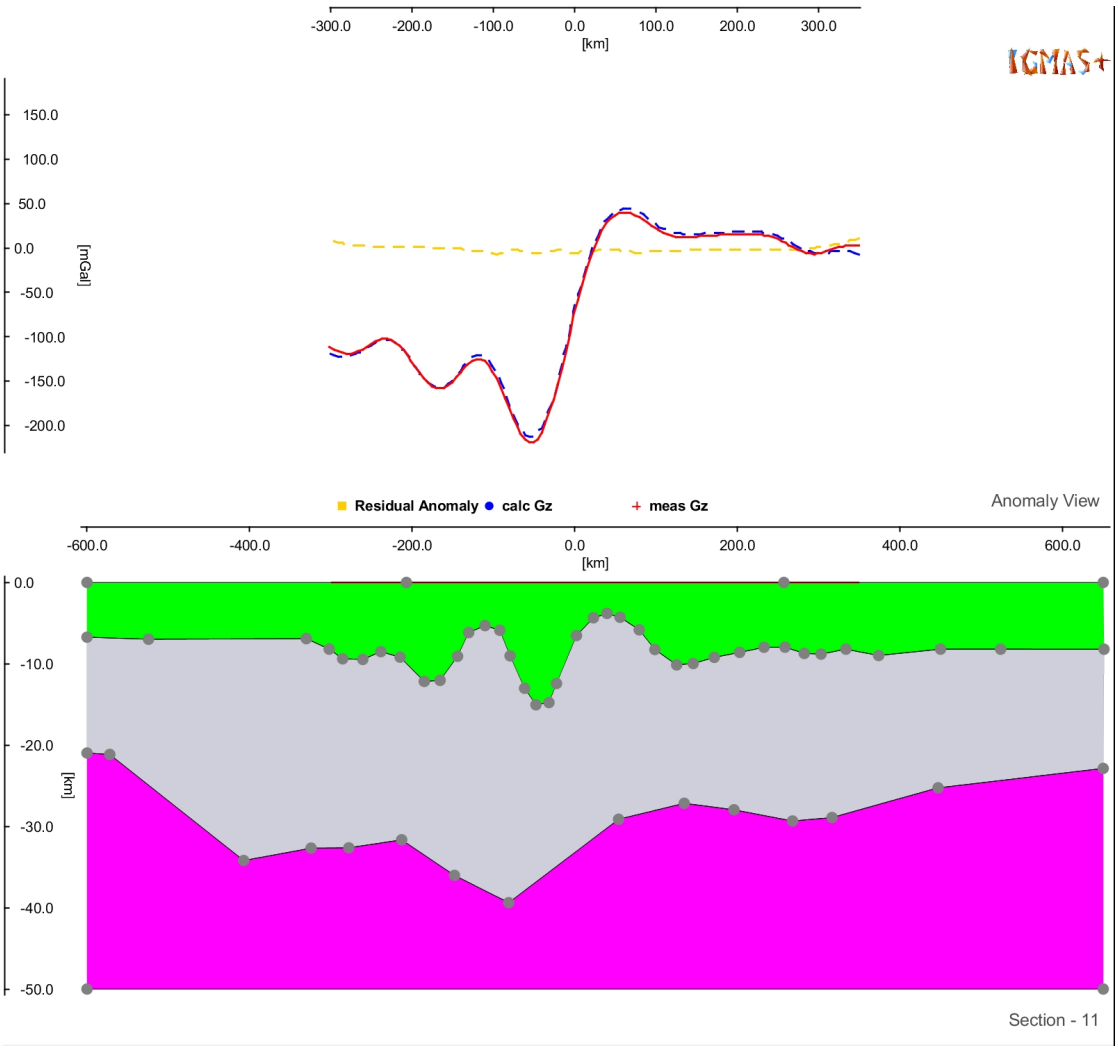

Figure C.11: Section 11 at 50 km northing.

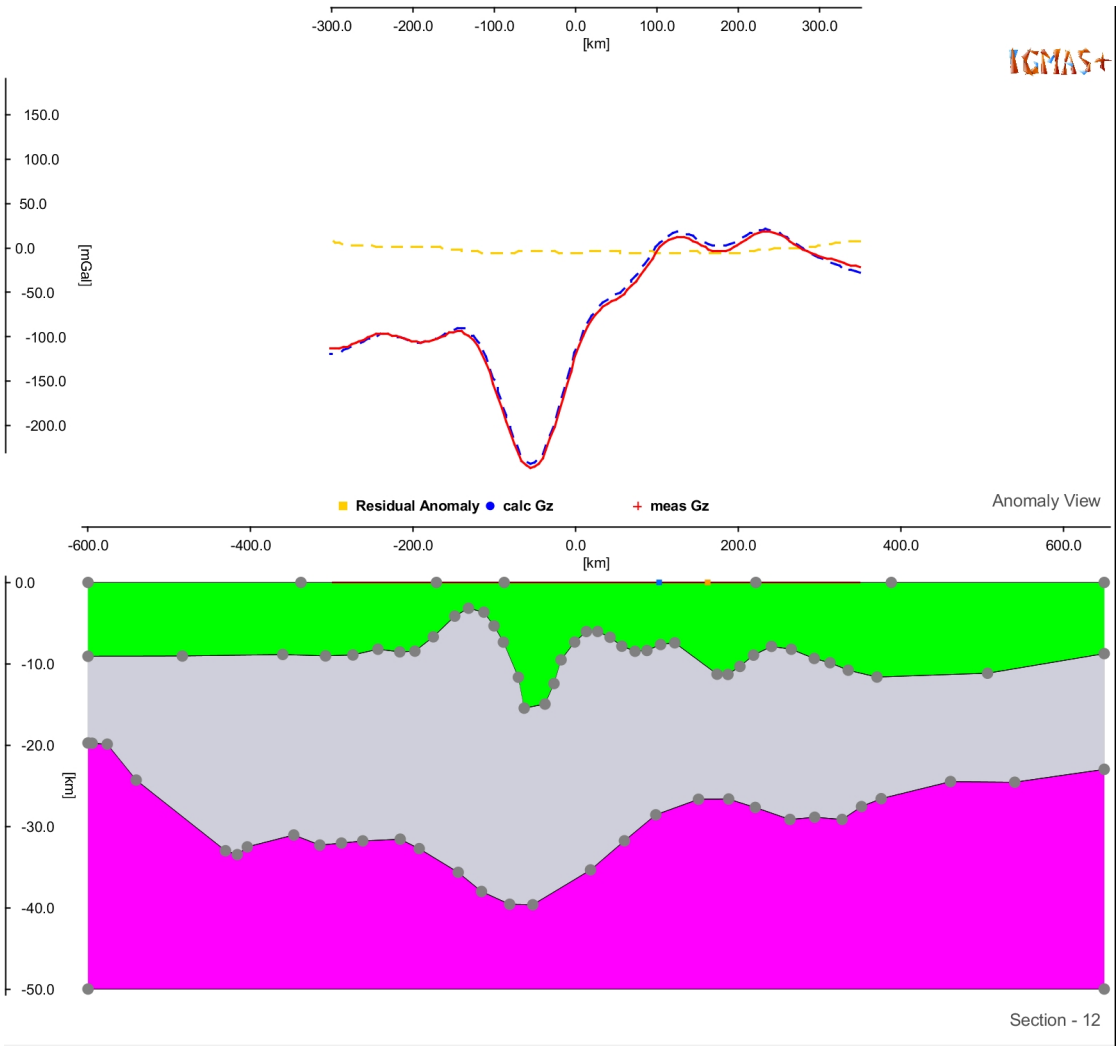

Figure C.12: Section 12 at 100 km northing.

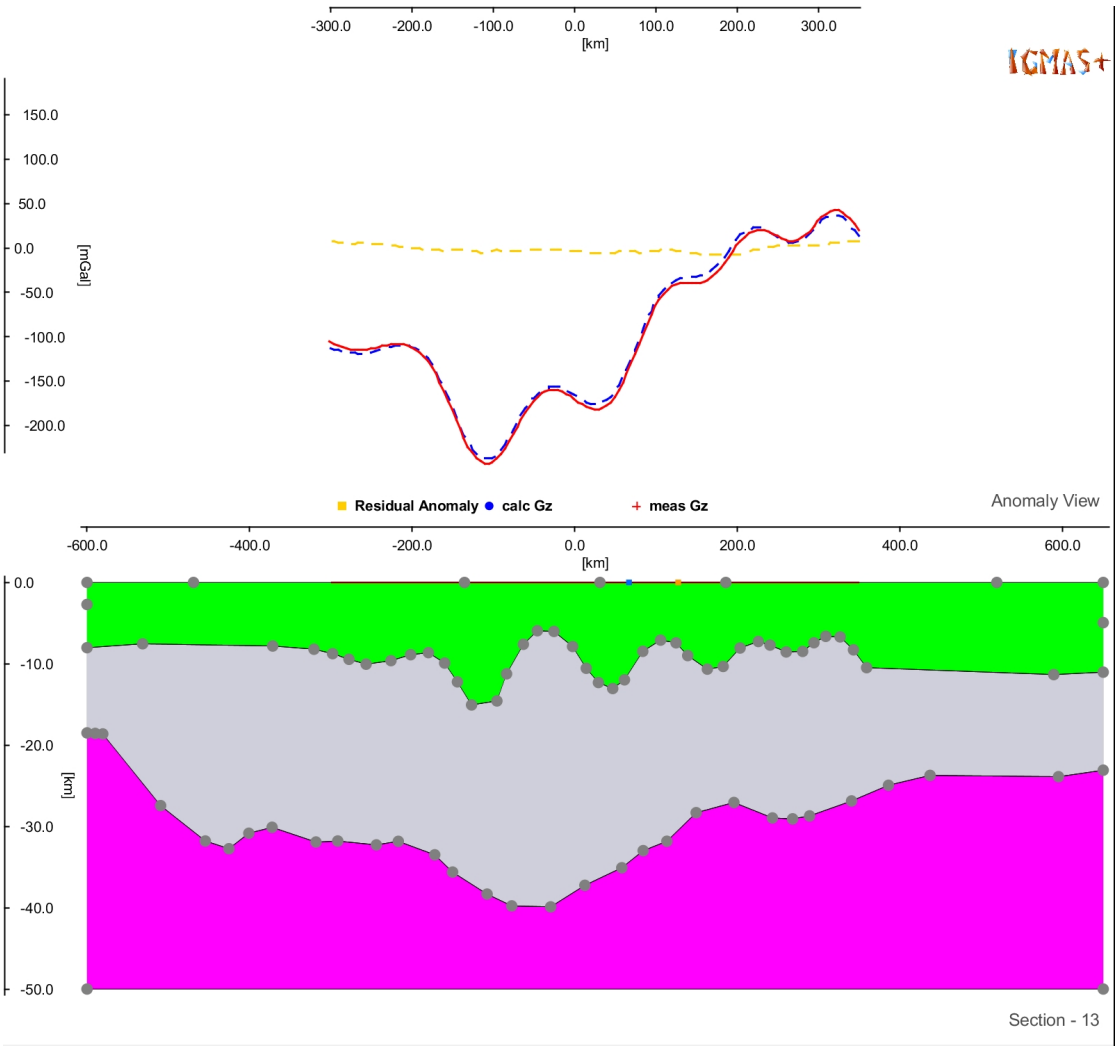

Figure C.13: Section 13 at 150 km northing.

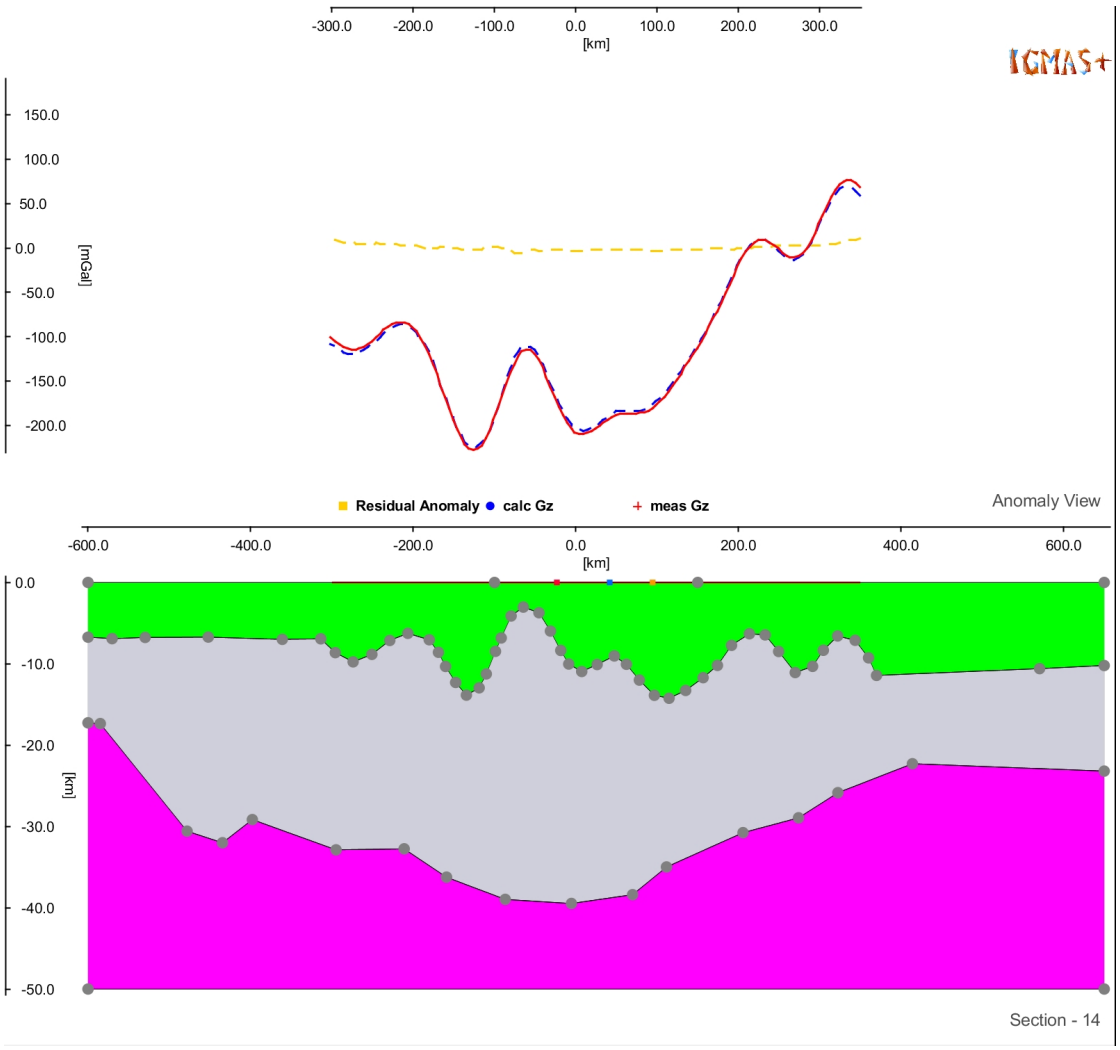

Figure C.14: Section 14 at 200 km northing.

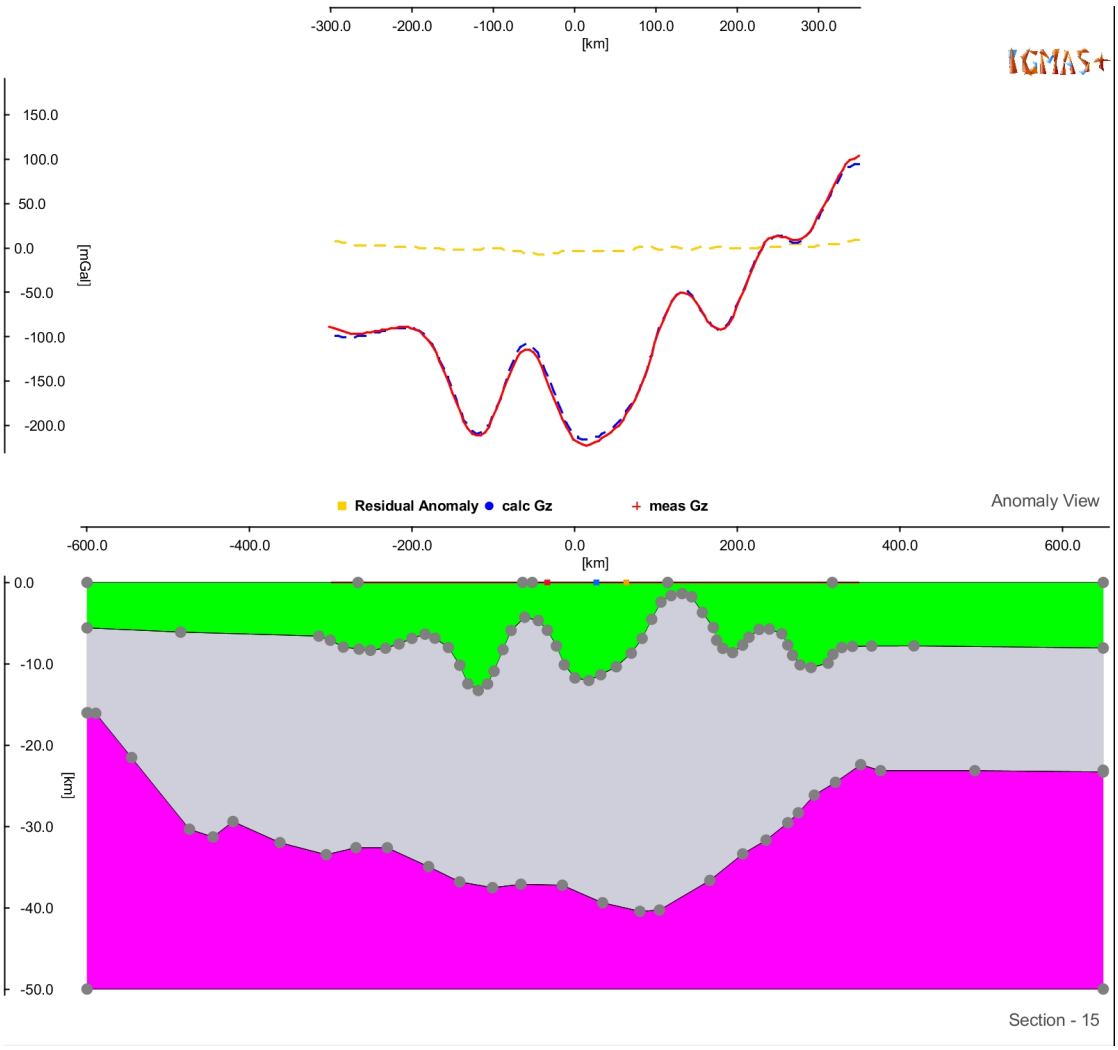

Figure C.15: Section 15 at 250 km northing.

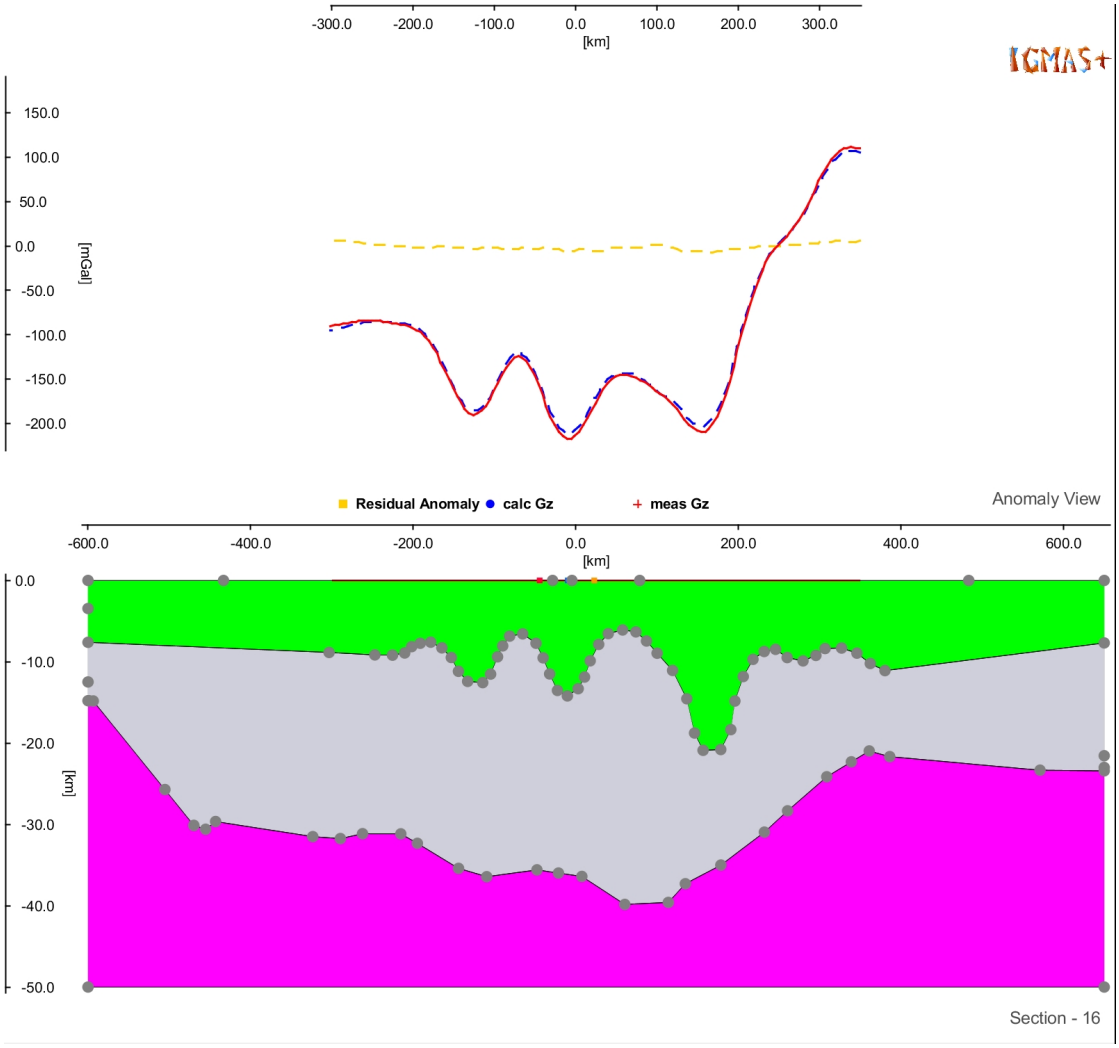

Figure C.16: Section 16 at 300 km northing.

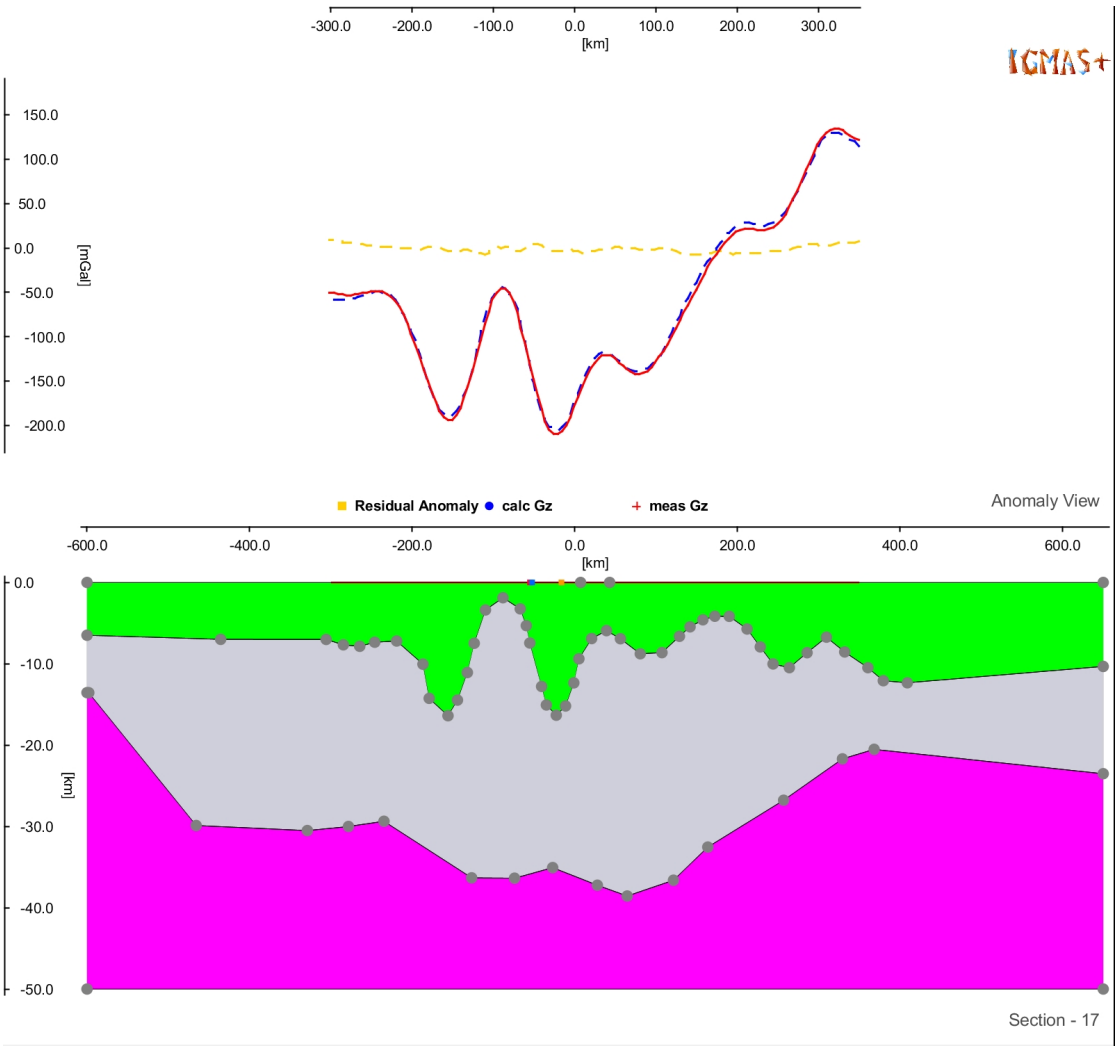

Figure C.17: Section 17 at 350 km northing.

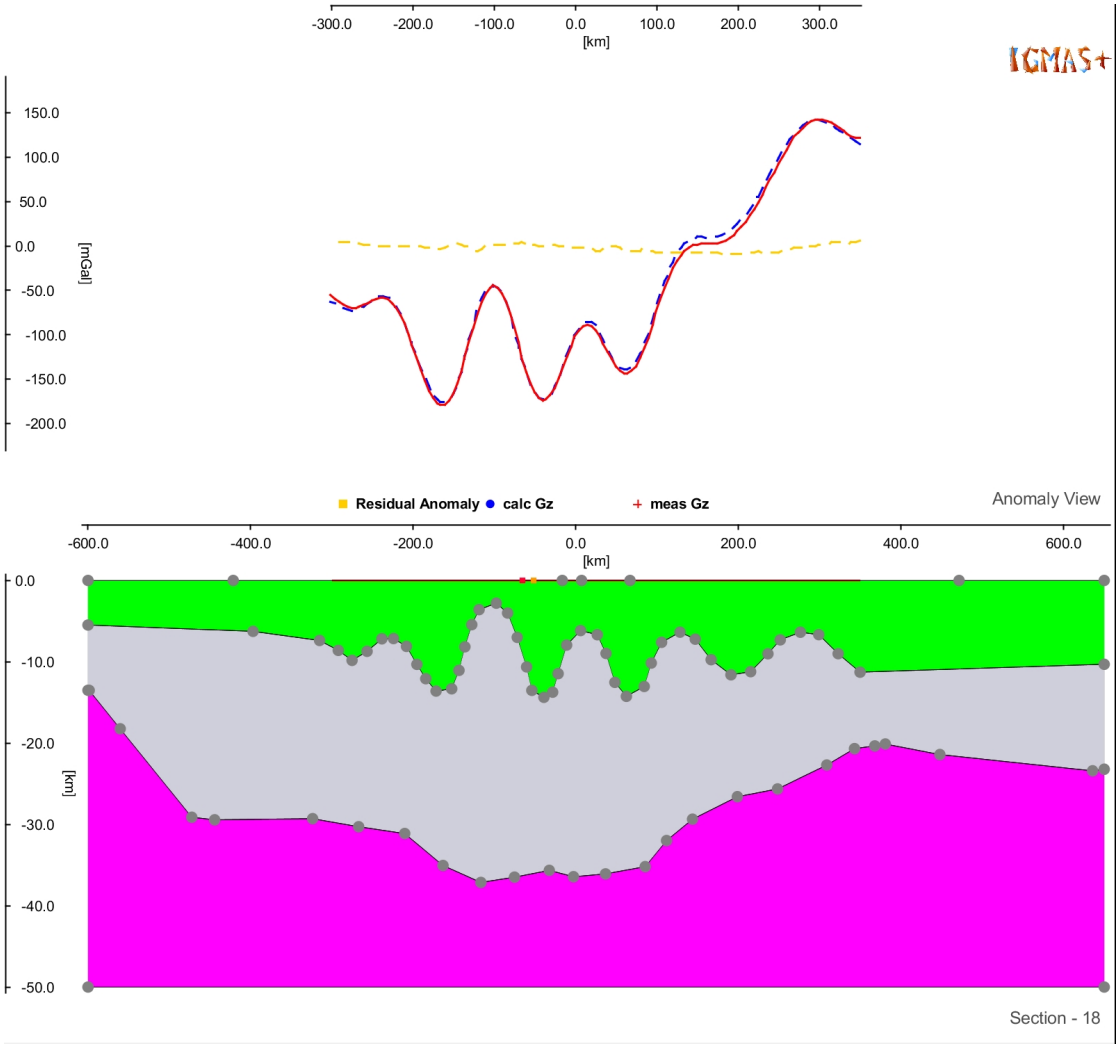

Figure C.18: Section 18 at 400 km northing.

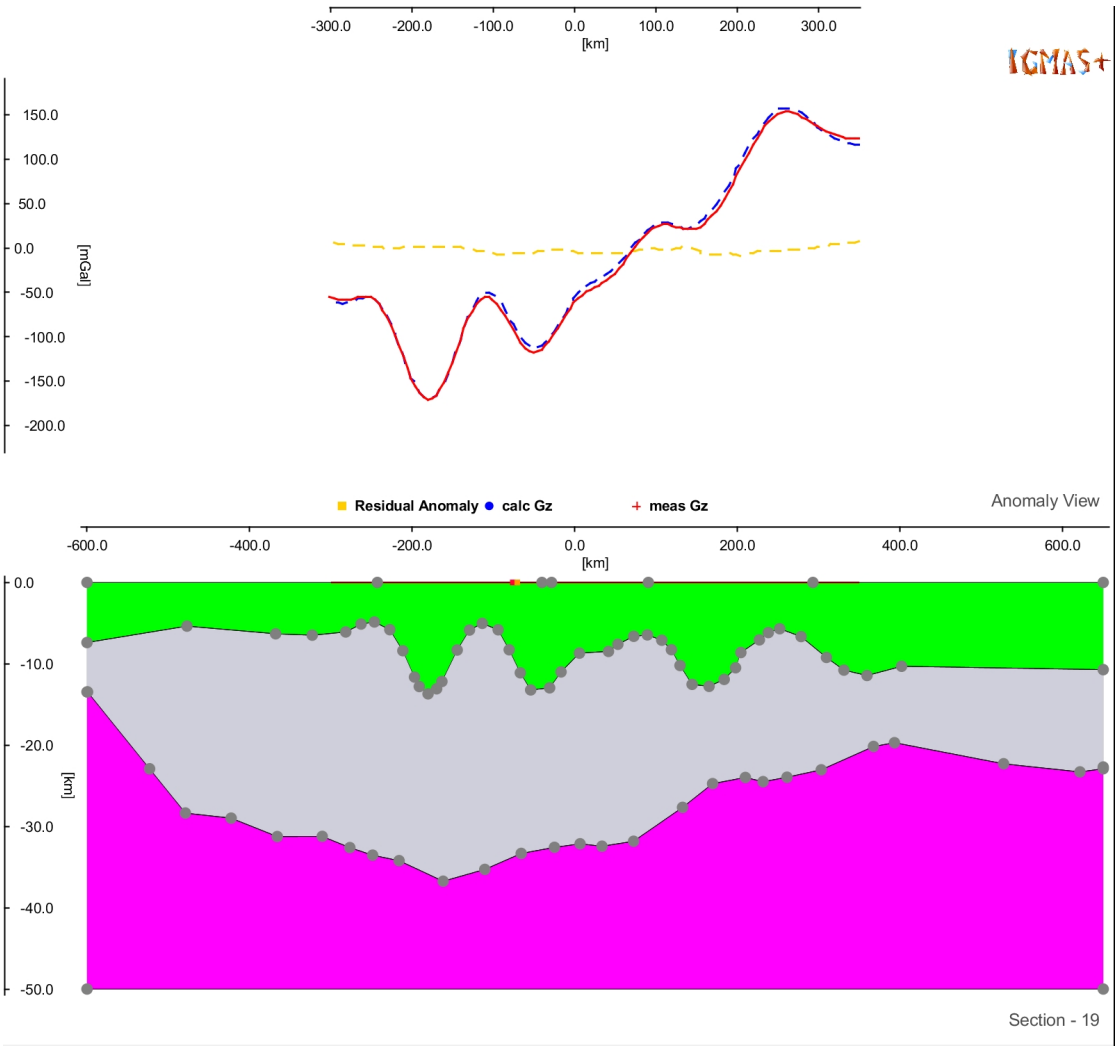

Figure C.19: Section 19 at 450 km northing.

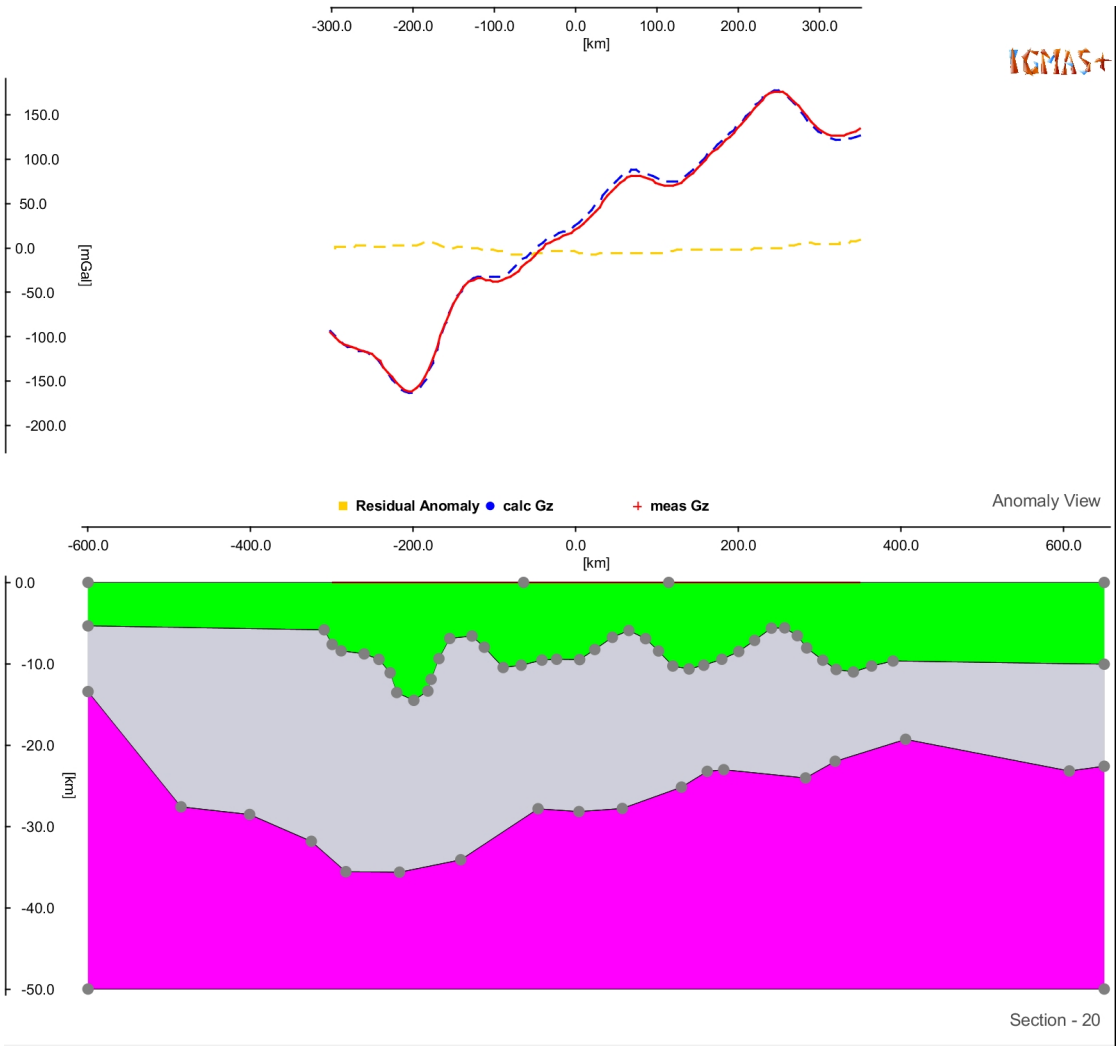

Figure C.20: Section 20 at 500 km northing.

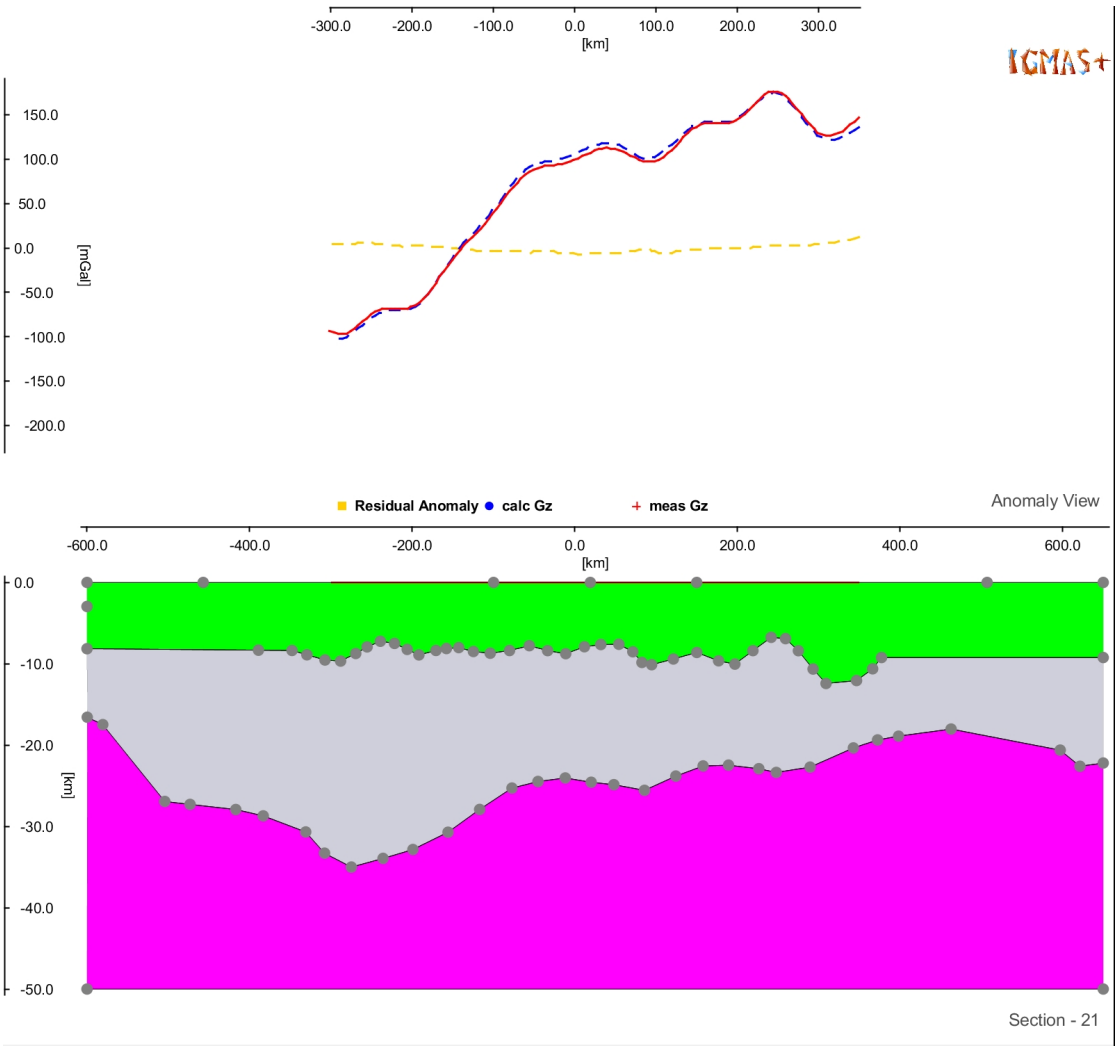

Figure C.21: Section 21 at 550 km northing.

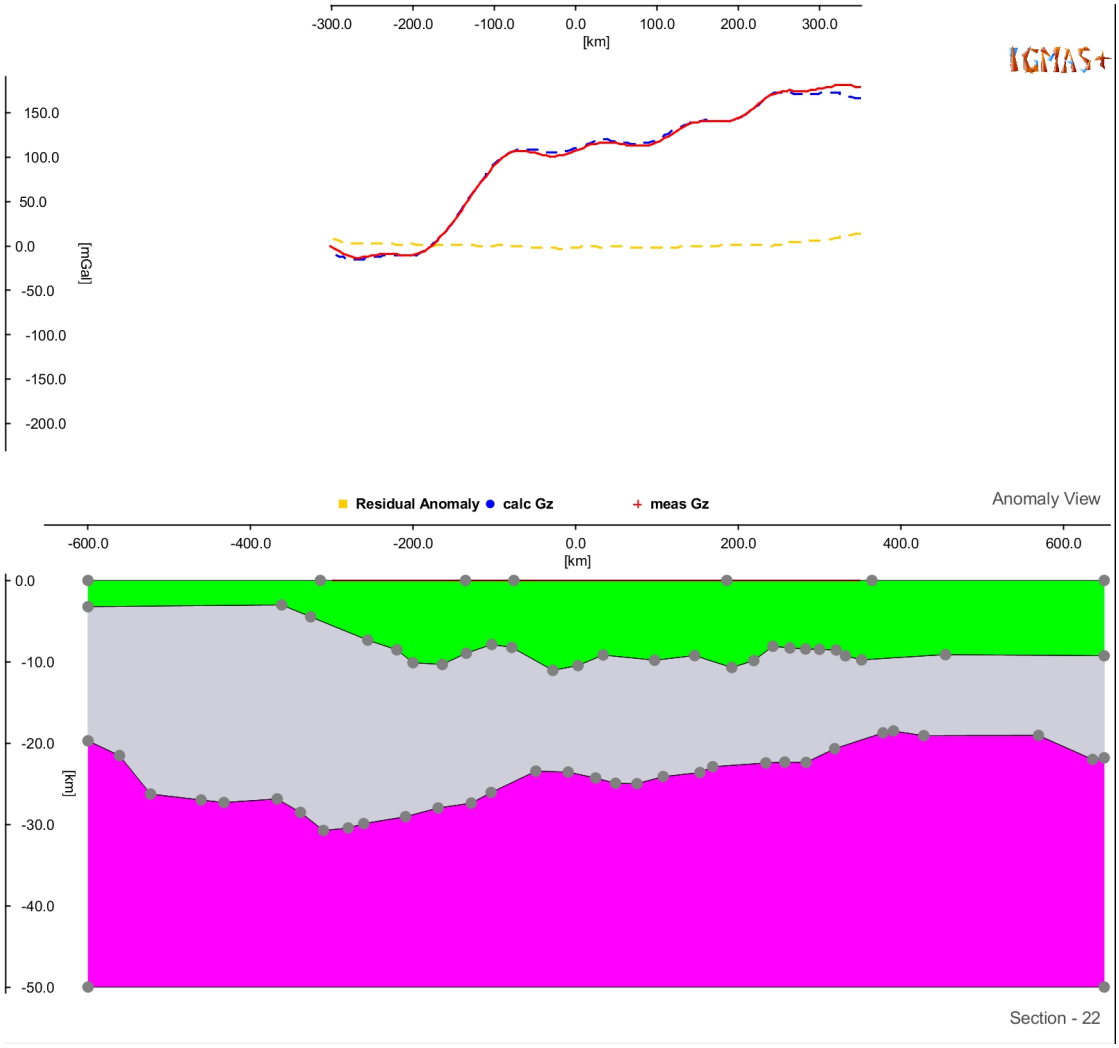

Figure C.22: Section 22 at 600 km northing.

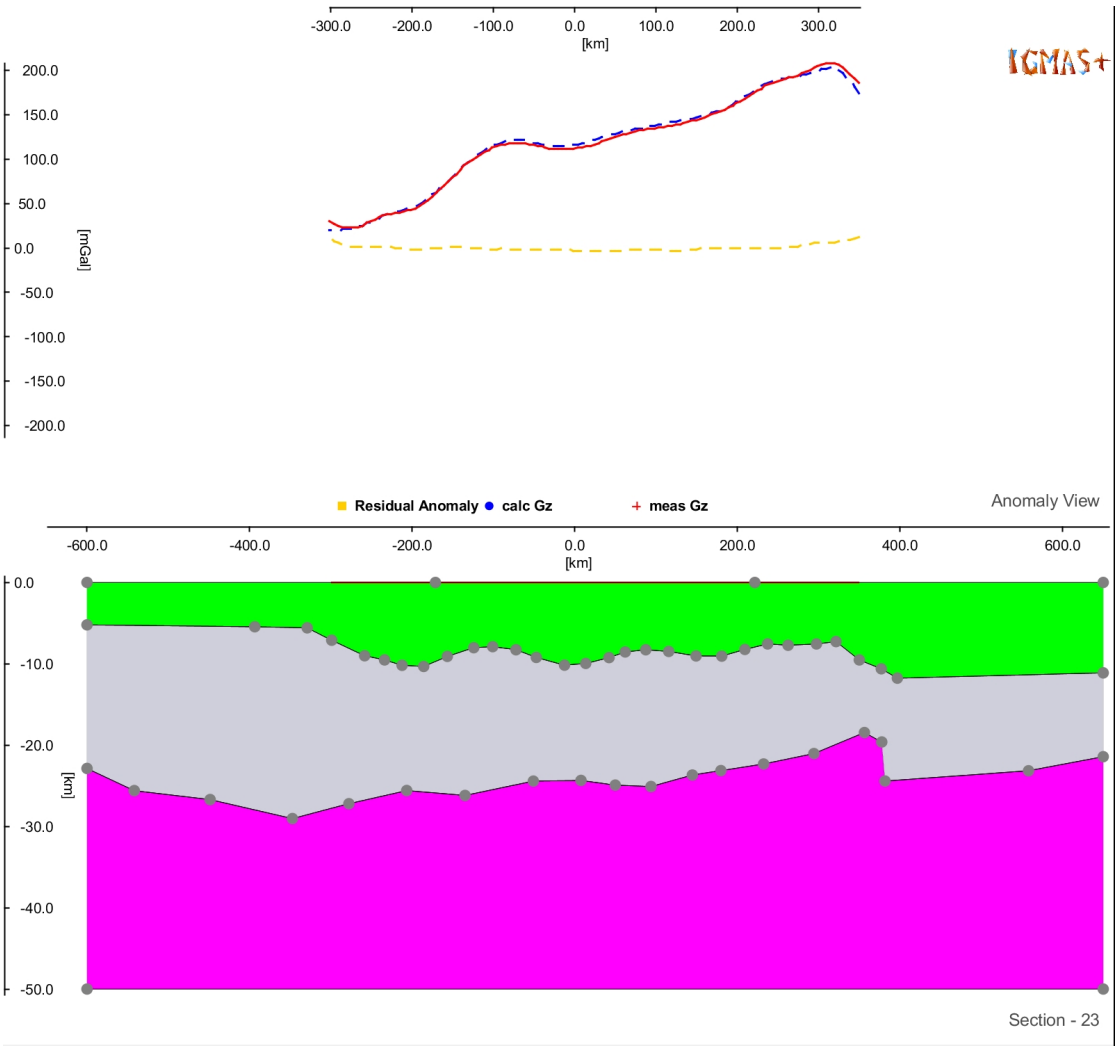

Figure C.23: Section 23 at 650 km northing.

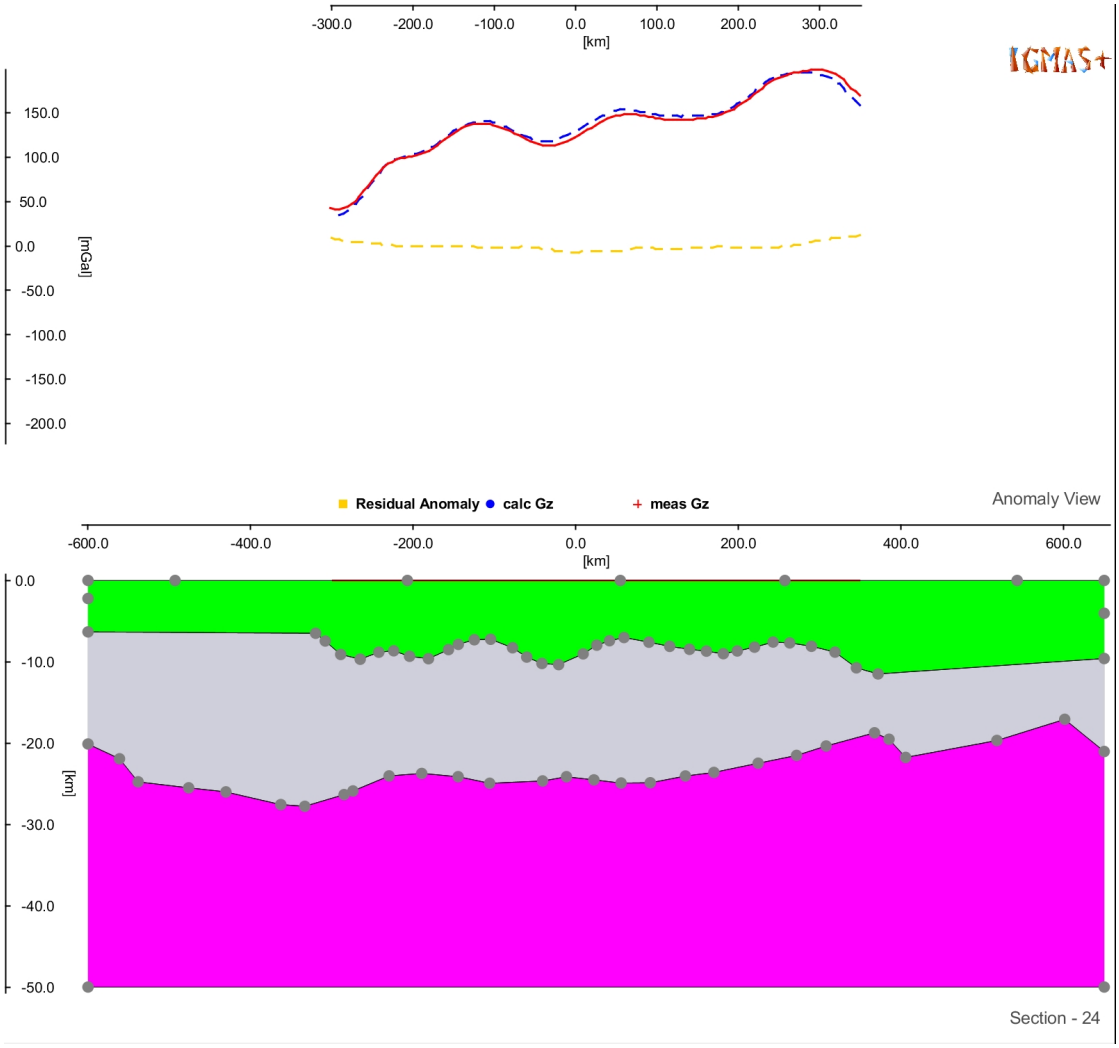

Figure C.24: Section 24 at 700 km northing.

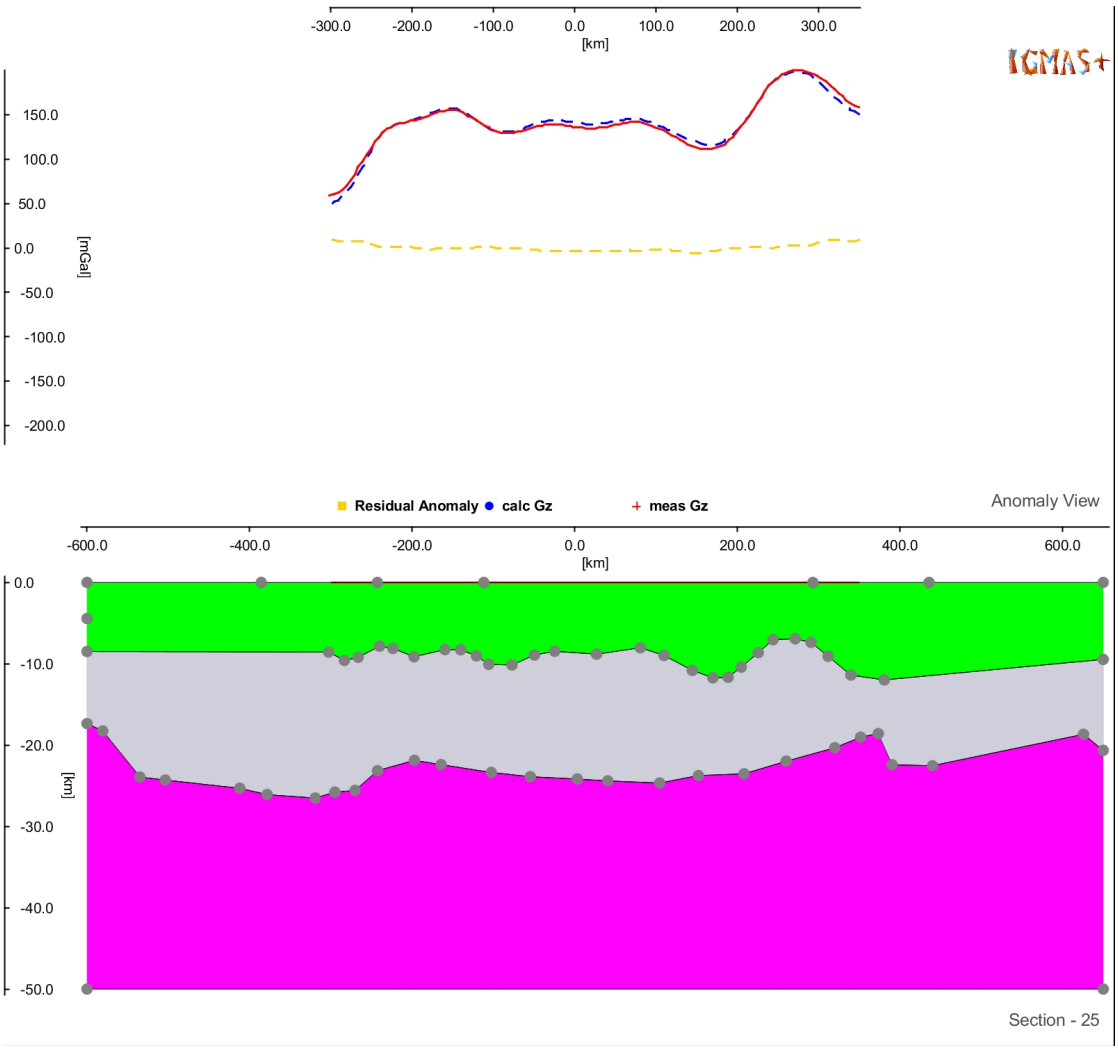

Figure C.25: Section 25 at 750 km northing.

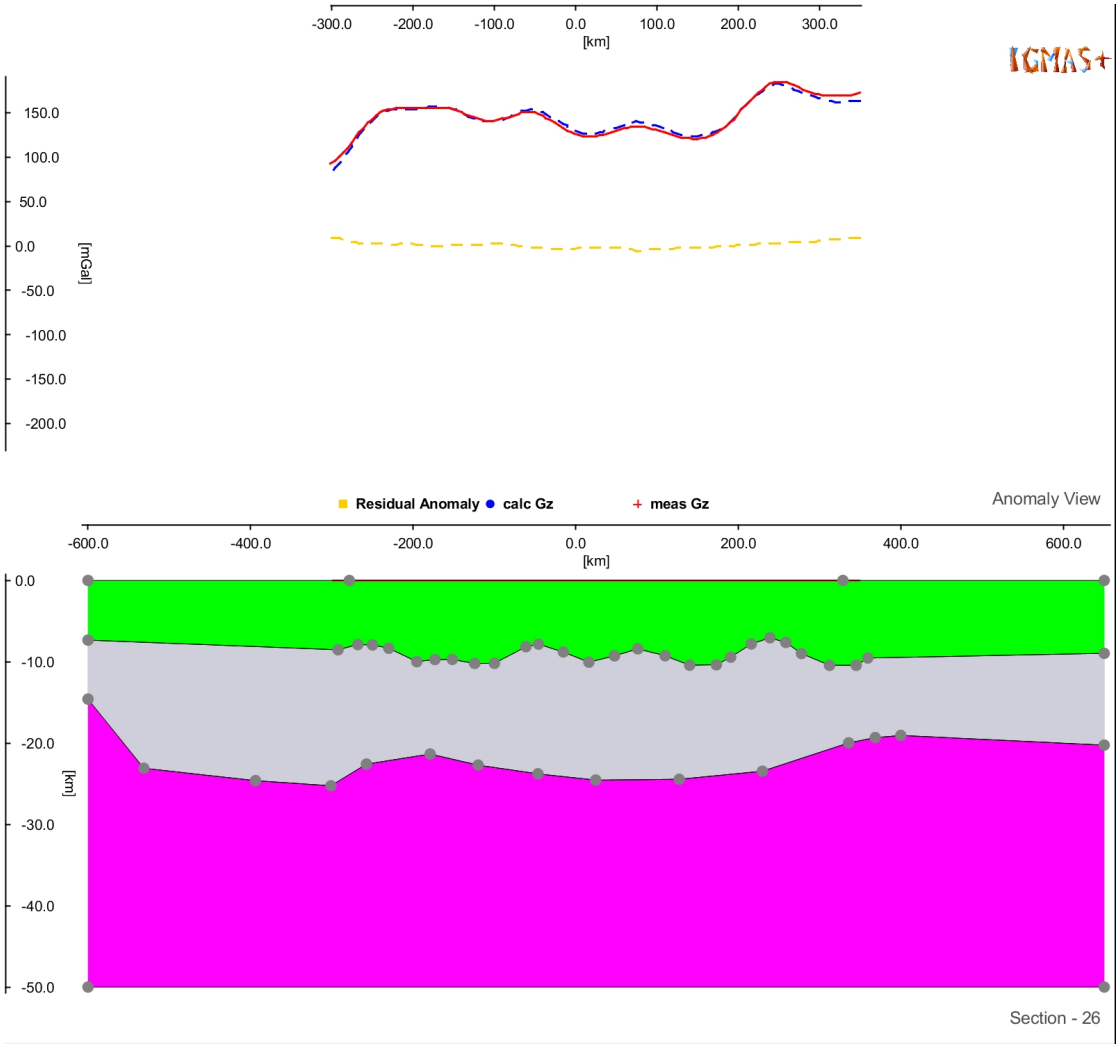

Figure C.26: Section 26 at 800 km northing.

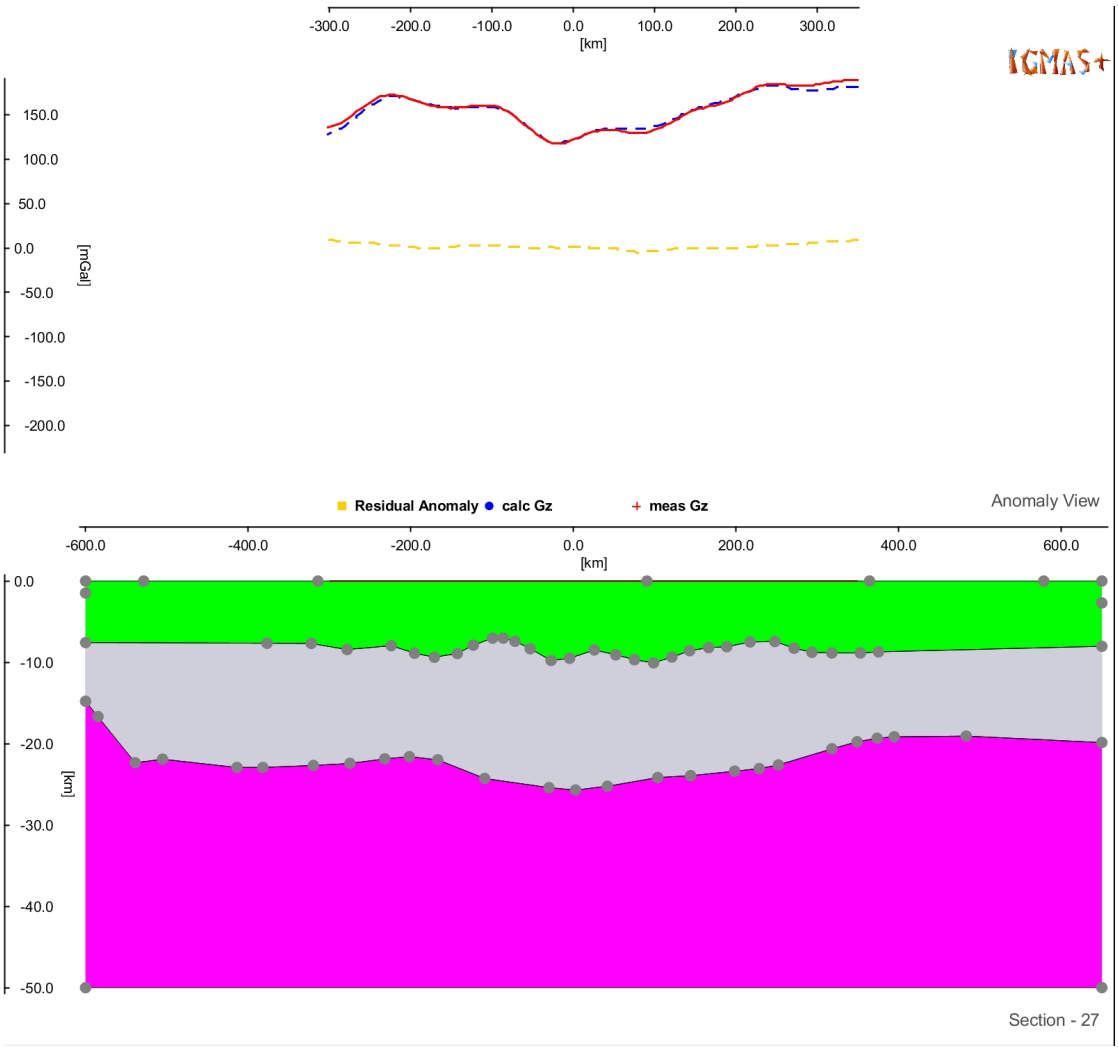

Figure C.27: Section 27 at 850 km northing.

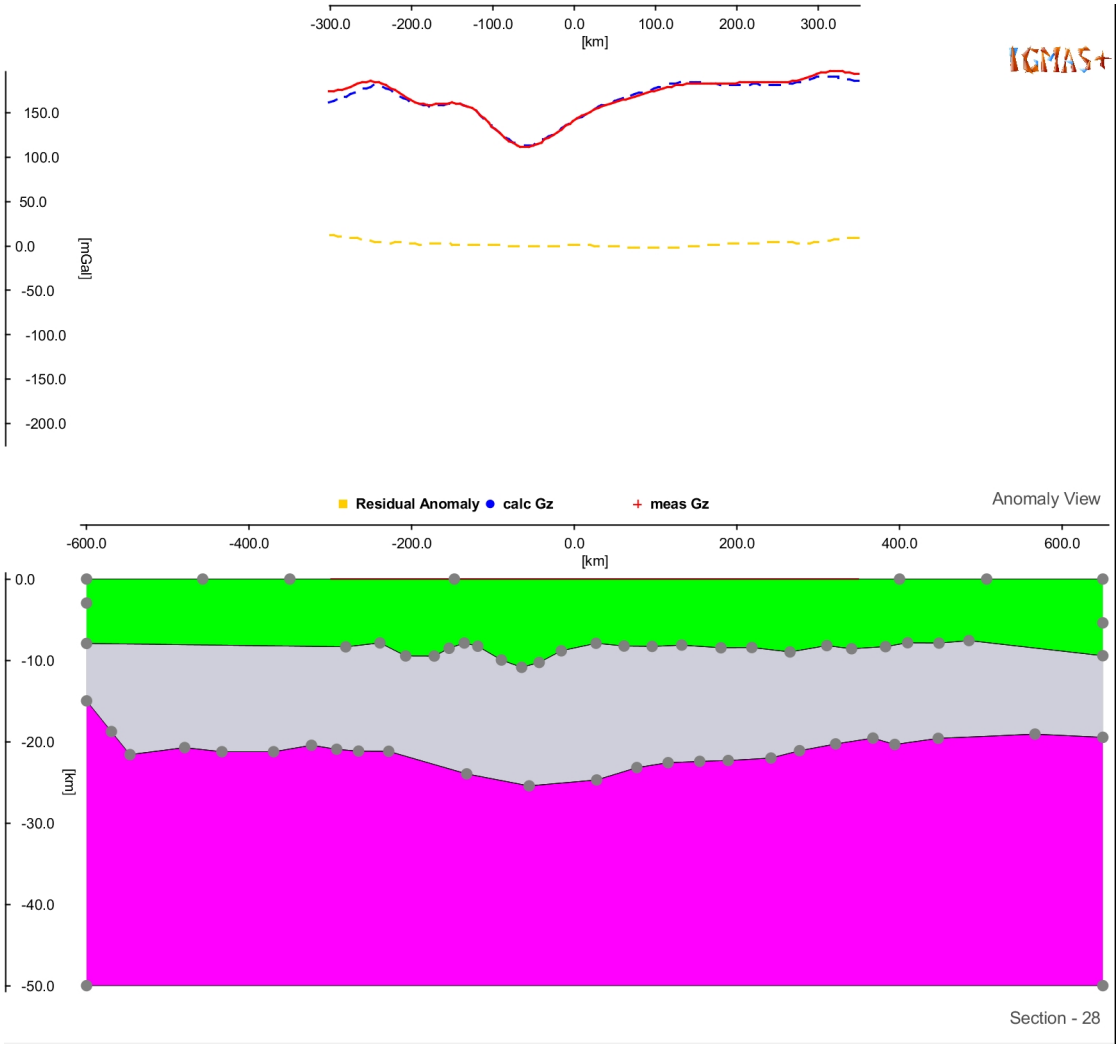

Figure C.28: Section 28 at 900 km northing.

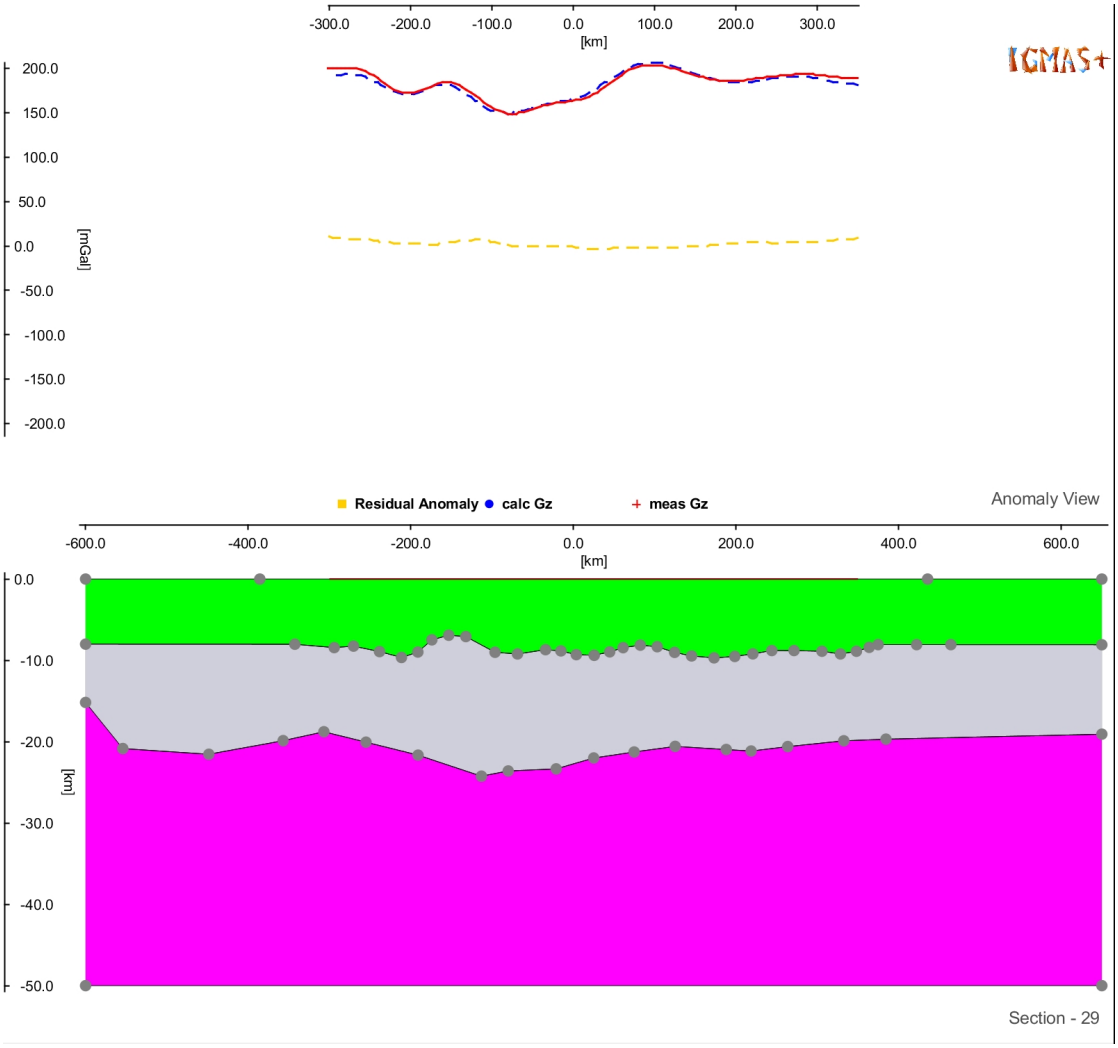

Figure C.29: Section 29 at 950 km northing.

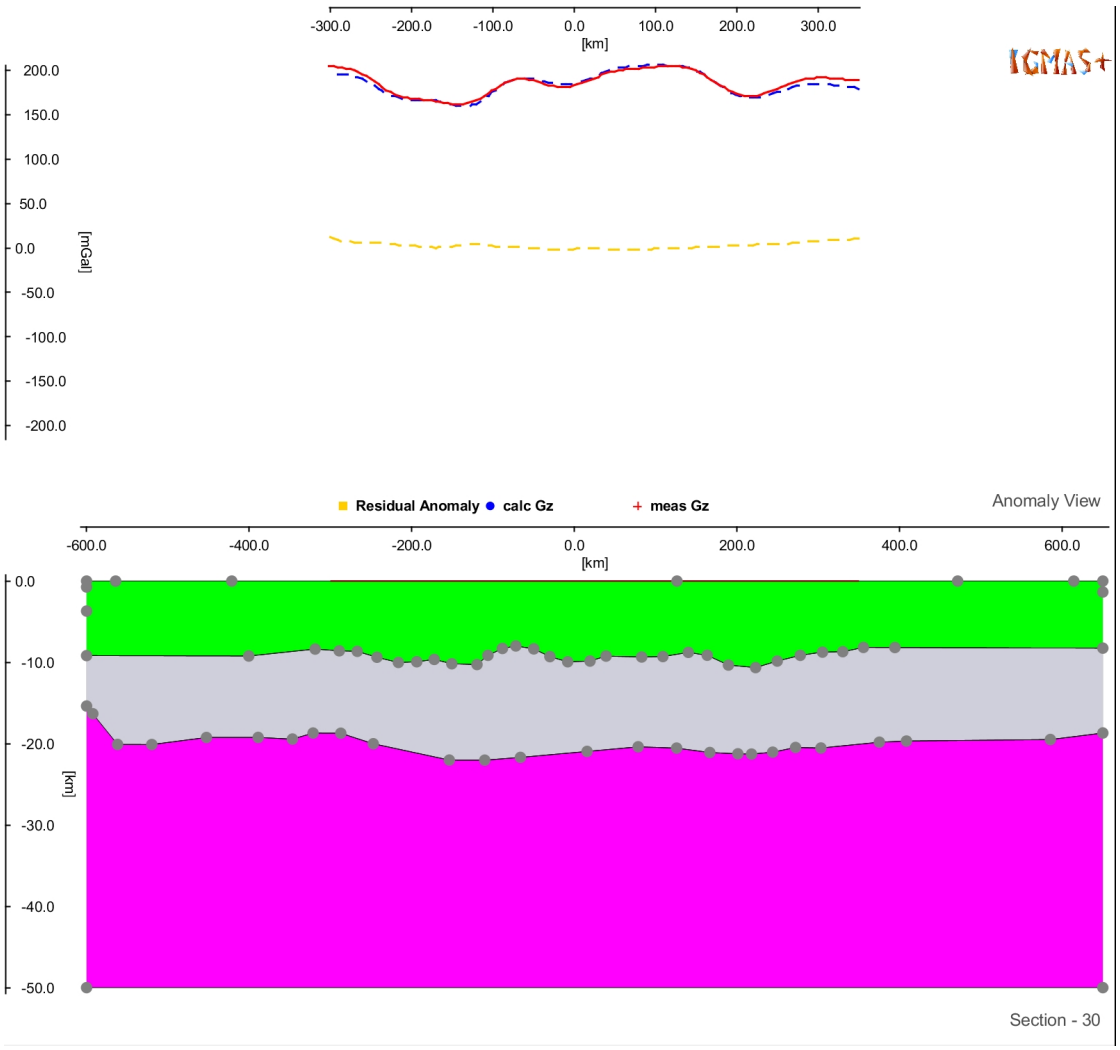

Figure C.30: Section 30 at 1.000 km northing.

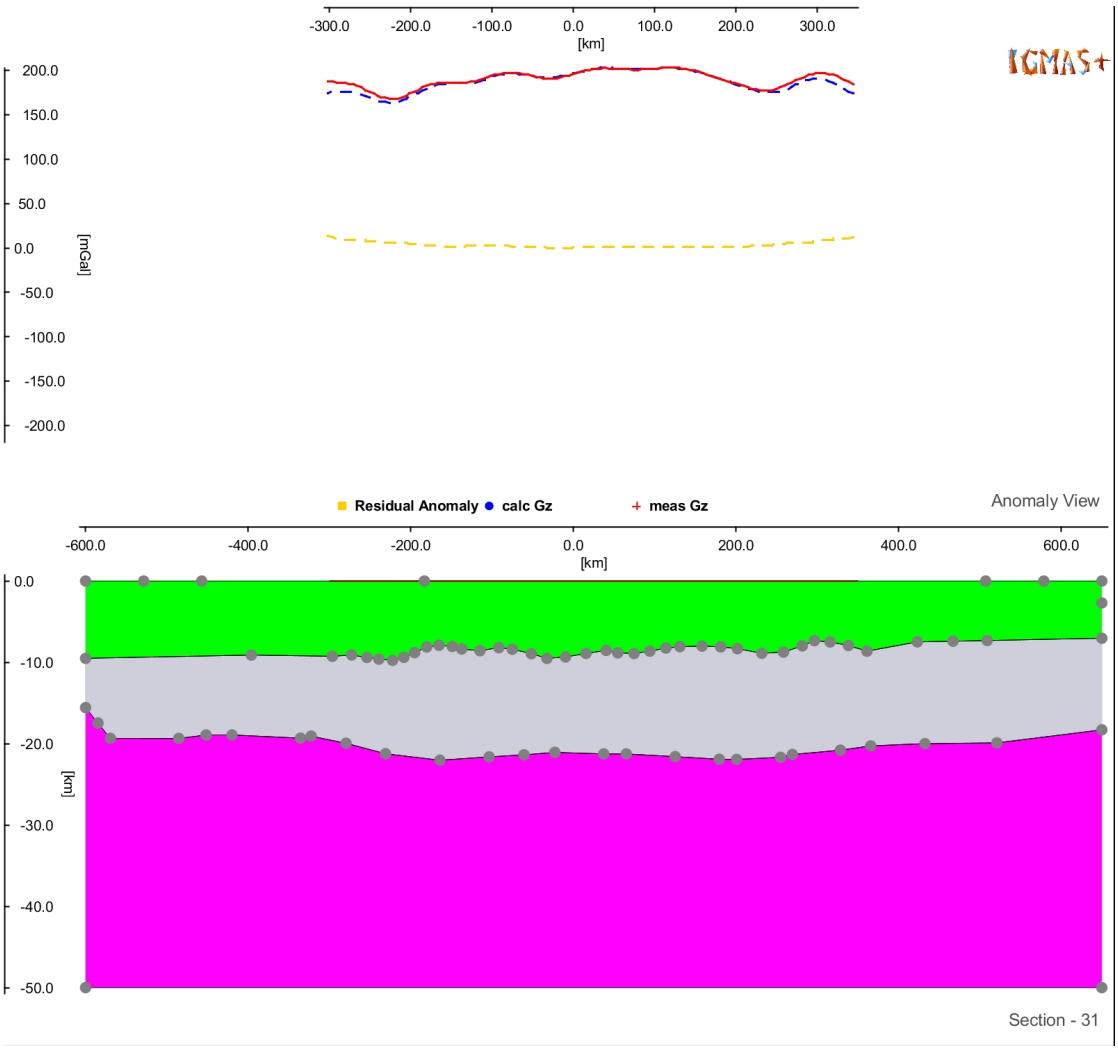

Figure C.31: Section 31 at 1.050 km northing.

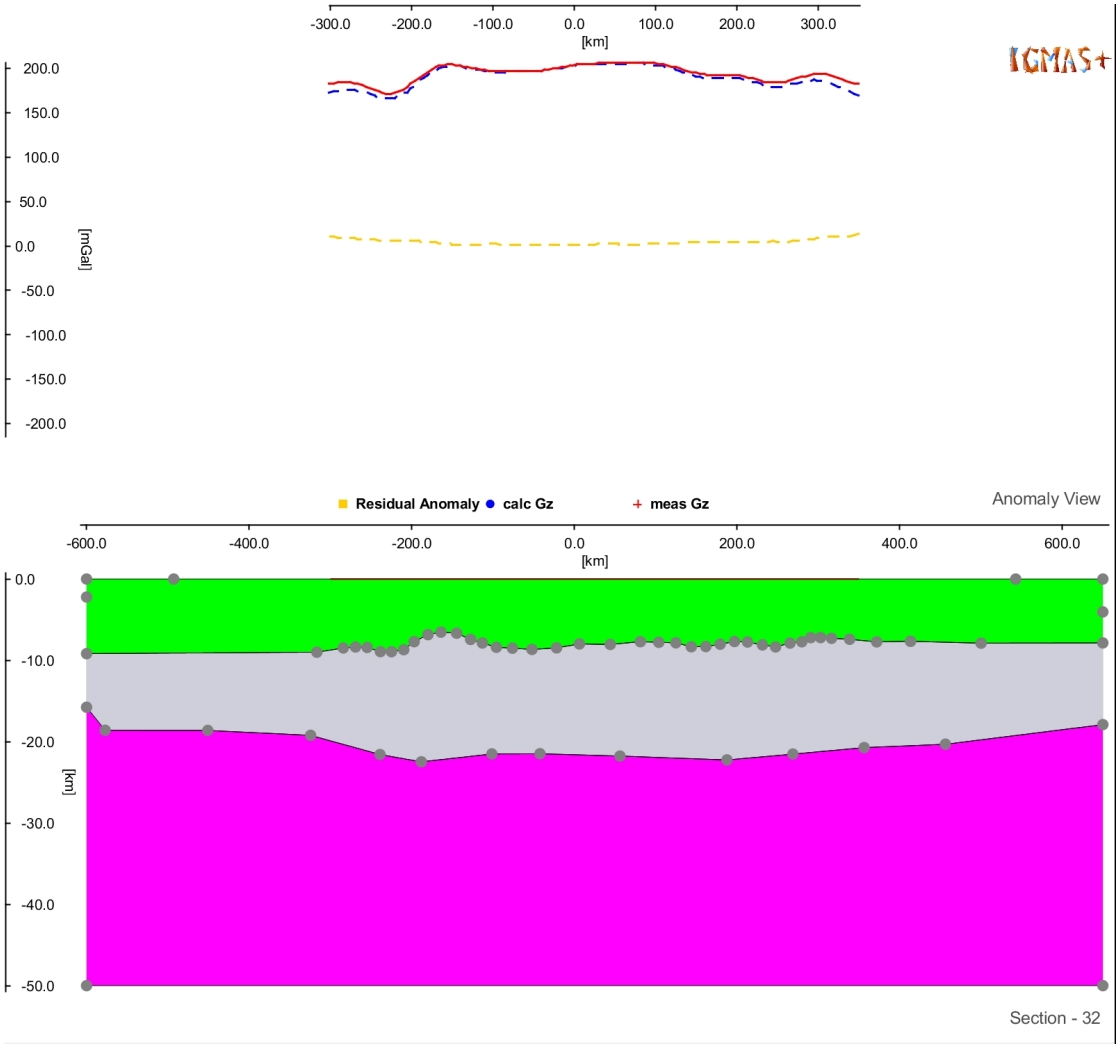

Figure C.32: Section 32 at 1.100 km northing.

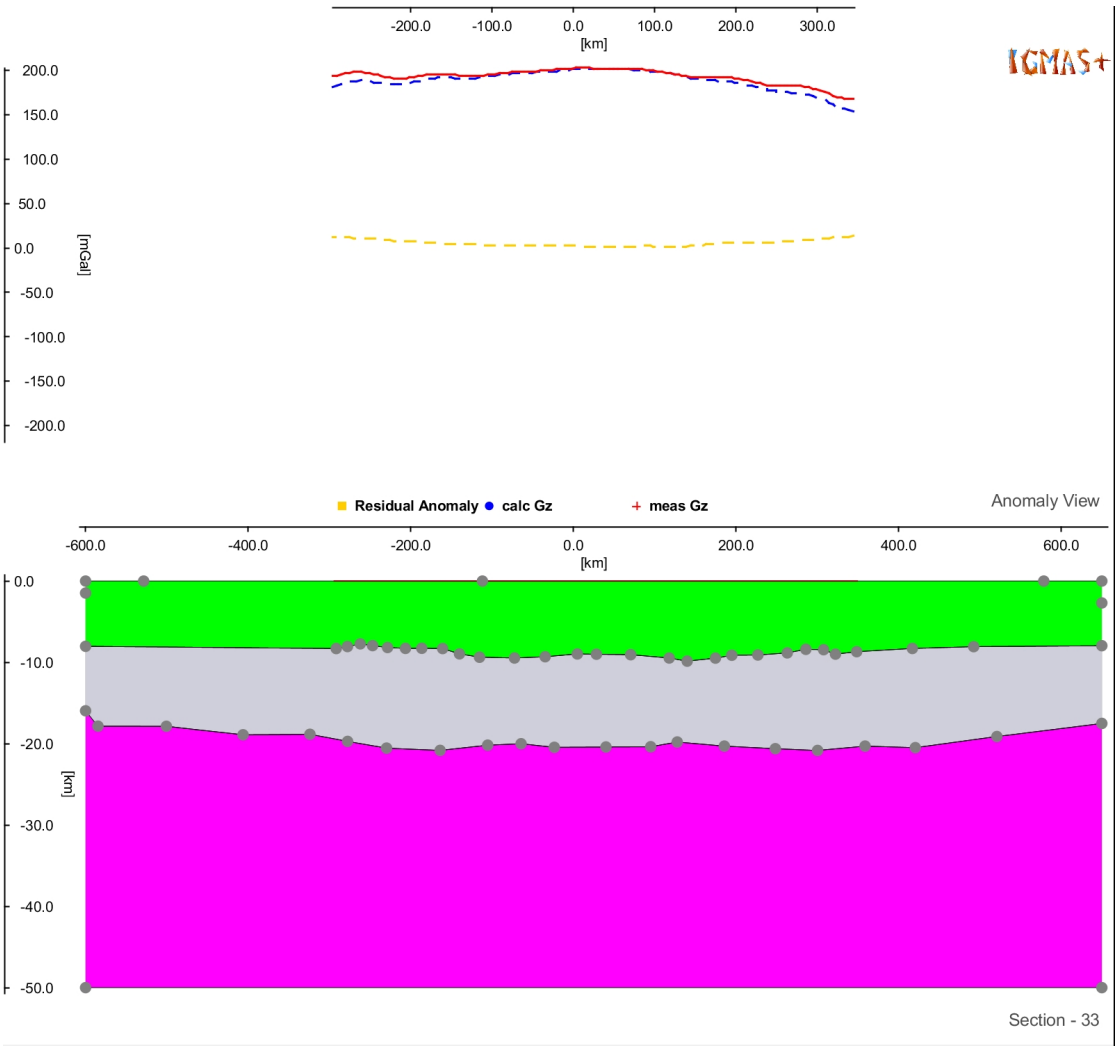

Figure C.33: Section 33 at 1.150 km northing.

Appendix D

Magnetic field model

This chapter summarizes the 26 sections of the *IGMAS+* model which was developed based on part of the combined aeromagnetic anomaly data. The sections are sorted from south to north and represented in Fig. D.1 to Fig. D.26. For better comparison between the figures, the anomaly axis is the same for all sections. As before, the subsurface is vertically exaggerated by a factor of 10 in all sections.

As before, the upper part of each figure shows the anomalies: measured anomaly (red), calculated anomaly (yellow), and residual anomaly (blue). The subsurface structure consists of the lower crust or basement (blue), and the upper crust (green). Black dots mark the approximate intersection with a strike-slip fault, whereas red dots mark the intersection with a normal fault; blue dots indicate a thrust fault (all faults after Läufer et al., 2011).

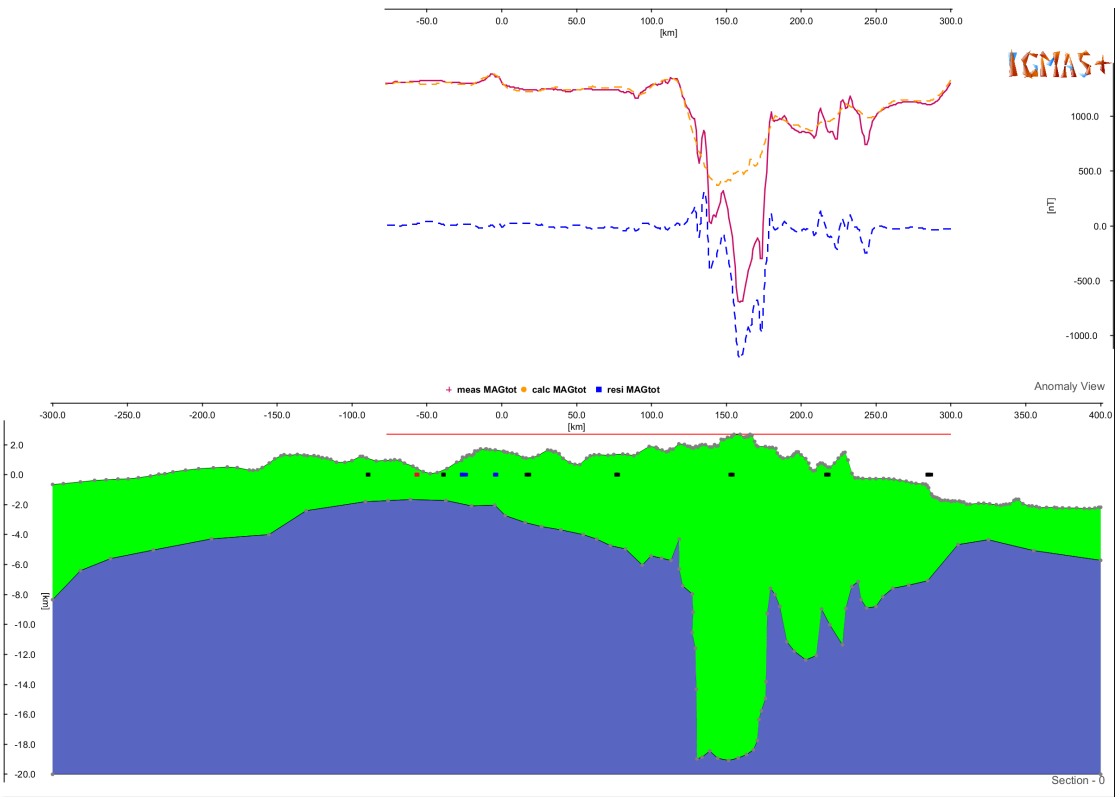

Figure D.1: Section 0 at 300 km northing.

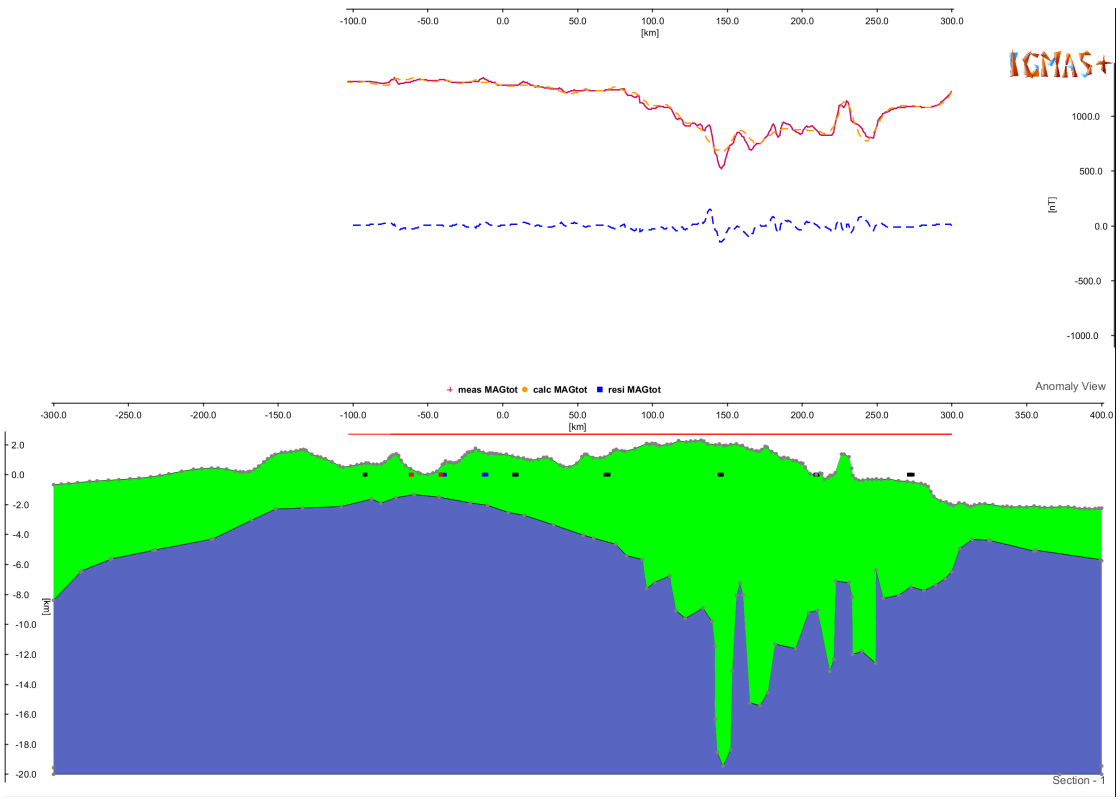

Figure D.2: Section 1 at 310 km northing.

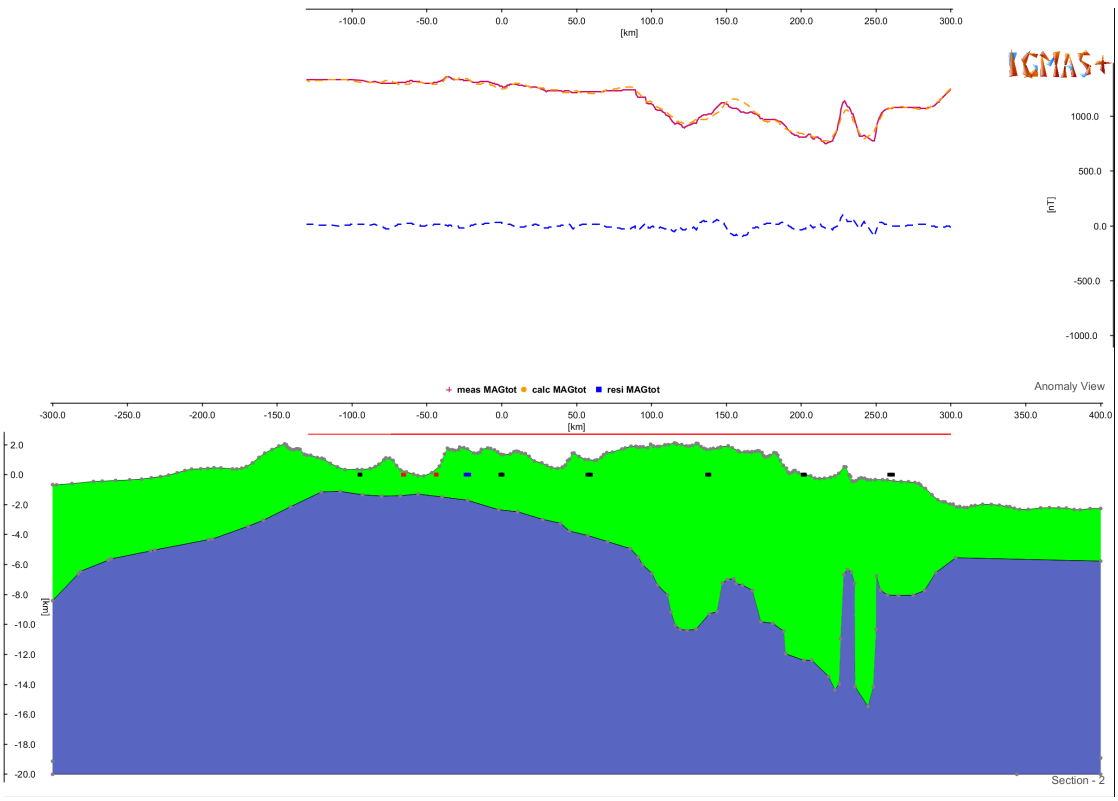

Figure D.3: Section 2 at 320 km northing.

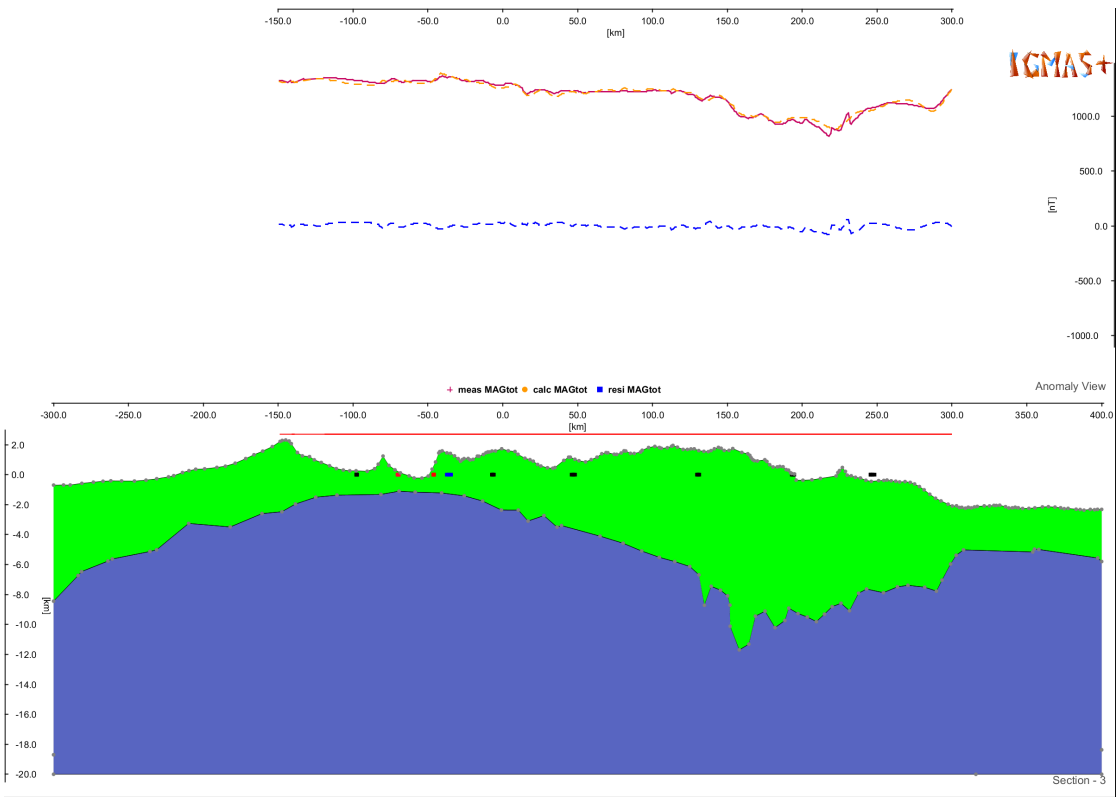

Figure D.4: Section 3 at 330 km northing.

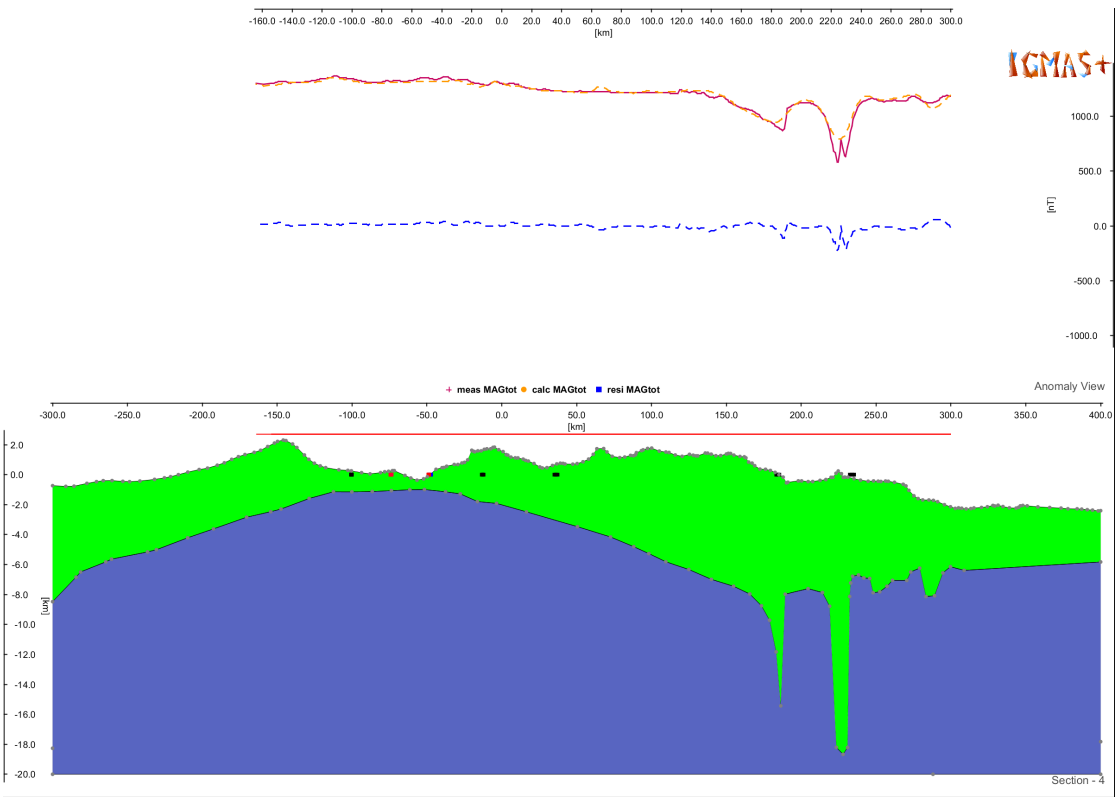

Figure D.5: Section 4 at 340 km northing.

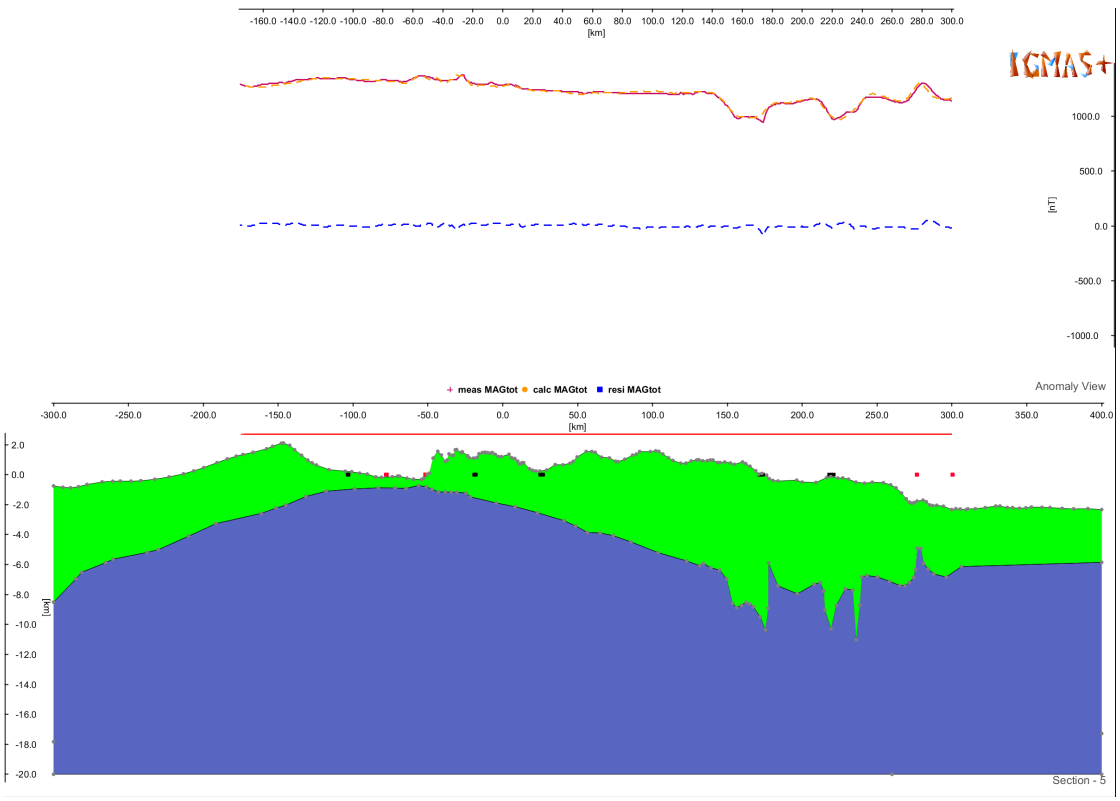

Figure D.6: Section 5 at 350 km northing.

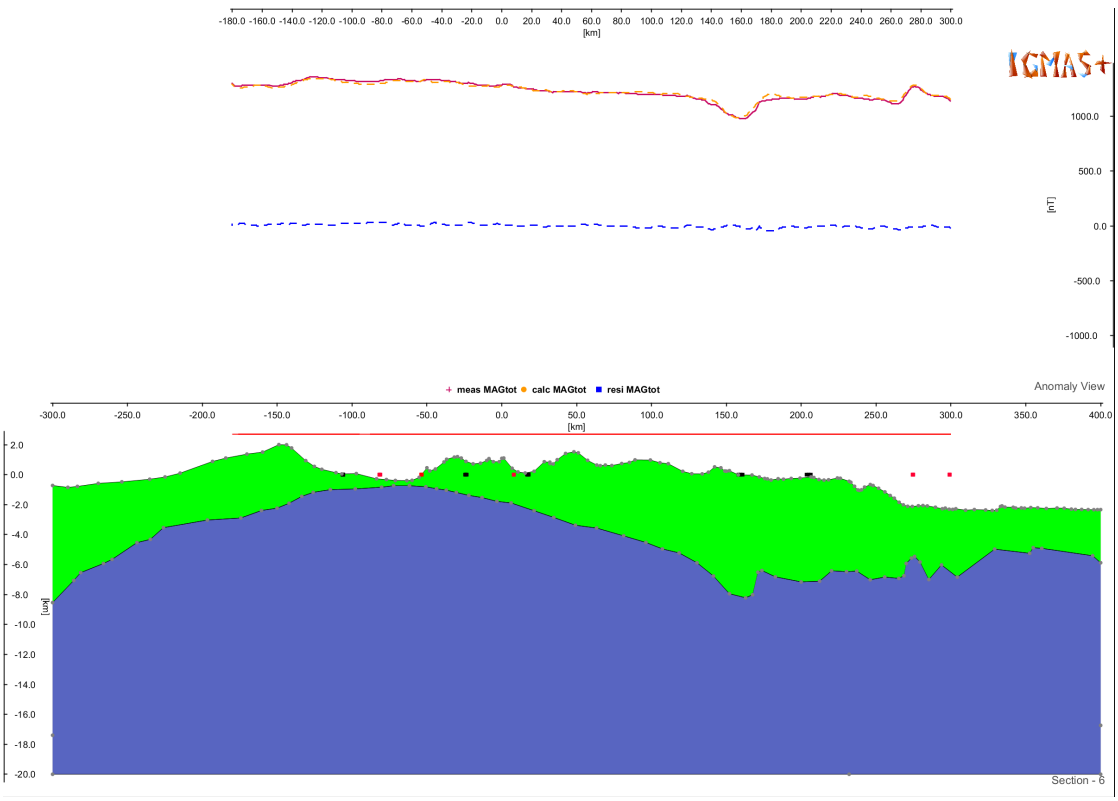

Figure D.7: Section 6 at 360 km northing.

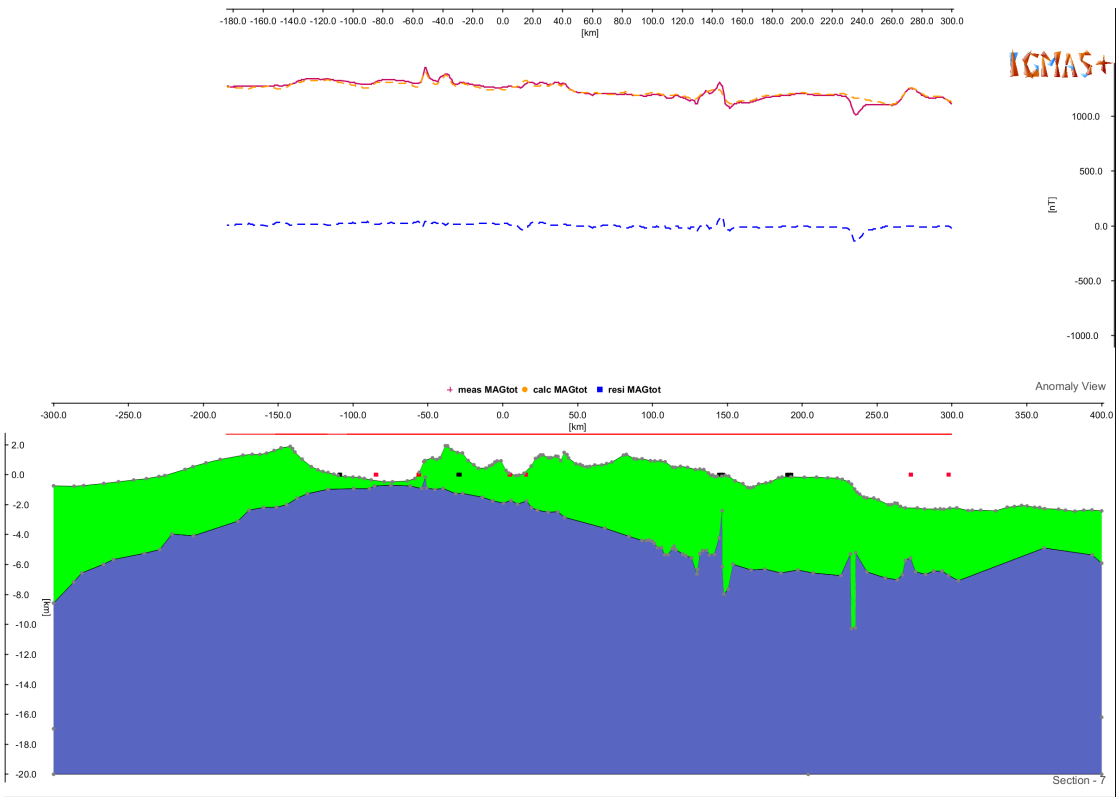

Figure D.8: Section 7 at 370 km northing.

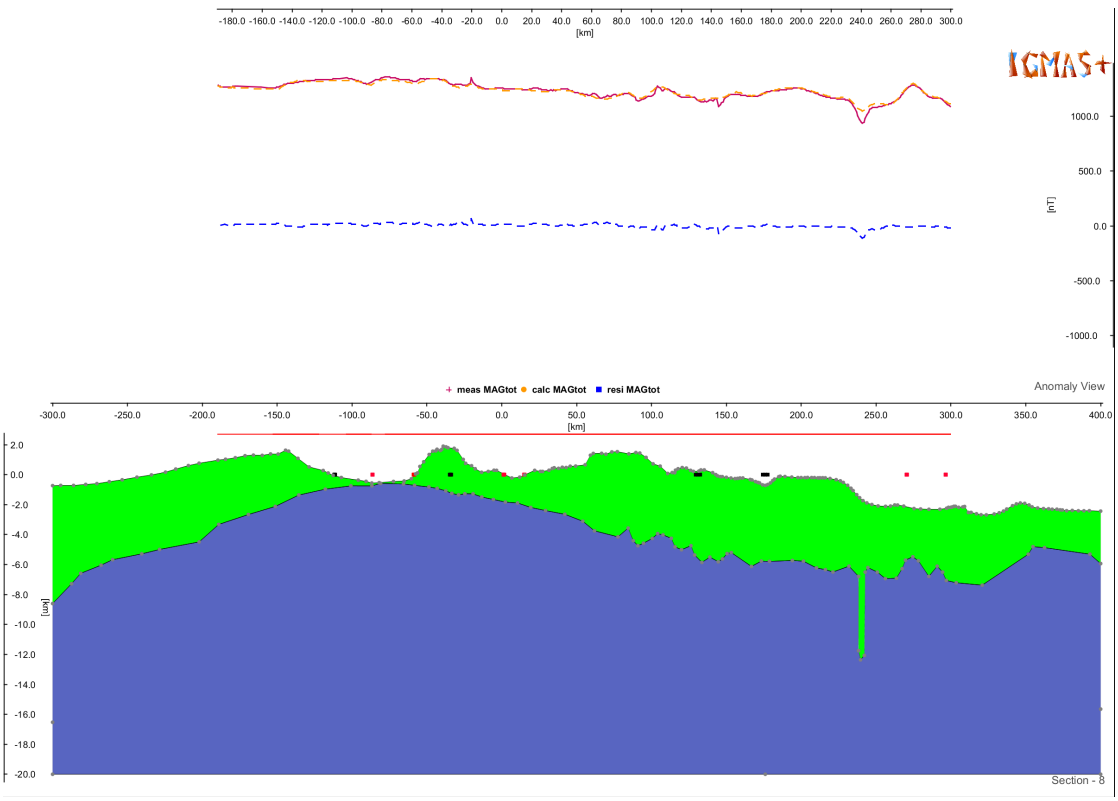

Figure D.9: Section 8 at 380 km northing.

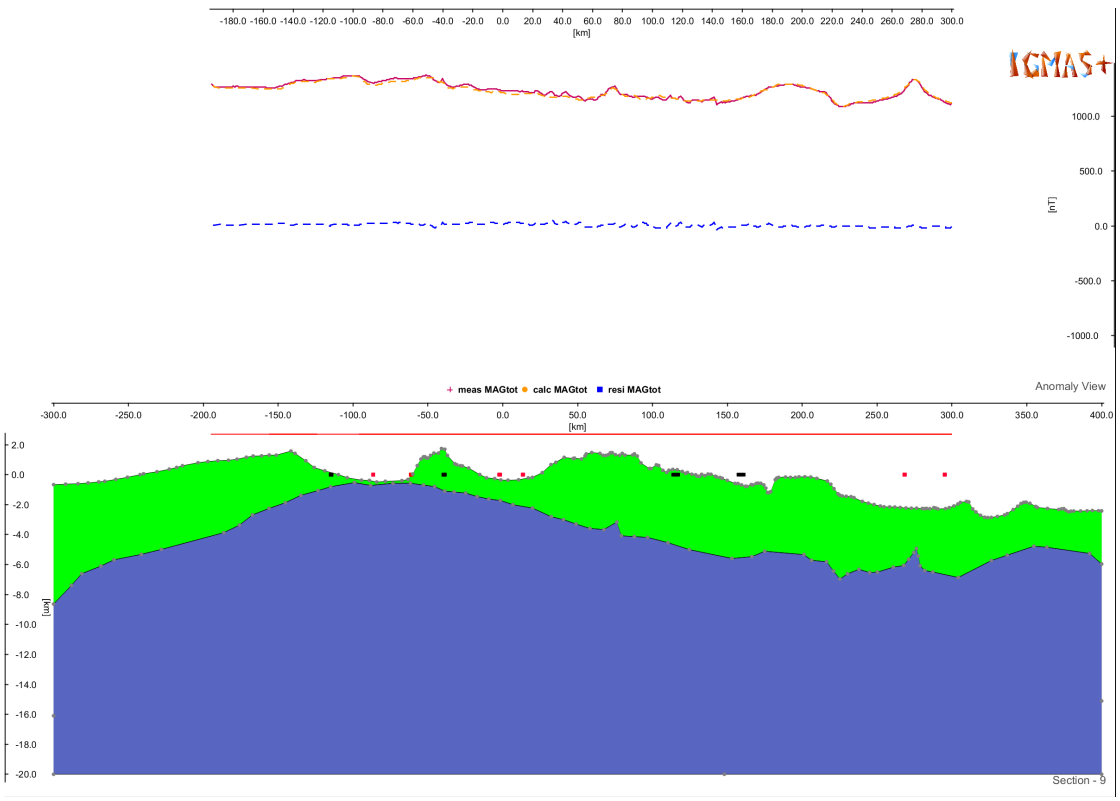

Figure D.10: Section 9 at 390 km northing.

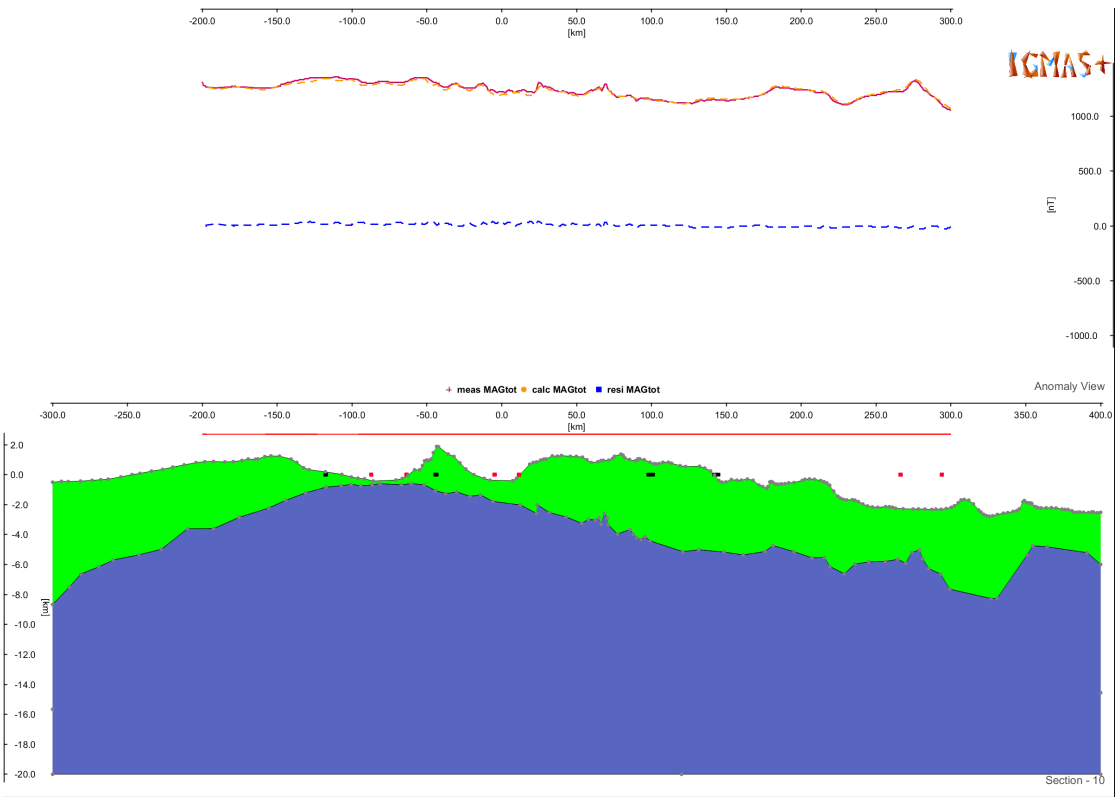

Figure D.11: Section 10 at 400 km northing.

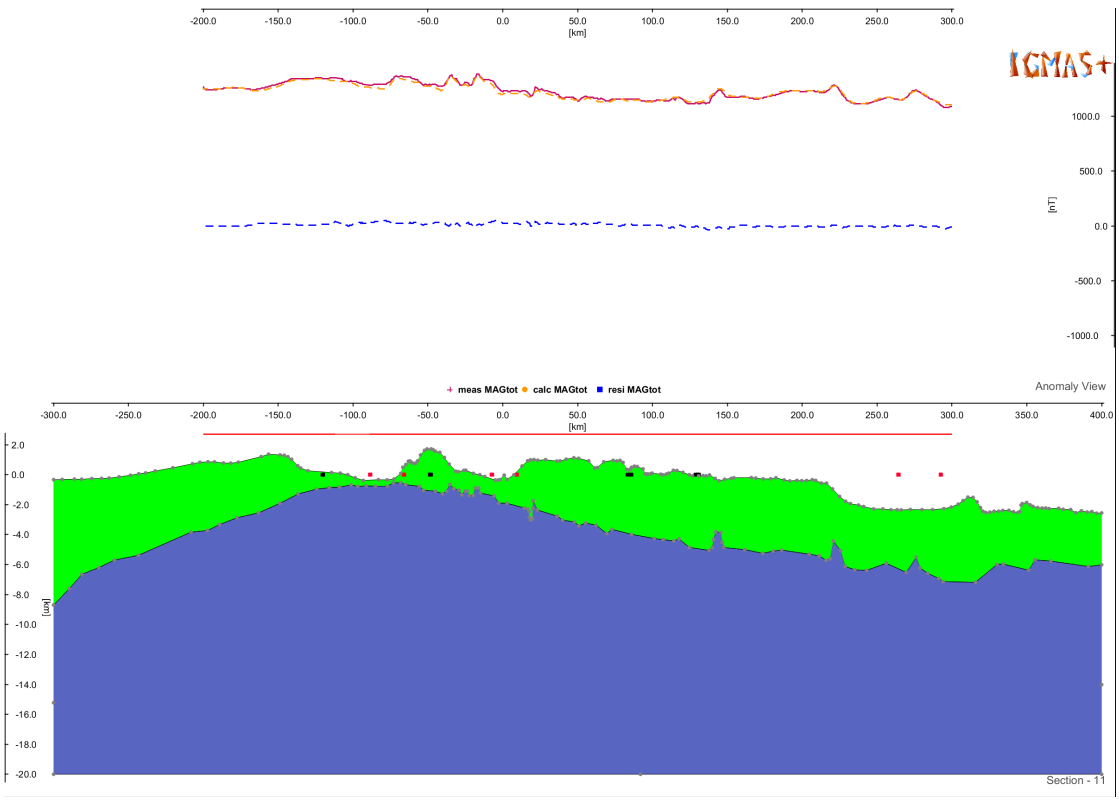

Figure D.12: Section 11 at 410 km northing.

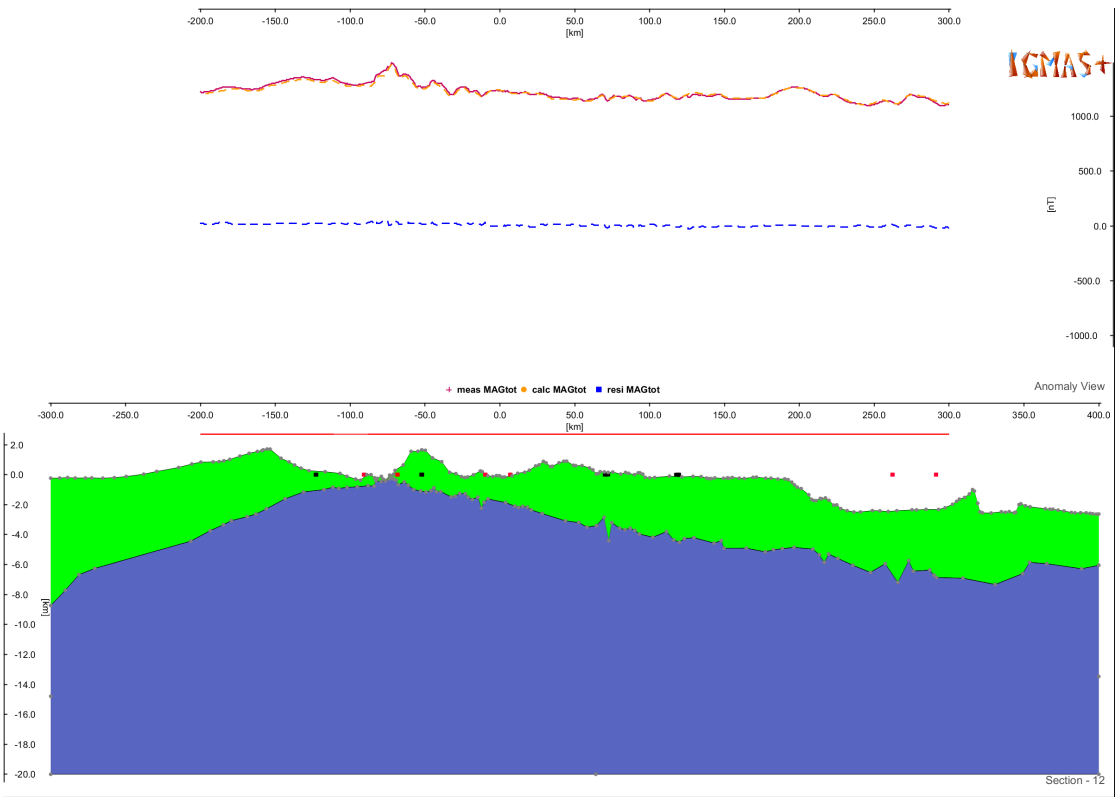

Figure D.13: Section 12 at 420 km northing.

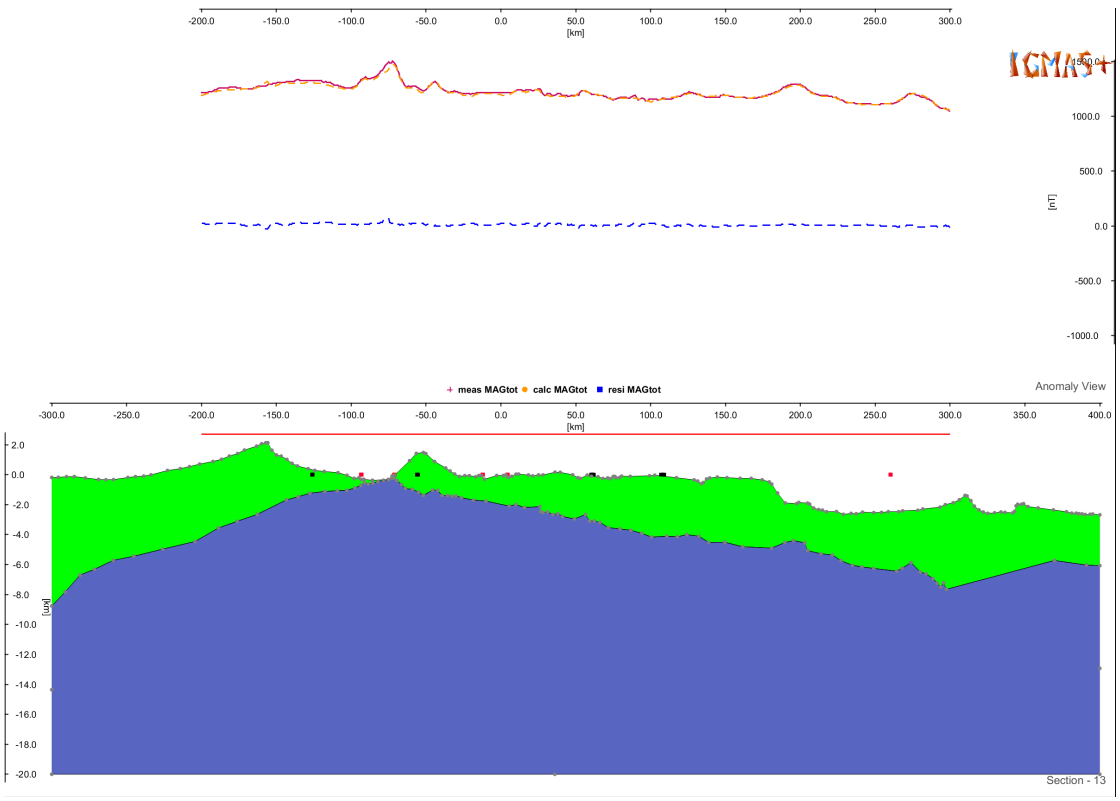

Figure D.14: Section 13 at 430 km northing.

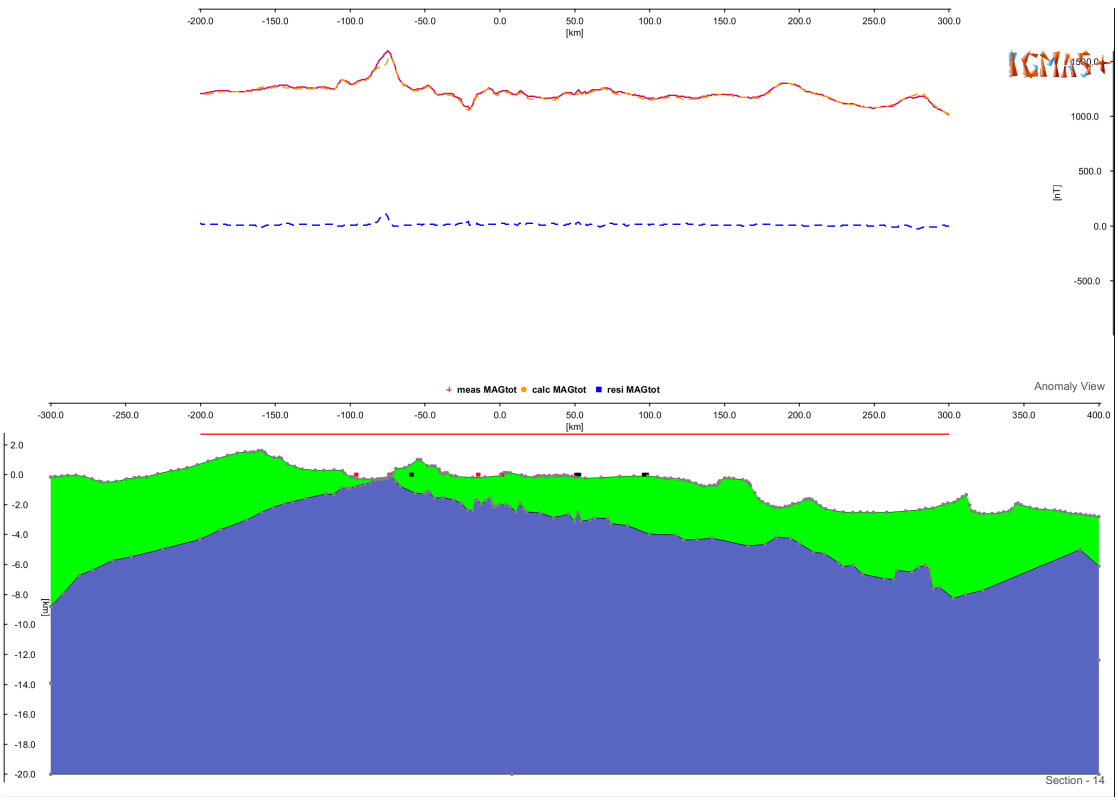

Figure D.15: Section 14 at 440 km northing.

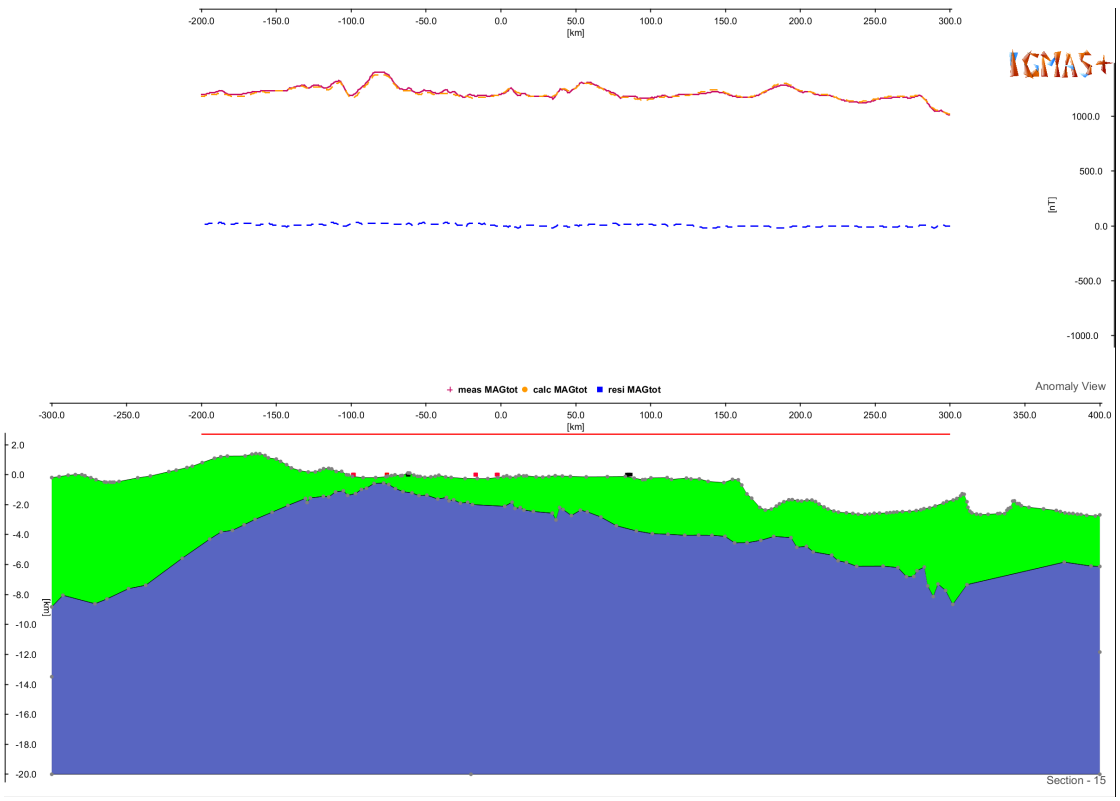

Figure D.16: Section 15 at 450 km northing.

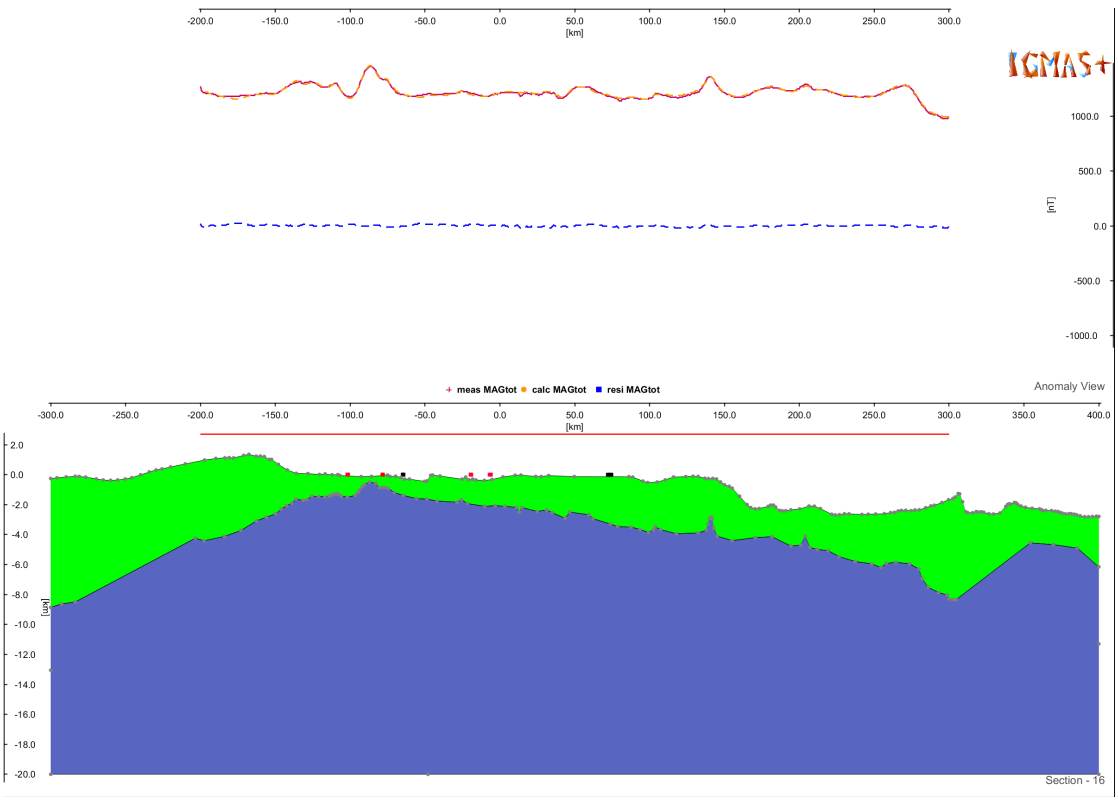

Figure D.17: Section 16 at 460 km northing.

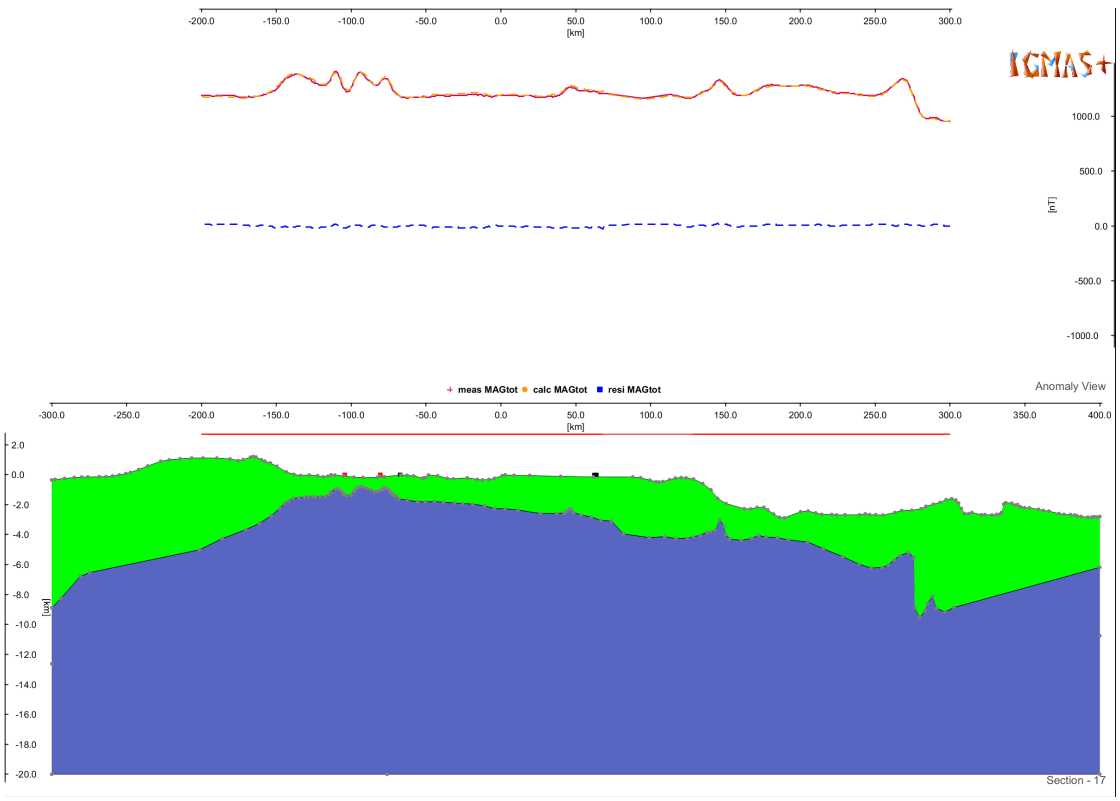

Figure D.18: Section 17 at 470 km northing.

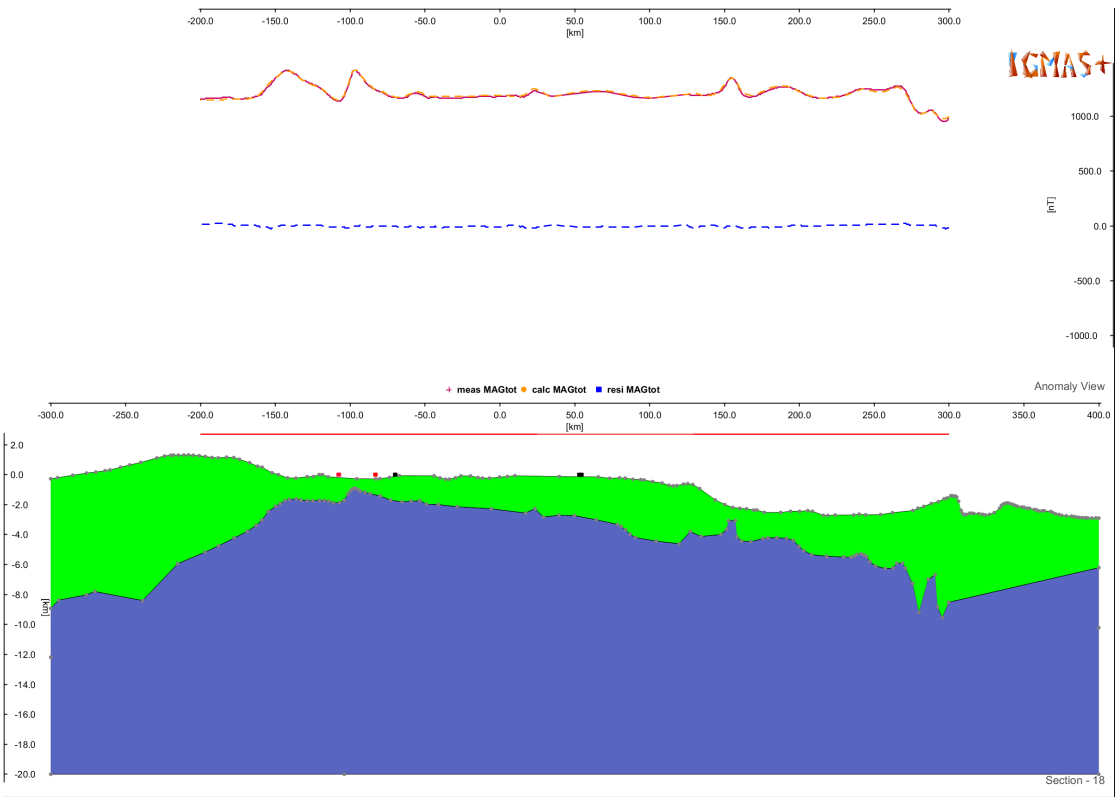

Figure D.19: Section 18 at 480 km northing.

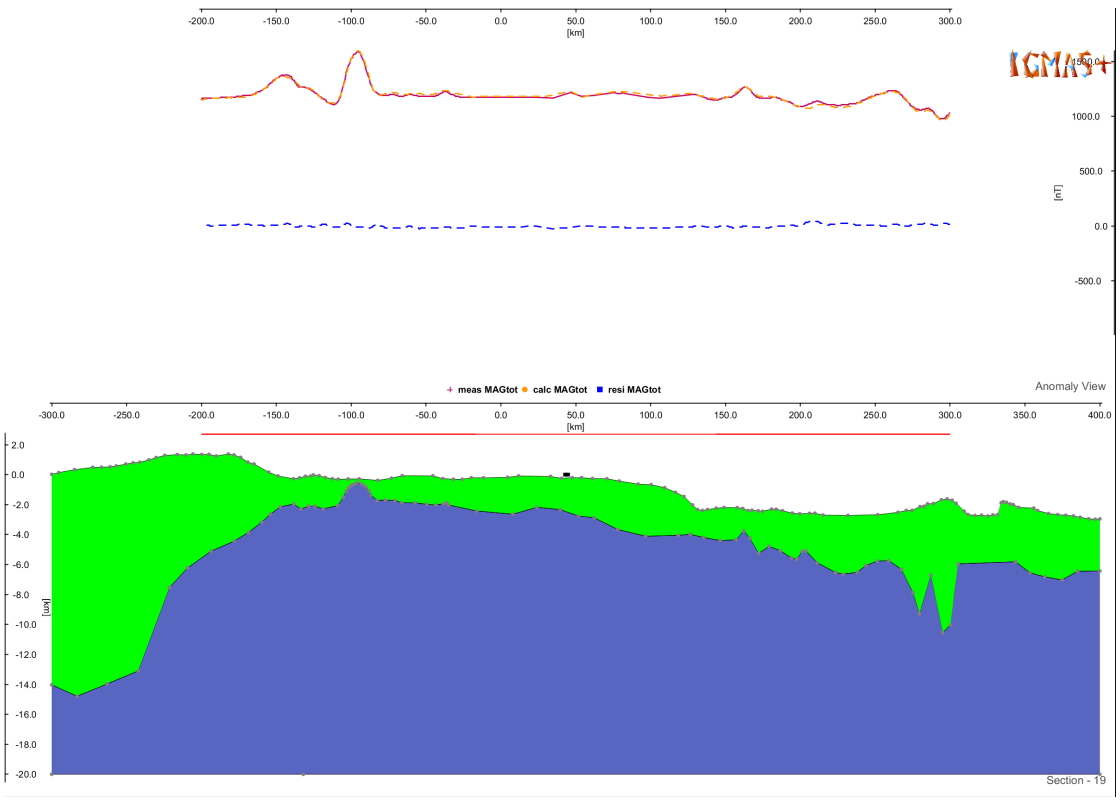

Figure D.20: Section 19 at 490 km northing.

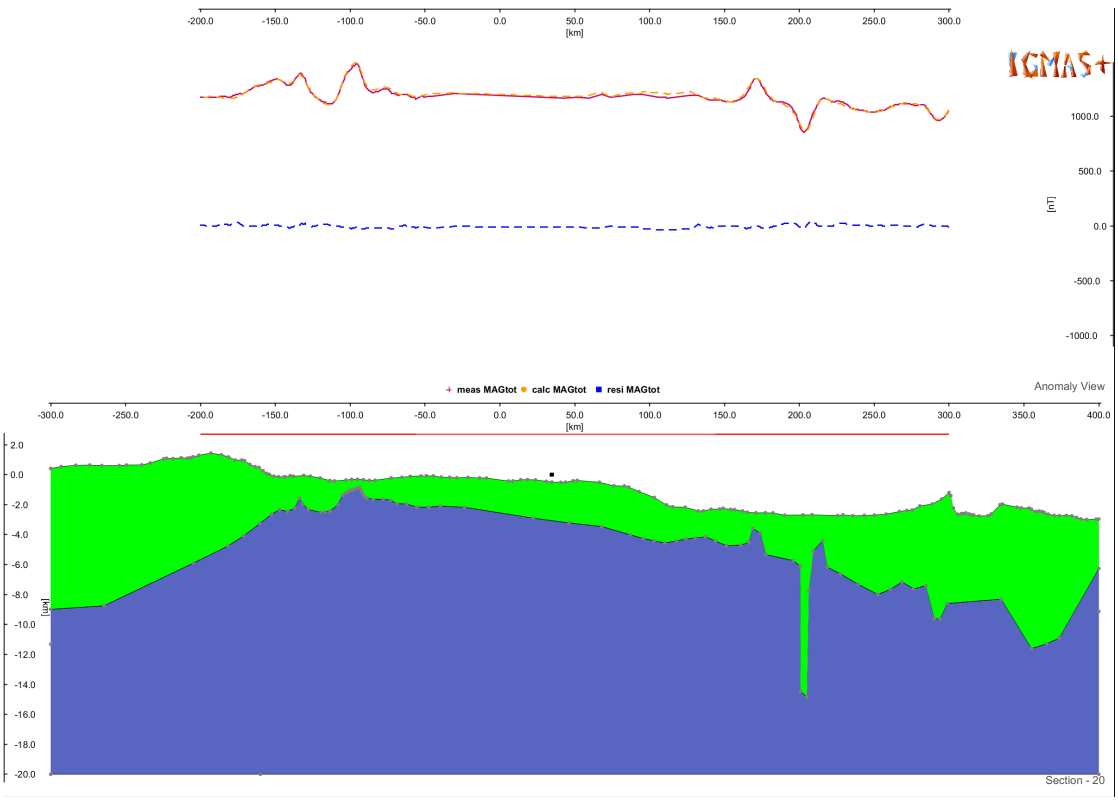

Figure D.21: Section 20 at 500 km northing.

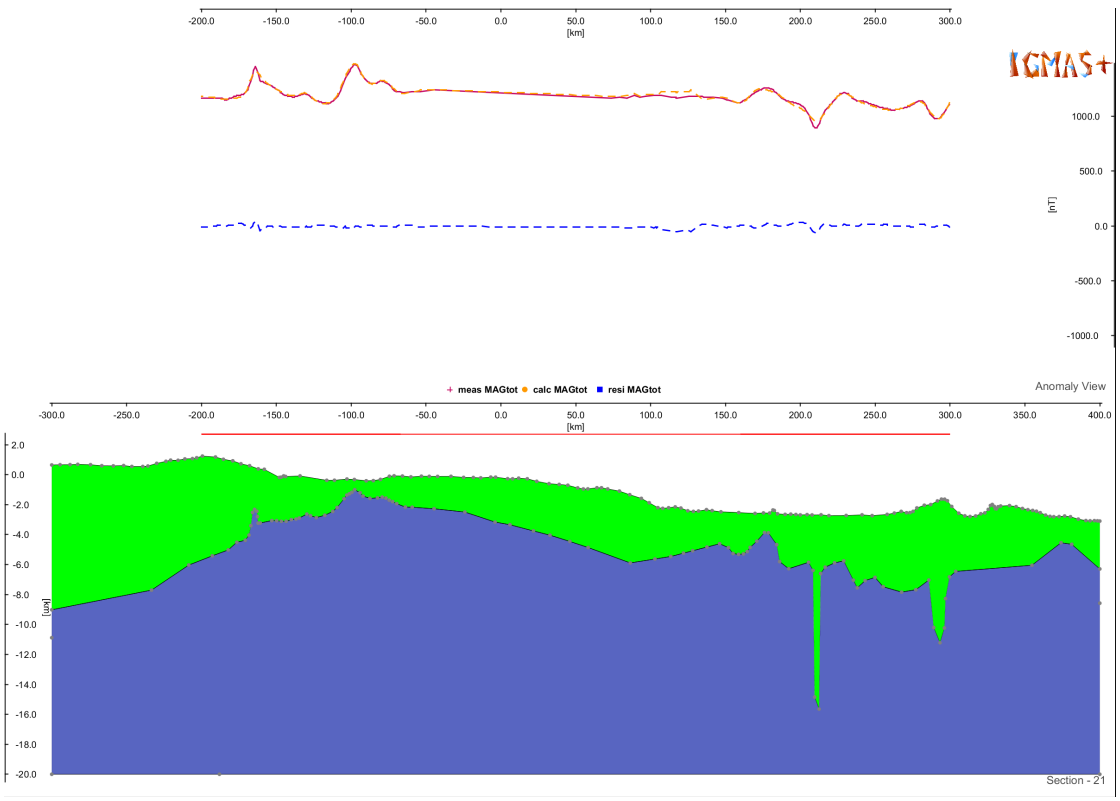

Figure D.22: Section 21 at 510 km northing.

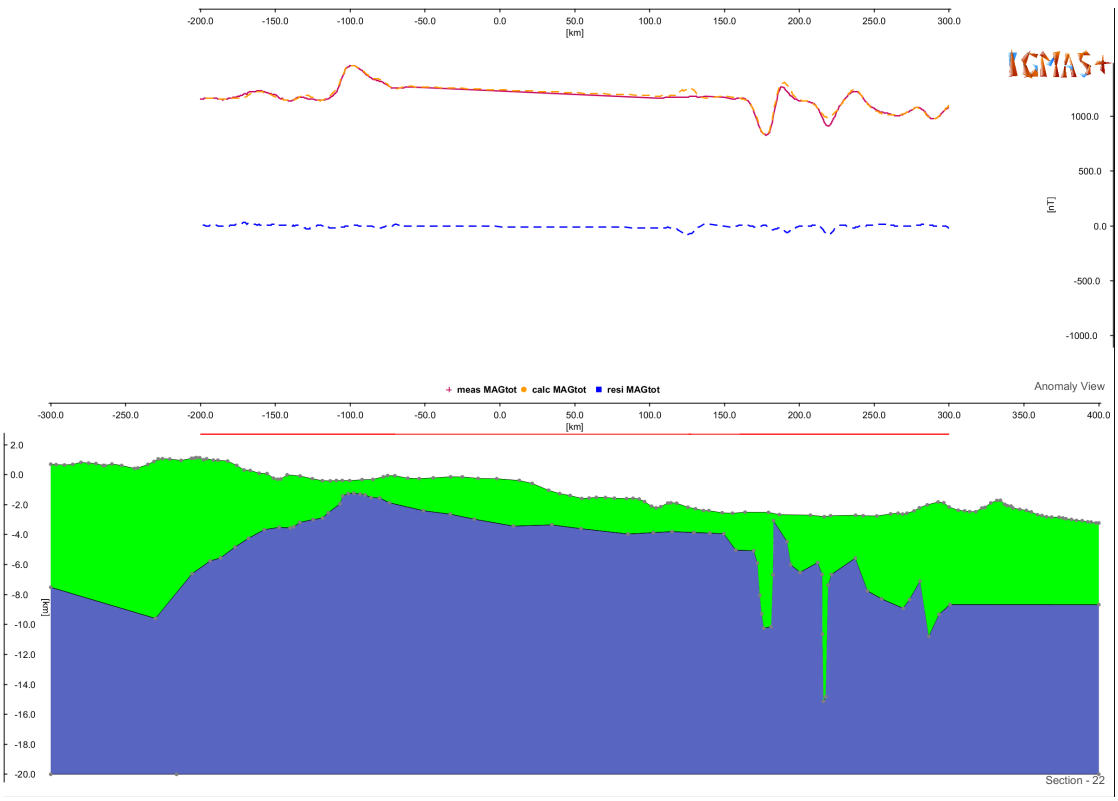

Figure D.23: Section 22 at 520 km northing.

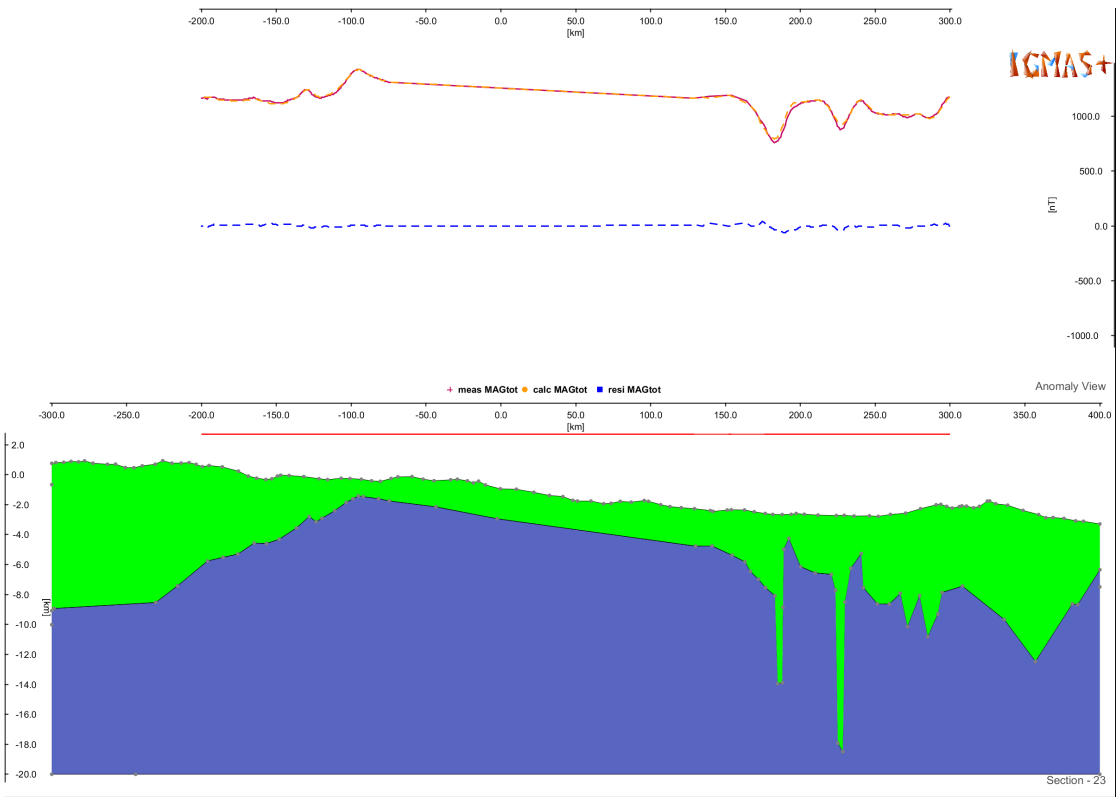

Figure D.24: Section 23 at 530 km northing.

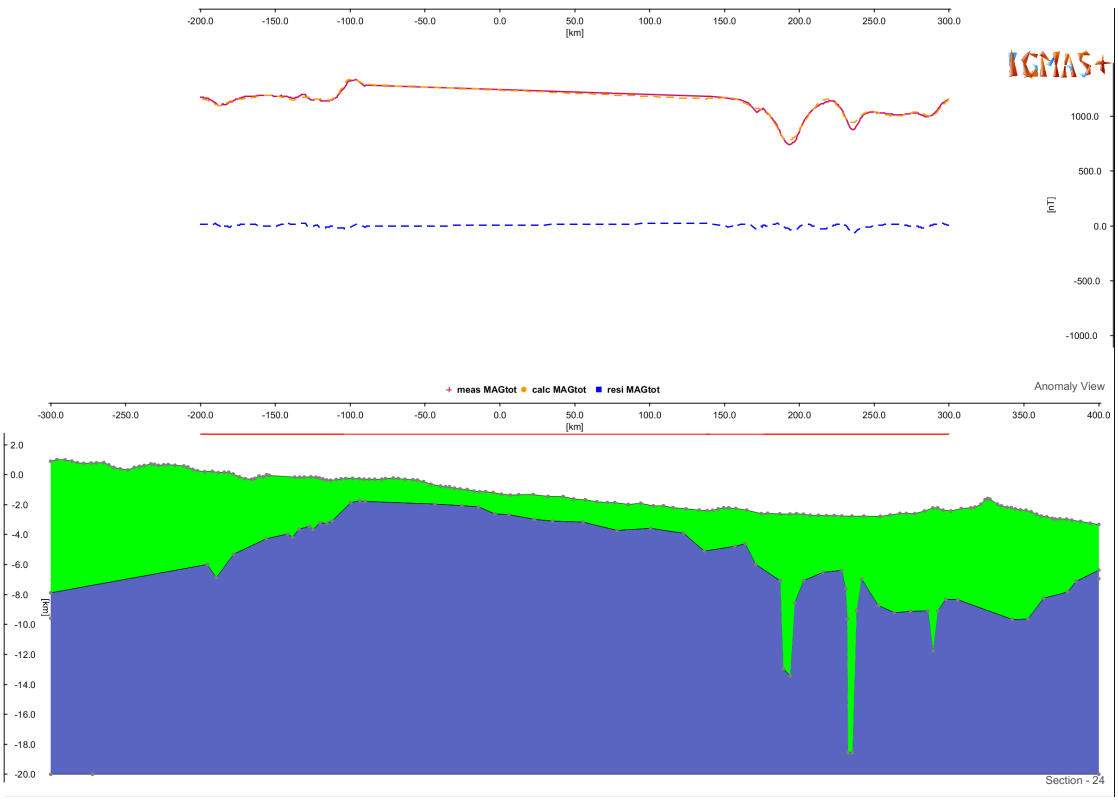

Figure D.25: Section 24 at 540 km northing.

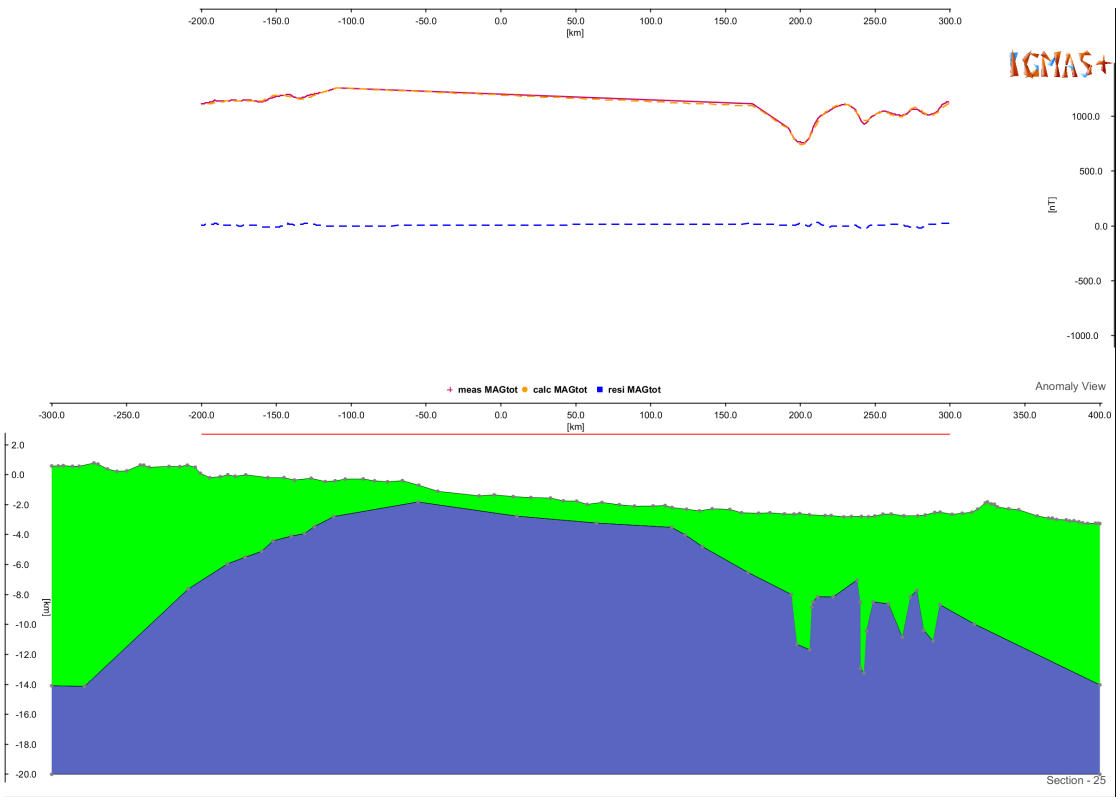

Figure D.26: Section 25 at 550 km northing.

Die vorliegende Arbeit habe ich selbständig angefertigt; alle verwendeten Quellen und Hilfsmittel sind angegeben.
I hereby confirm that I have carried out this thesis entirely myself and that all sources used during the work are cited as references.

Jena, den 27. Oktober 2017

Peter Schindler